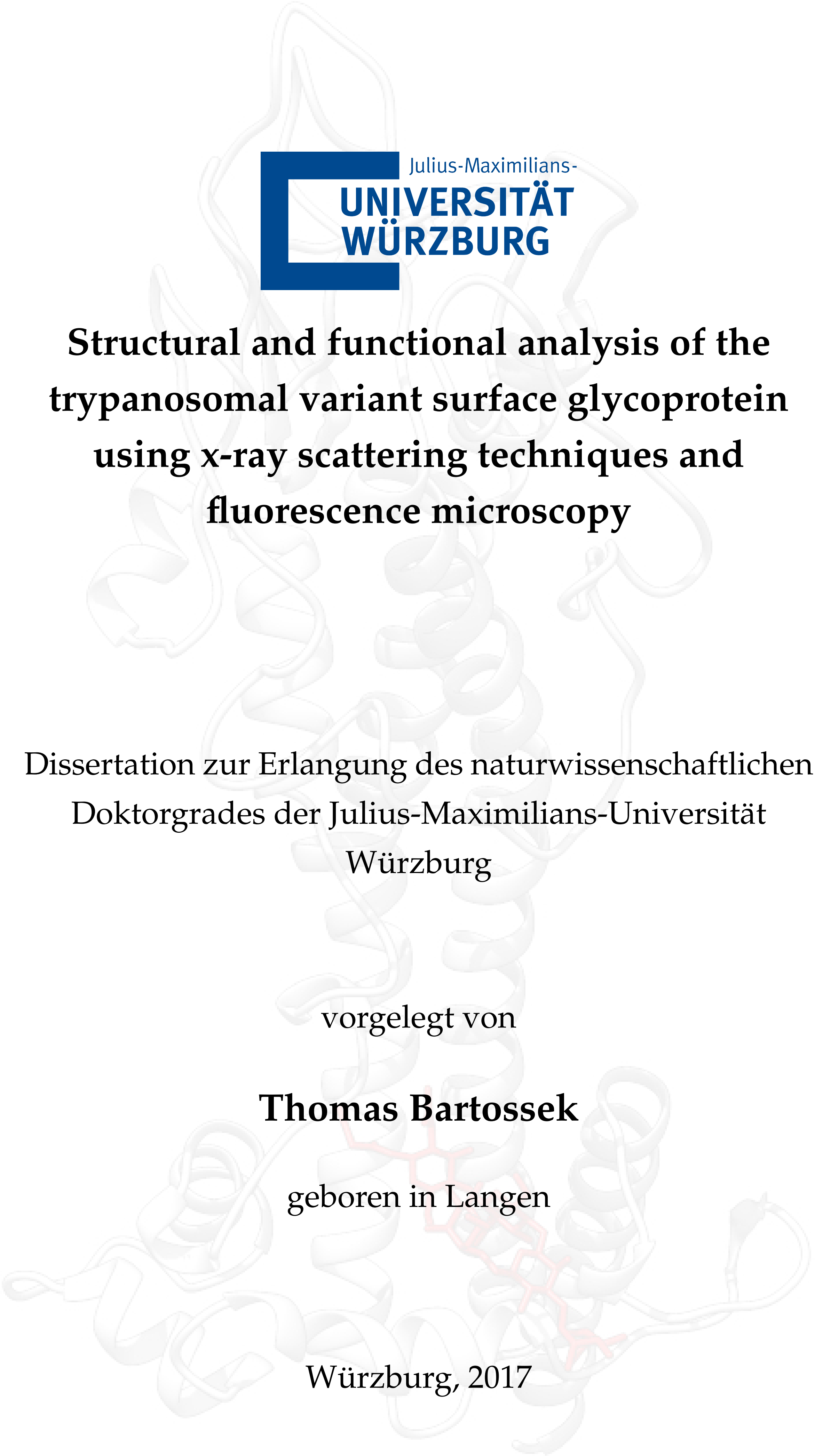

Julius-Maximilians-
UNIVERSITÄT
WÜRZBURG

Structural and functional analysis of the trypanosomal variant surface glycoprotein using x-ray scattering techniques and fluorescence microscopy

Dissertation zur Erlangung des naturwissenschaftlichen
Doktorgrades der Julius-Maximilians-Universität
Würzburg

vorgelegt von

Thomas Bartossek

geboren in Langen

Würzburg, 2017

Eingereicht am:

Mitglieder der Promotionskomission:

Vorsitzender: Prof. Dr. Thomas Rudel

1. Gutachter: Prof. Dr. Markus Engstler

2. Gutachter: Prof. Dr. Thomas Dandekar

Tag des Promotionskolloquiums:

Doktorurkunde ausgehändigt am:

”Your assumptions are your windows on the world. Scrub them off every once in a while, or the light won’t come in.”

-Isaac Asimov

Contents

1 Summary 7

2 Introduction 1

2.1 **The Parasite *Trypanosoma brucei*** . . . 2

2.2 VSG Architecture . . . 5

2.3 VSG fluorescence emissions . . . 5

2.4 Protein crystallography . . . 9

2.5 Diffraction data analysis . . . 10

2.6 Small angle x-ray scattering (SAXS) . . . 12

3 Materials and methods 15

3.1 Materials . . . 16

3.1.1 Oligonucleotides . . . 16

3.1.2 Antibodies . . . 17

3.1.3 Enzymes, Kits and Screens . . . 18

3.1.4 Buffers and solutions . . . 19

3.1.5 Trypanosome strains . . . 22

3.1.6 Plasmids . . . 23

3.1.7 Equipment . . . 23

3.1.8 Software . . . 24

3.2 Methods . . . 25

3.2.1 *T. brucei* cell cultivation . . . 25

3.2.2 Working with *E. coli* . . . 27

3.2.3 DNA techniques . . . 28

3.2.4 Protein techniques . . . 29

3.2.5 X-ray crystallography . . . 32

3.2.6 Small angle x-ray scattering (SAXS) . . . 33

3.2.7 Fluorescence microscopy . . . 36

4 Results 37

4.1 Structural analysis of VSGs . . . 38

4.1.1 sVSG purification . . . 38

4.1.2 X-ray crystallography . . . 42

4.1.2.1 VSG′Y′ . . . 42

4.1.2.2 Deglycosylated VSG′Y′ . . . 43

4.1.2.3 MITat1.1 . . . 47

4.1.2.4 MITat1.2 . . . 54

4.1.2.5 MITat1.2-TPM cocrystallisation . . . 57

4.1.2.6 MITat1.4 & MITat1.5 . . . 59

4.1.3 The complete structure of VSG MITat1.1 by SAXS . . . 61

4.1.4 The complete structure of VSG ILTat1.24 by SAXS . . . 65

4.1.5 VSG′Y′ SAXS analysis . . . 67
4.2 Characterization of VSG′Y′ fluorescence . . . 68
4.2.1 VSG′Y′ fluorescence excitation . . . 68
4.2.2 Cell density . . . 69
4.2.3 On-slide incubation . . . 70
4.2.4 Pre-excitation . . . 71
4.2.5 Medium substitution . . . 72
4.2.6 Medium depletion . . . 73
4.2.7 pH variations . . . 73
4.2.8 HPLC analysis of cultivation media . . . 74
4.2.9 Fluorescence quenching by BPB competition . . . 75
4.2.10 VSG′Y′ phosphorescence analysis . . . 76
4.2.11 Fluorescence quenching by surface labeling . . . 76
4.2.12 Fluorescence in artificial bilayers . . . 77
4.2.13 sVSG fluorescence in solution . . . 77
4.2.14 Live cell tryptic treatment . . . 77
4.2.15 Calorimetric detection of PR binding . . . 78
4.3 The trypanocidal effect . . . 80
4.3.1 Trypanocidal effect triggering . . . 80
4.3.2 Influence of TPM concentrations . . . 81
4.3.3 Influence of antioxidants . . . 82
4.3.4 Reversibility of cell photo-paralysis . . . 83
4.4 Fluorescence of VSG′Y′ mutants . . . 84
4.4.1 Generating mutants . . . 84
4.4.2 Western Blot analysis . . . 85
4.4.3 Immunofluorescence . . . 85
4.4.4 Cell cultivation . . . 87
4.4.5 Cell fluorescence analysis . . . 88
4.4.6 TPM docking simulations . . . 88

5 Discussion **90**
5.1 Structural analysis of VSGs . . . 91
5.2 Characterization of VSG′Y′ fluorescence . . . 99
5.3 The trypanocidal effect . . . 104
5.4 Fluorescence of VSG′Y′ mutants . . . 106

6 Abbreviations **110**

7 References **112**

8 Appendix **I**
8.1 Composition of x-ray screens . . . II
8.2 Affidavit . . . XVII

8.3 Publications XVIII
8.4 Acknowledgements XIX

1 Summary

Summary

Trypanosoma brucei is an obligate parasite and causative agent of severe diseases affecting humans and livestock. The protist lives extracellularly in the bloodstream of the mammalian host, where it is prone to attacks by the host immune system. As a sophisticated means of defence against the immune response, the parasite's surface is coated in a dense layer of the variant surface glycoprotein (VSG), that reduces identification of invariant epitopes on the cell surface by the immune system to levels that prevent host immunity. The VSG has to form a coat that is both dense and mobile, to shield invariant surface proteins from detection and to allow quick recycling of the protective coat during immune evasion. This coat effectively protects the parasite from the harsh environment that is the mammalian bloodstream and leads to a persistent parasitemia if the infection remains untreated. The available treatment against African Trypanosomiasis involves the use of drugs that are themselves severely toxic and that can lead to the death of the patient. Most of the drugs used as treatment were developed in the early-to-mid 20th century, and while developments continue, they still represent the best medical means to fight the parasite. The discovery of a fluorescent VSG gave rise to speculations about a potential interaction between the VSG coat and components of the surrounding medium, that could also lead to a new approach in the treatment of African Trypanosomiasis that involves the VSG coat. The initially observed fluorescence signal was specific for a combination of a VSG called *VSG'Y'* and the triphenylmethane (TPM) dye phenol red. Exchanging this TPM to a bromo-derivative led to the observation of another fluorescence effect termed *trypanicidal effect* which killed the parasite independent of the expressed VSG and suggests a structurally conserved feature between VSGs that could function as a specific drug target against *T. b. brucei*. The work of this thesis aims to identify the mechanisms that govern the unique VSG'Y' fluorescence and the trypanocidal effect. Fluorescence experiments and protein mutagenesis of VSG'Y' as well as crystallographic trials with a range of different VSGs were utilized in the endeavour to identify the binding mechanisms between TPM compounds and VSGs, to find potentially conserved structural features between VSGs and to identify the working mechanisms of VSG fluorescence and the trypanocidal effect. These trials have the potential to lead to the formulation of highly specific drugs that target the parasites VSG coat.

During the crystallographic trials of this thesis, the complete structure of a VSG was solved experimentally for the first time. This complete structure is a key component in furthering the understanding of the mechanisms governing VSG coat formation. X-ray scattering techniques, involving x-ray crystallography and small angle x-ray scattering were applied to elucidate the first complete VSG structures, which reveal high flexibility of the protein and supplies insight into the importance of this flexibility in the formation of a densely packed but highly mobile surface coat.

Zusammenfassung

Trypanosoma brucei ist ein eukaryotischer Parasit welcher bei Menschen und Nutztieren schwere Krankheiten auslöst. Der Protist lebt extrazellulär im Blutstrom seines Säugetier-Wirtes, in welchem er unter konstantem Angriff durch das Wirts-Immunsystem steht. Als ausgeklügelte Methode zur Umgehung der Immunantwort besitzt der Parasit einen dichten Oberflächenmantel des variablen Oberflächen-Glycoproteins (VSG), welcher die Identifikation invariabler Oberflächenproteine durch das Immunsystem erschwert und Wirts-Immunität gegen den Parasiten verhindert. Der gebildete VSG-Mantel muss gleichzeitig eine hohe Dichte besitzt, um invariable Oberflächenproteine vor Immundetektion zu beschützen, und eine hohe Mobilität aufweisen, um ein schnelles Recycling des Schutzmantels während Immunantworten zu gewährleisten. Dieser Mantel schützt den Parasiten effektiv vor dem Wirts-Immunsystem und führt bei fehlender Behandlung des Patienten zur persistenten Parasitemie durch *Trypanosoma brucei*. Die verfügbaren Behandlung gegen die Afrikanische Trypanosomiasis beinhaltet die Benutzung von Medikamenten welche ihrerseits z.T. stark toxisch sind und den Tod des Patienten verursachen können. Ein Großteil der verfügbaren Medikamente wurden zu Beginn des letzten Jahrhunderts entwickelt und stellen trotz anhaltenden Entwicklungen noch immer die beste Lösung im Kampf gegen den Parasiten dar. Die Entdeckung eines fluoreszierenden VSGs deutete auf eine Interaktionen zwischen dem VSG Mantel und Bestandteilen des umgebenden Medium hin, welche die Entwicklung von Medikamenten mit dem VSG Mantel als Drug Target ermöglichen könnte. Das ursprünglich beobachtete Fluoreszenz-Signal war spezifisch für eine Kombination eines VSG namens *VSG'Y'* und dem Triphenylmethan (TPM) Phenolrot. Der Austausch von Phenolrot gegen ein Brom-Derivat führte zur Beobachtung eines weiteren Fluoreszenz-Effekts, welcher unabhängig vom exprimierten VSG auftritt und letal für den Parasiten ist. Dieser so genannten *Trypanozide Effekt* lässt auf konservierte Strukturen schließen, welche von allen VSGs geteilt werden und als hochspezifisches Drug Target gegen *T. b. brucei* fungieren könnten. Das Ziel der vorliegenden Arbeit war es, die Mechanismen zu identifizieren, welche die einzigartige VSG'Y'-Fluoreszenz und den Trypanoziden Effekt auslösen. Fluoreszenz-Experimente und Protein-Mutagenese von VSG'Y', sowie röntgenkristallographische Analysen mit mehreren unterschiedlichen VSGs wurden in dem Bestreben durchgeführt, die Bindung zwischen VSGs und TPMs zu charakterisieren, potentiell konservierte Strukturen von VSGs zu finden und die Mechanismen der einzigartigen VSG'Y'-Fluoreszenz und des Trypanoziden Effekts zu identifizieren. Diese Arbeiten haben das Potenzial die Formulierung hochspezifischer Medikamente mit VSGs als Drug Target anzutreiben.

Im Rahmen der kristallographischen Analysen wurden die ersten vollständigen VSG Strukturen ermittelt, welche eine hohe Bedeutung für das Verständnis über die Bildung des VSG-Mantels haben. Die VSG Strukturen wurden u.a. per Röntgenkristallographie und Kleinwinkel-Röntgenstreuung aufgeschlüsselt und zeigten dass VSGs ein hohes Maß an Flexibilität besitzen. Diese Flexibilität ist wichtig für die Bildung eines dichten und hochmobilen VSG-Mantels.

2 Introduction

2.1 The Parasite *Trypanosoma brucei*

Trypanosoma brucei is a unicellular, flagellated, eukaryotic parasite and the causative agent of Nagana in human livestock in Africa (Bruce, 1895) and of human African trypanosomiasis (HAT). *T. brucei* is transmitted to the mammalian host by the insect vector *Glossina spp.* when it takes a blood meal. The parasite's two environments, mammalian bloodstream and tsetse-fly digestive system, require individual cell-biological and morphological adaptations by the parasite. The parasite is transmitted to the mammalian host in form of metacyclic trypomastigotes and differentiate into the proliferating long slender bloodstream form. Eventually, cells develop into short stumpy forms that are cell-cycle arrested and pre-adapted for survival in the tsetse fly (MacGregor *et al.,* 2011). Upon uptake by the tsetse-fly during a blood meal, the parasite enters the midgut and differentiate into procyclic trypomastigotes that express procyclins on their cell surface. Procyclic trypomastigotes are proliferative and migrate through the peritrophic matrix and the proventriculus to the salivary ducts and ultimately to the salivary gland of the tsetse fly. In the proventriculus the trypomastigotes differentiate into long epimastigotes and short epimastigotes by means of asymmetric division (Van Den Abbeele *et al.,* 1999). In the salivary glands, the life cycle is completed as the short epimastigotes differentiate asymmetrically into metacyclic trypomastigotes (Rotureau *et al.,* 2012) that exchange procyclines for the variant surface glycoprotein (VSG) on their cell surface. Once transmitted, the parasite lives extracellularly in the bloodstream of the host, where it is under constant attack by the immune system and requires the dense VSG coat as a sophisticated means of defence against the immune response (Fig. 1a) (Vickerman, 1969). The VSG coat shields invariant surface proteins and reduces identification by the immune system sufficiently to prevent host immunity (Cross, 1975; Cardoso de Almeida & Turner, 1983; Ziegelbauer & Overath, 1993; Sullivan *et al.,* 2013). The VSG constitutes the mayor antigenic target displayed by BSF trypanosomes and once identified the parasite is quickly killed by the host immune system (Macaskill *et al.,* 1981; McLintock *et al.,* 1993). To establish persistent parasitemia *T. brucei* can change the expressed VSG to an antigenically distinct VSG from a subtelomeric archive composed of more than 1200 VSG genes (Berriman *et al.,* 2005). Alternatively, the parasite can switch the active expression site (ES), a specialist expression locus from which the current VSG is actively transcribed, to one of approximately 20 - 30 inactive expression sites (Vanhamme *et al.,* 2001). This results in deactivation of the previously active ES and in the expression of a different VSG from the now active ES. Only a single type of VSG is transcribed at any given time and during the so called *antigenic variation* the VSG coat is completely exchanged after approximately one week (Seyfang *et al.,* 1990), forcing the host immune system to adapt anew. The single actively transcribed VSG is located in one of approximately 20 specialized subtelomeric expression sites of which only one is active at any given time (Navarro & Cross, 1996; Hertz-Fowler *et al.,* 2008). The active expression site changes stochastically with a rate of 1×10^{-4} per generation (Aitcheson *et al.,* 2005) and an antigenically new VSG form is displayed on the cell surface. While the immune system adapts to the newly expressed

VSG, a subpopulation of the parasite has already begun changing the surface coat to yet another distinct VSG, repopulating and causing reoccurring waves of parasitemia (Fig. 1b) (Ross & Thomason, 1910).

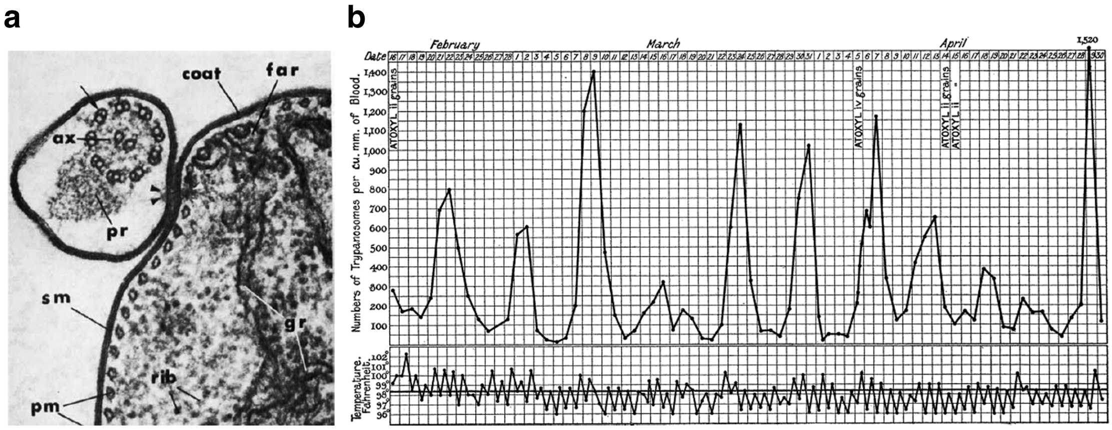

Figure 1 – Parasitemia of trypanosomiasis and EM tomography of the VSG coat. a) First recording of the VSG coat (denominated ’coat’) by Vickerman *et al.* 1969. b) Display of the periodic course of *T. b. gambiense* parasitemia from Ross and Thomson 1910.

An additional mechanism that delays the host immune response involves the removal of antibody-bound VSGs by hydrodynamic drag forces (Engstler *et al.*, 2007). During the so called *antibody clearance* the antibody-VSG-complexes are transported to the flagellar pocket, a membrane cavity on the cell surface which is responsible for all endo- and exocytosis. Here, the complexes are endocytosed and the antibodies are transported to the lysosome (Fig. 2) while the VSGs are re-cycled to the cell surface. This mechanism relies on high mobility of the densely packed surface coat. Part of the required mobility can be attributed to the glycosylphosphatidylinositol (GPI) anchors that attach the VSG to the cell membrane. The GPI anchor, which is covalently linked to the VSG C-terminal domain is composed of at least four sugar residues and a phosphatidylinositol phospholipid acid that are connected to the outer layer of the cell membrane by two myristoyl moieties.

While antigenic variation relies on a VSG layer of high density to protect invariable surface proteins, antibody clearance requires high mobility of the same layer. Simultaneous function of the two defensive mechanisms must rely both on the structure of the GPI anchor and the VSG protein itself.

Due to the trypanosome’s remarkable capabilities of immune evasion the course of African trypanosomiasis is chronic persistent and, if untreated, will lead to the death of the human host in case of *T. b. rhodiense* and *T. b. gambiense*. Livestock infected by *T.b. brucei* is affected by fever, weakness and lethargy, which leads to weight loss and anaemia. However, most of the livestock does not decease by the infection, but presents a reservoir for further propagation of the disease via the tsetse fly vector (Penchenier *et al.*, 2005). However, the precise epidemiological role of this reservoir is still unknown.

African trypanosomiasis is spread through sub-Saharan Africa, covering a total of 36 countries and 60 million people (Fig. 3) (Kennedy, 2006; Brun & J. Blum, 2012). As of 2009 the number of infections among the human population has dropped below 10,000

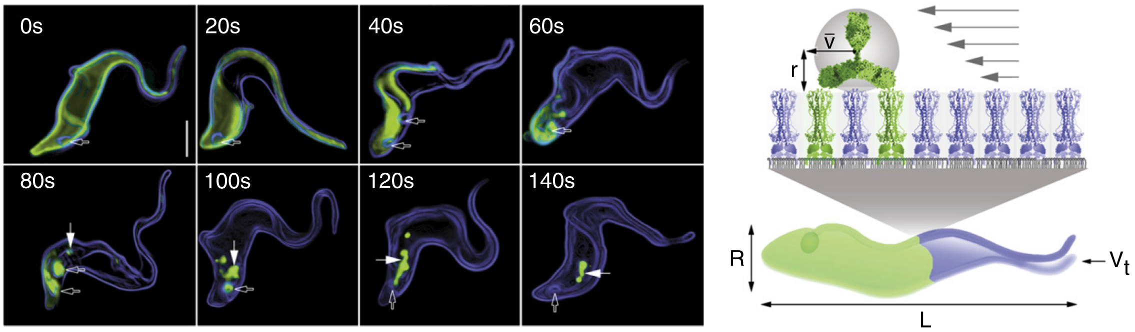

Figure 2 – Illustration of antibody clearance. VSG-antibody-complexes are transported to the posterior end of the cell by hydrodynamic drag forces, where they are endocytosed. Figure edited from Engstler *et al.* (2007).

people for the first time in 50 years, however many cases are assumed to go unreported. In 2014, 3796 cases of trypanosomiasis were recorded (WHO, 2016).

Symptoms of HAT occur in two distinctive phases. Symptoms of the first phase are headaches, fever, joint pains, itching and swelling of lymph nodes to a hugely increased size. If the infection remains untreated, more severe symptoms including anemia, endocrine, cardiac and kidney dysfunction will eventually follow. During the second phase, the parasite passes through the blood-brain barrier and infects the central nervous system. Symptoms of this neurological phase include confusion, reduced coordination and disruption of the patients sleep cycle. If further untreated the infection eventually leads to coma and death of the patient.

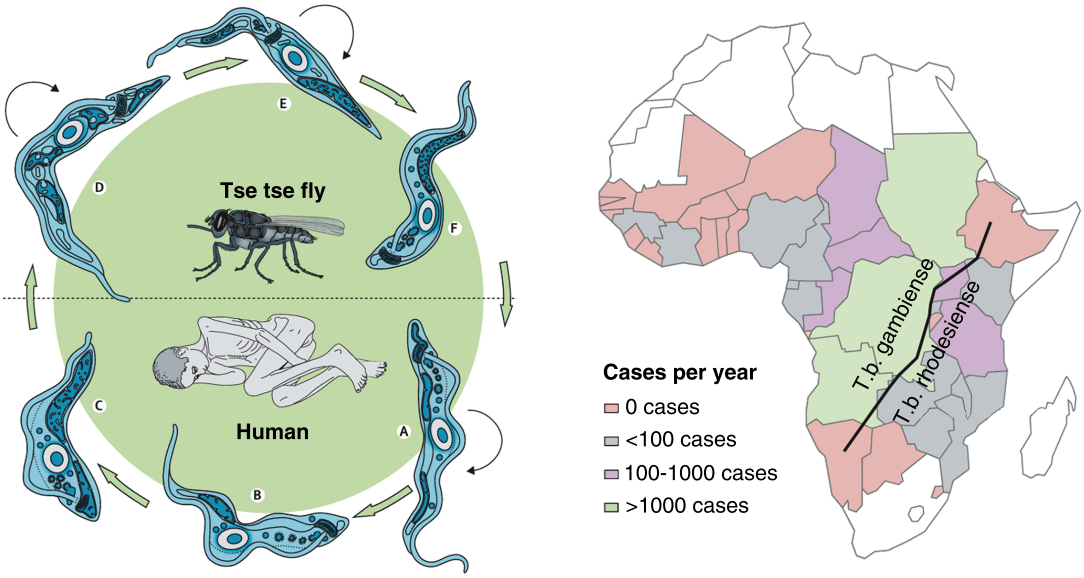

Figure 3 – Life cycle of trypanosomes and parasite distribution. Left: life cycle of human pathogen trypanosomes in the host and the tse tse fly vector. Right: Distribution of human-pathogenic subspecies *T. b. gambiense* and *T. b. rhodesiense*. Figure edited from Brun *et al.* 2012.

2.2 VSG Architecture

The previously described defensive mechanisms of *T. b. brucei* rely on the structure-function-relationship of the VSG protein within the surface coat. VSGs are membrane proteins that form homodimers with a size of 100 - 120 kDa that connect to the exterior of the parasites cell surface by a glycosylphosphatidylinositol (GPI) anchor. The dimeric NTD is connected to highly flexible C-terminal domains (CTDs) by a short, flexible linker. This linker is prone to degrade during crystallisation, which is the main reason why no complete VSG structure could be solved to date. The VSG NTD consists of 350 - 400 residues and is grouped into two types (type A and B) by the number and position of conserved cystein residues (Carrington, Miller, *et al.*, 1991; Marcello & Barry, 2007). The published NTD structures of MITat1.2 and ILTat1.24 suggest conservation of the tertiary structure despite high sequence variability (Fig. 4) (D. Freymann *et al.*, 1990; M. L. Blum *et al.*, 1993). The domain forms a long coiled coil with a total diameter of approximately 10 nm that is expected to stretch perpendicular to the cell membrane, several short helices close to the C-terminal domain end, an antiparallel β-strand and a set of variable surface loops at the membrane distal end. The shorter and more flexible CTD is grouped into six types (type 1 - 6) by the number of conserved cystein residues (Berriman *et al.*, 2005; Carrington, Miller, *et al.*, 1991) and the formation of either one (S) or two (S1 and S2) structured segments with a size of 20 - 40 residues that are flanked by unstructured segments L1 and L2 in the case of segments S and S1 and by L2 and the GPI anchor in case of segment S2. The unstructured linkers L1 and L2 connect the CTD to the NTD and the GPI anchor, respectively (Chattopadhyay *et al.*, 2005; Jones *et al.*, 2008).

2.3 VSG fluorescence emissions

In addition to the VSG description that relies on structural modelling alone, interactions of the proteins with compounds from the cultivation medium may give insights into the structure-function-relationship of VSGs. For example could the binding of a cofactor to VSGs identify a conserved structural feature with a pH dependent binding strength. During a series of experiments focused on VSG endocytosis performed by Markus Engstler, GFP-fused VSG mutants were established and tracked by the reporter fluorescence. Eventually, during this series of experiments, a fluorescent VSG protein was discovered that was not linked to a GFP reporter, but displayed a reporter-independent fluorescence. The novel VSG that was expressed in a subpopulation following antigenic variation of the parasite was labelled VSG'Y' due to the unique yellow fluorescence signal. Emissions from this VSG required the presence of a compound from the cultivation medium, which was identified as the pH indicator phenol red. Removing phenol red from cultivation media extinguished fluorescence emissions. The pH indicator belongs to the chemical family of triphenylmethanes (TPMs) and is the only member that enables the unique VSG'Y' fluorescence. Exchanging PR with bromophenol blue (BPB), another member of the TPM family, results in weak fluorescence emissions that are independent of the

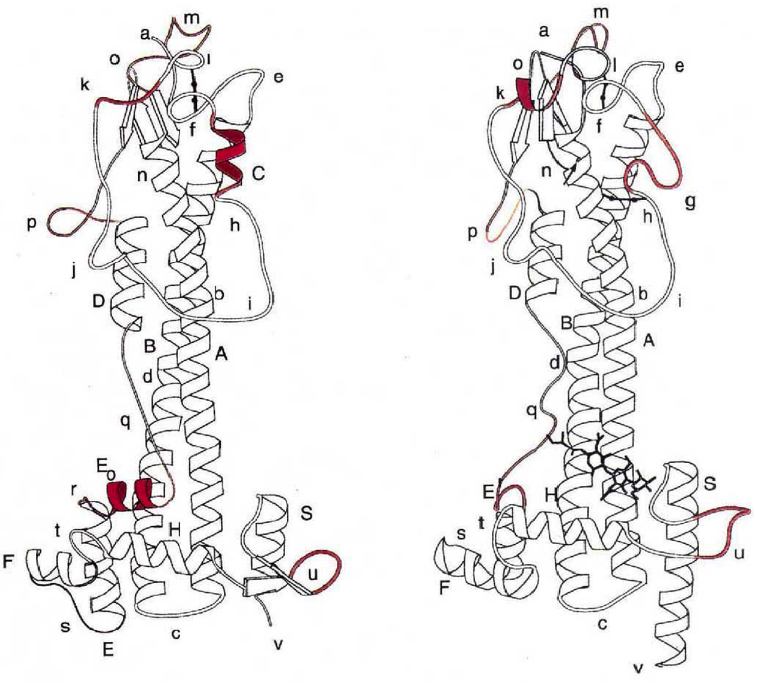

ILTat 1.24 MITat 1.2

Figure 4 – Comparison of the NTD structure of MITat1.2 and ILTat1.24. Displayed are the monomers for both proteins. Important features are the membrane distal surface loops, the central coiled coil that is formed by α-helices A & B and the flanking minor helices C, D, E_0, E, F, H, S. Structural differences between both VSGs are highlighted in red. Figure edited from M. L. Blum *et al.* (1993).

expressed VSG (Fig. 5). However, upon excitation with light of a wavelength corresponding to the absorption maximum of BPB, a fluorescence wave emerged along the cell surfaces and spread through the complete cell, resulting in the death of the respective parasite. This observation was termed *trypanocidal effect* (TE) and could be observed for all BSF trypanosomes independent of the expressed VSG. Furthermore, the effect was tested for 7 members of the TPM family of which all bromo-derivatives (bromophenol red, bromophenol blue, bromocresole purple and bromocresole green) lead to the trypanocidal effect. Trypanosomes with insect stage morphology, expressing procyclin instead of VSG are immune to the TPM-derived trypanocidal effect. This observation leads to the assumption that, despite high sequence variability between VSGs, there might be a common structural attribute shared by all VSGs, to which TPM derivatives can bind and transfer energy upon excitation. Only the combination of PR and VSG'Y' leads to energy transfer in form of strong fluorescence emission, while the binding of bromo-derivatives to any VSG causes energy transfer that eventually results in cell death through the TE.

VSGs and TPMs may interact through π-stacking due to the strong aromatic character of thriphenylmethanes. Sufficiently close proximity of aromatic residues F6 and F10 to allow intercalation of TPMs and activation of fluorescence emissions can be observed in MITat1.2 (Fig. 6). Additionally, aromatic moieties Y7 and W10 in ILTat1.24 show resemblance to this putative TPM binding domain of MITat1.2. While the structure of VSG'Y' is unknown, an alignment of the VSG'Y' amino acid sequence to the structure of

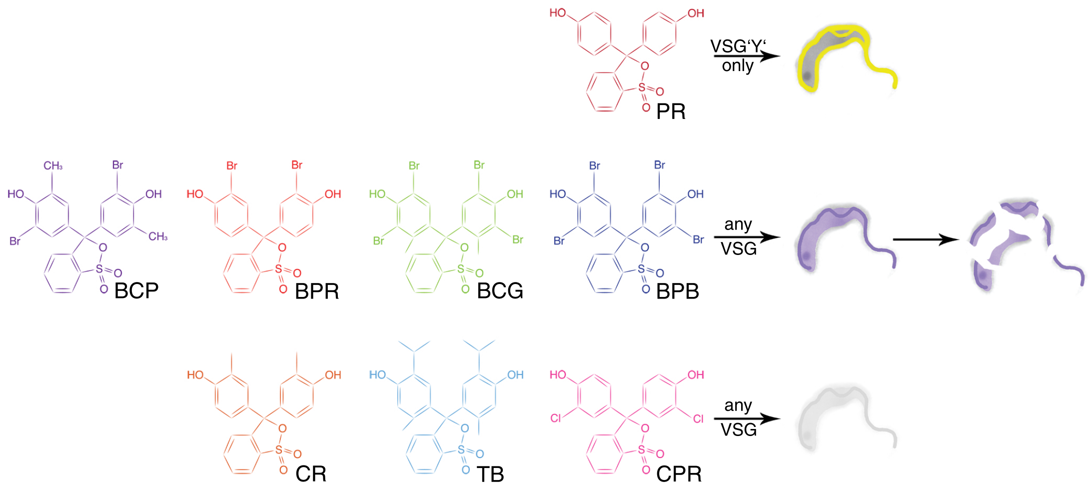

Figure 5 – Influence of various TPMs on cell fluorescence. Phenol red (PR) is the only TPM that expresses yellow surface fluorescence in the presence of VSG′Y′ on the cell surface. Bromo derivates including bromocresol purple (BCP), bromophenol red (BPR), bromocresol green (BCG) and bromophenol blue (BPB) lead to weak surface fluorescence and a trypanocidal effect which causes the cell to die upon excitation of the TPM. Additional members of the TPM family including cresol red (CR), thymol blue (TB) and chlorophenol red (CPR) fail to induce fluorescence emissions or the TE.

MITat1.2 can be used to construct a structural approximation of VSG′Y′. The so generated model shows that positions F8 and W11 in VSG′Y′ are occupied with aromatic amino acids that may form a motif similar to those hypothesized for ILTat1.24 and MITat1.2 (Fig. 6). Docking studies and protein mutagenesis of key aromatic residues in VSG′Y′ were performed during this thesis to identify a potential binding motif for TPMs. Additionally, fluorescence experiments were performed to identify the mechanism of the unique VSG′Y′ fluorescence as well as all of it’s influencing factors and how energy transfer from VSG to the cell body leads to the trypanocidal effect.

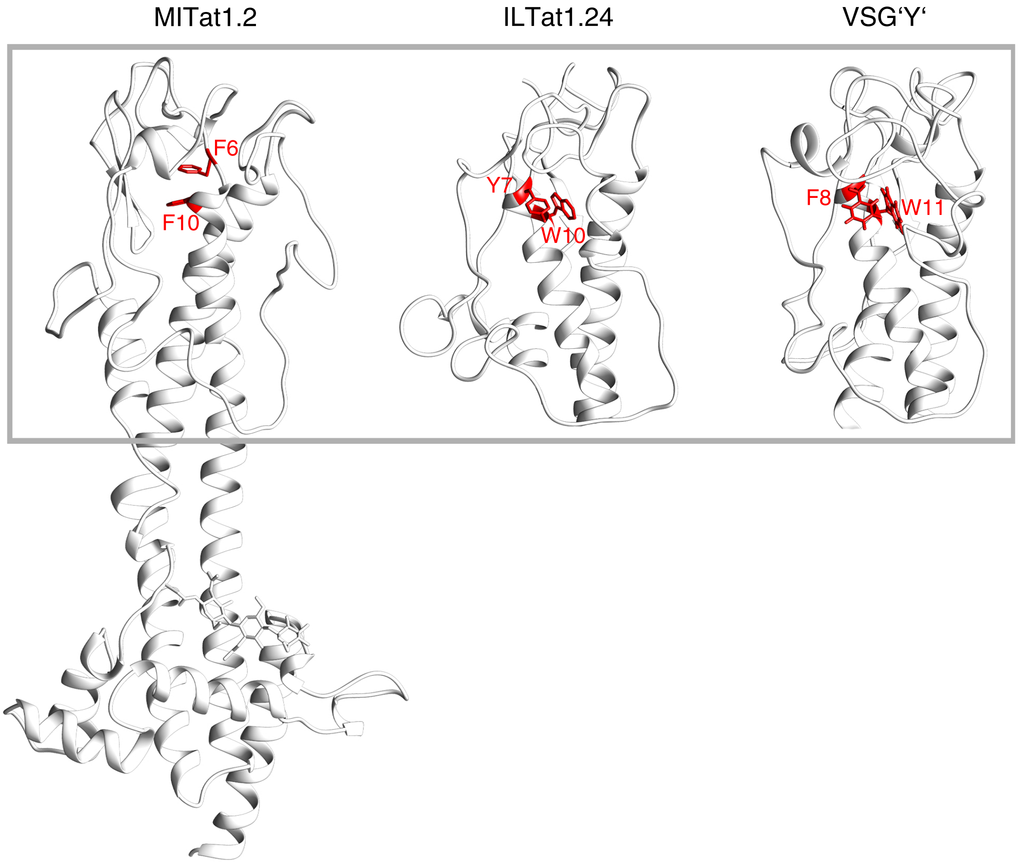

Figure 6 – Visualization of the potential binding motif in MITat1.2, ILTat1.24 and VSG′Y′. Displayed is the complete monomeric NTD of MITat1.2 and the part of all three VSGs that is closest to the surrounding medium on live cells (box). The motif is formed by two aromatic amino acids at the beginning of helix A that are in sufficient proximity to allow intercalation of TPM compounds. The VSG′Y′ structure is derived from the amino acid sequence alignment of VSG′Y′ to the structure model of MITat1.2.

2.4 Protein crystallography

The most common method for structural analysis of proteins is x-ray crystallography, which may require several milligrams of the protein of interest due to the trial-and-error approach inherent to the method. BSF trypanosomes are coated in approximately 5×10^6 VSG dimers that form a monolayer on the cell surface (Cross, 1975; Auffret & Turner, 1981; D. M. Freymann *et al.,* 1984; Jackson *et al.,* 1985). This VSG coat constitutes approximately 10 % of the total protein abundance in trypanosomes (Böhme & Cross, 2002) and is sufficient that no additional expression system is required to supply the required protein amounts.

While technological advancements in recent years have lead to an improvement in the quality of protein purification and diffraction measurements (Lottspeich *et al.,* 2008), protein crystallisation still depends on the unique characteristics of the protein of interest. Since slightest changes in protein compositions can already lead to a strong impact on the crystallisation of a protein, the process of protein crystallisation is based on trial-and-error and success relies strongly on chance. To approach this circumstance, crystallographic trials start with broad parameter screenings that include hundreds of different parameters which are chosen randomly or per an educated guess based on proteins similar to the protein of interest (POI). In most cases, the initial search for crystallographic parameters that allow good x-ray diffraction defines the time-determining step during protein structural analysis by x-ray crystallography.

To allow crystal growth from soluble protein, the solubility of the POI has to be altered by the addition of salts and precipitants while maintaining protein stability. The solution is oversaturated through the application of additives, temperature change and volume reduction, which ultimately leads to protein precipitation. If adjusted correctly, this precipitate can form highly ordered crystals. VSG crystallisation is performed by hanging- and sitting drop vapour diffusion (Fig. 7a), where a small drop (0.3 - 1 μl) composed of 50 % protein solution and 50 % mother liquor is placed next to a larger reservoir (0.06 - 1 ml) of 100 % mother liquor. The mother liquor is composed of a unique combination of buffer, precipitant, salts and additives. The well holding the protein drop is sealed to avoid vapour exchange with the environment and the different concentrations of mother liquor between drop and reservoir lead to vapour flow towards the reservoir. During this equilibration, the volume of the protein solution is gradually reduced, leading to an oversaturation within the drop, which will optimally lead to ordered protein precipitation. During this thesis, all parameter screens and most of the final diffracting crystals were produced by sitting-drop vapour diffusion in 96-well-plates, while cocrystallisation of VSGs and TPMs was performed by the hanging-drop method in 24-well-plates.

There are three additional methods of protein crystallisation besides vapour diffusion, which are displayed in the phase diagram in fig. 7b and that are differentiated by the route involved in reaching nucleation and metastable conditions. In vapour diffusion, the single method used in this thesis, the nucleation zone is reached by increased concentrations of both protein and additives through water evaporation from the drop to the reservoir. As the protein crystallises, concentrations eventually reach the metastable zone, where saturation is sufficient for existing crystals to grow while being too low for further nucleation events. The supersolubility curve defines the margin between conditions that induce nucleation of soluble components from the metastable zone. Initial nucleation events may lead to the formation of numerous but small crystals that are insufficient to yield good diffraction data. Under optimal conditions, the minimum reported crystal diameter that allowed structure determination was 1.2 μm (Holton & Frankel, 2010). However, during screening when crystallisation quality is yet unknown, a crystal diameter of at least 100 μm should be aimed for (Ducruix & Giegé, 2000). A reduction of precipitant and protein concentration is usually sufficient to move conditions within the nucleation zone closer to the supersolubility curve, resulting in fewer but bigger crystals. Should protein and precipitant concentrations be chosen too high, conditions will enter the precipitation zone where mass precipitation in unordered form will occur. Too low concentrations will result in undersaturation, where the solution remains clear and no precipitation takes place.

For broadband screening, commercial sparse-matrix screens are used that contain unique combinations of precipitants, salts and additives that have proven successful in previous crystallisation trials. Special sitting drop 96-well-plates are used, that require low volumes (600 nl drop volume, 60 μl reservoir volume) and that allow fast equilibration. Using crystallisation robots that can precisely apply nanoliter volumes to individual wells, the required amount of protein during screening can be minimized. Parameters that are successful in initial screens can be tweaked and refined manually to improve crystals.

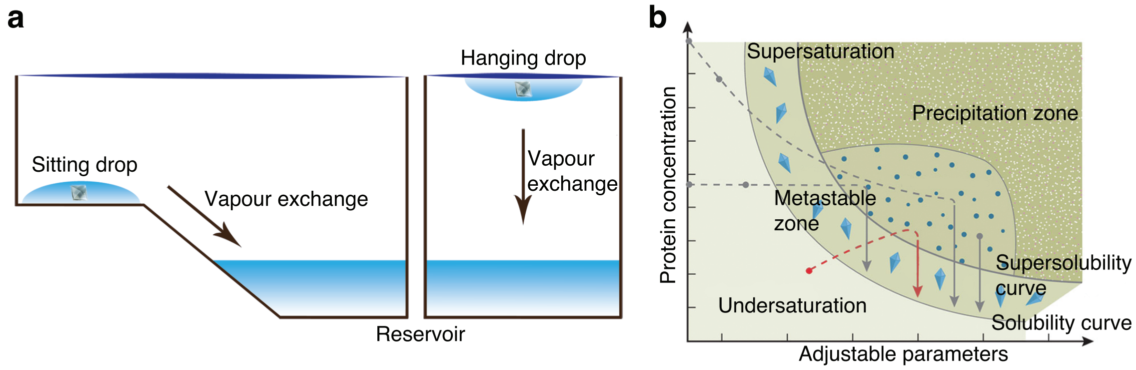

Figure 7 – Illustration of vapour diffusion and the phase diagram. a) Sitting drop and hanging drop vapour diffusion crystallisation. Each well is sealed and water is exchanged from drop to reservoir, eventually oversaturating the protein drop and precipitating crystalline protein. b) Phase diagram that displays the route different crystallographic methods take to achieve nucleation and a metastable condition. The vapour diffusion route is highlighted in red. Figure b edited from Caffrey & Cherezov (2009).

2.5 Diffraction data analysis

Once protein crystals of sufficient size and order have grown they can be analysed by means of x-ray diffraction. Highest order of the protein within the crystal is required due to the physical basis of structure-elucidation from the diffraction measurements.

Crystals are per definition (under optimal conditions) highly ordered and densely packed repetitions of atoms or molecules. These molecules can be described by the planes they form in three dimensional space and which are defined by three axes and three angles in between. The smallest parallelepiped that can describe a non-repeating arrangement of atoms within the crystal structure is called *unit cell* and defines the single building blocks from which the crystal is formed. The position of every plane of atoms within the unit cell is described by the Miller indices *k, l, m* which refer to the unit cell axes. Crystals are analysed by irradiation with monochromatic x-ray beams. When x-rays hit a crystal, most of the beam will pass through the crystal unaffected, while some x-rays will be scattered upon contact with an electron in the hull of an atom. Due to the high number of atoms within a crystal, almost every scattered ray will statistically be extinguished by another ray through destructive interference. Ultimately, only scattered rays that form constructive interferences will produce an observable signal. X-rays that are diffracted this way form a pattern that is unique for the crystallised material and that can be detected by a photon detector. Bragg's law describes the phenomenon of constructive interference on three dimensional lattices (Jauncey, 1924), and allows the precise determination of the distance between diffracting lattices within a crystal (Fig. 8a). Since each lattice is defined by relatively few atoms, the intensity (or x-ray amplitude) of the scattered rays is directly influenced by the arrangement of atoms within the unit cell and the number of atoms within the lattice. Planes in *position-* or *real space* (the physical crystal) that fulfil Bragg's law are transformed into so called *reciprocal-* or *momentum space* by the scattered x-rays and form a reciprocal lattice on the detector. Applying the so called *Ewald sphere* to this lattice allows to define the unit cell dimensions (Fig. 8b). All elastically scattered x-rays have a wave vector $\vec{k}$ of identical length that describe the surface of the Ewald sphere. These wave vectors produce a detectable signal only in positions where the sphere's surface crosses lattice points of reciprocal space (Fig. 8c) and thus where Bragg's law is fulfilled. When the crystal is rotated, the reciprocal lattice is rotated as well and signals disappear and reappear in respect to Bragg's law. These signals can be translated back into real space and observation of the scattering events allows the identification of the unit cell and its space group. Once unit cell, space group and resolution of the crystal are defined, the collected diffraction data can be translated into an electron density map and structural interpretation can be performed.

Photo detectors that collect x-rays can only measure the amplitude/intensity of the incoming beam, while the phase information is lost (as is all 3-dimensional information on a 2-dimensional detector). However, the relative phase information between the scattered and the original x-ray beam is required for the calculation of the electron density. To solve this so called *phase problem*, the phase relation has either to be replaced or restored. Replacement can be conducted if a related structure with a minimum sequence identity of approximately 25 % is available (Lottspeich *et al.*, 2008). By this so called *molecular replacement*, it is possible to apply the theoretical phase relation of the known structure to the experimental intensities to resolve the structure. If no suitable structure is available, *isomorphous replacement* has to be performed to recover the phase information. When applying this method, atoms with high electron density (e.g. heavy metal atoms) are added to the protein of interest either by cocrystallisation of the compound and the protein or by soaking of protein crystals in a solution of the electron-dense material. By comparison of the original data and the data including the locally well defined increase of electron density, the electron-heavy atoms can be located in the unit cell and the required phase relation can be obtained.

Once a resolution of approximately 3.5 Å or better is reached, electron density maps can be calculated into which individual amino acids are modelled to construct the tertiary structure of the protein of interest. Higher resolutions produce a more detailed electron density map, which reduces erroneous alignment of peptide bonds and amino acid moieties. Completed models can be improved in subsequent refinements to eliminate remaining errors. Programs can be applied to the rigid density map, that dynamically improve bonding geometries and that can adequately account for repulsive forces to finalize the protein structure.

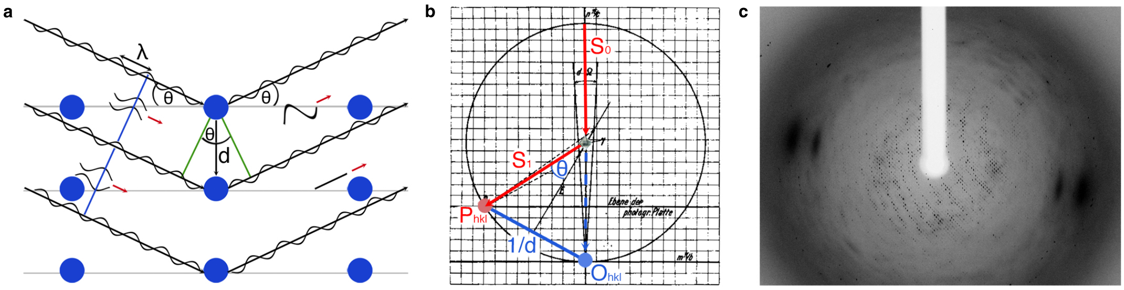

Figure 8 – Description of diffraction patterns by Bragg's law and the Ewald sphere. a) Bragg's law describes, that strong signals can only be detected when two waves that are reflected at a specific angle θ from planes in a distance d interfered constructively, which is given by $2d\sin\theta = n\lambda$. b) Edited original description of the Ewald Sphere by P.P. Ewald in 1913 (Ewald, 1913). Uninfluenced and reflected beams are highlighted in red and blue. The sphere can be applied to identify the unit cell dimensions and the maximum resolution at a given wavelength. It further demonstrates the relationship between incident and diffracted wave vectors, the diffraction angle for a given reflection and the reciprocal lattice of the crystal. c) Typical diffraction pattern. The white line in the centre originates from the beam stop which shields the photon detector from the non-diffracted high intensity x-ray beam.

2.6 Small angle x-ray scattering (SAXS)

In some cases, including VSGs, it is not possible to obtain complete protein structures by x-ray crystallography alone. Due to proteolytic cleavage in the linker region of VSGs during the long process of crystallisation, protein crystals are composed of the NTD alone (D. M. Freymann *et al.*, 1984). Alternative methods of structure elucidation are unsuitable for molecules larger than 20 kDa (NMR) or lack in resolution (≥4.5 Å) while also requiring large molecules of at least 170 kDa (cryo-electron microscopy). However, if structural information of all individual domains is available at high resolution, small-angle x-ray scattering can be applied to combine these domains into a complete protein model.

In this thesis, crystallographic (NTD) and NMR (CTD) data of MITat1.1 was combined by SAXS to experimentally describe the first complete VSG. Additional SAXS experiments were performed with ILTat1.24 and its published domain structures and allowed direct comparison of two complete VSG structures.

Similar to classical x-ray crystallography, in SAXS experiments x-rays scattered from protein molecules and collected by a photo detector. The main difference is that a collimated x-ray beam is aimed at small angles (typically 0.1 - 1°) at proteins in solution. The scattered intensity *I(s)* for the solvent and sample are recorded as a function of the momentum transfer s and subtracted from one another. The resulting scattering pattern (Fig. 9a) allows determination of the overall size and shape of the analysed protein. For a monodisperse protein sample the intensity distribution of all randomly positioned molecules is proportional to the scattering of a single particle averaged over all orientations. Thus, monodispersity of non-interacting samples is of utmost importance. At low angles (2 - 3 nm resolution) the scattering curve is quickly decaying, which is determined by the overall shape of the analysed particle and which is different for each molecule. At increasing resolutions, the scattering differences are less pronounced and become indistinguishable at minimum resolutions. Therefore, SAXS can only reliably produce information about the rough shape and domain compositions of proteins, while data on atomic scale is indistinguishable. At higher protein concentrations the signal-to-noise ratio improves, while inner-particle and inter-particle distances approach the same order of magnitude. While improving brilliance, the signal is also altered at the same time. At lower concentrations, brilliance is impaired while aggregation and repulsive and attractive interactions are reduced for low angles. Thus, in order to optimize the output, signals are detected at different protein concentrations and curves are merged to compose the final scattering data.

Parameters that can be derived by the evaluation of SAXS data include the molecular weight, the excluded particle volume, maximum dimensions D_{max} and the radius of gyration R_g. R_g is the average RMS distance to the centre of density, providing a measure of the overall molecule size. For proteins with identical amino acid composition R_g increases with more extended conformations. D_{max} is derived from the distance distribution function *P(r)* (Fig. 9b) which is a histogram of distances between all possible pairs of atoms within a particle. This distribution is symmetrically bell-shaped for globular proteins and displays a tail for extended protein conformations. The so called Kratky plot (Fig. 9c + d) can be employed to further analyse the folded state of a protein and is used to qualitatively identify disordered states and to distinguish them from globular proteins.

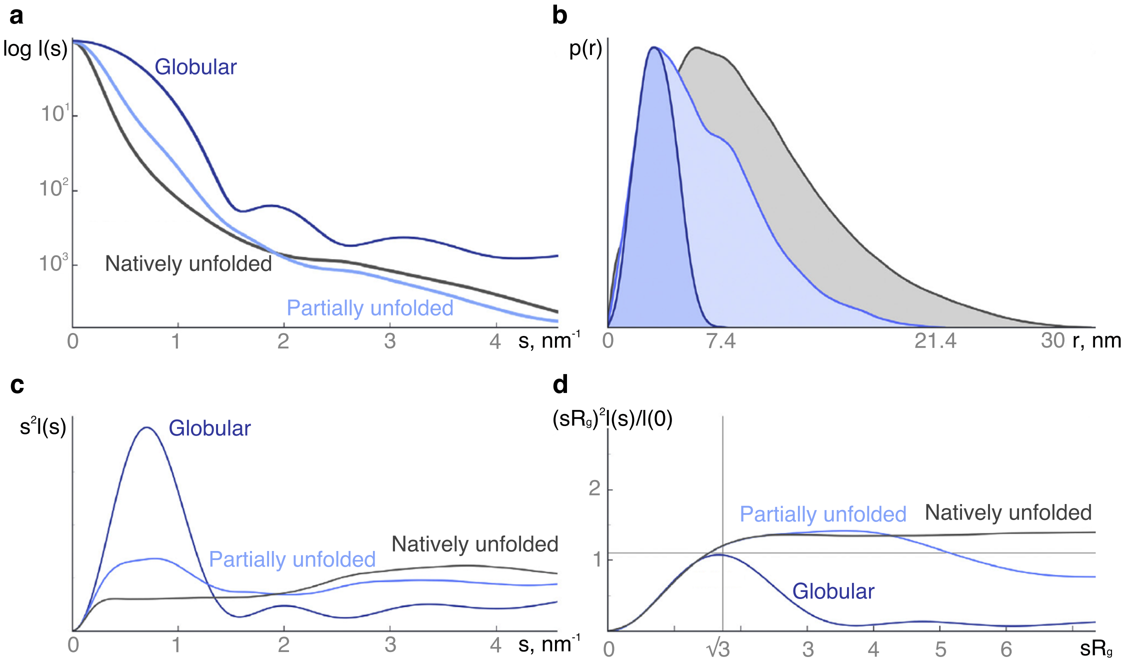

Figure 9 – Illustration of SAXS data. Exemplary data for three differently folded proteins with identical amino acid composition illustrating the difference of protein folding. a) Logarithmic plot of the experimental scattering data. b) Distance distribution function p(r). c) Kratky plot. d) Dimensionless Kratky plot. Figure taken and edited from Kikhney & Svergun (2015).

Once determined, the parameters of symmetry and fold, complemented by high resolution domain structures can be employed to construct complete protein models through rigid body modelling. These models are then compared to the experimental scattering data and refined to improve the discrepancy χ^2 between model and experiment. Multimeric states and symmetry restrictions can be applied to improve model quality. As a general guideline, the model that combines the most specific modelling restrictions with the lowest discrepancy is the best.

3 Materials and methods

3.1 Materials

3.1.1 Oligonucleotides

All oligonucleotides used in this work are listed in the following table with name, sequence, manufacturer and the user designing it. Primers above the separator were used in the construction of VSG′Y′ mutants, while primers below the separator were designed and purchased but not yet used.

Name	Sequence (5′→ 3′)	Manufacturer	Designed by
F8IU	cgc gat caa gat cga gac gtg gga gc	MWG	M. Engstler
F8IL	tcc cac gtc tcg atc ttg atc gcg	MWG	M. Engstler
F8WU	cgc gat caa gtg gga gac gtg gga	Sigma Aldrich	T. Bartossek
F8WL	gcg cta gtt cac cct ctg cac cct	Sigma Aldrich	T. Bartossek
W11FU	gtt tga gac gtt cga gcc gct ctg	MWG	M. Engstler
W11FL	cag agc ggc tcg aac gtc tca aac	MWG	M. Engstler
Y121AU	caa caa aca aag cgg gct gcc t	Sigma Aldrich	T. Bartossek
Y121AL	gtt gtt tgt ttc gcc cga cgg a	Sigma Aldrich	T. Bartossek
W254FU	ctc cag atc ttc cgg gcc ttc aaa ac	MWG	K. Bayer
W254FL	gt ttt gaa ggc ccg aag gat ctg gag	MWG	K. Bayer
Y269AU	aca agc ggc gct agc cga cca t	Sigma Aldrich	T. Bartossek
Y269AL	tgt tcg ccg cga tcg gct ggt a	Sigma Aldrich	T. Bartossek
W329FU	gca aaa act ctt cga tgc cat gga taa g	MWG	M. Engstler
W329FL	c tta tcc atg gca tcg aag agt ttt tgc	MWG	M. Engstler
W475FU	ggg ttg caa att cga ggg tga aac ttg	MWG	M. Engstler
W475FL	caa gtt tca ccc tcg aat ttg caa ccc	MWG	M. Engstler
T3	aat taa ccc tca cta aag gg	MWG	Commercial
T7	taa tac gac tca cta tag gg	MWG	Commercial
W11AU	gtt tga gac ggc aga gcc gct ctg	Sigma Aldrich	T. Bartossek
W11AL	caa act ctg ccg tct cgg cga gac	Sigma Aldrich	T. Bartossek
F8IW11AU	cgc gat caa gat cga gac ggc aga gc	Sigma Aldrich	T. Bartossek
F8IW11AL	gcg cta gtt cta gct ctg ccg tct cg	Sigma Aldrich	T. Bartossek
F107AU	ctg aag ctc tag agg tca tg	Sigma Aldrich	T. Bartossek
F107AL	gac ttc gag atc tcc agt ac	Sigma Aldrich	T. Bartossek
Y212AU	tag atg aac cgg tcc ctg ccg	Sigma Aldrich	T. Bartossek
Y212AL	atc tac ttg gcc agg gac ggc	Sigma Aldrich	T. Bartossek

3.1.2 Antibodies

Primary antibodies for western blot

Anti VSG121
Rabbit, polyclonal, 1:1,000 (M. Carrington, Cambridge, UK)

Anti VSG221 C-terminus
Rabbit, polyclonal, 1:5,000 (M. Carrington, Cambridge, UK)

Anti PFR L13D6
Mouse, monoclonal, 1:20 (P. Bastin, Paris, France)

Secondary antibodies for western blot

Anti rabbit IRDye 800cw
Goat, polyclonal, 1:10,000 (LI-COR Biosciences)

Anti mouse IRDye 680ct
Goat, polyclonal, 1:10,000 (LI-COR Biosciences)

Primary antibodies for immunofluorescence

Anti MITat1.5 C-terminus
Rabbit, polyclonal, 1:100 (M. Carrington, Cambridge, UK)

Anti VSG121 V7B11
Mouse, monoclonal, 1:100 (M. Navarro, Granada, Spain)

Anti VSG221 C-terminus
Rabbit, polyclonal, 1:100 (M. Carrington, Cambridge, UK)

Secondary antibodies for immunofluorescence

Anti mouse Alexa 488
Goat, polyclonal, 1:500 (Life Technologies)

Anti rabbit Alexa 594
Goat, polyclonal, 1:500 (Life Technologies)

3.1.3 Enzymes, Kits and Screens

Enzymes

All enzymes used to modify DNA, including endonucleases, polymerases and ligases were purchased from Thermo Scientific and used in accordance to the manufacturer's instructions.

Kits

Basic Parasite Kit 2	Lonza
CloneJET PCR cloning Kit	Thermo Scientific
NucleoSpin Gel and PCR clean-up Kit	Macherey-Nagel
Plasmid Midi Kit	QIAGEN
Plasmid Mini Kit	QIAGEN
QIAEX II Gel extraction Kit	QIAGEN

Crystal Screens

Crystal Screen	Hampton Research
Crystal Screen 2	Hampton Research
Index	Hampton Research
MIDAS HT-96	Molecular Dimensions
Nextal PEG	QIAGEN
Nextal pH Clear	QIAGEN
Nextal Protein Complex	QIAGEN
Topaz Optimix	Fluidigm
Topaz Optimix 2	Fluidigm
Topaz Optimix 3	Fluidigm
Topaz Optimix PEG	Fluidigm

3.1.4 Buffers and solutions

Trypanosoma brucei cultivation

HMI-9 medium

Modified by Vassella (Vassella & Boshart, 1996) after Hirumi (H. Hirumi & K. Hirumi, 1989): 17.66 g Iscove's modified Dulbecco's MEM (IMDM) powder, complemented with 3.024 g sodium bicarbonate, 136 mg hypoxanthine, 28.2 mg bathocuproine sulfonate, 14 μl β-mercaptoethanol, 39 mg thymidine, 100,000 U penicillin, 100 mg streptomycin, 182 mg cysteine and 10 % (v/v) fetal calf serum (FCS). The medium was prepared using filtered and deionized water (ddH_2O) and the pH adjusted to 7.5. Finally the medium was sterilized by filtration (pore size 0.2 μm). Prior to addition, FCS was heat-inactivated for 1 h at 56 °C. Quantities refer to 1 l of medium.

HMI-9 agarose

0.6 % (w/v) agarose in HMI-9.

Fluorescence solution (FMix)

1 μM albumin, 80 μM phenol red and 1.25 mM trolox in TDB.

2x Freezing mix

HMI-9 medium complemented with 20 % (v/v) glycerol and filter sterilized.

Protein analysis

1 x Laemmli running buffer

25 mM tris base, pH 8.5, 192 mM glycine, 0.1 % (w/v) SDS in ddH_2O.

2 x Laemmli loading buffer

200 mM tris base, pH 6.8, 10 % (w/v) SDS, 10 % (v/v) glycerol, 10 % β-mercaptoethanol, 0.05 % (w/v) bromophenol blue in ddH_2O.

Coomassie staining solution

0.025 % (w/v) Coomassie brilliant blue R-250, 10 % (v/v) 2-propanol, 5 % (v/v) glacial acetic acid in ddH_2O.

Coomassie destaining solution

10 % (v/v) 2-propanol, 5 % (v/v) glacial acetic acid in ddH_2O.

Resolving gel buffer

1.5 M tris base, pH 8.8, 0.4 % (w/v) SDS in ddH_2O.

Acrylamide solution

Rotiphorese gel 30: 30 % (w/v) acrylamide, 0.8 % (w/v) bisacrylamide.

Stacking gel buffer

0.5 M tris base, pH 6.8 and 0.4 % (w/v) SDS in ddH_2O.

12.5 % Resolving gel

2 ml acrylamide solution, 1.5 ml resolving gel buffer, 2.5 ml ddH_2O, 100 μl 10 % (w/v) APS and 10 μl TEMED per gel.

Stacking gel

3 ml stacking gel mix, 30 μl 10 % (w/v) APS and 6 μl TEMED per gel.

Stacking gel mix

26.3 ml Rothiphorese gel 30, 50.5 ml stacking gel buffer and 123.2 ml ddH_2O per 200 ml.

Protein size marker

Prestained protein marker (PageRuler 10 - 170 kDa, Fermentas). Diluted 1:5 in 1 x Laemmli running buffer.

Western blot buffer

1 x Laemmli running buffer supplemented with 20 % methanol.

Western blot blocking solution

PBS supplemented with 5 % (w/v) milk powder.

DNA analysis

1x TAE buffer

40 mM tris base, 40 mM acetic acid, pH 8.0 and 1 mM EDTA.

10x DNA loading buffer

0.1 M EDTA, pH 8.0, 0.05 % bromophenol blue, 0.05 % Xylencyanol and 40 % saccharose.

Protein Crystallisation

Saturated ammonium sulphate solutions (SAS)

3.9 g - 5.6 g $(NH_4)_2SO_4$ (corresponding to 60 - 80 % saturation) in 10 ml ddH_2O.

Anion exchange loading buffer

20 mM tris base, pH 8.0, filter sterilized.

Anion exchange elution buffer

20 mM tris base, pH 8.0 and 1 M NaCl, filter sterilized.

Size exclusion chromatography buffer

20 mM tris base, pH 8.0 and 150 mM NaCl, filter sterilized.

100x TDB-PR

4 mM phenol red in TDB.

100x TDB-BPB

4 mM bromophenol blue in TDB.

Other solutions

1 M sodium-phosphate buffer pH 8.0

13.23 g Na_2HPO_4 and 0.82 g NaH_2PO_4, per 100 ml ddH_2O, pH 8.0.

Phosphate buffered saline (PBS)

135 mM NaCl, 2.5 mM KCl, 10 mM Na_2HPO_4 and 2 mM KH_2PO_4 in ddH_2O.

Trypanosome dilution buffer (TDB) pH 7.6

5 mM KCl, 80 mM NaCl, 1 mM $MgSO_4$, 20 mM Na_2HPO_4, 2 mM NaH_2PO_4 and 20 mM glucose in ddH_2O.

Luria-Bertani (LB) medium

10 g bacto-tryptone, 5 g yeast extract and 10 g NaCl per litre, adjusted to pH 7.0.

Transformation and storage solution (TSS)

LB medium with 10 % PEG 3,350, 5 % DMSO and 50 mM $MgCl_2$.

3.1.5 Trypanosome strains

Wildtype strains

Strain Lister 427; Molteno Institute Trypanozoon antigen type 1.1, 1.2, 1.4, 1.5 and M1.6 (VSG'Y'); bloodstream form (G. Cross, 1975).

Transgenic strains

MITat1.2 13-90

The MITat1.2 13-90 cell line is based on the MITat1.2 bloodstream form, which was modified to constitutively express a T7 RNA polymerase and a tetracycline repressor (Wirtz *et al.*, 1999). This allows inducible control of T7 promoter-regulated expression. 13-90 cells were cultivated with 5 μg/ml hygromycin and 2.5 μg/ml G418 selection. All VSG'Y' mutants were expressed in inducible double-expressor cell lines expressing VSG MITat1.2 which is downregulated by expression of the ectopic VSG'Y', while ILTat1.24 and the glycosylation mutants of MITat1.4 and VSG'Y' were expressed from knock-out cell lines, expressing only the VSG of interest.

Table 4 – List of cell lines and selection.

Cell line	Selection
MITat1.1	-
MITat1.2	-
MITat1.4	-
MITat1.5	-
VSG'Y'	-
13-90	H (5 μg/ml), G418 (2.5 μg/ml)
13-90_VSGY_F8I	H (5 μg/ml), G418 (2.5 μg/ml), Ph (1 μg/ml)
13-90_VSGY_F8W	H (5 μg/ml), G418 (2.5 μg/ml), Ph (1 μg/ml)
13-90_VSGY_W11F	H (5 μg/ml), G418 (2.5 μg/ml), Ph (1 μg/ml)
13-90_VSGY_Y121A	H (5 μg/ml), G418 (2.5 μg/ml), Ph (1 μg/ml)
13-90_VSGY_W254F	H (5 μg/ml), G418 (2.5 μg/ml), Ph (1 μg/ml)
13-90_VSGY_Y269A	H (5 μg/ml), G418 (2.5 μg/ml), Ph (1 μg/ml)

13-90_VSGY_W329F	H (5 μg/ml), G418 (2.5 μg/ml), Ph (1 μg/ml)
13-90_VSGY_W475F	H (5 μg/ml), G418 (2.5 μg/ml), Ph (1 μg/ml)
13-90_M1.2-KO_ILTat1.24[a]	H (5 μg/ml), G418 (30 μg/ml), P (0.3 μg/ml)
13-90_M1.2-KO_VSGYΔglyc[a]	H (5 μg/ml), G418 (30 μg/ml), P (0.3 μg/ml)
13-90_M1.2-KO_M1.4Δglyc[a]	H (5 μg/ml), G418 (30 μg/ml), P (0.3 μg/ml)

Abbreviations: H, Hygromycin; Ph, Phleomycin; P, Puromycin; [a], cell lines provided by Nicola Jones

3.1.6 Plasmids

Cloning and mutagenesis was conducted either in pBlueskript SK(+) (Stratagene) or with blunt end vector pJet1.2 (Thermo Scientific). Final DNA fragments were cloned into the tetracycline-inducible pLew82v4 transfection vector (G. Cross), which locates to ribosomal spacers.

3.1.7 Equipment

Alpha 2-4 LD plus freeze dryer	Christ
AMAXA Nulceofector II	Lonza
Äktaprime plus	GE Healthcare
AVC 2-24 CD plus rotational concentrator	Christ
DMI 6000B	Leica
DMI IRB	Leica
Foxy R1 fraction collector	Teledyne Isco
HoneyBee 963 crystallisation robot	Zinsser Analytic
iMIC	Till Photonics
Infinite M200 Plate Reader	Tecan
Labovert binocular microscope	Leitz
Laborlux S binocular microscope	Leitz
M3Z binocular microscope	Wild Heerbrugg
MicroMax-007 HF x-ray generator	Rigaku
MZ 16 FA stereo microscope	Leica
Odyssey Infrared Scanner	Li-COR Biosciences
R-Axis HTC x-ray detector	Rigaku
UV System	Intas
xCAD ultrapure water facility	TKA
X-stream 2000 cryo system	Rigaku

3.1.8 Software

4 Peaks	Macentosj
Adobe Creative Suite 5	Adobe Systems Incorporated
ATSAS 2.7.1	EMBL Hamburg
Chimera	UCSF
CLC Main Workbench	CLC bio
Crystal clear 1.3.5	Rigaku
Graphpad Prism 5.0	GraphPad Software, Inc.
HoneyBee	Zinsser Analytic
i-control	Tecan
ImageJ 64	National Institutes of Health
Image SXM 197	Steve Barrett
LA Aquisition	Till Photonics
Leica Application Suite	Leica Microsystems
Odyssey V3.0.21	Li-Cor
Prime View	GE Healthcare
ProtParam	SIB
SITUS	Biomachina.org
VMD molecular graphics viewer	TCB Group
ZARunner	Zinnser Analytic

3.2 Methods

3.2.1 *T. brucei* cell cultivation

Cultivation of *Trypanosoma brucei*

Bloodstream form *T. brucei* cells were cultivated *in vitro* in HMI-9 medium supplemented with 10 % FCS at 37 °C in an atmosphere containing 5 % CO_2. Avoiding cell densities beyond 8 x 10^5 cells/ml ensured exponential growth. Before cells reached this density threshold, a dilution with pre-warmed HMI-9 was conducted. Cell densities were determined using a Neubauer chamber. Small volumes ranging from 10 ml to 200 ml were cultivated in cell culture flasks. Larger volumes were cultivated in conical flasks and agitated on an orbital shaker at revolutions specific for each cell line (Tab. 7). Care was taken to fill conical flasks to no more than 20 % of their maximum volume, since higher levels decrease the optimal surface/volume ratio between cultivation medium and the atmosphere and thus trypanosomal growth due to reduced CO_2 uptake.

Cultivation of trypanosomes on HMI-9 agarose plates was tested as an alternative to cultivation in suspension. To prepare the plates, HMI-9 medium was pre-warmed to 37 °C and 500 ml sterile SCHOTT bottles and measuring cylinders were pre-warmed to 50 °C. 20 ml hot and sterile agarose solution (6.5 % (w/v)) and 200 ml warm HMI-9 were mixed and homogenized in the SCHOTT bottle and distributed in volumes of 25 ml into 92 x 16 mm Petri dishes. As soon as the medium solidified after approximately 30 min, the plates were stored at 4 °C for 12 - 24 h to complete setting of the medium. Plates were pre-incubated at 37 °C and 5 % CO_2 for 24 h prior to use. 5 x 10^5 cells in 200 μl were distributed on each agarose plate and incubated for 72 h. Cells were subsequently harvested by vigorous washing of plates with 5 x 1 ml HMI-9. Following the initial harvest, 2 ml of HMI-9 were distributed on the plate and incubated for 15 min. After incubation the 2 ml cell suspension was collected, combined with the previous harvest and used for subsequent experiments. A total of 0.7 - 1.5 x 10^8 cells per dish could be harvested this way.

Freezing and thawing of trypanosomes

2 - 4 x 10^6 cells were harvested per stabilate by centrifugation for 10 min at 1,500 x *g* and 10 °C and frozen in 1 ml HMI-9 supplemented with 10 % glycerol for long time storage at -150 °C. Care was taken to avoid prolonged exposure of cultivated trypanosomes to glycerol as it is a cycotoxic agent. For re-cultivation, stabilates were thawed quickly at 37 °C and diluted in a tenfold excess volume of pre-warmed HMI-9. Cells were centrifuged for 10 min at 1,500 x *g* and 10 °C, freed of glycerol-containing supernatant and resuspended in pre-warmed HMI-9. Following cultivation for 1 h, cell densities were determined and cells were diluted. Antibiotic selection for transgenic cell lines was added if required.

Transfection of bloodstream form *T. brucei*

Per transfection 3 x 10^7 cells were harvested by centrifugation, resuspended in 100 μl Basic Parasite Solution II (Lonza), mixed with 10 μl of the linearised plasmid (1 μg/μl) and placed in the transfection cuvette. Electroporation was conducted with the Amaxa Nukleofektor program X-001. Transfected cells were diluted in 30 ml of HMI-9 supplemented with antibiotic selection for the 13.90 cell line immediately following electroporation. Cell dilutions of 1:10, 1:50 and 1:100 were prepared and each distributed to a 24-well plate in 1 ml fractions. Following an incubation time corresponding to one cell division, 1 ml of HMI-9 supplemented with the final antibiotic selection (described for all mutants in Tab. 4) was added to each well. After 4 - 6 days of incubation in wells, cell populations were transferred to culture flasks and cultivated as described at the beginning of this section and including antibiotic selection.

Immunofluorescence

5 x 10^6 trypanosomes were harvested by centrifugation and washed twice in 1 ml TDB. Cells were subsequently resuspended in 500 μl TDB and fixed by addition of 125 μl 8 % formaldehyde for 15 min of incubation at room temperature. Subsequently, cells were washed three times in PBS, resuspended in 300 μl PBS and 100 μl of the cell suspension were placed on a poly-L-lysine coated slide. After 15 minutes of incubation the cells had settled and adhered to the slide, which was then washed once with PBS before blocking with 1 % BSA in PBS for 30 minutes at room temperature. Cells were then incubated with the primary antibody (see subsection 3.1.2 for antibody dilutions) in 0.1 % BSA in 50 μl PBS for 60 minutes. After primary antibody incubation, the slide was washed three times with PBS for 5 minutes and incubated with the secondary antibody in 0.1 % BSA in 50 μl PBS for 60 minutes. Following incubation with the secondary antibody, the slide was washed two times in PBS, incubated 2 minutes in 30 μl DAPI (1 μg/ml) and washed a third time before the cells were mounted by the addition of 80 % glycerol in PBS to the slide. Finally, the slide was sealed with nail polish and stored at 4 °C for analysis.

Covalent surface labelling of bloodstream form *T. brucei*

The surface of VSG'Y'-expressing cells was covalently labelled with sulfo-NHS reactive compounds carrying either fluorescence dyes or biotin. 1 x 10^7 bloodstream form trypanosomes expressing VSG'Y' were harvested by centrifugation, washed three times in cold TDB and resuspended to a concentration of 1 x 10^8 cells/ml. A final concentration of 1 μM of the sulfo-NHS compound was added to the cell solution, which was then incubated on ice and under light exclusion for 15 min. Unbound, excess sulfo-NHS compounds were removed by three washing steps with 1 ml TDB each.

Live cell tryptic digestion of VSG’Y’

Membrane bound VSG’Y’ was cleaved proteolytically at the flexible L1 region by trypsin digestion. 0.5 - 1 x 10^7 trypanosomes were harvested and washed three times in cold TDB. Subsequently, cells were suspended in 1 ml TDB supplemented with 10 - 200 μg trypsin (Roth) and incubated at 37 °C for 5 - 15 min. Cells were then washed three times to remove trypsin and the soluble part of the cleaved VSG from the supernatant and used immediately for fluorescence measurements. Except for the incubation at 37°C all of the protocol was performed on ice to slow trypanosome metabolism and thus increase the delay until an undigested VSG coat can be re-established on the cell surface.

3.2.2 Working with *E. coli*

E. coli strains

E. coli *TG1 rec0*

Genotype: K-12Δ (lac-proAB) supE thi hsd D5/F′ tra D36 proA+B laclq LacZΔM15 rec0::Tn5.

E. coli *Top10*

Genotype: F-mcrA, Δ(mrr-hsdRMS-mcrBC), Φ80lacZΔM15, ΔlacX74 nupG recA1 araD139, Δ(ara-leu)7697 galE15 galK16 rpsL(Str^R) endA1 λ^-

Generation of chemically competent *E. coli*

100 ml LB-Medium were inoculated with 1 ml of *E. coli* suspension and incubated at 37 °C on an orbital shaker at 250 rpm until the culture reached an OD_{600} of 0.3 - 0.4. The *E. coli* solution was centrifuged at 900 x *g* at 4 °C for 10 minutes after which the supernatant was discarded. The sedimented bacteria were resuspended in 2.5 ml TSS, aliquoted into pre-cooled reaction tubes and flash-frozen in liquid nitrogen. Cells were stored at -80 °C.

Transformation of chemically competent *E. coli*

Competent *E. coli* aliquots were thawed on ice for 10 minutes and supplemented with 20 - 30 ng of the target plasmid. After incubation on ice for 30 minutes, the transformation was conducted by heat shock at 42 °C for 50 - 55 s. The transformed cells were subsequently spread on LB-agar plates and incubated over night at 37 °C.

Plasmid isolation

Depending on the requirements in regards to quantity and purity of the target DNA, different protocols were used for plasmid isolation. 1 ml of LB-medium was inoculated with *E. coli* and incubated over night at 37 °C on an orbital shaker at 250 rpm for low-quantity and low-quality isolations. The purification of plasmid DNA was conducted by alkaline lysis. High-purity plasmids were prepared with either the QIAGEN Plasmid mini or midi kit according to the manufacturer's instructions.

3.2.3 DNA techniques

Gel electrophoresis

DNA samples were mixed in a 9:1 ratio with 10 x DNA loading buffer and loaded onto a 0.8 % agarose gel that was immersed in TAE buffer. Electrophoresis was conducted at 10 V/cm gel. Following electrophoresis, the gel was incubated in 3 μg/ml ethidium bromide and analysed by visualizing the DNA bands with UV light at 310 - 350 nm. GeneRuler Ladder Mix (Thermo Scientific) was used for size determination.

DNA extraction from agarose gels

During gel extraction, DNA was visualised at a wavelength of 350 nm to reduce radiation damage induced by lower wavelengths. Visible bands of interest were cut from the gel with a scalpel and purified using the QIAEX II gel extraction kit according to the manufacturer's instructions.

2-propanol precipitation of DNA

To precipitate DNA, 1/10 volume 3 M sodium acetate and 1 volume 2-propanol were added to DNA solutions. The mixture was inverted several times and centrifuged at 20,000 x *g* for 20 minutes at 4 °C and the supernatant was discarded. The precipitated DNA was then washed twice in 70 % ethanol, dried at room temperature and solubilised in a desired volume of ddH_2O. For transfection of *T. brucei* with linearised plasmids, the final ethanol supernatant was removed under sterile conditions and the plasmid was solubilised to a final concentration of 1 μg/μl in sterile ddH_2O.

DNA modification

Dephosphorylation of DNA was performed using either Calf Intestine Alkaline Phosphatase (Fermentas) or FastAP (Thermo Scientific). 5′ sticky ends were blunted by filling in receded 3′ ends by Klenow fragments. Ligation was performed using T4 DNA ligase with a vector to insert ratio of 1:3 and a total DNA amount of 100 ng. Ligation was performed for 2 - 4 hours at room temperature after which the product was ready to use for transformation. All enzymes were used according to the manufacturer's instructions.

Polymerase chain reaction

Amplification of DNA fragments was performed using the Phusion High-Fidelity DNA polymerase, 10 pmol oligonucleotides and 10 ng of the DNA template. Size determination and purification of PCR products was performed by gel electrophoresis. Following purification from the gel, amplified fragments were ligated into cloning- or transfection-vectors and verified by sequencing by GATC Biotech. All reactions were carried out according to the manufacturer's instructions.

Two step mutagenesis

VSG sequences were mutated in two consecutive PCRs to introduce base exchanges that consecutively lead to single amino acid exchanges. First, the template DNA was amplified, ranging from the target sequence to a flanking sequence, using the mutagenesis primers and primers T3 and T7. The two amplified fragments stretched from the site of mutation to either the T3 or T7 primer region. In the subsequent PCR reaction, equimolar amounts of the two products were used as templates with primers T3 and T7 to generate the full sequence, carrying the mutation of interest. During mutagenesis the VSG sequence was carried by the cloning vector pBluescript SK(+) and was cloned into the plew82v4 expression vector after verification of successful mutagenesis.

3.2.4 Protein techniques

Protein harvesting and purification

This method is a heavily modified version of previous protocols (Cross, 1984; Manthri *et al.*, 2008). Approximately 3.2 - 7.2 x 10^9 cells were harvested by centrifugation at 5,000 x *g* and 4 °C for 30 min and washed twice in TDB. Subsequently, cells were resuspended in 4 ml 10 mM sodium phosphate buffer, pH 8.8 supplemented with protease inhibitors (0.1 mM TLCK, 7.5 μM leupeptin, 0.5 μM aprotinin). Cells were then incubated three consecutive times at 37 °C in a water bath for 5 minutes, followed by centrifugation at 14,000 x *g* for ten minutes and collection of the supernatant. The collected supernatant was concentrated to a total volume of 1.5 ml using Amicon Ultra-15 30k centricons at 5,000 x *g* and 4 °C for 30 min. Buffer exchange to 20 mM tris-HCl, pH 8.0 was performed using a HiTrap desalting column on the Äktaprime plus chromatographic system and the buffer exchange program template. Injection volumes were set to a maximum of 1.5 ml due to column overload for higher volumes. Elution speed was set to 3 - 5 ml/ min, corresponding to the highest possible flow rate that did not exceed the maximum system pressure. Protein was eluted in 10 x 1 ml fractions, which were unified and used for HITrap Q anion exchange chromatography using the HiTrapQ program template. Instead of concentrating the protein solution, anion exchange chromatography was performed in 5 consecutive cycles, reducing protein concentration per cycle to approximately 20 %, to avoid column overload. The volume of each cycle was 2 ml and elution speed was set to 0.4 - 1 ml/min, corresponding to the highest possible flow rate that did not exceed maximum system pressure. Purified protein was eluted in 10 fractions each, which were analysed for sVSG content and purity by SDS-PAGE. Pure sVSG fractions, which eluted from volumes 5 - 8, were unified and concentrated using Amicon Ultra-15 30k centricons. Subsequently, the protein concentration was determined by OD_{280} and the Beer-Lambert law, using an extinction coefficient derived from the online tool exPASy ProtParam applied to the mature VSG amino acid sequence. Protein samples were either lyophilised or flash-frozen and stored at -20 °C. If not stated otherwise, protein solutions were kept on ice during purification to reduce protein degradation. Installation and removal of chromatographic columns was conducted drop-to-drop to avoid air bubbles in the system, which could otherwise impair chromatographic results.

Protein lysate preparation

Bloodstream form trypanosomes were sedimented at 1,400 x *g* for 10 min at 4 °C and the supernatant was discarded. Cell pellets were washed twice in 1 ml TDB each and resuspended to 5×10^5 cells/10 μl in 1 x Laemmli running buffer. Subsequently, protein samples were denatured for 5 min at 100 °C and stored at -20 °C.

Discontinuous SDS polyacrylamide gel electrophoresis

Separation of proteins according to their mass was achieved by denaturing, discontinuous, one-dimensional sodium dodecyl sulphate polyacrylamide gel electrophoresis (Laemmli, 1970). Polyacrylamide gels, consisting of a 2.5 % stacking gel and a 12.5 % resolving gel were prepared. An equivalent of 1×10^6 cells was loaded per sample. Electrophoresis was carried out in Laemmli running buffer at 120 V in the stacking gel and up to 220 V in the resolving gel. Molecular weights were estimated by comparison with the PageRuler protein standard. Electrophoresis was stopped once the bromophenol blue dye front had completely bled from the gel. Subsequently, the gel was dyed by incubation in Coomassie R-250 solution for at least 10 min and destained by incubation in destaining solution for 0.5 - 24 h on an orbital shaker.

Western blot

Prior to blotting, 12 pieces of whatman paper, size 6 x 8 cm, were soaked in western blotting buffer. SDS-PAGE was performed with the protein of interest as described previously. The gel was then placed on a nitrocellulose membrane and stacked with six pieces of soaked whatman paper on either side of the gel and membrane. This stack was placed in the blotting apparatus with the gel on top of the membrane and the lower plate used as the anode. Proteins were blotted 90 minutes at 0.8 mA/cm^2. After blotting, the gel and whatman papers were removed and the membrane was incubated in blocking solution for 60 minutes followed by incubation in PBS supplemented with 1% (w/v) milk powder, 0.1% (v/v) Tween-20 and the 1° antibody (see section 3.1.2 for antibody dilutions) for another 60 minutes. Subsequently, the membrane was washed five times in 0.2 % Tween-20 in PBS and incubated in PBS supplemented with 1 % milk powder, 0.1 % Tween-20 and the 2° antibody for 60 minutes. The blot was then washed four times in 0.2 % Tween-20 in PBS for 5 minutes each and a final washing step in PBS for 5 minutes. The membrane was dried between two sheets of whatman paper before scanning. Care was taken to handle the membrane only with tweezers, as it is sensitive to touch. Once the 2° antibodies incubated on the membrane, the workflow was carried out in the dark to preserve fluorophores. Antibody complexes were detected by excitation of the secondary antibody-coupled fluorophores IRDye 700 and IRDye 800, using the LI-COR Biosciences Odyssey infrared Imaging System.

Isothermal titration calorimetry

Isothermal titration calorimetry was used to determine the binding of phenol red to VSG'Y' in solution. Lyophilized VSG'Y' and phenol red were each resuspended in 20 mM tris pH 8.0 from the same batch to avoid thermal noise from dilution effects. Both solutions were filtered using filters with a pore size of 0.22 μm, to remove precipitate. A concentration of 25 μM VSG'Y' and a 10-fold excess of phenol red were used for measurements with an ITC200 (MicroCal). Phenol red was used as titrant and 20 mM tris-HCl, pH 8.0 as titration control.

Atomic force microscopy

Atomic force microscopy experiments were conducted with 10 μM purified VSG MITat1.1 and resolubilised MITat1.1 crystals in 20 mM tris-HCl, pH 8.0. Approximately 10 μl of protein solution were used to adhere to slides. Serial dilutions were produced if protein densities on the slide were too high. Measurements were executed by Ingrid Tessmer at the Rudolf-Virchow-Zentrum für experimentelle Biomedizin, Würzburg.

Protein quantification

Absolute protein concentrations were measured by amino acid specific UV-absorption, using the Tecan infinite 200 plate reader at 280 nm. Protein concentrations were calculated using the Beer-Lambert law:

$$Absorption_{\mathrm{280nm}} = E \cdot c \cdot l$$

The extinction coefficient E was calculated based on the amino acid sequence for the mature chain of each VSG by the online tool Expasy Protparam. VSG sequences were acquired from the uniprot online servers. The path length l of the nanodrop plate measured 0.1 cm.

Reconstitution of membrane form VSG into lipid vesicles

To construct proteoliposomes that incorporate VSG'Y' at high densities, the membrane form (mfVSG) of VSG'Y' (purified using the procotol from (Hartel *et al.*, 2016)) was incorporated into lipids using a previously published protocol (Erb *et al.*, 1997; Hu *et al.*, 2000). Maximum protein densities were reached by mixing mfVSG and lipids in a 1:50 ratio and subsequent supplementation with 1 % (w/v) sodiumdeoxycholat. This mixture was then incubated at 30 °C for 120 minutes. Detergents were removed in two steps of incubation with Bio-Beads SM (Bio-Rad laboratories, Inc.) for 30 minutes at room temperature. Bio-Beads were removed by centrifugation. Vesicles with incorporated mfVSG were placed on microscopy slides and analysed by FRAP and fluorescence microscopy. 10 % of total mfVSG was fluorescence-labelled with sulfo-NHS-Atto488 as a reporter for successful VSG incorporation into artificial membranes. The reconstitution of VSG'Y' in lipid vesicles was conducted by Marius Glogger in the lab of Susanne Fenz at the 'Lehrstuhl für Zell- und Entwicklungsbiologie', Würzburg.

3.2.5 X-ray crystallography

Protein crystallisation

Protein crystals were obtained by vapour diffusion either by the hanging drop or sitting drop method, which were performed in 24-well and 96-well-plates, respectively. Initial screens were generated by the HoneyBee 963 crystallisation robot, which dispensed 300 nl VSG solution and 300 nl of a unique mother liquor in each of the 96 wells and 60 μl of mother liquor into a reservoir. The plates were then sealed and incubated at 18 °C. To collect crystals, the top seal was removed by scalpel and a small drop of approximately 200 - 300 nl of mother liquor was added to the unsealed crystal drop to prevent sudden precipitation. The crystals were then carefully picked with CryoLoops and transferred to a cryo-solution consisting of mother liquor supplemented with 25 % glycerol. After incubation for 0.5 - 5 min in the cryo-solution, crystals were transferred to liquid nitrogen. 24-well-plates were used to grow larger crystals and to introduce additives in the crystallisation set up. Wells were filled with 1 ml of mother liquor, while 1 μl of protein solution and mother liquor were mixed on a hydrophobic cover slide. The slide was carefully inverted and placed upside-down on the well, which was prepared with vacuum grease to seal the well and avoid evaporation. The plates were stored at 18 °C and crystal growth was monitored on a weekly basis. Care was taken to avoid agitation of the plate, as minor vibrations suffice to swiftly precipitate highly concentrated particles that could potentially destroy crystals. Subsequent handling of crystals was conducted as detailed earlier for 96-well-plates.

Scattering data collection

Early x-ray analysis of protein crystals was carried out in the laboratory of Prof. Kisker in the ’Lehrstuhl für Strukturbiologie’, Rudolf-Virchow-Zentrum, Würzburg. Loop-mounted protein crystals were transferred from liquid nitrogen to a goniometer, which centres the rotational axis of the crystal within the diffractometer beamline. Crystals were gas-flushed with a stream of nitrogen vapour to protect them from thermal- and radiation damage during x-ray crystallographic measurements. An R-Axis HTC x-ray detector (Rigaku) collected the diffraction pattern of a 1.2 kW monochromatic x-ray beam generated by a MicroMax-007 HF x-ray generator (Rigaku). The initial diffraction data was used to find crystals of sufficient quality for the collection of a high-resolution diffraction image at a synchrotron radiation facility. Later measurements were performed at the ’Berliner Elektronenspeicherring-Gesellschaft für Synchrotronstrahlung m.b.H.’ (BESSY) and the ’European Sychrotron Radiation Facility’ (ESRF) in Grenoble, France.

Model building from diffraction data

X-ray diffraction data was collected at beamline BL14.1 at the BESSY with detector PILATUS 6M. Diffraction data was integrated using iMosflm (Leslie & Powell, 2007) and scaled with Scala (Evans, 2006) or Aimless (Evans, 2011). Phasing was carried out by molecular replacement using Phaser (McCoy *et al.*, 2007) using the N-terminal domain of MITat1.2 with 28 % sequence identity in respect to MITat1.1 as a search model. Initial automatic model building was performed using ARP/wARP (Langer *et al.*, 2008) and Buccaneer (Cowtan, 2006), followed by manual model building with Coot (Emsley *et al.*, 2010) and structure refinement by REFMAC (Murshudov *et al.*, 1997; Winn *et al.*, 2011). Structure representations were generated with UIUC visual molecular dynamics (Humphrey *et al.*, 1996) and UCSF chimera (Pettersen *et al.*, 2004).

3.2.6 Small angle x-ray scattering (SAXS)

Sample preparation

Protein samples were prepared as described in subsection 3.2.4. SAXS experiments depend strongly on protein purity. Thus, monomodal size exclusion chromatography was performed to achieve maximum protein purity and to avoid degraded or aggregated protein. Following purification, protein samples were either flash-frozen in liquid nitrogen or lyophylised and then stored at -20 °C. Subsequent size exclusion chromatography of thawed or resolubilised protein samples was performed to elucidate which storage method is best suited to preserve protein integrity. Peaks corresponding to contaminants, aggregates and degradation products were discarded and only eluted fractions corresponding to pure and uncompromised VSG, identified by monomodal elution were pooled, concentrated in Amicon Ultra-15 30k centricons at 5,000 x *g* at 4 °C for 10 min, flash-frozen in liquid nitrogen and stored at -20 °C. Protein samples were transported to beamline BM29 at the ESRF in Grenoble in a frozen state on dry ice and were stored on site at -20 °C. Approximately 30 minutes in advance of the SAXS experiments, the protein samples were thawed on ice and centrifuged at 15,000 x *g* and 4 °C for 15 minutes. The protein concentration of the supernatant was subsequently measured photometrically with a Nanodrop photometer and used to create a serial dilution, with a total of 5 different concentrations in filtered 20 mM tris, pH 8.0, 150 mM NaCl. It is important to use the same batch of buffer for all experiments, including the final SEC purification steps during protein preparation, as minor differences in the buffer composition can already influence the BioSAXS measurements.

Primary data collection and processing

Synchrotron x-ray solution scattering data for VSGs was collected at beamline BM29 at ESRF, Grenoble. Protein serial dilutions of 100 μl stock solution were prepared in 8-tube PCR strips in 5 consecutive steps with a concentration range of 2.53 - 0.16 mg/ml for MITat1.1, 3.39 - 0.21 mg/ml for ILTat1.24 and 2.81 - 0.18 mg/ml for VSG'Y'. Two individual gradients of each protein were measured following injection by a robotic sample changer (Round *et al.*, 2008). The scattering data was recorded with a PILATUS 1M detector (Dectris, Bade, Switzerland) at 293 K at a sample-to-recorder distance of 2.7 m and a wavelength of 1.5 Å. The linear Guinier range, the Radius of gyration *Rg* and the zero-angle scattering intensity *I(0)* were determined by AUTORG (M. V. Petoukhov, P. V. Konarev, *et al.*, 2007). Data points preceding the resulting Guinier range and the noisy scattering beyond q = 3 Å were removed from scattering data prior to scaling and extrapolation to 0 concentration with PRIMUS (P. V. Konarev *et al.*, 2003). The pair-distance distribution function *P(r)*, the maximum particle dimension D_{max} and *Rg* were calculated using GNOM (Svergun, 1992) and were consistent with the estimates from the Guinier approximation. The molecular mass was derived using the Porod invariant on the excluded volume of the hydrated particle (M. V. Petoukhov, Franke, *et al.*, 2012).
All experimental data that was gathered at BM29 was stored both locally on a hard drive and to a user account on the Information System for Protein Crystallography Beamlines (ISPyB) (De Maria Antolinos *et al.*, 2015).

Modeling of complete VSGs

Structure modelling of complete VSG molecules was performed with the previously processed scattering data. *Ab initio* low-resolution shape determination was performed by DAMMIN (Svergun, 1999), using the previously generated GNOM output, applying P2 and prolate symmetry. 10 DAMMIN shapes were subsequently averaged in DAMAVER (Volkov & Svergun, 2003), applying P2 symmetry and running the program in automatic mode. The generated DAMSTART output file from DAMAVER was used in Situs pdb2vol (Wriggers, 2010) to generate a pdb volume map. No mass weighting or B-factor selection, a voxel space of 1 Å, a kernel width of 6 Å and a hard sphere-smoothing kernel without

smoothing correction were selected for this operation. The volumetric map was used for manual and automated fitting of high-resolution structural domains in UCSF Chimera (Pettersen *et al.,* 2004) and VMD (Humphrey *et al.,* 1996) to define initial coordinates for modelling. Subsequently, the fitted individual domains were combined in a single file and the rotational axis was set to the origin (xyz = 0) in Massha (p. V. Konarev & D. I. Petoukhov M. V. a. S., 2001) before separation into individual domains again. This helps placing the symmetry axis correctly for the complete model, while retaining individual placement of domains during rigid body modelling.
Amplitudes for individual high-resolution domains were calculated using CRYSOL (Svergun, Barberato, *et al.,* 1995) with standard parameters and *4*π*sinθ/λ [1/nm]* angular units, but without fitting to experimental data to avoid artefacts from an inaccurate hydration layer. The extrapolated scattering data was used in BUNCH (M. V. Petoukhov & Svergun, 2005), CORAL (M. V. Petoukhov, Franke, *et al.,* 2012) and EOM (Bernadó *et al.,* 2007; Tria *et al.,* 2015) to calculate domain arrangements for complete VSGs. Contact restrictions derived from N-terminal crystal structures were applied to preserve the dimerisation surface for monomers in CORAL and BUNCH, while the dimer for N-terminal domains was fixed during EOM. P2 symmetry was applied to monomers of individual domains and initial coordinates were derived from a manual fit of domains with the respective pdb2vol file. Linkers L1 and L2 of the C-terminal domain were removed manually from pdb files to allow BUNCH and CORAL a flexible fitting of these regions and to increase the linker length to at least 5 residues for correct linker modelling. PRE_BUNCH was used to implement a dummy CA chain for linkers and missing residues prior to BUNCH modelling. If the individual VSG chains were not shifted to the origin previously, this could also be done during PRE_BUNCH. A maximum scattering vector of 1.8 - 3.0 $Å^{-1}$ (36 - 60 % of the scattering curve) was chosen individually for each dataset to include all information relevant for domain positioning while avoiding errors from low-resolution data. Complete symmetric multi chains and a native linker folding were chosen for EOM. Since VSGs retain the glycan fraction of the GPI anchor during purification, this motif had to be included into the model. The structure file for the GPI anchor was provided by Terry Smith, University of St Andrews, UK, and was added covalently to the C-terminal amino acid with VMD and Chimera. The conformation between the S2 domain and the GPI in ILTat1.24 was chosen according to previous minimizations (Jones *et al.,* 2008), while the GPI anchor and final C-terminal residue were provided as individual domains for MITat1.1.

3.2.7 Fluorescence microscopy

VSG'Y' fluorescence excitation

5 x 10^5 trypanosomes expressing VSG'Y' were harvested by centrifugation, washed twice in TDB and resuspended in either 100 μl HMI-9, 200 - 400 μM TDB-PR or fluorescence solution and incubated at 37 °C for 10 min. 2.0 μl cell suspension was placed on a microscopy slide. Fluorescence emission was excited at 360 - 420 nm with an exposure time of 150 ms. Measurements were performed immediately after preparation of slides to reduce incubation effects. Deviations from this protocol for specific experiments are described in the corresponding subsections of the results.

Fluorescence activated trypanocidal effect

1 x 10^5 - 1 x 10^7 cells/ml of exponentially growing trypanosomes expressing VSG'Y' were harvested by centrifugation, washed twice in TDB and resuspended in 200 - 800 μM TDB-BPB solution. The cell solution was then incubated at 37 °C for 10 min and 2.0 μl of the suspension was placed on a microscopy slide. Fluorescence emission was excited at 560 nm with an exposure time of 20 - 150 ms and measurements were performed immediately after preparation of slides to reduce incubation effects. Deviations from this protocol for specific experiments are described in the corresponding subsections of the results.

To test the influence of various compounds on the trypanocidal effect, the BPB solution was supplemented with trolox (TDB), butylated hydroxytoluene (0.1 % DMSO in TDB), ascorbic acid (TDB), glutathione (TDB) and N-acetylcysteine (TDB) prior to resuspension of cells. The duration of cell survival was measured from the beginning of excitation at 560 nm until the onset of the characteristic fluorescence wave on the cell surface.

4 Results

4.1 Structural analysis of VSGs

4.1.1 sVSG purification

X-ray crystallography is the primary method for structural analysis of proteins and has a high demand in terms of protein abundance. This is due to the trial-and-error approach that is inherent to protein crystallisation. Additionally, protein crystals are required to grow to a minimum diameter of approximately 50 μm to provide a minimum diffraction intensity and in sufficient quantity to guarantee successful handling of the sensitive crystals until measurements can be conducted.

A common approach to meet the high protein demands is to clone the gene of the protein of interest into high-yielding expression systems, e.g. *E. coli* or yeast. However, in *Trypanosoma brucei* VSGs make up approx. 10 % of the parasites total protein. Therefore, if a sufficient cell density can be established *in vitro*, VSGs can be purified directly from cultured *T. brucei*, which ensures correct folding and post-translational modifications (e.g. glycosylations), while these could be problematic when using expression systems.

Every *T. brucei* culture expresses a single type of VSG and was regularly controlled, to avoid mixed VSG populations arising from antigenic variation. Normal cell cultivation is performed in tissue culture flasks in volumes ranging from approx. 10 -200 ml. However, to obtain the required quantities of purified VSG, culture volumes of up to 2 l are required per purification at increased cell densities. To avoid problems arising from insufficient nutrient supply, cells are cultivated in Erlenmeyer flasks with a maximum volume of 20 % for optimal CO_2 uptake and flasks are shaken on an orbital shaker to avoid sedimentation. Maximum achievable cell densities varied for each cell line and cultivation parameters had to be calibrated individually to maximize protein yield. MITat1.4 and MITat1.5 were sensitive at high cell densities and high revolutions per minute (rpms), which resulted in a reduced and linear growth behaviour in the case of MITat1.5 and in growth stalling for MITat1.4. Best cultivation parameters for each cell line, including revolutions on an orbital shaker and maximum achievable cell densities are displayed in Tab. 7.

The original protocol for high-density cultivation of bloodstream form trypanosomes (Hermann, 2008) included supplementing HMI-9 medium with a total of 20 % FCS at cell densities beyond 1×10^6 cells/ml. However, recent tests with the current batch of FCS displayed no change in growth behaviour when cells were cultivated at high densities with only the original 10 % total FCS. Thus, protocols were changed to include a maximum of 10 % FCS for cultivation.

Table 7 – Cultivation parameters and maximum cell densities.

Cell line	max rpm	max cells/ml
MITat1.1	80	4 - 6 x 10^6
MITat1.2	80	3.6 - 4.3 x 10^6
MITat1.4	25	1.1 - 1.7 x 10^6
MITat1.5	25	1.8 - 2.5 x 10^6
VSG'Y'	40	1.8 - 3.5 x 10^6
13-90 M1.2$_{\text{KO}}$ VSG'Y'Δglyc	60	2.5 - 3.3 x10^6
13-90 M1.2$_{\text{KO}}$ ILTat1.24	40	3.5 - 4 x 10^6

The original protocol for sVSG purification (Cross, 1984; Manthri *et al.*, 2008) included a single incubation step of cell lysate for 5 min at 37 °C to cleave the membrane bound mfVSG by cellular GPI-specific phospholipase C (GPI-PLC) and to release the soluble sVSG (Ferguson *et al.*, 1985). However, all cellular VSG that was potentially still bound to the membrane was lost during the subsequent centrifugation. Instead of immediately discarding the cell pellet, the incubation of cell debris at 37 °C with the subsequent collection of the sVSG-enriched supernatant was repeated two more times and electrophoretic analysis of the supernatant fractions revealed a total VSG recovery that was increased by 100 % (Fig. 10). The maximum load volume for anion exchange- and desalting columns was 1.5 ml and 2 ml, respectively. Amicon Ultra-15 30k and Ultra-0.5 10k centricons were used to concentrate the protein extracts to the appropriate volumes where necessary. Using the Ultra-0.5 10k centricons resulted in a noticeable loss of protein compared to centrifugation in Ultra-15 30k centricons and was discarded in favour of the Ultra-15 30k.

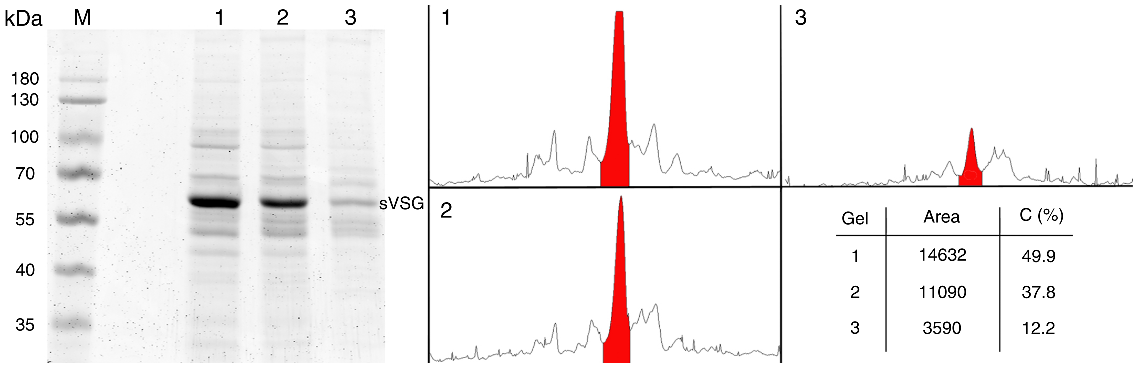

Gel	Area	C (%)
1	14632	49.9
2	11090	37.8
3	3590	12.2

Figure 10 – VSG release by GPI-PLC in multiple steps. sVSG was released in three consecutive steps (left). Each lane (1 - 3) corresponds to the supernatant of one step of phospholipase C induced sVSG release at 37 °C. ImageJ64 was used to calculate the intensity plots for each gel lane and the integrals (right). sVSG is highlighted in red within the plot and the total sVSG release is displayed in the table. The initial GPI-PLC treatment released 49.9 % sVSG, while the second and third release amounted to 50.1 %, effectively doubling the total sVSG yield.

During protein loading onto the anion exchange column, a broad peak was detected suggesting column overload. To avoid a loss of protein extract by overloading, subsequent purifications were not concentrated prior to anion exchange but sample loading was conducted in five consecutive steps and the pure fractions were pooled afterwards. sVSG eluted in fractions 5 - 11 in an NaCl gradient ranging from 0 - 1 M NaCl. sVSG free from contaminations was identified in fractions 5 - 8, corresponding to 200 - 340 mM NaCl. The ratio of purified sVSG to residual proteins (≥95 % purity) in fractions 5 - 7 was sufficient for protein crystallisation and fractions were combined for further processing.

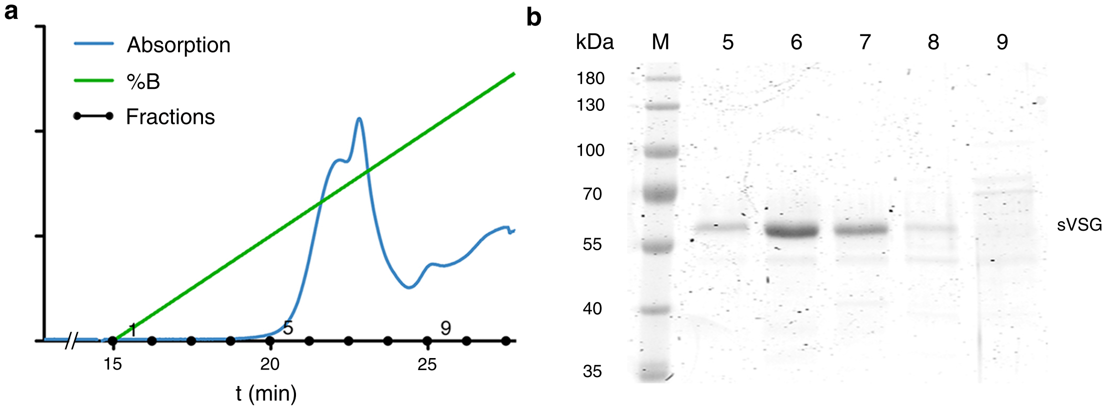

Figure 11 – VSG elution during anion exchange chromatography. a) Anionic protein bound to the anion exchange column started eluting from fraction 5 at a concentration of 20 % solvent B (20 mM tris-Cl, pH 8.0, 1 M NaCl), corresponding to 200 mM NaCl. b) Electrophoretic analysis of each fraction showed a high VSG abundance in fractions 5 - 8. Fractions 5 - 7 displayed pure protein and were concentrated and used for crystallisation.

In cases where initial chromatographic purity of sVSG was insufficient or during protein preparation where maximum purity was required (e.g. SAXS applications), size exclusion chromatography was performed to further increase protein purity. Additionally, aggregates from protein samples stored at -80 °C were removed by size exclusion chromatography. Since protein yield was diminished by 10 - 50 % during SEC, this was only performed where necessary.

It was discovered during previous Thermofluor tests of sVSG stability (Bartossek, 2011) that high salt concentrations (>150 mM NaCl or KCl) reduce VSG stability in solution, advising the removal of salts prior to crystallisation. During desalting by dialysis, purified sVSG had a tendency to precipitate, resulting in loss of protein. As a consequence, desalting columns and the Äktaprime plus were since used to desalt protein fractions and to conduct buffer exchange in a single step, avoiding the problem of protein loss through precipitation and protein instability during dialysis.

Process optimization and reduced loss of VSG during purification led to an increase in protein abundance of up to 2.5-fold. This improvement was most noticeable during purification of high-yield cell lines, e.g. MITat1.1 with an increased output from 1.5 mg to 3.8 mg per purification. The theoretically achievable amount of a MITat1.1 cultured at 6×10^6 cells/ml, in a total volume of 1.6 l, expressing a total of 5×10^6 VSG dimers with a molecular weight of 96 kDa is 7.68 mg. Therefore, a maximum of 49.5 % of the theoretical yield can be achieved for MITat1.1. More sensitive cell lines displayed a weaker increase of yield by the adapted protocol. Effective yields increased by 0 % (37,5 % theoretical yield) for MITat1.2, 217 % (87.5 % theoretical yield) for MITat1.5 and -6 % (32.5 % theoretical yield) for VSG'Y'. Missing or reduced protein yields of the optimized protocol indicate an increase of cell sensitivity towards high-density cultivation and orbital shaking that was generally observed in the course of this thesis due to changes in cultivation medium composition. Cell lines and protein yield are listed in Tab. 8.

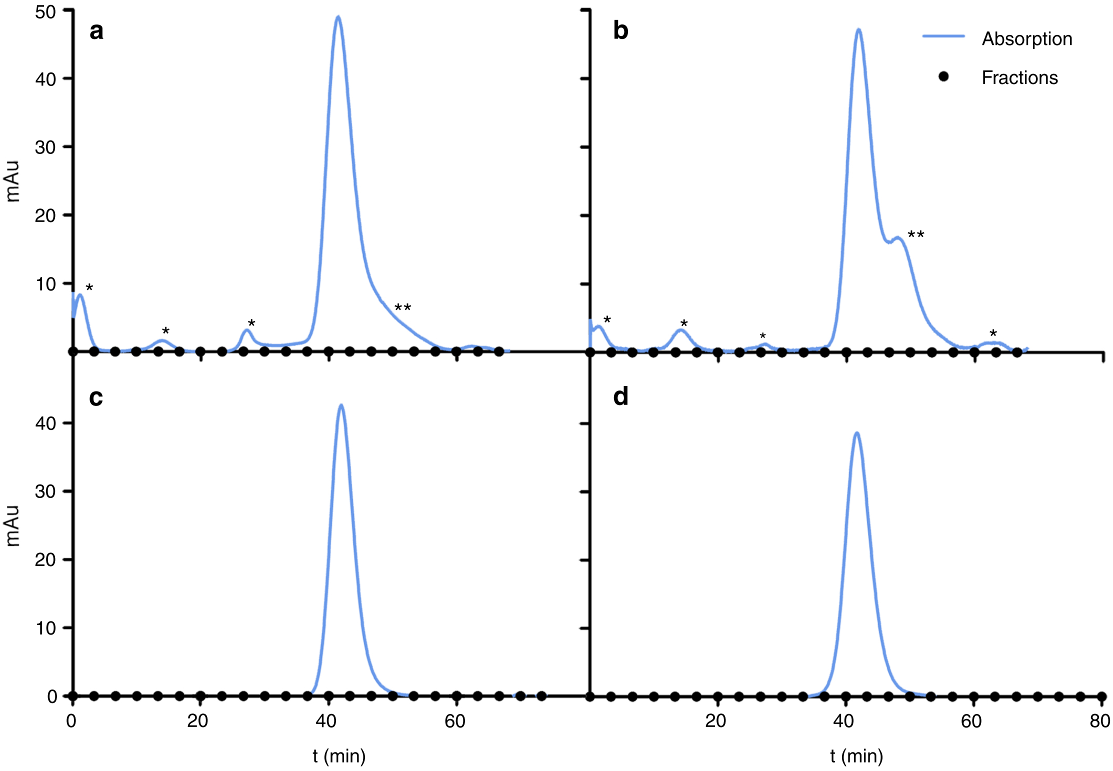

Figure 12 – Improvement of protein purity by SEC. a+b) Impurities (*), sVSG degradation (*) (which cannot be distinguished and thus share the same symbol) and sVSG aggregates (**) were detectable following purification (a) and reconstitution of lyophilised protein (b). c) SEC isolation of fractions 11 - 13 from protein solution a+b resulted in highly purified sVSG. d) Consecutive flash freezing and re-thawing of liquid fraction c retains protein stability and was the superior method for sVSG storage and transportation compared to lyophilisation and reconstitution.

Table 8 – Protein yield per cell line.

Cell line	Initial protein yield (mg)	Optimized protein yield (mg)
MITat1.1	1.5	3.8
MITat1.2	2	2
MITat1.4	1.3	/
MITat1.5	1.2	2.6
VSG'Y'	1.7	1.6
ILTat1.24	/	2.7

4.1.2 X-ray crystallography

Once the different VSG types could be purified reproducibly and both in sufficient quality and quantity, crystallographic trials were commenced. It should be noted that minor difference in the protein structure can already result in vastly different requirements for crystallisation parameters. Thus the search for successful crystallisation conditions has to be conducted for each VSG individually.

4.1.2.1 VSG′Y′

Previous work on the determination of the VSG′Y′ structure (Bartossek, 2011) resulted in a number of conditions that allowed the formation of VSG′Y′ crystals with a diffraction resolution of 4.5 - 7 Å. During this thesis the optimized purification procedure (section 4.1) was utilized to crystallise VSG′Y′ under previously successful conditions to determine whether the improved quality of the starting material also improved crystal formation and thus diffraction. Screening of previously untested conditions was performed to extend the search for optimal crystallisation parameters. All compositions resulting in crystal growth are displayed in Tab. 9. See Tabs. 5 through 15 in the appendix for a detailed list of screen compositions.

Table 9 – List of successful conditions for the crystallisation of VSG′Y′.

Protein (Buffer)	c (mg/ml)	Screen	Well no.
VSG′Y′ (H_2O)	20	MITat Screen	B4 - B6, C5
VSG′Y′ (H_2O)	15	MITat Screen	B5, B6
VSG′Y′ (H_2O)	30	Nextal pH Clear	E8 - E11
VSG′Y′ (H_2O)	20	Optimix 3	B6
VSG′Y′ (H_2O)	25	Nextal PEG	G5

Screen	Composition
MITat Screen B4	0.1 M citric acid, pH 4.5, 2.8 M ammonium sulphate
MITat Screen B5	0.1 M citric acid, pH 4.5, 3.0 M ammonium sulphate
MITat Screen B6	0.1 M citric acid, pH 4.5, 3.2 M ammonium sulphate
MITat Screen C5	0.1 M citric acid, pH 5.0, 3.0 M ammonium sulphate
Nextal pH clear E8	0.1 M citric acid, pH 5.0, 1.6 M ammonium sulphate
Nextal pH clear E9	0.1 M MES, pH 6.0, 1.6 M ammonium sulphate
Nextal pH clear E10	0.1 M HEPES, pH 7.0, 1.6 M ammonium sulphate
Nextal pH clear E11	0.1 M tris, pH 8.0, 1.6 M ammonium sulphate
Optimix 3 B6	2.0 M ammonium sulphate, 0.1 M HEPES, pH 7.5
Nextal PEG G5	0.2 M potassium acetate, 20 % (w/v) PEG 3,350

Previous Thermofluor experiments with VSG′Y′ indicated increased conformational stability when the protein was solubilised in ddH_2O only and when avoiding salt concentrations above 150 mM. Thus, protein buffers were exchanged to ddH_2O in following VSG purifications. This also reduced the complexity of the crystallisation setup to a single buffer (mother liquor) instead of two buffers (mother liquor and protein solution). Growth of 1 - 5 crystals per well was detected after approximately 25 - 30 days of incubation at 18 °C which formed in bipyramidal morphology with diameters ranging from 50 - 250 μm. Crystals were sensitive to physical stress and could easily decompose into unordered precipitate or smaller fragments. Crystals were carefully extracted from crystallisation drops with CryoLoops (Hampton Research) and transferred to a cryo-solution comprising of the crystallisation mother liquor supplemented with 25 % glycerol. In some cases prolonged incubation in cryo-solution resulted in damage and degradation of the crystal, which may have had detrimental effects on the diffraction resolution. Reducing incubation times in cryo-solution however, increases the chance of the formation of ice crystals during flash freezing due to incomplete cryo-protection. As a result, crystals were incubated in cryo-solution for a time ranging from 0.5 to 5 minutes to minimize both soaking- and cryo-hazards. Crystal morphology was constantly monitored during incubation, which was aborted when crystal degradation was observed. Initial diffraction measurements were conducted using the Rigaku MicroMax-007 HF x-ray generator and the HTC x-ray detector. Crystals with a protein diffraction pattern of sufficient resolution and devoid of artefacts were stored for further measurements at synchrotron radiation facilities. Crystals with low resolution, strong twinning or strong ice- and precipitant-diffraction were discarded after measurements. Collection of high-resolution diffraction data was conducted at beamline MX 14.1 at BESSY II, using a PILATUS 6M detector to collect the diffraction data from a single crystal mounted in a cold N_2 gas stream. The diffraction data of VSG′Y′ and all other VSGs was analysed by Christin Schäfer from the ′Lehrstuhl für Strukturbiologie′ at the Rudolf-Virchow-Zentrum, Universität Würzburg. The final resolution of the crystals was 4.5 - 7 Å and did therefore not improve upon previous trials (Bartossek, 2011). No condition could be established in the course of this project that improved the experimental diffraction resolution for wildtype VSG′Y′ any further and the current resolution was insufficient for structure determination.

4.1.2.2 Deglycosylated VSG′Y′

A possibility to improve diffraction resolution of protein crystals is to increase the monodispersity of the protein of interest prior to crystallisation. A source of heterogeneity that may influence sample monodispersity is glycosylation. VSGs differ by the degree and position of glycosylations (Mehlert *et al.*, 1998; Zamze *et al.*, 1990) and VSG′Y′ is known to possess a single glycosylated Asn residue within the C-terminal domain, carrying a $Man_{9\text{-}5}GlcNAc_2$. Even though $Man_7GlcNAc_2$ is the most abundant oligomannose structure in VSG′Y′, the overall glycosylation remains heterogeneous. Removing the glycan may improve monodispersity and reduce crystal mosaicity, thus improving diffraction resolution of the resulting crystals. The deglycosylated form of VSG'Y' (VSG'Y'Δglyc) was purified from cell line 13.90 (Wirtz *et al.,* 1999), originally expressing MITat1.2. The 13.90 cell line was transfected to constitutively express the mutant VSG'Y'Δglyc, where either Ser or Thr of the tripeptide recognition sequence for asparagine-linked glycosylation was exchanged, while the original MITat1.2 was exchanged with a puromycin resistance cassette. The transgenic cell line expressing the mutant VSG was established by Nicola Jones from the 'Lehrstuhl für Zell- und Entwicklungsbiologie', Universität Würzburg. Antibiotic selection for transgenic cell lines was omitted in cultivation volumes exceeding 100 ml. Instead of antibiotic selection, immunofluorescence analysis was used to verify the cultivated cells for VSG'Y' fluorescence emission prior to protein purification. VSG purification and crystallisation screens were conducted as described previously. Conditions that resulted in growth of VSG'Y' crystals were prioritized over untested conditions during screening for crystallisation of the VSG'Y'Δglyc mutant. Within 20 - 30 days crystals with a cubic morphology and a diameter of 14 - 40 μm formed in several wells, which are listed in Tab. 10. A detailed composition of the used screen can be found in the manufacturer's product manual or in Tab. 15 in the appendix.

Table 10 – List of successful conditions for the crystallisation of VSG'Y'Δglyc.

Protein (Buffer)	c (mg/ml)	Screen	Well no.
VSG'Y'Δglyc (H_2O)	20	MITat Screen	B1, D1, D8, E8, F2, G2

Screen	Composition
MITat Screen B1	0.1 M citric acid, pH 4.5, 1.6 M ammonium sulphate
MITat Screen D1	0.1 M citric acid, pH 5.5, 1.6 M ammonium sulphate
MITat Screen D8	0.1 M bicine, pH 8.0, 2.0 M ammonium sulphate
MITat Screen E8	0.1 M bicine, pH 8.5, 2.0 M ammonium sulphate
MITat Screen F2	0.1 M tris, pH 7.5, 2.0 M ammonium sulphate
MITat Screen G2	0.1 M tris, pH 8.0, 2.0 M ammonium sulphate

Crystals were harvested and cryo-protected without visible damage to the surface. Diffraction measurements from beamline MX 14.1 at BESSY II revealed a resolution of up to 1.6 Å but also a twinning of crystal lattices. In twinned crystals more than one set of diffraction spots is observed simultaneously, which makes indexing and integration problematic and may lead to the assignment of wrong symmetry and unit cell dimensions. Although the overall cubic morphology of the crystals did not suggest a problem in lattice formation, crystallisation of VSG'Y'Δglyc always resulted in complex signals from crystal twinning, and were difficult to translated into an electron density map. Additionally, crystals were too small to isolate non-twinned areas. Despite the twinning problems it was attempted to solve a structure from the diffraction data, for which the phase problem had to be solved. The differences in sequence between VSG'Y' and the published VSG structures, however, is too high to solve the structure by molecular replacement (see Tab. 14). This method requires a sequence identity between the protein of interest and the search model of roughly 30 % to obtain good results and a high structural similarity can further compensate for a lack of sequence identity. The sequence identities between VSG'Y' and known VSG structures varies between 8.8 % and 10.7 %, while the structural similarity varies between 13.9 % and 15.8 % and are therefore not considered optimal. Instead of molecular replacement, sulphur phasing was tested. The anomalous signal of the protein sulphur atoms was supposed to be used to solve the phase problem, however no sulphur signal was detectable from the scattering data. Due to a lack of alternatives, molecular replacement was attempted nonetheless. The diffraction data was integrated using iMosflm and scaled with Aimless (Vonrhein *et al.*, 2011). Phasing was tested by molecular replacement with Phaser, using the N-terminal domain of MITat1.2 (PDB-ID: 1VSG) and MITat1.1 (described in section 4.1.2.3) as a search model. The model was built manually with Coot, and the structure was refined with Phenix Refine (Adams *et al.*, 2010) to a final resolution of 1.6Å (see Tab. 11 for crystal parameters). The R-values of the model are 39.22 (R_{work}) and 44.13 (R_{free}). The final model consisted of approximately 250 residues and had no resemblance to known VSG structures. The model was generated on the basis of molecular replacement with two VSGs of insufficient homology and represents only an early attempt of structure building for VSG'Y'Δglyc.

Table 11 – Experimental parameters for VSG'Y'Δglyc crystals.

Crystallisation condition	0.1 M citric acid pH 5.5, 1.6 M $(NH_4)_2SO_4$
Detector	PILATUS 6M
Oscillation	0.1
Wavelength	0.918409
Time	0.04
No. of images	3600
Space group	H3
Cell dimensions	120.44 x 120.44 x 121.18, 90,90,120°
Resolution	47.90 - 1.85
Completeness (%)	100 (96.5)
∅ Redundancy	7.8 (5.5)
I/σ (I)	12.3 (1.5)
R_{merge}/R_{pim}	11 (102)/4.2 (46.8)
Correlation coefficient ($CC_{1/2}$)	99.9 (58.5)
V_M ($Å^3$/Da)	2.56
Monomers per AU	2
Solvent (%)	52.03
R_{free}	44.13 (MR29, Refine30)
R_{work}	39.22 (MR29, Refine30)
RMSD bond angle	1.969
Bond length	0.014

4.1.2.3 MITat1.1

Due to the more robust cultivation and consequently higher maximum densities of MITat1.1 cell lines compared to VSG'Y', MITat1.4 and MITat1.5 (see Tab. 8), an increased protein yield was available per purification, resulting in a higher throughput of crystallisation screens. Eventually, parameters were discovered that led to the formation of long needle-shaped crystal clusters. Crystals appeared after approximately 14 - 20 days of incubation in Nextal PEG suite condition C12 comprising of 0.1 M MES pH 6.5 and 15 % PEG 20,000. This composition was subsequently used to formulate an individual screen (Tab. 14, appendix) to further improve crystal quality. Tab. 12 lists conditions that led to growth of MITat1.1 crystals. A detailed composition of each screen can be found in the manufacturer's product manual or in Tabs. 5 through 15 in the appendix. Crystals from wells B8 - B11, C7 - C11, D8 - D12 and E9 from the fine screen based on condition Nextal C12 were used for x-ray analysis. To avoid problems arising from complex signals of twinned protein crystals, only single needles and small fragments were collected for x-ray analysis. Protein crystals were soaked in mother liquor supplemented with 25 % glycerol for 0.5 - 5 min and flash frozen in liquid nitrogen. Crystals proved to be mechanically robust during harvesting and cryo-soaking.

Table 12 – List of successful conditions for the crystallisation of MITat1.1.

Protein (Buffer)	c (mg/ml)	Screen	Well no.
MITat1.1 (H_2O)	15	Nextal PEG	C12, E8, E9
MITat1.1 (H_2O)	30	Nextal PEG	C12
MITat1.1 (H_2O)	24	Nextal C12 fine screen	B8 - B11, C7 - C11, D8 - D12, E9
MITat1.1 (H_2O)	20	Nextal C12 fine screen	B8 - B11, C8 - C11, D11
MITat1.1 (H_2O)	20	MITAT Screen	B8, C8, E2, F8
MITat1.1 (H_2O)	20	Index	D6, D7, G7, F12
MITat1.1 (H_2O)	20	Crystal Screen	G2

Screen	Composition
Nextal PEG C12	0.1 M MES, pH 6.5, 15 % (w/v) PEG 20,000
Nextal PEG E8	0.2 M potassium chloride, 20 % (w/v) PEG 3,350
Nextal PEG E9	0.2 M ammonium chloride, 20 % (w/v) PEG 3,350
Nextal C12 fine B8	0.1 M MES pH 5.5, 14 % PEG 20,000
Nextal C12 fine B9	0.1 M MES pH 5.5, 15 % PEG 20,000
Nextal C12 fine B10	0.1 M MES pH 5.5, 16 % PEG 20,000
Nextal C12 fine B11	0.1 M MES pH 5.5, 17 % PEG 20,000
Nextal C12 fine C7	0.1 M MES pH 6.0, 13 % PEG 20,000
Nextal C12 fine C8	0.1 M MES pH 6.0, 14 % PEG 20,000

Nextal C12 fine C9	0.1 M MES pH 6.0, 15 % PEG 20,000
Nextal C12 fine C10	0.1 M MES pH 6.0, 16 % PEG 20,000
Nextal C12 fine C11	0.1 M MES pH 6.0, 17 % PEG 20,000
Nextal C12 fine D8	0.1 M MES pH 6.5, 14 % PEG 20,000
Nextal C12 fine D9	0.1 M MES pH 6.5, 15 % PEG 20,000
Nextal C12 fine D10	0.1 M MES pH 6.5, 16 % PEG 20,000
Nextal C12 fine D11	0.1 M MES pH 6.5, 17 % PEG 20,000
Nextal C12 fine D12	0.1 M MES pH 6.5, 18 % PEG 20,000
Nextal C12 fine E9	0.1 M tris pH 7.0, 15 % PEG 20,000
MITat screen B8	0.1 M MES pH 6.0, 2.0 M ammonium sulphate
MITat screen C8	0.1 M MES pH 6.5, 2.0 M ammonium sulphate
MITat screen E2	0.1 M tris pH 7.0, 2.0 M ammonium sulphate
MITat screen F8	0.1 M bicine pH 9.0, 2.0 M ammonium sulphate
Index D6	0.1 M bis-tris, pH 5.5, 25 % (w/v) polyethylene glycol 3,350
Index D7	0.1 M bis-tris, pH 6.5, 25 % (w/v) polyethylene glycol 3,350
Index G7	0.2 M ammonium acetate, 0.1 M bis-tris, pH 6.5, 25 % (w/v) polyethylene glycol 3,350
Index F12	0.2 M sodium chloride, 0.1 M HEPES, pH 7.5, 25 % (w/v) polyethylene glycol 3,350
Crystal screen G2	0.2 M ammonium sulphate, 0.1 M MES monohydrate, pH 6.5, 30 % (w/v) polyethylene glycol monomethyl ether 5,000

Crystals were tested with the Rigaku MicroMax-007 HF x-ray generator on the HTC x-ray detector, and crystals of promising quality in regards to purity (good signal-to-noise ratio) and resolution (approx. 4 - 7 Å initial resolution) were used for data acquisition at the BESSY synchrotron radiation facility (see Tab. 13 for the crystal parameters). The overall mechanical stability of protein crystals was high, which resulted in reduced lattice degradation and a high diffraction resolution. No twinning occurred and the protein was free of ice crystals. Final measurements were conducted at beamline MX 14.1 at BESSY II, using a PILATUS 6M detector to collect the diffraction data from a single crystal mounted in a cold N_2 gas stream. Unit cell dimensions were 78.51/95.04/103.75 $Å^3$ and 90/90/90° in space group $P2_12_12_1$. The diffraction data was integrated using iMosflm and scaled with XDSAPP (Krug *et al.*, 2012). Phasing was carried out by molecular replacement with Phaser using the N-Terminal domain of MITat1.2 with 28 % sequence identity in respect to MITat1.1 as a search model (PDB-ID: 1VSG). The model was built manually with Coot, and the structure was refined with Phenix Refine and REFMAC to a final resolution of 1.65 Å. The R-values of the model are 0.168 (R_{work}) and 0.20 (R_{free}).

Table 13 – Crystallographic parameters of MITat1.1.

Crystallisation condition	0.1 M MES pH 6.5, 25 % PEG 4,000
Detector	PILATUS 6M
Oscillation	0.1
Wavelength	0.918409
Time	0.5
No. of images	1800
Space group	$P2_12_12_1$
Cell dimensions	78.51 x 95.04 x 103.75, 3x90°
No. of used reflections	617,499
No. of unique reflections	93,916
Resolution	47.52 - 1.65
Completeness (%)	99.6 (98.1)
∅ Redundancy	6.6 (5.9)
I/σ (I)	13.89 (1.89)
R_{merge}/R_{pim}	11.9 (108.0)
Correlation coefficient (CC $_{1/2}$)	0.998 (0.746)
Wilson B-factor	18.419
V_M (Å^3/Da)	2.42
Monomers per AU	2
Solvent (%)	49.19
R_{free}	20.43
R_{work}	16.81
Average B factor (Å^2)	19.68 (A: 16.58, B: 17.46, C: 28.69, D: 49.34, S: 35.38)
Figure of merit (%)	8.8058
RMSD bond angle	1.8917
Bond length	0.0197
Ramachandran	Outlier: 1 (0.14 %); Allowed: 2.57 %; Favoured: 718 (97.29 %)

The diffraction data, and thus the crystals, included only the NTD of MITat1.1. Electrophoretic analysis of resolubilised crystals confirmed cleavage of the VSG during crystallisation (Fig. 13a), similar to previously published observations (D. M. Freymann *et al.*, 1984). Subsequent atomic force microscopy (AFM) of fresh protein samples and resolubilised crystals also revealed degradations for the crystallised form. While the freshly purified samples display a mean molecular weight of 64.8 kDa, the crystal sample has a mean molecular weight of 38.4 kDa, which is in accordance to the electrophoretic analysis. Additionally, AFM experiments of fresh VSG shows a volume heterogeneity for molecules that are of the approximately same size. This suggests conformational heterogeneity for complete VSG MITat1.1. Some VSG molecules are very compact while others stretch out and display an increase in total volume. This suggest that MITat1.1 could fold into different conformations. It is important to note that the automated volume analysis of the AFM spots separates multiple domains of a single protein molecule into individual volumes. In Fig. 13b the left circle outlines spots that are identified by the AFM analysis as two molecules of approx. 50 kDa which might also be a single molecule of 100 kDa. Therefore, while highlighting the molecular heterogeneity, the bar diagram is misguiding when compared to the electrophoretic analysis in Fig. 13a. Many of the smaller spots are actually a single larger molecule. While the diagram in Fig.13b displays a relatively homogeneous distribution of molecules that range in size from 0 200 kDa, the actual size distribution should tend towards higher molecular weights, roughly concentrating around 55 kDa which correspond to the size of the sVSG monomer.

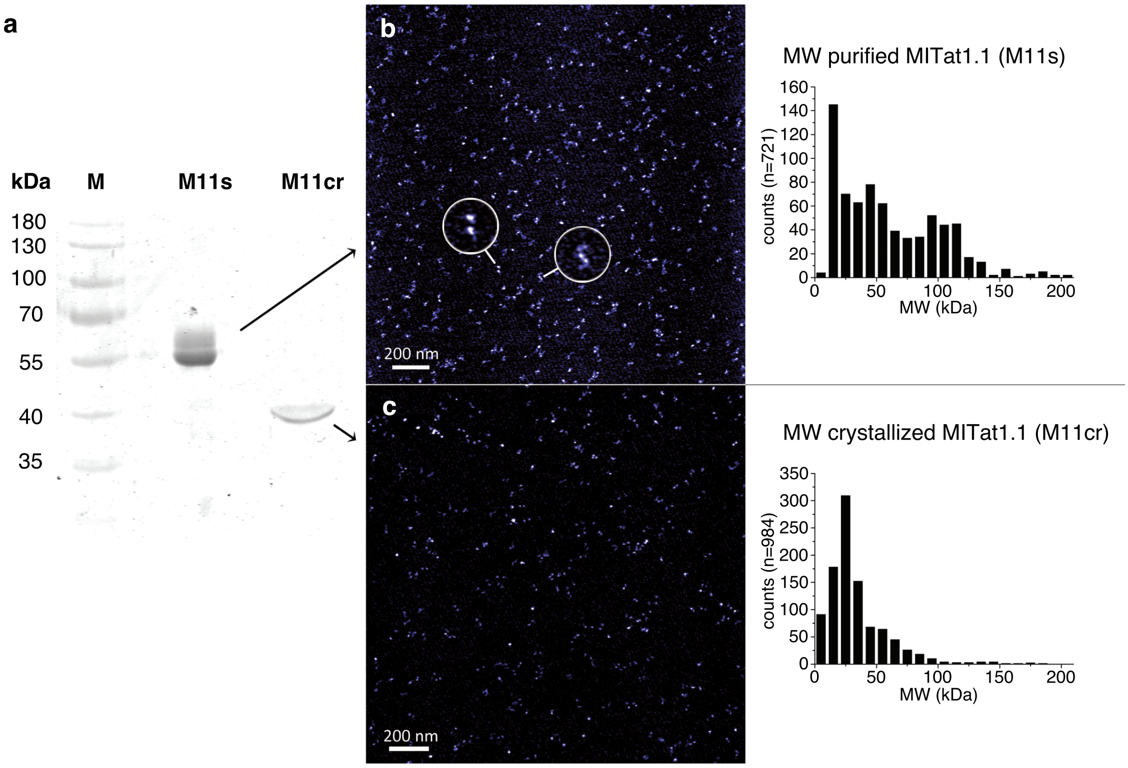

Figure 13 – SDS-PAGE and AFM analysis of MITat1.1 before and after crystallisation. a) A sample of freshly purified VSG MITat1.1 displays an electrophoretic size of approximately 55 kDa (M11s). Following crystallisation the size of the protein band is reduced to 40 kDa (M11cr), matching the size of the NTD. b+c) AFM analysis of both protein samples underline electrophoretic results. Fresh samples display a higher heterogeneity in size (b) while crystallised protein is reduced to a mean size of approximately 40 kDa. Highlights (b) of two individual spots show that molecules of the approximately same size display different volumes during AFM, suggest that MITat1.1 could fold into different conformations.

The central structure of the NTD of MITat1.1 comprises of a coiled coil formed by two antiparallel α-helices (Fig. 14b and c) that span a distance of 9.4 nm which are most likely oriented perpendicular to the cell membrane. Near the C-terminal end of the domain, the coiled coil is flanked by five shorter helices, which extend perpendicular to the central helical elements for a distance of 6.4 nm in the NTD dimer. These helices are located 2.0 nm from the C-terminal end of the domain and form its widest part. The residues

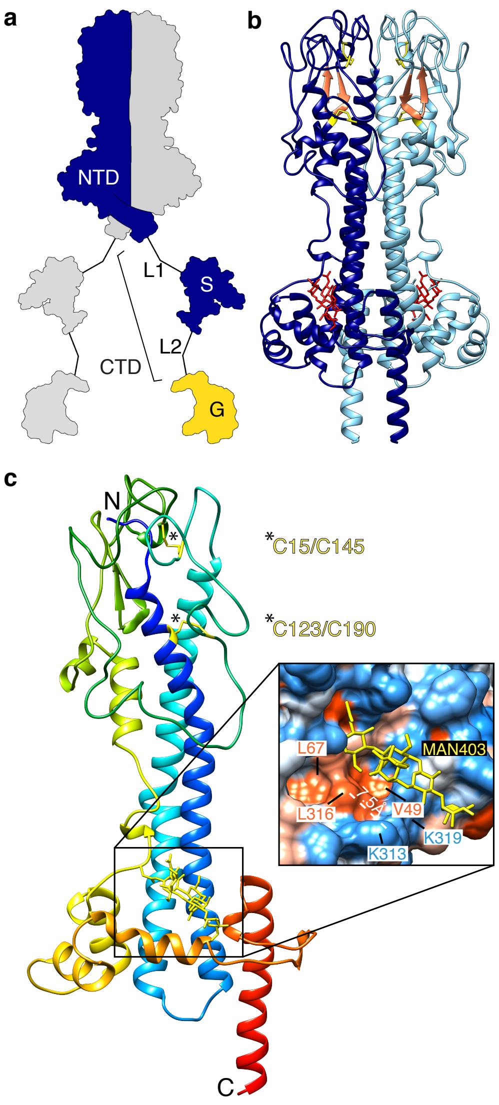

Figure 14 – Structure of the MITat1.1 N-terminal domain. a) Overview of the domain composition of MITat1.1. The dimeric NTD connects to the CTD that is composed of the structured domain (S) flanked by two linkers (L1 and L2). Linker L2 connects the protein to the GPI anchor (G). b) The dimeric structure of the NTD. Chains A and B are coloured in dark blue and light blue, respectively. Additional highlights display the glycan connected to N266 (red), disulphides (yellow) and the antiparallel beta-sheet (orange). c) A monomer of the NTD coloured in a rainbow colour scheme from light blue (N-terminus) to red (C-terminus). The structure includes a long coiled coil (blue, turquoise), encircled by shorter α-helices near the C-terminal end (yellow, orange), a longer α-helix that connects the NTD to the CTD (red) and variable surface loops near the N-terminal end (green). The two cysteine pairs that form disulphide bonds are marked with asterisks. The assignable part of the glycan, $(Man)_3(GlcNAc)_2$ which is covalently attached to residue N266 is shown in yellow. Inset: A hydrophobic pocket is formed around L316 and is shielded by the oligosaccharide. The distance of L316 to the nearest neighbouring surface residue K313 is 7.5 Å.

near the N-terminal end of the domain form variable surface loops, which span an area of 17 nm^2 per dimer. Disulphide bonds are formed between residues C15 and C145 and residues C123 and C190 (Fig. 14c). An oligosaccharide with $(Man)_3(GlcNac)_2$ composition is linked to residue N266. However, additional electron density suggests a longer glycan, which could not be resolved due to its heterogeneous and flexible nature. Most likely the glycan is of type $(Man)_{4\text{-}9}(GlcNAc)_2$ which is common in VSGs, e.g. $(Man)_4(GlcNAc)_2$ in MITat1.2 (Bangs *et al.*, 1988; Zamze *et al.*, 1990; Strang *et al.*, 1993). The glycan is in a position that screens the hydrophobic residues Val49, Leu67, Leu316 and Lys319, which are recessed by approximately 7.5 Å from the oligosaccharide (Fig. 14c).

Distance-based similarity measures were determined by superimposing MITat1.1 and MITat1.2 over 264 Cα-pairs and showed a low RMSD of 0.9 Å, whereas superimposing MITat1.1 and ILTat1.24 over 84 Cα-pairs lead to an RMSD of 1.3 Å, despite sequence identities of only 27.1 % and 10.6 %, respectively (all values calculated with UCSF Chimera MatchMaker).

The NTD of MITat1.1 was further analysed by a comparison with ILTat1.24 and MITat1.2 by visual molecular dynamics (VMD) using the STAMP (Russell & Barton, 1992) plug-in in the MultiSeq tool panel, calculating the RMSD, sequence identities and the *QH* which is a measure of similarity (which is based on the structural similarity measure Q and includes the effect of gaps on the alignment). Additionally, sequence identities were calculated using 'sequence identities and similarities' (SIAS, UCM) and clustalW2 (EMBL-EBI) which produced identical results (see Tab. 14). Note that the RMSD values are higher in VMD compared to the values obtained from Chimera MatchMaker , because MatchMaker reduces the number of superimposed Cα atoms to improve the fit, while STAMP only performs rigid-body rotations and translations for optimization.

Table 14 – Comparison of structural similarities of MITat1.1 (M11), MITat1.2 (M12) and ILTat1.24 (I124).

Structure	Chain	*QH*	RMSD (VMD)	RMSD (Chimera)	SI(VMD)	SI(SIAS)
M11:M12	A	0.6969	2.1398	1.317 (84 res)	25.67	27.76
M11:M12	B	0.7136	2.6047		25.54	27.76
M11:I124	A	0.4872	3.0313	0.953 (264 res)	11.74	13.54
M11:I124	B	0.4668	3.2219		11.55	13.54
M12:I124	A	0.4746	3.0084		12.7	15.70
M12:I124	B	0.4742	2.883		12.07	15.70

Abbreviations: *QH*, adaptation of the structural homology measure *Q*;

RMSD, Root-mean-square deviation; SI, sequence identity

A comparison of structural motifs of MITat1.1, MITat1.2 and ILTat1.24 was conducted by visualization and alignment of the individual NTDs in UCSF Chimera (Fig. 15a). Most secondary structure elements, including the long coiled coil, and all but two of the shorter helices show a high similarity (Fig. 15a). The most notable structural differences are the short helix L linking the C- and N-terminal domain, which is missing in ILTat1.24, helix D, that is only present in MITat1.1, a beta strand near J that is only present in ILTat1.24 and the presence of N-glycosylation in MITat1.1 and MITat1.2. A more detailed analysis is listed in Fig. 15.

Subsequently, hydrophobicities of the VSG monomers were compared. The hydrophobicity was visualized with UCSF Chimera, using the interactive hydrophobicity surface preset and applying the Kyte-Doolittle scale (Fig. 15) (Kyte & Doolittle, 1982). The protein surface is characterized by hydrophilic residues (Fig. 15b) while the dimerisation surface is mostly hydrophobic (Fig. 15c). The glycosylation of MITat1.1 shields hydrophobic residues underneath, while ILTat1.24 has a short hydrophilic loop in the same position (Fig. 15b).

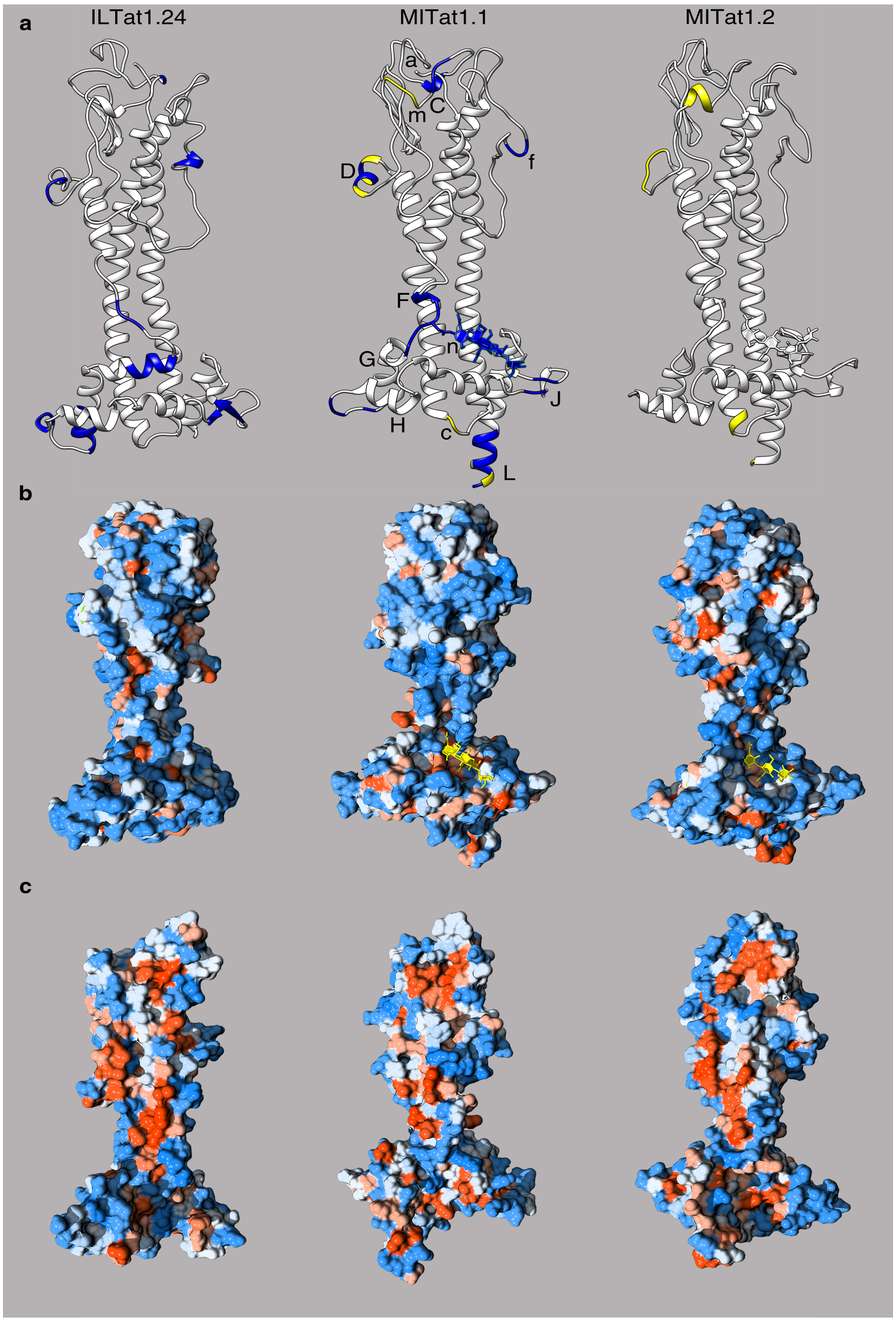

Figure 15 – Comparison of the NTD monomers of ILTat1.24 (left), MITat1.1 (middle) and MITat1.2 (right). a) The structural differences between MITat1.1 and ILTat1.24 are highlighted in blue and include a missing helix near loop f, two missing helices in the N-terminal unstructured region near the N-terminus a, the additional helix D, a glycosylation in position n, shortened helices G and H, a missing beta strand near J and a longer helix L. Structural differences between MITat1.1 and MITat1.2 are highlighted in yellow and include a shortened helix B near loop c, a missing helix in the region around loop m, an additional helix D and a longer helix L. b+c) Comparison of VSG hydrophobicity. Hydrophobic residues are coloured red, while hydrophilic residues are coloured blue. The stronger the attribute, the stronger the colour of the residue. N-glycans are displayed in yellow. b) Surface view of the individual monomers with overall strong hydrophilic residue distribution. The N-glycan is shielding hydrophobic residues underneath. c) View of the dimerisation interface with strong hydrophobic residue distribution.

4.1.2.4 MITat1.2

Working crystallisation parameters for MITat1.2 are published (D. Freymann *et al.,* 1990) and were used to successfully create the first crystals during this thesis. While reproducing already published data on MITat1.2 did not yield new structural insight, it remained important in the course of this thesis. MITat1.2 was used to establish protocols for VSG crystallisation in the lab of Markus Engstler in Würzburg. The VSG was used as a benchmark to verify sufficient protein quality for crystallographic trials and to calibrate experimental procedures with a protein that is known to produce good diffracting crystals. Additionally, these crystals could be used for binding studies between VSGs and TPMs in advance of other successful crystallographic trials, e.g. of VSG'Y'. The list of crystallisation conditions was further expanded to optimize crystal quality and to get a margin of successful conditions. A complete list of successful crystallisation parameters is displayed in Tab. 15. A detailed composition of each screen can be found in the manufacturer's product manual or in Tabs. 3, 4, 8 and 9 in the appendix.

Table 15 – List of successful conditions for the crystallisation of MITat1.2.

Protein (Buffer)	c (mg/ml)	Screen	Well no.
MITat 1.2 (35 mM Tris pH 7.5)	20	Nextal PEG	C1, D2
MITat 1.2 (H_2O)	30	Index D7/D8/F11, Nextal PEG C8	D7, D8
MITat 1.2 (H_2O)	25	Optimix PEG	A4
MITat 1.2 (H_2O)	25	Index	D7, D9, H6
MITat 1.2 (H_2O)	25	Index	D8, E8
MITat 1.2 (Na-phosphate pH 7.5)	25	Index	D8

Screen	Composition
Nextal PEG C1	0.1 M sodium acetate, pH 4.6, 25 % (w/v) PEG 3,000
Nextal PEG C8	0.1 M MES, pH 6.5, 25 % (w/v) PEG 4,000
Nextal PEG D2	0.1 M sodium HEPES, pH 7.5, 25 % (w/v) PEG 4,000
Nextal PEG D7	0.1 M tris, pH 8.5, 25 % (w/v) PEG 3,000
Nextal PEG D8	0.1 M tris, pH 8.5, 25 % (w/v) PEG 4,000
Index D7	0.1 M bis-tris, pH 6.5, 25 % (w/v) polyethylene glycol 3,350
Index D8	0.1 M HEPES, pH 7.5, 25 % (w/v) polyethylene glycol 3,350
Index D9	0.1 M tris, pH 8.5, 25 % (w/v) polyethylene glycol 3,350
Index E8	0.2 M potassium chloride, 0.05 M HEPES, pH 7.5,

	35 % (v/v) pentaerythritol propoxylate (5/4 PO/OH)
Index F11	0.2 M sodium chloride, 0.1 M bis-tris, pH 6.5, 25 % (w/v) polyethylene glycol 3,350
Index H6	0.2 M sodium formate, 20 % (w/v) polyethylene glycol 3,350
Optimix PEG A4	1.0 M ammonium formate, 0.1 M sodium citrate, pH 5.6, 23 % (w/v) polyethylene glycol 4,000

The crystals of highest protein order grew in 0.1 M Bis-Tris pH 6.5, 25 % polyethylene glycol 3,350 and 0.1 M HEPES pH 7.5, 25 % polyethylene glycol 3,350. The equilibration time until crystals of sufficient size appeared in crystallisation wells was 4 weeks on average. Crystals grew to bipyramidal morphology with a feed size of 100 - 250 μm and were cryo-protected by incubation in mother liquor substituted with 25 % glycerol for 0.5 - 5 min. Crystals were subsequently flash frozen and stored in liquid nitrogen. X-ray analysis of protein crystals was conducted at beamline MX 14.1 at BESSY II, using a PILATUS 6M detector. Evaluation of the diffraction data and the model building were conducted as described in the results for MITat1.1 and VSG’Y’, using Pointless (Evans, 2006) to perform the scaling. The final resolution was 2.4 Å with R-values of 0.168 (R_{work}) and 0.24 (R_{free}). Individual parameters for MITat1.2 crystals can be reviewed in Tab. 17.
The experimental structure of MITat1.2 was compared to the published data (D. Freymann *et al.*, 1990) with visual molecular dynamics, using the STAMP plug-in in the MultiSeq tool panel, which calculated the *QH* and RMSD. The overall structural identities of individual chains are 97.16 % and 96.39 %, respectively (Tab. 16). The dataset for MITat1.1, including sequence identities is displayed for comparison.

Table 16 – Comparison of structural similarities of the published MITat1.2 (M12p), the own experimental dataset (M12e) and MITat1.1 (M11).

Structure	Chain	*QH*	RMSD	SI(VMD)	SI(SIAS)
M12e:M12p	A	0.9716	0.4619	100	100
M12e:M12p	B	0.9639	0.5274	100	100
M12e:M11	A	0.7125	2.0383	25.40	27.76
M12e:M11	B	0.7225	1.8792	25.54	27.76

Abbreviations: *QH*, adaptation of the structural homology measure *Q*;

RMSD, Root-mean-square deviation; SI, sequence identity

Table 17 – Crystallographic parameters for MITat1.2.

Crystallisation condition	0.05 M HEPES pH 7.0, 10 % Sokalan CP 5, 0.15 M ammoniumformate
Detector	PILATUS 6M
Oscillation	0.1
Wavelength	0.918409
Time	0.5
No. of images	1500
Space group	$P4_12_12$
Cell dimensions	95.91 x 95.91 x 110.42, 3x90°
No. of used reflections	199,060 (29,090)
No. of unique reflections	20,791 (2,946)
Resolution	72.41 - 2.40 (2.53 - 2.40)
Completeness (%)	100 (100)
∅ Redundancy	9.6 (9.9)
$I/\sigma\ (I)$	10.0 (2.8)
R_{merge}/R_{pim}	11.8 (78.0)/4.0 (25.9)
Wilson B-factor	49.846
V_M ($Å^3$/Da)	3.26
Monomers per AU	1
Solvent (%)	62.24
R_{free}	0.2401
R_{work}	0.1679
Average B factor ($Å^2$)	67.0 (A: 67.3 (2777 atoms); D: 70.5 (6 atoms); S: 52.8 (64 atoms)
RMSD bond angle	1.220
Bond length	0.010
Ramachandran	Outlier: 0 (0%); Allowed: 4.1 %; Favored: 95.9 %

A comparison of the tertiary structure of MITat1.1 and MITat1.2 was performed by superimposition of the atomic coordinates of each structure with UCSF Chimera, using the Needleman-Wunsch algorithm (Needleman & Wunsch, 1970) and a Blosum-62 matrix (S. Henikoff & J. G. Henikoff, 1992). 2 Å pruning and a secondary structure score were enabled to calculate the superposition. The comparison was performed between the own experimental dataset for MITat1.2 and either MITat1.1 or the published data for MITat1.2 (see Fig. 16).

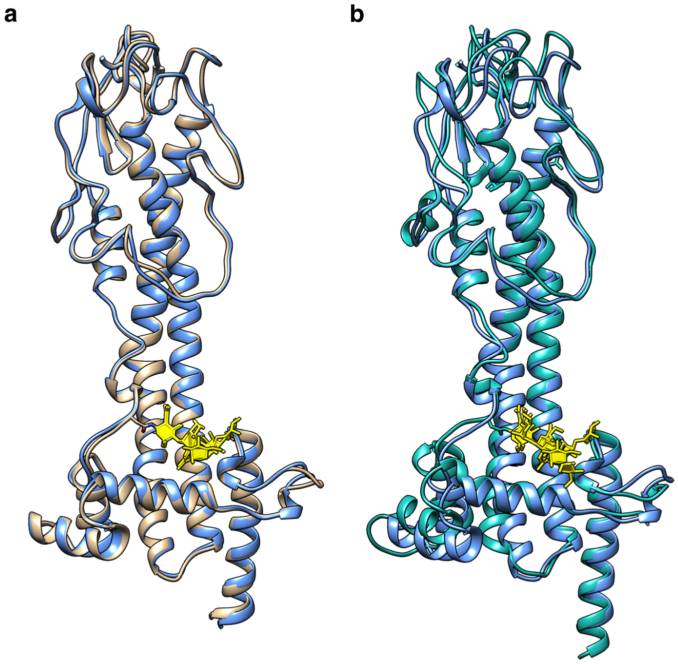

Figure 16 – Superposition of models for MITat1.1 and MITat1.2 a) The structure for the own experimental model of MITat1.2 (blue) is superimposed on the published structure for MITat1.2 (brown, PDB-ID: 1VSG). b) The superposition of the own experimental data for MITat1.2 (blue) and MITat1.1 (cyan). Minor structural differences occur in flexible and unstructured regions.

4.1.2.5 MITat1.2-TPM cocrystallisation

A goal of this thesis was to identify the mechanisms in the interaction of VSGs and TPMs by means of fluorescence microscopy and structural analysis. The latter requires structural information of the protein of interest to identify the interaction with cofactors. The first VSG structure that was successfully obtained in the course of this thesis was MITat1.2. Therefore, to identify the exact position where binding between TPMs and VSGs takes place, cocrystallisation of the triphenylmethane dyes bromophenol blue, and phenol red was performed with MITat1.2. Supplementing of VSG crystals with TPM compounds should yield protein crystals that, in the case of active binding of the TPM to the VSG, include exact structural information about their binding position. The original parameters for the mother liquor and cryo-protectant of MITat1.2 introduced in this thesis were used unchanged, while the protein buffer was substituted by TPM solutions (see Tab. 18). In these cocrystallisation trials, the crystal-drops were set up manually in 24-well plates. The screen composition was identical for each well (Index D7), while different protein- and TPM-concentrations were tested. Therefore, instead of the screen composition, Tab. 18 features the number of successful crystallisation events for each VSG/TPM-concentration. Eventually, additional screens were tested for cocrystallisation as well, which were performed in 96-well plates and for which each well with successful crystallisation is displayed in Tab. 18 as well. A detailed composition of the used screens can be found in Tabs. 3 through 9 in the appendix.

Table 18 – List of crystallisation conditions for the cocrystallisation of MITat1.2 and TMP dyes.

Protein (Buffer)	c (mg/ml)	Screen	Well no./Hits
MITat 1.2 (TDB + 0.8 mM BPB)	25	manual (Index D7/D8)	3 hits
MITat 1.2 (TDB + 0.8 mM BPB)	25	manual (Index D7/D8)	1 hit
MITat 1.2 (TDB + 33.5 mM PR)	28	manual (Index D7/D8)	1 hit
MITat 1.2 (TDB + 16.5 mM PR)	28	manual (Index D7/D8)	2 hits
MITat 1.2 (H_2O + 1.6 mM PR)	20	manual (Index D7/D8)	4 hits
MITat 1.2 (TDB + 5.5 mM PR)	25	Optimix PEG	/
MITat 1.2 (TDB + 5.5 mM PR)	31	MIDAS HT-96	A7, G2, H12
MITat 1.2 (TDB + 5.5 mM PR)	25	Nextal PEG	D2, D7, D8
MITat 1.2 (TDB + 5.5 mM PR)	20	Optimix PEG	D2 - D10
MITat 1.2 (TDB + 5.5 mM PR)	20	manual (Index F11)	/
MITat 1.2 (TDB + 5.5 mM PR)	30	manual (Index D7/D8)	8 hits
MITat 1.2 (TDB + 5.5 mM PR)	25	Index	D7, D8, F11

Screen	Condition
Index D7	0.1 M bis-tris, pH 6.5, 25 % (w/v) polyethylene glycol 3,350
Index D8	0.1 M HEPES, pH 7.5, 25 % (w/v) polyethylene glycol 3,350
Index F11	0.2 M sodium chloride, 0.1 M bis-tris, pH 6.5, 25 % (w/v) polyethylene glycol 3,350
MIDAS HT 96 A7	10 % (v/v) polypropylene glycol 400
MIDAS HT 96 G2	20 % (v/v) Sokalan CP 5, 0.3 M ammonium formate, 0.1 M HEPES NaOH, pH 7.0
MIDAS HT 96 H12	15 % (w/v) poly(vinyl pyrrolidone) K15, 25 % (w/v) PEG MME 5,000, 0.1 M tris HCl, pH 8.0
Nextal PEG D2	0.1 M sodium HEPES, pH 7.5, 25 % (w/v) PEG 4,000
Nextal PEG D7	0.1 M tris, pH 8.5, 25 % (w/v) PEG 3,000
Nextal PEG D8	0.1 M tris, pH 8.5, 25 % (w/v) PEG 4,000
Optimix PEG D2	0.1 M glycyl-glycine, pH 8.5, 27 % (w/v) polyethylene glycol 4,000
Optimix PEG D3	0.1 M tris HCl, pH 8.0, 23 % (w/v) polyethylene glycol 4,000
Optimix PEG D4	0.1 M TAPS, pH 9.0, 23 % (w/v) polyethylene glycol 4,000
Optimix PEG D5	0.1 M magnesium chloride, 0.1 M tris HCl, pH 8.5, 18 % (w/v) polyethylene glycol 4,000
Optimix PEG D6	0.1 M potassium sulphate, 0.1 M tris HCl, pH 8.5, 18 % (w/v) polyethylene glycol 4,000
Optimix PEG D7	0.1 M ADA, pH 6.5, 23 % (w/v) polyethylene glycol 4,000
Optimix PEG D8	0.1 M MOPS, pH 7.0, 18 % (w/v) polyethylene glycol 4,000

Optimix PEG D9	0.1 M tris HCl, pH 8.5, 18 % (w/v) polyethylene glycol 4,000
Optimix PEG D10	23 % (w/v) polyethylene glycol 4,000

Crystal growth was equivalent to the original MITat1.2 crystals of this thesis, with approximately 4 weeks of incubation until formation of crystals with bipyramidal morphology. Both the protein drop and the protein crystal were of intense colour by the TPM dye, both initially and after soaking in cryo-protectant. X-ray analysis of collected crystals was conducted and resulted in datasets of various qualities albeit with no signal resulting from dye molecules incorporated into the crystal lattice. Varying dye concentrations and buffer pHs did not yield co-crystal diffraction data.

4.1.2.6 MITat1.4 & MITat1.5

Both MITat1.4 and MITat1.5 cell lines were problematic to adapt to high cell concentrations and orbital shaking. During cultivation both cell lines were kept within exponential growth without agitation for as long as possible by cultivation in 200 ml cell culture flasks. Subsequent orbital shaking in conical flasks was conducted at reduced revolutions (see Tab. 7) once cell densities exceeded 1×10^6 cells/ml. Even then, MITat1.4 cell lines continued to show severe impairments during cultivation. Harvesting 1.6 l of cultured cells at 1.3×10^6 cells/ml resulted in protein yield sufficient for only a single screen (see Tab. 20), which is in stark contrast compared to a total of 25 screens that were required to elucidate the structure of MITat1.1. The adaptation of MITat1.5 to high-density cultivation was more successful and sufficient protein (Tab. 8) was purified for crystallisation trials of 7 screens. Standard sparse-matrix screens were tested for crystal growth and prioritising screens that were successful for MITat1.1 and MITat1.2 previously. All conditions that were tested are shown in Tab. 20. Displayed are the wells, if any, that contained crystals for a specific screen and protein concentration of MITat1.4 and MITat1.5. A detailed composition of the used screen can be found in Tabs. 3 through 14 in the appendix.

During MITat1.5 screening, crystals with a feed size of approximately 50 - 100 μm and bipyramidal morphology formed. The crystallisation conditions with maximum diffraction resolution were 0.1 M tris-Cl pH 8.0, 20 % (w/v) PEG 4,000 and 0.1 M HEPES pH 7.0, 20 % (w/v) PEG 8,000. Crystal analysis was performed as described previously for MITat1.1 and VSG'Y', using XDSAPP for scaling. The final resolution of protein crystals was 3.6 Å (see Tab. 21), but the protein structure could not be solved by molecular replacement with MITat1.1 or MITat1.2 due to low structural homology. The R-factors were diverging during refinement of the model and the data set remained incomplete.

Table 20 – List of crystallisation conditions for the crystallisation of MITat1.4 and MITat1.5.

Protein	c (mg/ml)	Screen	Well no.
MITat 1.5 (H_2O)	20	Optimix PEG	/
MITat 1.5 (H_2O)	20	Nextal PEG	E6
MITat 1.5 (H_2O)	20	Nextal C12 Fine	/
MITat 1.5 (H_2O)	20	Protein Complex	F1, G9, G10
MITat 1.5 (H_2O)	24	Protein Complex	C5, F1
MITat 1.5 (H_2O)	20	MIDAS HT-96	/
MITat 1.5 (H_2O)	25	Index	/
MITat 1.4 (H_2O)	18	Nextal PEG	/

Screen	Composition
Nextal PEG E6	0.2 M sodium chloride, 20 % (w/v) PEG 3,350
Protein Complex C5	0.1 M tris pH 8.0, 20 % (w/v) PEG 4,000
Protein Complex F1	0.1 M HEPES, pH 7.0, 20 % (w/v) PEG 8,000
Protein Complex G9	1.3 M potassium/sodium phosphate, pH 7.0
Protein Complex G10	1.6 M potassium/sodium phosphate, pH 6.5

Table 21 – List of experimental parameters for MITat1.5 crystals.

Crystallisation condition	0.1 M tris-Cl pH 8.0 20 % PEG 4,000
Detector	PILATUS 6M
Oscillation	0.1
Wavelength	0.918409
Time	0.2
No. of images	1800
Space group	$C222_1$
Cell dimensions	42.85 x 169.01 x 175.70, 3x90°
No. of used reflections	33,611
No. of unique reflections	6,419 (2,946)
Resolution	87.86 - 3.66
Completeness (%)	86 (68.2)
I/σ (I)	9.59 (5.02)
R_{merge}/R_{pim}	15.7 (29.2)
Correlation coefficient ($CC_{1/2}$)	98.9 (91.3)
Wilson B-factor	40.175
Monomers per AU	1

4.1.3 The complete structure of VSG MITat1.1 by SAXS

VSG structures that were established by x-ray crystallography have in common that the proteins degraded during crystallisation. The hinge region between the NTD and CTD is prone to proteolytic cleavage, reducing the structural information that can be gathered by crystallography to the NTD. However high-resolution structural information of the individual NTD (by x-ray crystallography) and CTD (by NMR spectroscopy) can be combined by small angle x-ray scattering of intact soluble VSGs to construct a complete VSG.

Using beamline BM 29 at the ESRF in Grenoble allowed to collect scattering data of intact VSGs that describe the shape and size of the complete protein on the nanometre scale. This rough shape can then be used as a map to fit the previously acquired high resolution data of all protein domains to construct a complete high-resolution model. Since the SAXS data was collected from complete proteins, the following modelling needs to include all individual protein domains as well. The ATSAS software package (M. V. Petoukhov & Svergun, 2005; M. V. Petoukhov, Franke, *et al.*, 2012) that was used, performs rigid-body modelling to compute complete protein models. This means that all individual domains, described by the atom coordinates in their respective .pdf file, are rigid entities that are each placed as a single, inflexible building block within the whole structure. To increase the flexibility of the system, large domains can be separated into smaller building blocks by splitting the .pdf file into multiple smaller files. Additionally, regions that are known from high-resolution NMR data to be highly flexible can be cut from the data entirely and will be modelled by the program package as flexible Cα chains. MITat1.1 features a CTD with a structured domain S, which connects to the NTD and the GPI anchor through flanking linkers L1 and L2, respectively. To account for the flexibility of linkers L1 and L2 residues L368 - Q376 (L1) and K426 - G442 (L2) were removed from models and re-modelled by BUNCH and CORAL from the ATSAS software package as Cα chains. The individual building blocks from which the models are computed are therefore the NTD, the structured domain S and the GPI anchor. Residues A1 - N367 (NTD), T377 - E425 (structured domain S) and the terminal residue S443, including the attached GPI anchor and $(Man)_3(GlcNAC)_2$ were modelled into spatial relationship and connected by the re-modelled Cα chains of L1 and L2. Initial models did not correctly form dimeric NTDs and contact conditions were formulated as a result, which restricted atoms along the dimerisation area to drift further than 3 - 10 Å from one another. This resolved problems with wrong placement of the symmetry axis and dimer formation. The quality of the computed models was then assessed by their discrepancies χ^2, which compares the calculated scattering data of the models with the experimental data. Four of the resulting models (M1 - M4) fit well to the experimental data, characterized by a χ^2 of 0.49 - 1.01. These models differ in the conformation of the CTD (Fig. 17) and span a width that ranges from 8.2 nm to 10.8 nm. The average height of MITat1.1 derived from the models was 15.2 nm, however model M2 only shows a relatively short height of 14.1 nm while being the widest model with a width of 10.8 nm. Models M1, M3 and M4 share a similar height but differ in the orientation of the CTD and the total protein width. In the course of modelling, the input parameters for the VSG models were varied constantly, including different NTD-dimer contact conditions and a computation by either CORAL or BUNCH. Models M1 - M4 were also generated using different parameters from one another. To guarantee that the differences observed in model M2 are not caused by the variance in input parameters, consecutive iterations of BUNCH using input parameters identical to M2 (called M2a in the context of model reiterations) were performed and produced models M2b and M2c. These models displayed the same range of dimensions as the initial models M1 - M4 (Fig. 18a), showing that the range of conformations acquired in these experiments are not modelling artefacts. These results also illustrate the robustness of the chosen modelling approach.

Superpositioning the NTDs of models M1 - M4 highlights the flexibility of the CTDs, which varied in position to one another along the interdomain axis by up to 121° and which was facilitated through rotational freedom of linker L1 (Fig. 19a).

The area a single VSG can occupy was calculated using the non-hydrated surface area of each model and varied between 25 nm^2 and 31 nm^2, enabling a total of 4.7 - 5.7 x 10^6 VSGs to fit a surface area of 144 $\mu\mathrm{m}^2$ (Grünfelder *et al.*, 2002) of a single cell (Tab. 22), which is close to the previous estimations of 5.1 x 10^6 VSGs by Grünfelder *et al.*, 2002. However, this calculation neglects protein flexibility and likely underestimates the total area a VSG occupies. To address the previously mentioned rotational freedom between domains, the area was calculated as a circle, using the maximum protein diameter (width W in Tab. 22) and a theoretical hydration layer of 1 nm. The resulting area varied from 77 nm^2 to 123 nm^2 (Fig. 20), allowing a total of 1.2 - 1.9 x 10^6 VSGs per cell.

Models M1 - M4 used contact conditions and P2 symmetry to restrain the movement of NTD monomers. Omitting contact conditions and using P1 symmetry resulted in models with a correctly dimerised NTD and an otherwise asymmetric structure (Fig. 18b), with chain A of the CTD extending parallel to the axis of symmetry and chain B folded back towards the NTD.

Table 22 – Model dimensions for MITat1.1

Model	M1	M2	M3	M4	Mean
Height (H, nm)	15.3	14.1	15.7	15.6	15.2
Width (W, nm)	9.4	10.5	8.3	7.9	9.0
Depth (D, nm)	5.2	6.0	5.4	6.0	5.7
χ^2	0.8	1.0	0.5	0.5	
Circular hydrated area (nm^2)	102	123	83	77	95
Static non-hydrated surface area (nm^2)	31	30	27	25	28
VSGs/cell (Circular model) (x 10^6)	1.4	1.2	1.7	1.9	1.5
VSGs/cell (Static model) (x 10^6)	4.7	4.8	5.3	5.7	5.1

Abbreviations: M1 - M4, models 1 - 4 of MITat1.1; χ^2; model discrepancy. Calculated areas are described in Fig. 20.

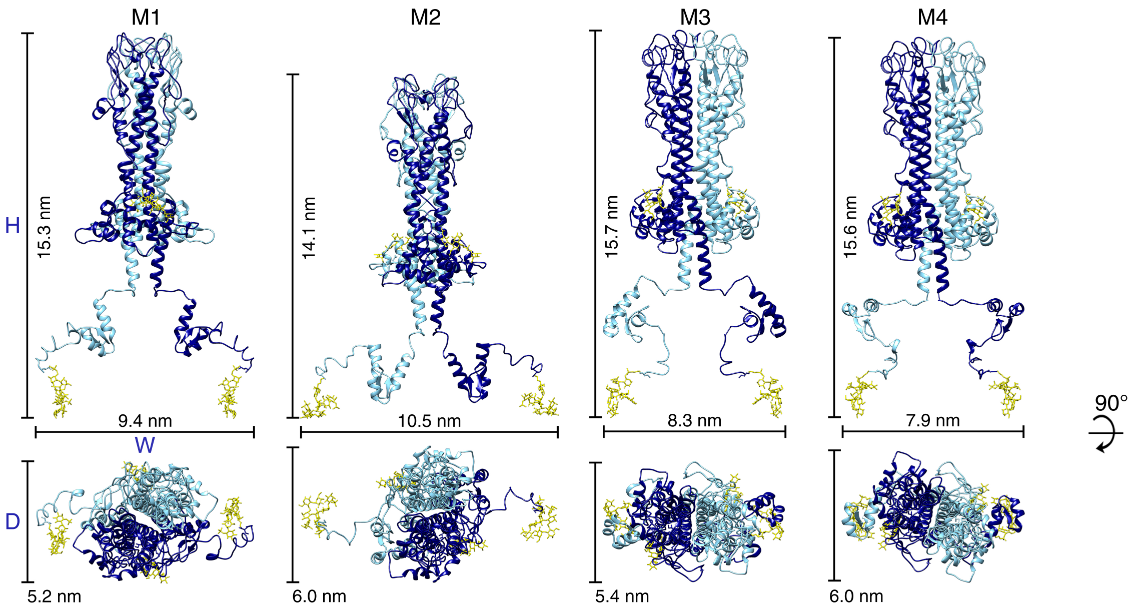

Figure 17 – Rigid body models of complete MITat1.1 Side-view and 90° tilted top-view of models M1 - M4 (from left to right) of MITat1.1, aligned along the NTD. Individual chains are coloured in light and dark blue and N-glycans and the GPI anchor are displayed in yellow. Protein dimensions (height H, width W and depth D) are displayed in Tab. 22. Model M2 has an increased width and a decreased height in respect to the other models.

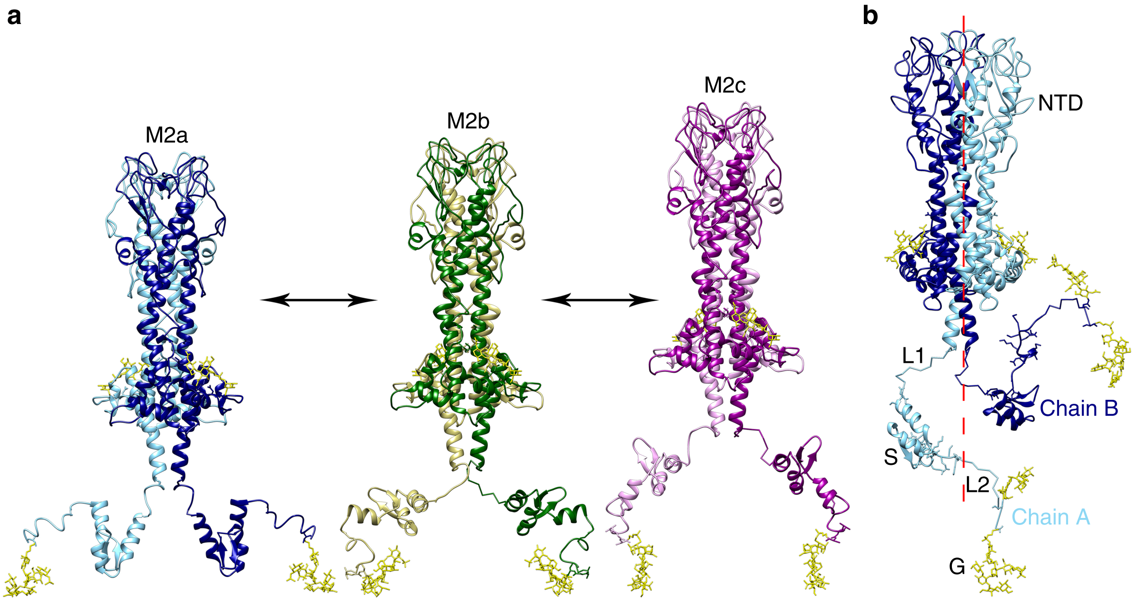

Figure 18 – Reiterations of model M2 and an asymmetric model of MITat1.1 a) Reiterations of BUNCH using the parameters employed in the generation of models M2 show multiple configurations that could represent intermediate folds. Models M1 - M4 vary slightly in their modelling parameters while models M2a - M2c were computed identically, using reiterations of BUNCH. M2a - M2c show conformations in the same range of diameters as the initial models M1 - -M4. b) The NTD of a model generated without symmetry constrains dimerized correctly without contact restrictions, while regions L1, S, L2 and G are asymmetric for both chains. While chain A (light blue) remains parallel to the central axis of symmetry, chain B (dark blue) folds back towards the NTD. This model is only viable for the soluble form of the VSG.

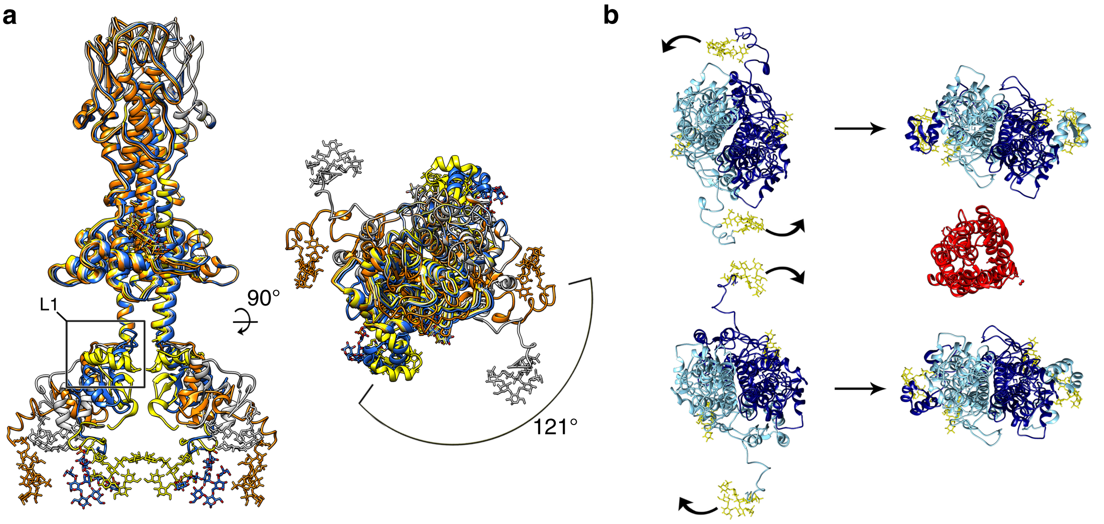

Figure 19 – Flexibility of linker L1 in VSG MITat1.1 a) Superimposed NTDs of M1 - M4 of MITat1.1 demonstrate the flexibility of the CTD, which varies in position along the inter-domain axis by up to 121° facilitated through linker L1. b) Top-down illustration of VSGs (blue) with a surface transmembrane protein (aquaporin 2, PDB-ID: 1FX8, red) shown to scale. The flexibility in linker L1 may allow the CTD to respond to obstacles, e.g. transmembrane proteins, while the NTD position remains unaffected.

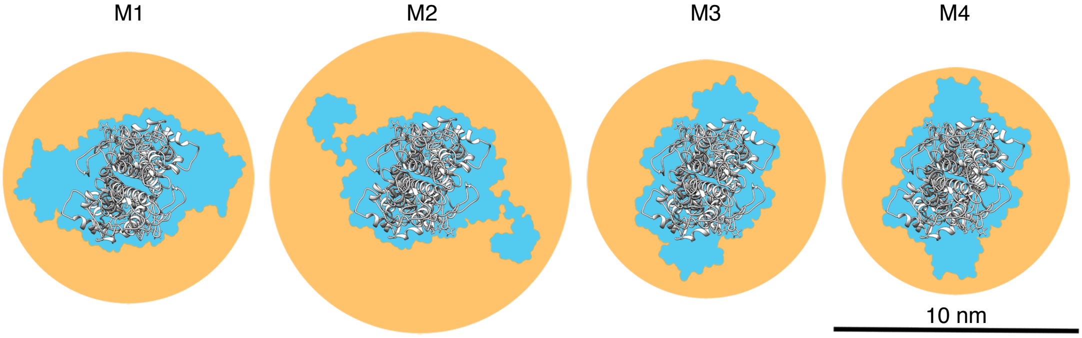

Figure 20 – Rigid and dynamic area occupied by models M1 - M4. The non-hydrated surface area that represents a rigid VSG is displayed in blue and was calculated from the percentage that the top-down silhouette of the model fills in a rectangle described by the width and depth of the model (W and D, Tab. 22). A dynamic VSG occupies a circular area, overlaid in orange, calculated by the diameter of the CTDs (W, Tab. 22) and augmented by a hydration layer of 1 nm. All models are aligned by the position of their NTDs, displayed in white.

4.1.4 The complete structure of VSG ILTat1.24 by SAXS

The CTD of ILTat1.24 has an additional structured region compared to MITat1.1. To compare the influence that different CTD compositions have on the overall VSG structure, SAXS measurements and rigid body modelling of ILTat1.24 were performed in parallel to MITat1.1. The CTD of ILTat1.24 consists of 109 residues, compared to 75 residues in MITat1.1. Published domain models of the NTD and CTD (pdb-id: 2VSG, 2JWG & 2JWH) (M. L. Blum *et al.*, 1993; Jones *et al.*, 2008) were used in the computation of complete VSGs from SAXS data. The *P(r)*-distribution and Kratky-Plot, which are measures for protein foldedness, derived from SAXS data for MITat1.1 and ILTat1.24 suggest a more compact structure for MITat1.1 as well (Fig. 21). Four of the resulting models for ILTat1.24 display a low discrepancy χ^2 of 0.96 - 1.39 (I1 - I4, Fig. 21). The model width W ranged from 9.7 nm to 11.0 nm with an average height of 15.5 nm. Even though the model dimensions of ILTat1.24 are slightly bigger than those of MITat1.1, both proteins show a similar range of compact and extended conformations (Fig. 22).

The non-hydrated surface area for models I1 - I4 ranges from 25 nm^2 to 35 nm^2 (Tab. 23) and allows 4.2 - 5.7 x 10^2 dimers to fit on the cell surface, matching the amounts calculated for MITat1.1 despite the increased protein size. The circular area that hydrated ILTat1.24 models can occupy spanned 107 - 133 nm^2, resulting in 1.1 - 1.3 x 10^6 VSGs per cell. This corresponds to a protein abundance on the cell surface that is decreased by 10 - 31 % in respect to MITat1.1.

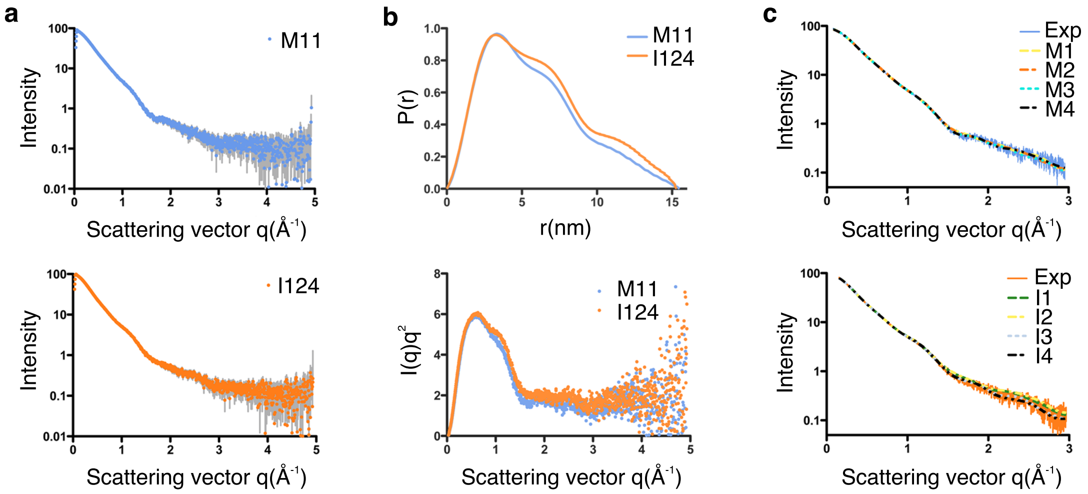

Figure 21 – SAXS scattering data for MITat1.1 and ILTat1.24 a) The scattering intensity as a function of the scattering angle (Å^{-1}) for MITat1.1 (top) and ILTat1.24 (bottom). The steep incline at low scattering angles (≤0.05) is a concentration-independent artefact that is removed during data processing and prior to rigid body modelling. b) The *P(r)*-function (top) displays the distance distribution between all pairs of atoms within the protein. While the maximum distance D_{max} is identical for both proteins, the point-distance values are larger for ILTat1.24 due to the increased size of its CTD. The Kratky-plot (bottom) displays a broad peak with multiple shoulders without a decline back to zero. This agrees with a flexible multi-domain protein that is partly unstructured. c) BUNCH and CORAL rigid body models (dotted lines) of M1 - M4 (top) and I1 - I4 (bottom) agree well with the experimental data (continuous line).

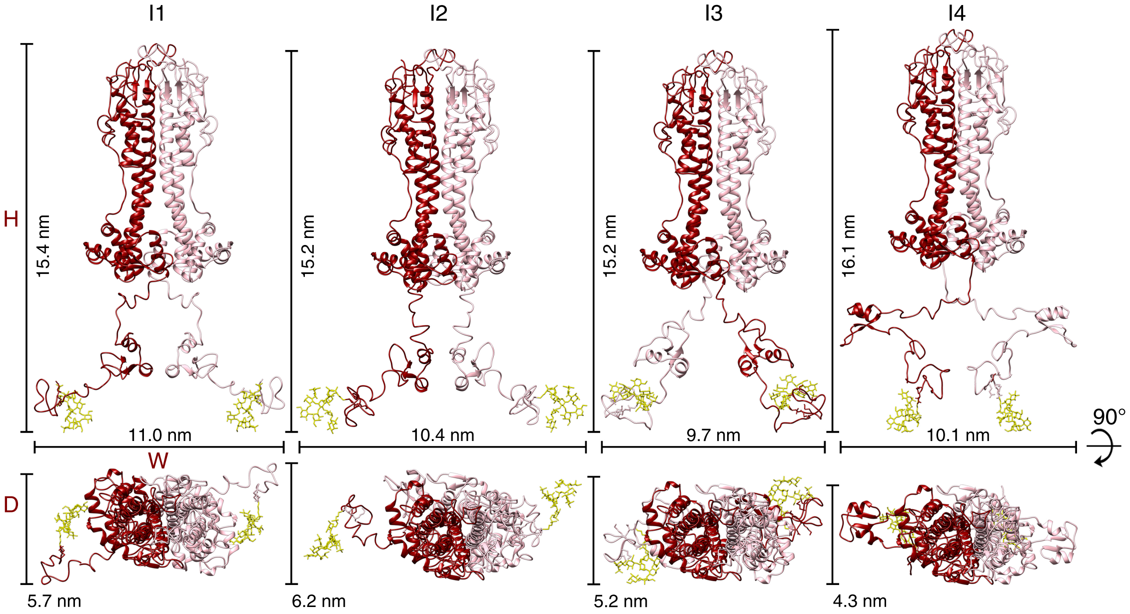

Figure 22 – Rigid body models of complete ILTat1.24. Side-view and 90° tilted top-view of models I1 - I4 (from left to right) of ILTat1.24, aligned along the NTD. Individual chains are coloured in light and dark red and the GPI is displayed in yellow. Protein dimensions (height H, width W and depth D) are displayed in Tab. 23. Protein dimensions of ILTat1.24 closely resemble those of MITat1.1 even though the CTD is approximately 30 % larger.

Table 23 – Model dimensions for ILTat1.24

Model	I1	I2	I3	I4	Mean
Height (H, nm)	15.4	15.2	15.2	16.1	15.5
Width (W, nm)	11	10.4	9.7	10.1	10.3
Depth (D, nm)	5.7	6.2	5.2	4.3	5.4
χ^2	1.4	1.2	1.0	1.1	
Circular hydrated area (nm^2)	133	121	107	115	119
Static non-hydrated surface area (nm^2)	35	33	28	25	30
VSGs/cell (Circular model) (x 10^6)	1.1	1.2	1.3	1.3	1.2
VSGs/cell (Static model) (x 10^6)	4.2	4.4	5.2	5.7	4.9

Abbreviations: I1 - I4, models 1 - 4 of ILTat1.24; χ^2; model discrepancy. Area calculation is described in Fig. 20.

4.1.5 VSG'Y' SAXS analysis

Even though the structure of VSG'Y' could not be elucidated yet, information of size, conformations, compactness and foldedness can be derived from SAXS analysis. SAXS experiments were conducted in parallel to MITat1.1 and ILTat1.24 using the same protocols. Evaluation through raw scattering data, the *P(r)*-distribution and the Kratky-plot were conducted, suggesting similar folding but a slightly larger core structure (Fig. 23). The data suggests that the overall structure of VSG'Y' is larger than that of MITat1.1 and ILTat1.24. Judging from sequencing data, that shows that the protein is composed of more amino acids and electrophoretic analysis that suggests a higher molecular mass, this is true.

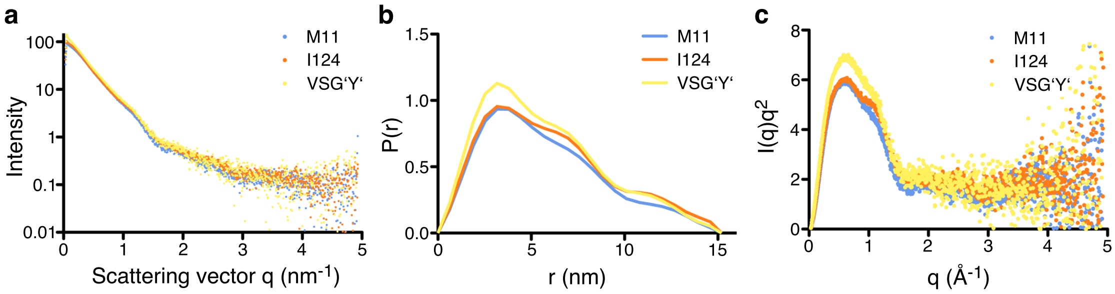

Figure 23 – SAXS data comparison between MITat1.1 (M11), ILTat1.24 (I124) and VSG'Y'. a) The raw scattering data for all three proteins show high alignment, including the artificial peak at very low scattering angles. b) The *P(r)*-distribution shows an increased *P(r)* value along the primary peak for VSG'Y', while the second and third plateau align with ILTat1.24. $D_{\max}$ is identical to the other VSGs (all cross the x-axis at $r = 15\,\text{nm}$). c) The peak in the Kratky-plot shows higher I(q)q^2 values for VSG'Y' than for the other VSGs, while the curve aligns with the other datasets at higher angles.

4.2 Characterization of VSG'Y' fluorescence

The previous section of this thesis dealt with the determination and analysis of VSG structures and the interaction of VSGs and TPMs by structural means. The following section will describe fluorescence microscopy as an alternative approach to crystallography for interaction analysis of TPMs and VSGs. Experiments combining different TPMs and VSGs both with the living parasite and the protein in solution were applied to characterise the fluorescence and the interaction between protein and TPM.
The initial discovery of the VSG'Y' fluorescence by Markus Engstler can be described mostly by qualitative means: Fluorescence emission depends on the presence of phenol red in the cell cultivation medium during excitation. If the pH indicator is removed, the protein ceases to be fluorescent. Fluorescence emission is delayed and eventually quenched, however both events are subject to influence by many factors, complicating quantitative analysis. In addition to the interaction analysis between VSGs and TPMs, this chapter endeavours to analyse VSG fluorescence from a quantitative point of view as well. The focus is placed on the analysis of cell cultivation parameters that can alter emissions of live parasites expressing VSG'Y' in addition to phenol red. These parameters include for example cell density, incubation times, pre-excitation of cells, medium depletion and medium substitution, pH changes, quenching experiments and TPM competition. Each of these parameters is changed individually, either during cell cultivation or directly prior to the experiment, while the other factors remain unaltered. Results from one experiment can influence the setup of another, for example the identification of phototoxic agents in the cell solution in one experiment leads to reformulation of the solution in all subsequent experiments. The identification of compounds that increased VSG'Y' fluorescence led to the formulation of an improved fluorescence solution, consisting of 1 μM albumin, 80 μM phenol red and 1.24 mM trolox in TDB that HMI-9 was exchanged for and which is further explained in section 4.2.5.

4.2.1 VSG'Y' fluorescence excitation

Fluorescence emission from live trypanosomes depends on the expression of VSG'Y' on the cell surface and the presence of phenol red in the cultivation medium. Additional factors may influence emissions but none were identified that seemed essential. Fluorescence was excited at 360 - 450 nm, while maximum emissions were detected at 500 - 580 nm. These spectra were determined by fluorescence microscopy of individual cells, since emissions were to weak for full spectrum analysis with a photometer. With a maximum intensity that was only 1 - 4 x stronger than background noise, VSG'Y' emission was relatively weak. It could generally be observed that fluorescence increased with broadening of the excitation spectrum. Upon excitation at 436 nm, a delay of several seconds could be observed before fluorescence emission was detectable. This emission-delay was subject to multiple factors including cell density, incubation times, pre-excitation of cells, medium depletion and medium substitution, pH changes, quenching experiments and TPM competition (Fig. 24a). Intensity increased with sigmoidal progression in the course of 1 - 4 s after which maximum intensity was reached. Fluorescence bleaching was observed after exposure for more than one minute or excitation with a power of 130 W and was influenced by buffer pH.

It was observed that dead cells often still displayed typical VSG'Y' fluorescence even when they deceased prior to the experiment (Fig. 24b). This emission was not always reproducible and intensities were highly variable, potentially depending on the time of death.

Experiments conducted in 96-well-plates with a volume of 50 - 200 μl suffered from weaker fluorescence, a stronger background signal and a higher freedom of cell movement. Eventually the buffer composition was altered from HMI-9 to the fluorescence solution (FMix, explained in section 4.2.5) which improved cell fluorescence in 96-wells (Fig. 24c).

During early experiments, fluorescence excitation of VSG'Y' was conducted with the Till Photonics iMIC system. However, the results were often unreliable and samples prepared under identical conditions displayed severe differences in fluorescence intensities between experiments. Samples (1 x 10^6 cells/ml resuspended in HMI-9, preincubated 10 min. at 37°C and 0 min on slides and with a total volume of 3 μl per slide) that displayed robust emissions on one day, often lacked any detectable emission when the experiment was repeated under identical conditions the following day. While minor fluctuations in cell preparation can have a detectable influence on signal intensity, it should not result in a complete loss of fluorescence emission. Troubleshooting of the microscopic setup and careful sample preparation could not identify the problem, which recurred irregularly in the following months. Therefore, subsequent experiments were conducted with the Leica DMI 6000B or Leica DMI IRB.

4.2.2 Cell density

The first analysed factor with an impact on the VSG'Y' fluorescence kinetics was cell density. Cells resuspended at 1 x 10^5 cells/ml in HMI-9, prepared without preincubation and measured immediately after preparation on the microscopy slide displayed a delay of 7 - 10 s (Fig. 24d). The same delay was observed for lower cell densities. An increase in density to 5 x 10^5 cells/ml reduced the initial delay to 2 - 3 s. A concentration of 1 x 10^6 cells/ml displayed emission after $\leq$1s, which was regarded as the minimum value and was not distinguished any further. Even though the delay could be influenced by multiple factors, there was always a temporal gap between excitation and emission, thus no instantaneous fluorescence signal could ever be observed. Due to the strong influence of incubation times on slides in respect to overall kinetics, samples were prepared immediately prior to measurements and usually discarded after no more than 5 minutes.

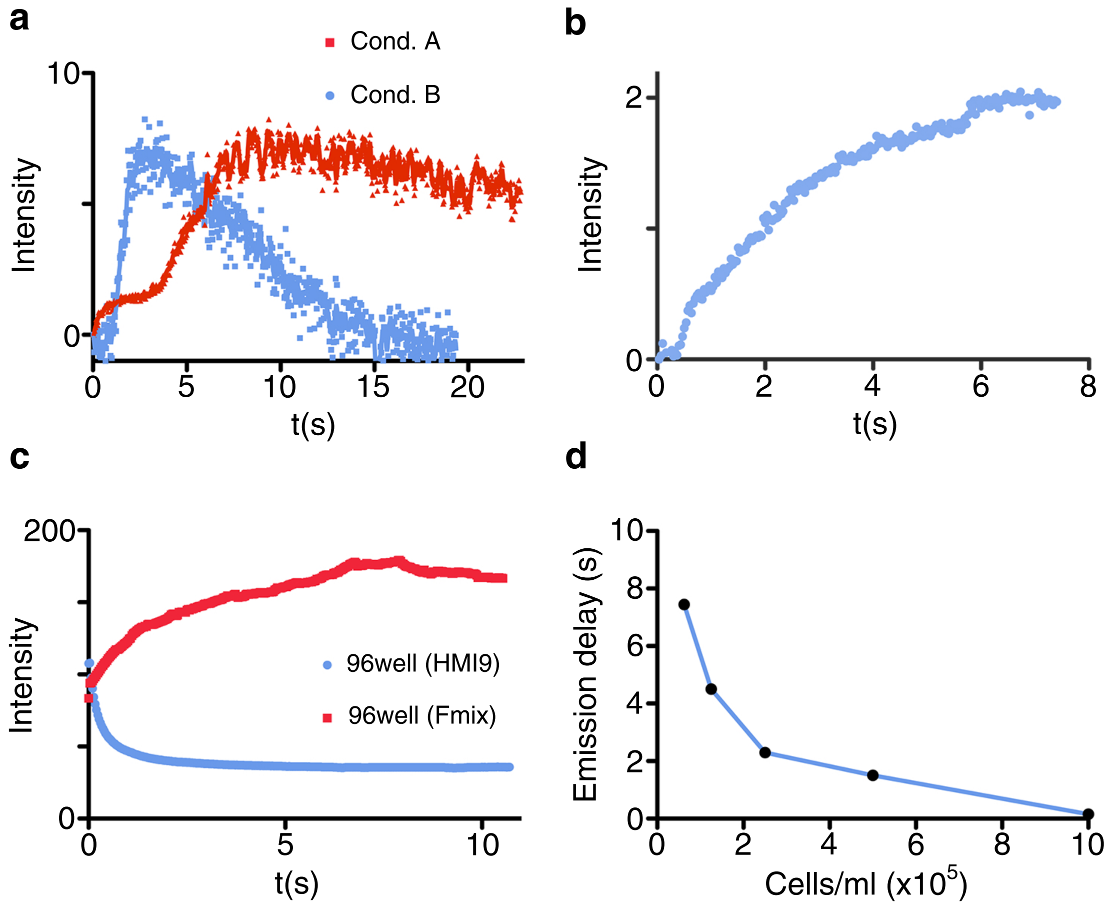

Figure 24 – Emission kinetics for VSG'Y'. a) Emissions of VSG'Y' increased with sigmoidal progression following a short delay of 1 - 7 s. When maximum intensities were reached, fluorescence started decreasing in dependence of a number of potential factors (e.g. pH, cell density, pre-incubation or medium composition). Differences in kinetics are visualised by exemplary conditions A and B in the graph that represent a decrease of the medium pH from 7.5 to 5.0. b) Deceased cells expressed surface fluorescence with semi-parabolic kinetics independent of pre-incubation or pre-excitation. c) Cell fluorescence was impaired in 96-well-plates when using HMI-9. Switching the medium to a fluorescence solution returned emission to semi-parabolic kinetics. d) The initial emission delay was influenced most notably by sample cell densities. Upon increasing density on slides from 1 x 10^5 cells/ml to 1 x 10^6 cells/ml the delay decreased from a maximum of 8 s to ≤1 s, accordingly.

4.2.3 On-slide incubation

Emission kinetics were influenced by the time that cells incubated on microscopy slides prior to measurements. Longer incubation resulted in shorter delays, with a minimum delay of ≤1 s (Fig. 25a). A sample density of 1 x 10^5 cells/ml displayed a delay of 7 - 10 s immediately after preparation. Following 10 min of incubation on slides at room temperature, the delay was reduced to 3 - 4 s and decreased to 1 - 2 s after 20 min of incubation. Extending incubation further resulted in a delay of ≤1 s. The described effect was also observed for cells prepared under exclusion of light and was thus not caused by pre-excitation of cells, leaving factors excreted by cells and from the surrounding medium and the atmosphere as possible contributors. An increase in sample volume from 1.8 μl to either 3 - 4 μl on slides or 50 - 100 μl in micro titre plates had no detectable effect on kinetics.

A parameter with a cumulative effect on kinetics to on-slide incubation was cell density. Higher density samples required shorter incubations to reach a delay of ≤1 s (Fig 25b). Samples with a density of 5 - 8 x 10^6 cells/ml required a pre-incubation of only 5 - 10 min to reach minimum delays, while samples with a density of 1 x 10^6 cells/ml required no additional incubation to reach a delay of ≤1 s.

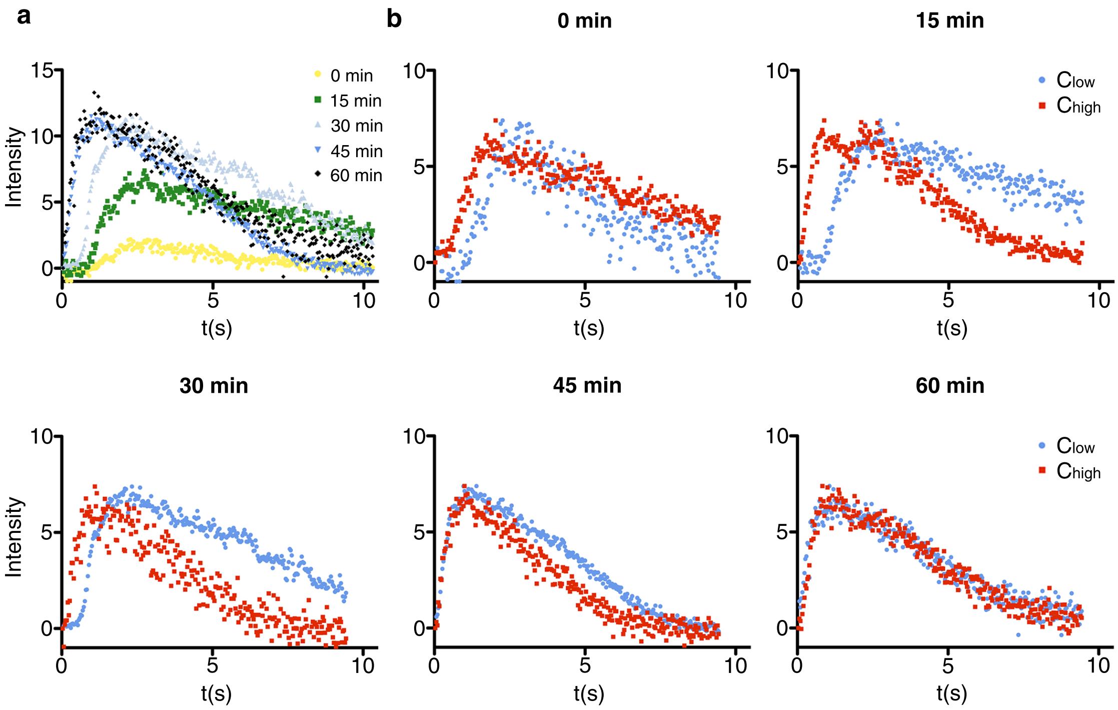

Figure 25 – Density dependent fluorescence kinetics of VSG'Y'. a) Prolonged incubation on slides decreased the emission delay and increased intensities. Maximum intensities were observed after 30 min of incubation while kinetics were fastest after 45 - 60 minutes. b) The shift in kinetics observed between a low- and high-density culture (5 x 10^5, C_{low} and 1 x 10^6, C_{high}) was reduced with continuous incubation on slides. Kinetics were indistinguishable after 60 min of incubation.

4.2.4 Pre-excitation

Fluorescence emission of VSG'Y'-expressing cells often fluctuated in intensity and displayed varying kinetics. To find out whether exposure to stray light during sample preparation may be a source of these fluctuations, cells were pre-excited with different light sources prior to measurements. The tested light sources and exposures included UV-filtered sunlight for 10 min, an ordinary 40 W table lamp for 10 min and 5 - 40 s bursts of focused light beams from an unfiltered 130 W mercury lamp. Cells exposed to (UV filtered) daylight displayed fluorescence kinetics and intensities that were indistinguishable from light-protected control samples. Pre-excitation at 25 - 100 % intensity with light from the mercury lamp for ≥30 s resulted in an instant fluorescence in subsequent measurements. This instant emission was detectable on the cell surface and reached 20 % of maximum intensity. Additionally to the instant emission, the cell fluorescence also displayed the typical sigmoidal kinetics following excitation at 360 - 420 nm. This second signal eventually outshone the initial instant fluorescence after the familiar 7 - 10 s. The cultivation medium was bleached by the prolonged exposure to the high-intensity mercury lamp, which resulted in a reduction of maximum fluorescence intensities by approximately 20 % and in the death of 80 - 90 % of the exposed cells.

4.2.5 Medium substitution

Breakdown of the HMI-9 cultivation medium revealed that the ingredient required for VSG'Y' fluorescence is the pH indicator phenol red. Washing cells in media that lacked the pH indicator abolished fluorescence. Substituting HMI-9 with 40 - 200 μM phenol red in TDB or PBS re-established fluorescence emission with the previously described kinetics, albeit at intensities that were reduced by approximately 50 - 80 % (Fig. 26a) and with impaired reproducibility and cell viability. The weak fluorescence is only 1 - 2 x higher than the background noise and minor fluctuations in emissions can result in signals that are undistinguishable from noise. Upon constant excitation, cells started dying after 30 - 60 s. Additionally, cells started dying after 10 min of incubation on slides even when omitting excitation. The addition of either foetal calf serum (FCS) or bovine serum albumin (BSA) shifted fluorescence kinetics towards longer delays and later quenching while maintaining cell viability and increasing maximum intensities (Fig. 26a).

Cultivating cells in HMI-9 medium that lacked FCS resulted in fluorescence intensities that were comparable to normal HMI-9 and vital cells while the background-to-signal ratio improved by approximately 20 %. A prominent ingredient in FCS is BSA, which is capable of binding phenol red (Y. C. Lee & Montgomery, 1962; Kragh-Hansen, 1981) and may influence VSG'Y' fluorescence by competition for PR binding, thus decreasing VSG'Y' fluorescence at higher BSA concentrations or by increasing noise through autofluorescence. Combining 100 μM BSA and 40 μM phenol red in TDB increased cell fluorescence 2-fold, while also increasing noise 20-fold and restoring cell viability. Changing the initial BSA concentration resulted in a change of noise while retaining similar maximum intensities: A reduction to 10 - 80μM BSA removed >80 % of the noise while higher BSA concentration increased noise linearly. At 150 μM BSA, background signals outshone the surface fluorescence, staining cells negatively. The earlier observation that

Trolox was another compound tested for influence on fluorescence emission and cell viability. Trolox is a water-soluble analogue of vitamin E with a similar antioxidative capacity. The addition of the vitamin E analogue had no influence on fluorescence intensities, but improved cell viability upon excitation in TDB and PBS media.

1 μM albumin, 80 μM phenol red and 1.25 mM trolox in TDB was the medium composition (termend *FMix*) resulting in maximum cell fluorescence, minimum noise and sufficient cell viability during experiments.

4.2.6 Medium depletion

The change of fluorescence kinetics during on-slide cultivation may result from increased metabolism/metabolite excretion or depletion of medium at higher cell concentrations. To test whether this is true, HMI-9 medium was depleted by cultivation of >8 x 10^5 cells/ml for 48 hours and subsequent removal of trypanosomes by centrifugation. Cells depleting the medium were expressing VSG′Y′ to avoid false negative fluorescence signals from residual cells in the medium during experiments. The used HMI-9 was coloured slightly orange-red, indicating acidification. Cells that were resuspended in depleted media displayed a shortened fluorescence delay of less than 1 to 3 s that bleached after a total of 8 - 9 s of continuous excitation, while samples in fresh medium had a delay of 10 s and quenching after >30 s (Fig. 26b).

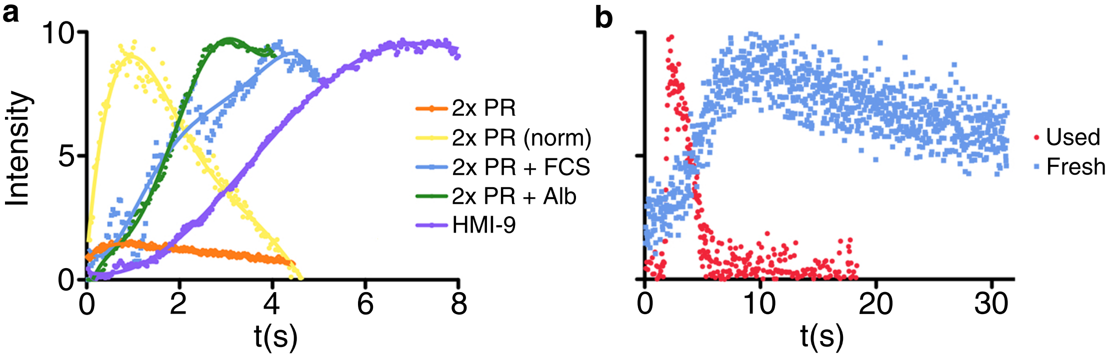

Figure 26 – Influence of medium substitution and depletion. a) TDB supplemented with 80 µM phenol red (2x PR) was sufficient to produce fluorescence emission. Supplementing the buffer additionally with 10 % FCS (2x PR + FCS) or 4 - 10 µM albumin (2x PR + Alb) increased the emission delay but also resulted in a more reproducible and strong signal and improved cell viability comparable to HMI-9. To highlight the different kinetics, the otherwise (approximately six-fold) weaker signal from 80 µM PR was normalized to the maximum intensities of albumin- and FCS-substituted samples (2x PR (norm)). b) Depleted media cause a shorter emission delay and quicker quenching compared to fresh medium.

4.2.7 pH variations

Acidification of HMI-9 during medium depletion suggests a role of medium pH in fluorescence kinetics. To test this hypothesis, fresh HMI-9 samples with a pH of 7.5 were adjusted to pH 5.0, 6.0 and 9.0, followed by filter sterilization. 1 x 10^5 cells/ml were re-suspended in the adapted media after washing. Due to the strong variances in the maximum intensity involved in all experiments, this experiment focused on fluorescence kinetics rather than intensities. The time until the relative maximum intensity I_{max} was detected was monitored together with the time until fluorescence quenching reduced the relative intensities back to the half-maximum intensity $I_{1/2}$. The delays for both emission and quenching were longest for samples that were not pre-incubated and decreased with prolonged incubation on slides (Fig. 27). In addition, cells displaying emission early also quenched earlier. Samples at pH 6.0 were the first to display emission, with a delay of

2.8 s, which quenched to $I_{1/2}$ after 8.7 s. Samples prepared in pH 9.0 followed with 5.4 s and 16.9 s for emission and quenching, respectively. Cells at pH 5.0 displayed maximum emission after 8.3 s of excitation, which quenched after a total of 18.7 s. After 45 minutes of incubation on slides, all cells with an adjusted pH displayed an almost identical emission delay of about 1 s, and a quenching time of 4 - 5 s. Cells at pH 7.5 started with the highest delays of 8.6 s and 31.7 s, respectively. The delays were reduced to 4.4 s and 19 s after 15 minutes of incubation and remained constant for the remainder of the experiment.

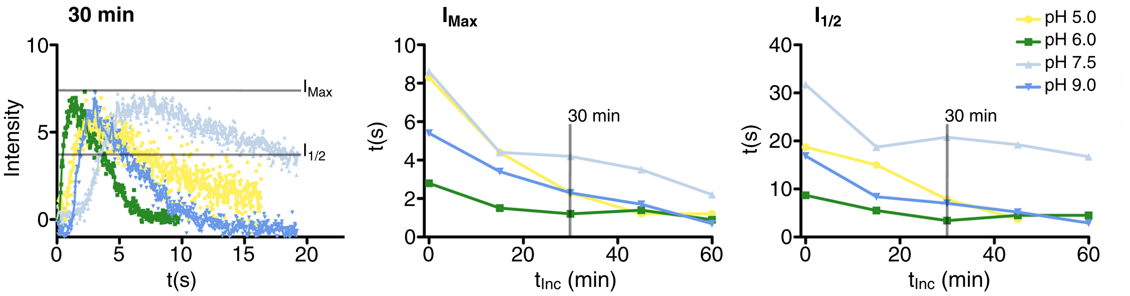

Figure 27 – Influence of medium pH on fluorescence kinetics. Medium pH influenced excitation and quenching of VSG'Y' fluorescence. HMI-9 at pH 6.0 produced quickest emission and quenching, followed by pH 9.0 and pH 5.0. Kinetics for neutral medium at pH 7.5 were slowest. The left graph shows kinetics for each pH after 30 minutes of cell incubation on slides. Guides mark maximum (I_{max}) and half-maximum ($I_{1/2}$) intensities. The middle and right graph display excitation times until I_{max} and $I_{1/2}$ was reached, respectively for a pre-incubation of 0 - 60 minutes. pH dependent differences in kinetics were neutralized after 45 - 60 min of incubation on slides for all but pH 7.5.

4.2.8 HPLC analysis of cultivation media

Potential changes of the HMI-9 medium were analysed by high performance liquid chromatography. HPLC was performed by Raina Seupel from the group of Prof. G. Bringmann in the 'Institut für organische Chemie', Universität Würzburg. 400 μl of each sample were diluted in 600 μl MeCN and pH adjusted to 6.0 or 9.0 by addition of 10 μl TFA or NaOH. The pH-adjusted samples were further diluted 10-fold in MeCN after which 50 μl of the dilution were injected into the HPLC system and OD_{447} (phenol red peak absorbance) was measured. Two different concentrations of phenol red in H_2O (0.8 mM and 5.6 mM) were measured to identify the phenol red peak. The pH indicator eluted in fractions two and three with two sharp peaks (Fig. 28). The peak in fraction two displayed a high absorption in basic and neutral conditions, while the peak in fraction 3 showed higher absorption in acidic and basic conditions. The concentration of phenol red in conventional HMI-9 medium was too low to be detected during HPLC. Therefore, medium depletion was performed as described in section 4.4.1.6 with HMI-9 medium enriched with 0.8 mM phenol red. Fresh and depleted samples were analysed by HPLC and displayed no differences for phenol red peaks. No other components of HMI-9 medium were traceable.

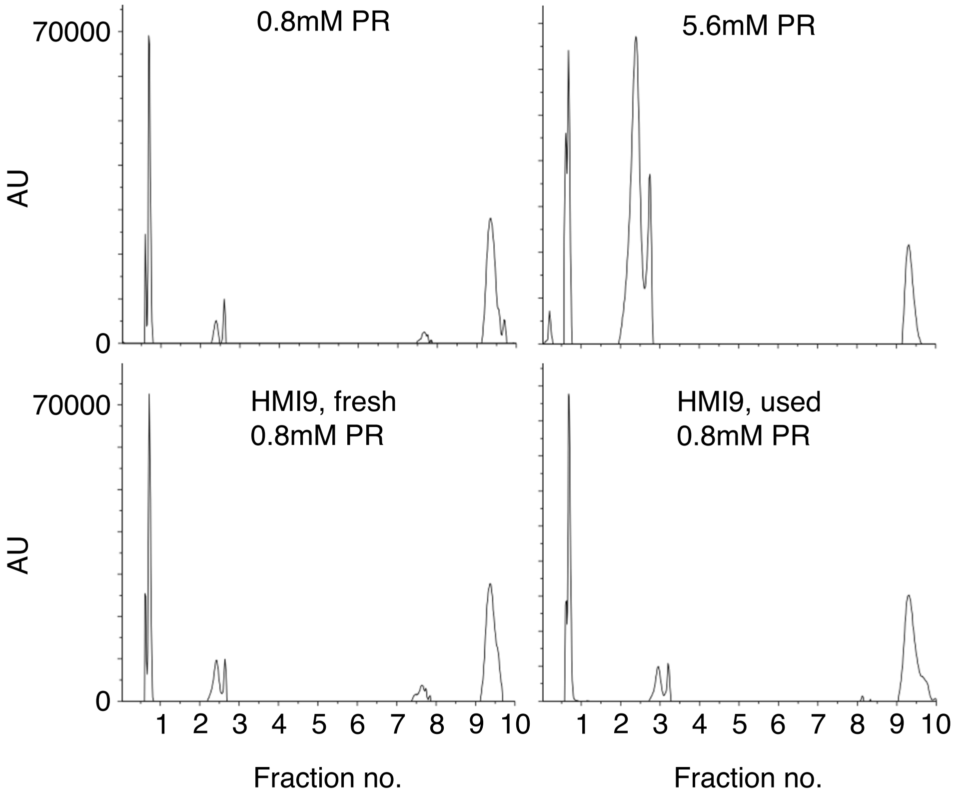

Figure 28 – HPLC analysis of fresh and depleted HMI-9 medium. The elution pattern of 0.8 mM and 5.6 mM PR identified the peak at fractions two and three as phenol red (upper left and upper right). The PR peak was identical for fresh and depleted HMI-9 samples while no other components of the medium could be detected (lower left and lower right).

4.2.9 Fluorescence quenching by BPB competition

If VSG′Y′ fluorescence requires binding of phenol red to VSG, other TPMs like bromophenol blue (BPB), that are highly similar in structure may bind to VSG′Y′ as well. During coincubation of PR and BPB with VSG′Y, BPB can compete to the same binding site as PR, without being able to induce the same fluorescence, resulting in diminished fluorescence emission for PR. Cells cultivated in 0.8 mM BPB and 0.8 mM PR in TDB died within seconds of excitation due to photo-toxicity of the TPM compounds. To circumvent this problem, TDB was substituted with HMI-9, which did not display these severe photo-toxic effects in previous experiments. While 0.8 mM PR added to HMI-9 displayed normal fluorescence kinetics and intensities, emission during coincubation of 0.8 mM PR and 0.8 mM BPB in HMI-9 was reduced to approximately 15 % of normal levels while emission delays increased from 4 s to 14 s (Fig 29a).

4.2.10 VSG′Y′ phosphorescence analysis

A phenomenon similar to the initial fluorescence delay of VSG′Y′ may cause the protein to display emission after termination of excitation. To test for this phosphorescence, emission was monitored at high frame rates during which excitation was stopped. Cells were prepared in HMI-9 and emission was monitored at 500 fps, corresponding to a temporal resolution of 2 ms. Emission ended in the same frame that excitation was terminated, resulting in a potential delay of fluorescence termination of <2 ms (Fig. 29b). Reopening the shutter resulted in signal response within 2 ms as well. No emission delay typical for phosphorescence could be detected.

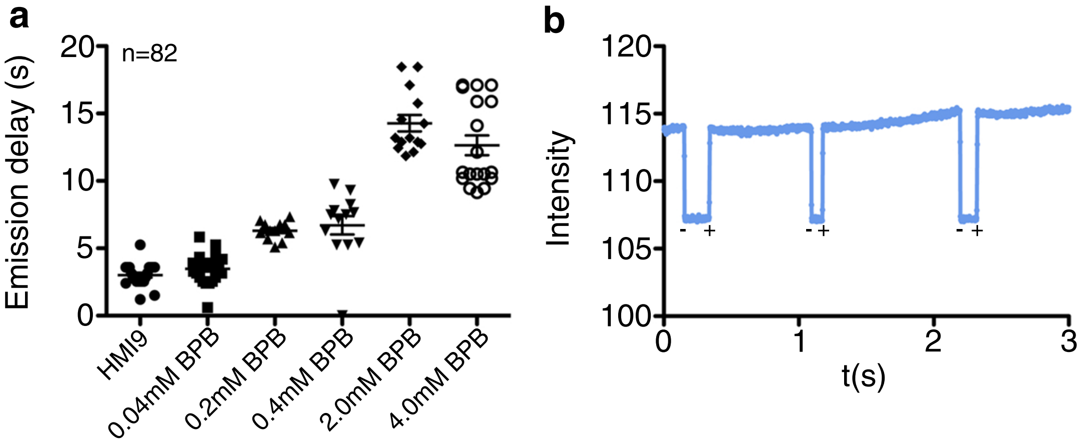

Figure 29 – Fluorescence quenching by BPB and signal phosphorescence a) Supplementing HMI-9 medium with increasing concentrations of BPB increased the emission delay from 4 s to 14 s. b) Cell emission was observed at 500 fps, corresponding to 2 ms per data point. Closing (-) and reopening (+) of the shutter resulted in immediate signal response. No emission delay typical to phosphorescence could be detected.

4.2.11 Fluorescence quenching by surface labeling

To test whether potential binding sites for PR in VSG′Y′ could be identified by blocking of surface areas, cells were labelled with Sulfo-NHS-Biotin and Sulfo-NHS-ATTO-488. After labelling for 15 min and subsequent washing, labelled cells were re-suspended in HMI-9 and analysed for VSG′Y′ fluorescence as described previously. ATTO-488 labelled cells showed an initial fluorescence signal on the cell surface that originated from the ATTO label. This signal was very weak and was outshone by normal VSG′Y′ fluorescence. Cells blocked with the ATTO labels displayed VSG′Y′ fluorescence with normal kinetics and intensities.

4.2.12 Fluorescence in artificial bilayers

To analyse whether the natural cell membrane environment is important for VSG'Y' fluorescence, the membrane form of VSG'Y' (mfVSG) was purified ((Hartel *et al.*, 2016)) and reconstituted in artificial bilayers. 10 % of the mfVSG was labelled with ATTO-488 as a fluorescence reporter for successful reconstitution of the protein in artificial bilayers. When VSG incorporation at trypanosome surface densities was tested positive via quantitative FRAP measurements of the ATTO label, a thin film of 0.8 mM PR in HMI-9 was overlaid onto the membrane system. Upon excitation at 400 nm, a weak uniform fluorescence signal was detected, which turned out to be intrinsic fluorescence of the overlaid PR buffer since an identical signal was detected for PR buffer on a bilayer without incorporated VSGs. No fluorescence emission could be detected for VSG'Y'.

4.2.13 sVSG fluorescence in solution

It was analysed whether soluble VSG'Y' without artificial bilayers or the trypanosomal surface could fluoresce. As a reference, fluorescence emission of HMI-9 and of albumin in PR were monitored. Normal HMI-9 displayed slow, linear increasing emissions (Fig. 30a). Albumin samples were resolubilised in 80 μM PR solution in TDB to final concentrations of 100 μM and 333 μM. While the 333 μM sample displayed a diffuse, linearly increasing fluorescence (Fig. 30b) the 100 μM sample failed to display detectable emissions.
Purified VSG'Y' at a concentration of 20 mg/ml was resolubilised in either HMI-9 or FMix. While the HMI-9 sample displayed sigmoidally progressing emissions that resembled live-cell kinetics, the FMix sample displayed semi-parabolic kinetics with a reduced delay (Fig. 30c).
To test the influence of protein folding on fluorescence emission, purified VSG'Y' at a concentration of 20 mg/ml was mixed with an equal volume of 0.4 mM PR to a final concentration of 10 mg/ml VSG'Y' and 0.2 mM PR in TDB. One sample was boiled at 100 °C for 5 min prior to the addition of PR, while another remained at 4 °C during that time. Upon excitation on slides, the intact VSG sample displayed a diffuse, semi-parabolic and increasing fluorescence emission while no emissions were detected from the denatured samples (Fig. 30d).

4.2.14 Live cell tryptic treatment

Cells expressing VSG'Y' were trypsin-treated to analyse the effect that digestion and the removal of the N-terminal domain of VSG'Y' have on fluorescence emission. Samples collected from the supernatant of trypsin-treated cells and the cell pellets were analysed electrophoretically (Fig. 31). Cells digested for 0 minutes displayed a band at 66 kDa in the supernatant, corresponding to trypsin, while there was a heterogeneous range of proteins in the cell pellet. Cells treated with trypsin for 5 minutes displayed two

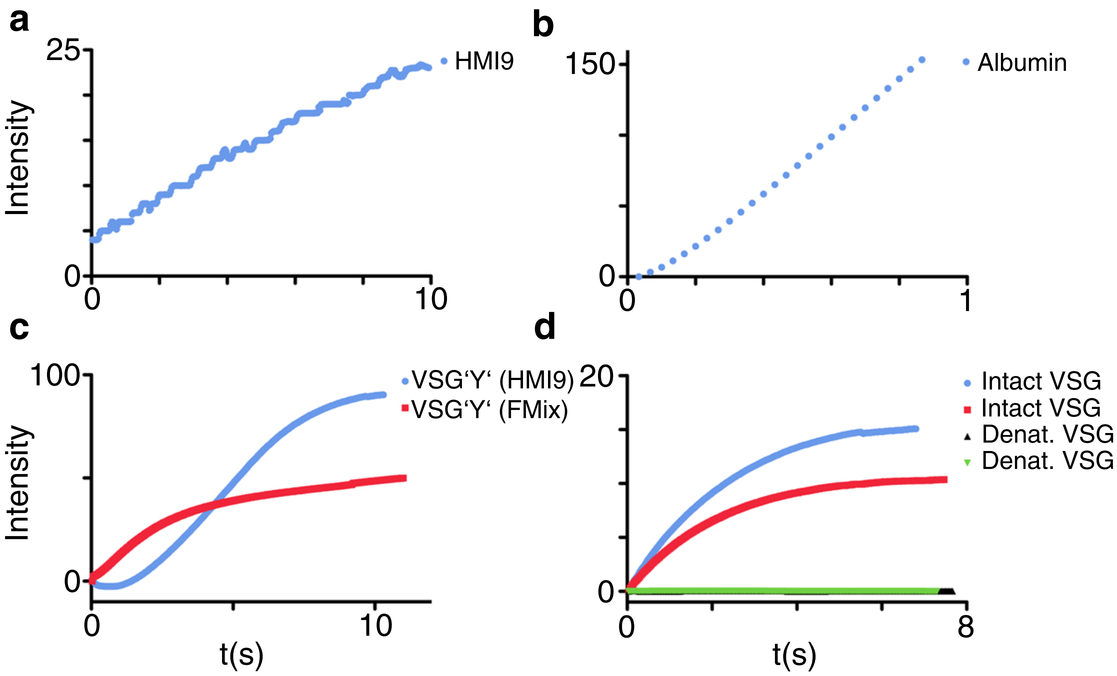

Figure 30 – Fluorescence emission by soluble VSG′Y′ and buffer references. a) Fluorescence of stock HMI-9 medium increased linearly. b) 0.5 mM albumin in 20 μM PR (TDB) solution expressed strong, linearly increasing fluorescence emission. c) 20 mg/ml soluble VSG′Y′ fluoresced with kinetics depending on the buffer setup. In HMI-9 the signal displayed sigmoidal kinetics while being semi-parabolic in FMix. d) An intact sample of soluble VSG′Y′ shows semi-parabolic increasing emissions. Denaturing soluble VSG′Y′ at 100 °C for 5 min extinguished fluorescence emission completely.

bands in the supernatant at approximately 66 kDa and 50 kDa, respectively, corresponding to trypsin and the NTD of VSG′Y′. The cell pellet of the digested sample showed an overall reduction of band intensity by approximately 50 % while the band-size distribution remained identical to the untreated sample. This could be either caused by a loss of cells during preparation, or trypsin treatment. Upon excitation of trypsin-treated live cells, the fluorescence kinetics and intensities were identical to untreated samples, most likely due to incomplete VSG cleavage. The trypsin concentration was doubled to 1 mg/ml in subsequent experiments, which led to a stronger 66 kDa band and a lack of other protein fractions in the supernatant while VSG′Y′ abundance in treated and untreated samples remained identical. So, while residual proteins were degraded by trypsin treatment, VSGs remained intact or were quickly recycled and exchanged by intact VSG. No differences in fluorescence emission was detected between treated and untreated cells.

4.2.15 Calorimetric detection of PR binding

Isothermal titration calorimetry was performed on an MicroCal ITC200 (Malvern) with soluble VSG′Y′ to find out if PR binds actively to VSG′Y′. 10 mg/ml VSG′Y′ and 0.2 mM PR were each prepared in identical TDB buffer to reduce thermic noise during experiments. The PR sample was added to VSG′Y′ in single drops for which the thermic change was measured. During the experiment signals retained a constant power of minus 0.1 μcal/s, which did not change significantly over a 5-fold molar increase of PR (Fig. 31). This means that no binding between VSG and PR could be detected.

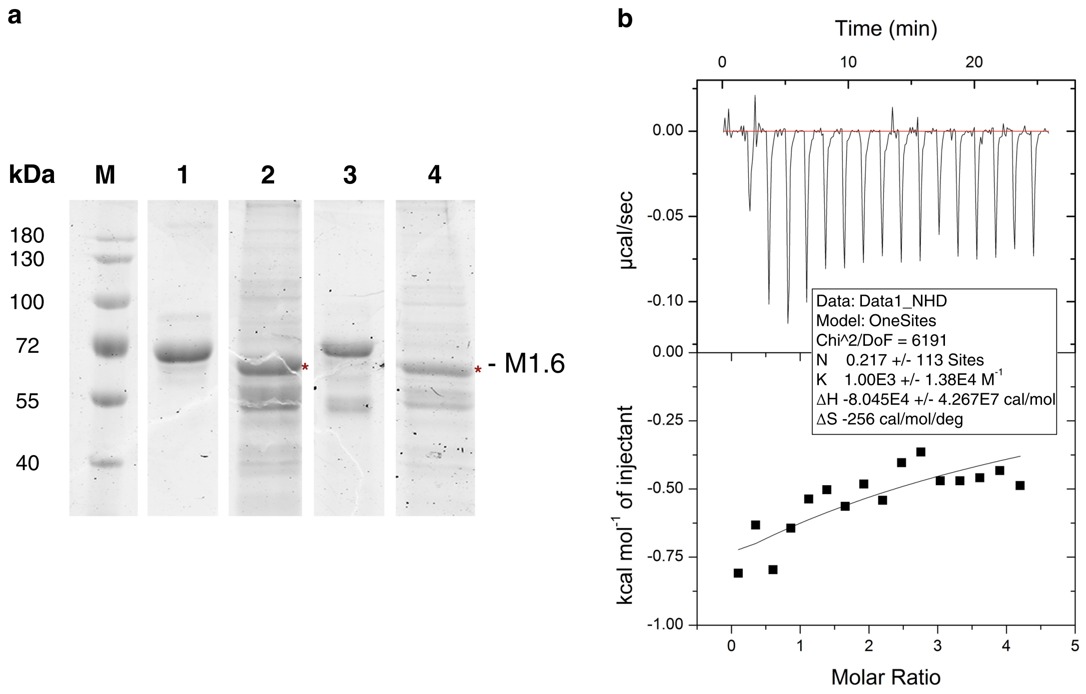

Figure 31 – Electrophoretic analysis of trypsin treatment and ITC200 analysis of soluble VSG′Y′. a) Lane 1 and 2 display samples prior to treatment. Samples produced after 10 min of tryptic treatment are displayed in lane 3 and 4. Supernatant is shown in lanes 1 and 3 and cell pellets in lane 2 and 4. Asterisks (*) mark the position of VSG′Y′. Trypsin treated samples showed an overall reduction of band intensity by approximately 50 % while the band-size distribution remained identical to the untreated sample. This could be either caused by a loss of cells during preparation, or trypsin treatment. b) During the calorimetric detection of cofactor binding the exothermic signal should decrease with saturating concentrations of the cofactor while the sigmoidal Wiseman plot characterizes the binding parameters. However, no saturation was detected by the addition of a 5-fold molar excess of phenol red to soluble VSG′Y′.

4.3 The trypanocidal effect

The triphenylmethane dye phenol red is important for the fluorescence emission of VSG'Y'. Bromo-derivates from the same family of TPM dyes display a much weaker fluorescence but are capable of triggering a trypanocidal effect (TE): Upon excitation in the presence of the bromo-derivate (bromophenol blue, bromocresol green, bromocresol purple or bromophenol red) at the wavelength corresponding to the absorption maximum of the TPM dye, the parasite will die. In contrast to the previously described VSG'Y' specific fluorescence, this trypanocidal effect and the accompanying fluorescence are independent of the expressed VSG. The endeavour of this section is the quantitative analysis of this trypanocidal effect. The focus is placed on factors that alter the potency of the TE, including TPM concentrations and antioxidant addition. In addition to the interaction analysis between TPMs and VSGs, this section aims to identify how VSGs can influence photo-induced cell-stress. While VSG'Y' + phenol red can relax from an excited state by means of fluorescence emission without harming the cell noticeably, other combinations of VSGs and TPMs seem to damage and kill the cell. It is the goal to find out which role both the TPM and the VSG play in this harmful energy transfer.

4.3.1 Trypanocidal effect triggering

The trypanocidal effect kills trypanosomes upon excitation in bromophenol blue (BPB) solution at the respective excitation maximum of 560 nm and is independent of the expressed VSG. In the time course of excitation, a weak, linearly increasing fluorescence could be detected, which was distributed homogeneously along the cell surface (Fig. 32). While emissions were increasing, the cell motility decreased simultaneously until it was undetectable. Eventually, a strong fluorescence wave originating from a single point along the cell surface spread through the cell, marking the time of cell-death. 54.2 % of the observed fluorescence waves originated on the cell body, of which 53 % occurred in the flagellar pocket. The remaining waves originated on the flagellum. In many cases a delay of several seconds was observed between the fluorescence wave along the flagellum and along the cell body. A complete lack of motility and a stiffening of the cell body could occur before, during or even after the fluorescence wave. The fluorescence wave itself is accompanied by a bulging of the cell body, indicating cell death. High BPB concentrations resulted in a shorter delay between fluorescence waves on the flagellum and the cell body and could trigger the fluorescence wave prior to the abolishment of cell motility. Accordingly, low BPB concentrations resulted in longer delays and a cell death prior to the fluorescence wave. Therefore, higher BPB concentrations can increase the potency of the trypanocidal effect as indicated by the earlier onset of the fluorescence wave.

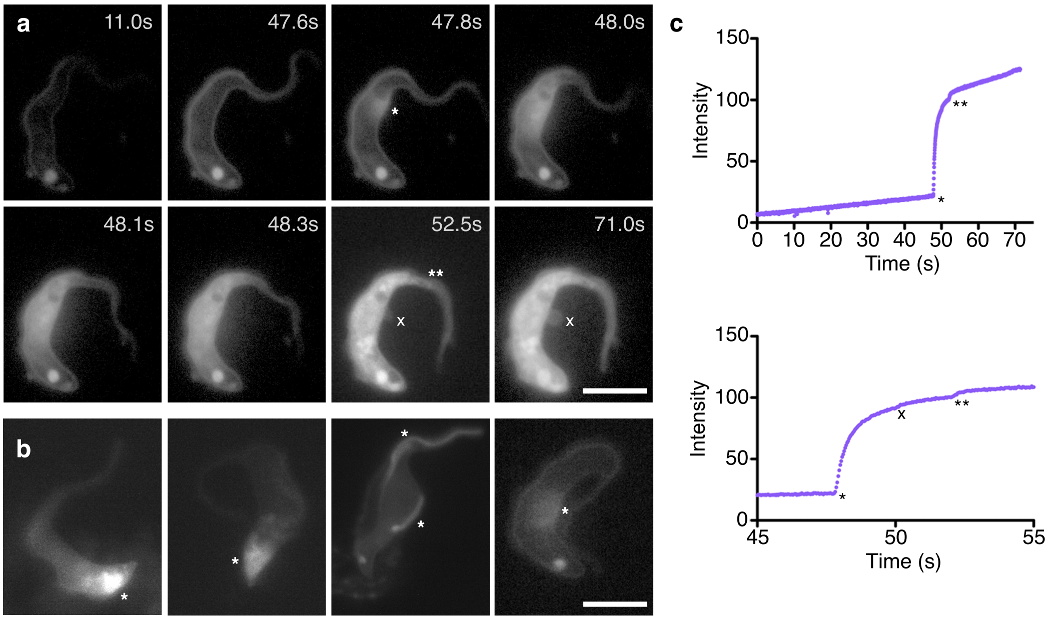

Figure 32 – Fluorescence kinetics of the trypanocidal effect. a) Time lapse of the fluorescence wave. After 47.8 s of constant excitation the wave appeared along the cell membrane (*) and spread homogeneously through the whole cell body. With a delay of 4.7 s the wave travelled through the flagellum (**). Disruption of the cell membrane is evident by the escape of fluorescent particles from the cell membrane (x). b) The origin of the fluorescence wave (*) varies for each individual cell. Displayed are cells with a fluorescence wave originating in the flagellar pocket, near the base of the flagellum, along the flagellum and on the cell body (from left to right). Scale bar = 5 μm. c) Emission signals increased linearly along the whole cell before and after the exponential increase at the onset of the fluorescence wave. The top plot displays the complete time course of the experiment while the lower plot is focused on the onset of the fluorescence wave. Membrane disruption and the initiation of both fluorescence-waves (cell body and flagellum) are marked within the plots.

4.3.2 Influence of TPM concentrations

When trypanosomes are prepared in 80 μM BPB in TDB, at 5 x 10^5 cells/ml on slides, the average survival upon excitation is 44 s. Cell survival decreased linearly with increasing BPB concentrations, with a maximum reduction to 17 s for incubation in 1.28 mM BPB (Fig. 33a). Further increasing the BPB concentration resulted in cyto-toxicity independent of excitation. When lowering BPB concentrations, the weak fluorescence was detectable to a lower concentration threshold of 4 μM BPB. However, concentrations below 80 μM BPB could not reproducibly induce the TE.

The trypanocidal effect may require BPB to bind to VSGs, which could be prone to competition by other TPM compounds like phenol red in the case that both TPM compounds bind to the same motif within VSGs. In case of a competitive binding, and provided that PR has the same or higher binding affinity to VSGs as BPB, coincubation of cells with both PR and BPB should improve the cell survivability upon excitation. However, incubation with equimolar amounts of BPB and PR (80 μM each) did not alter the survival of excited cells (Fig. 33b). Further increasing the TPM concentration to 160 - 320 μM even seemed to reduce cell survival to 30 - 35 s.

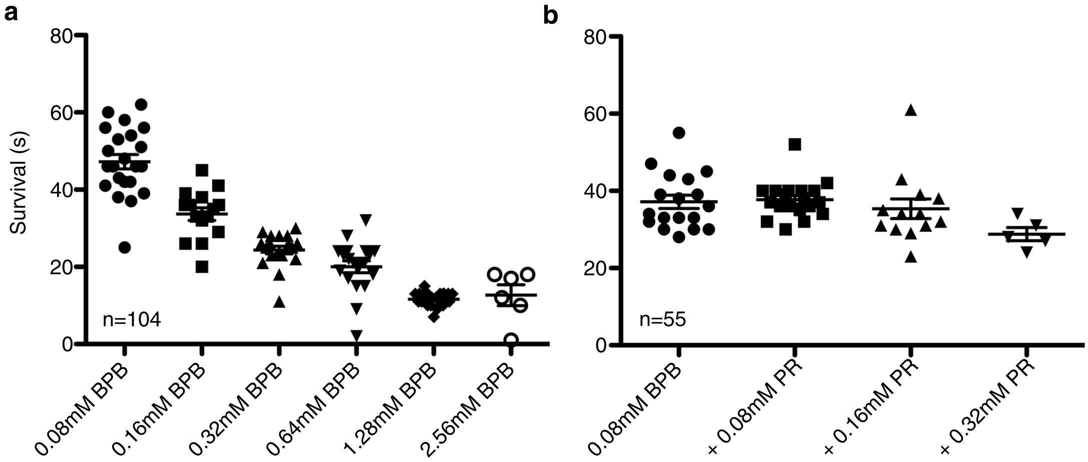

Figure 33 – Influence of TPM concentrations on the trypanocidal effect. a) A reproducible TE could be triggered by excitation in 0.08 mM BPB. Increasing the concentration resulted in a linear decrease in cell survival until a concentration of 1.28 mM BPB was reached at which point a further increase resulted in excitation-independent cyto-toxicity. b) Coincubation with increasing concentrations of PR did not improve cell survival, however cytotoxicity could be observed starting at 0.32 mM PR.

4.3.3 Influence of antioxidants

The signature fluorescence wave of the TE may be a result of oxidative damage to the cell membrane, which could be inhibited by the addition of antioxidants. 1 x 10^7 cells were prepared in TDB supplemented with 80 μM BPB and either 1.2 mM butylhydroxytoluol (maximum solubility), 400 μM n-propylgallate (highest non-toxic concentration), 1.8 - 3.6 mM trolox (maximum observable effect), 400 μM bathocuproine sulphate (10-fold excess compared to HMI-9 medium), 0.4 - 1.6 mM ascorbic acid (maximum observable effect) or 10 - 25 μM albumin (maximum concentration without background noise). Upon excitation at 560 nm, the trypanocidal effect was affected by the addition of trolox, ascorbic acid and albumin, while the other antioxidants failed to show any effect. Addition of 1.8 mM trolox increased cell survival from 24.4 ± 3.5 s to 40.7 ± 10.9 s, while doubling the concentration to 3.6 mM increased cell survival only to 45.5 ± 16.4 s (Fig. 34a, n = 36). Supplementing the cell solution with 4 μM albumin resulted in higher cell- and background fluorescence, while the cell survival increased from 39.6 ± 5.9 s to 78 ± 23.7 s (Fig. 34b, n = 78). Increasing the albumin concentration to 20 μM or higher resulted in very strong background emissions that outshone cell surface fluorescence and neutralized the TE. Adding 400 - 800 μM ascorbic acid prior to excitation resulted in a cell survival that increased to at least 95.7 s (Fig. 34c, n = 37). Increasing the concentration to 1.6 mM ascorbic acid resulted in survival of >360 s at which time point measurements were aborted. It was observed during these measurements, that pre-incubation on-slides could increase the cell survival time by 59 - 146 % to 75.7 - 126.1 s even in the absence of antioxidants (Fig. 34d).

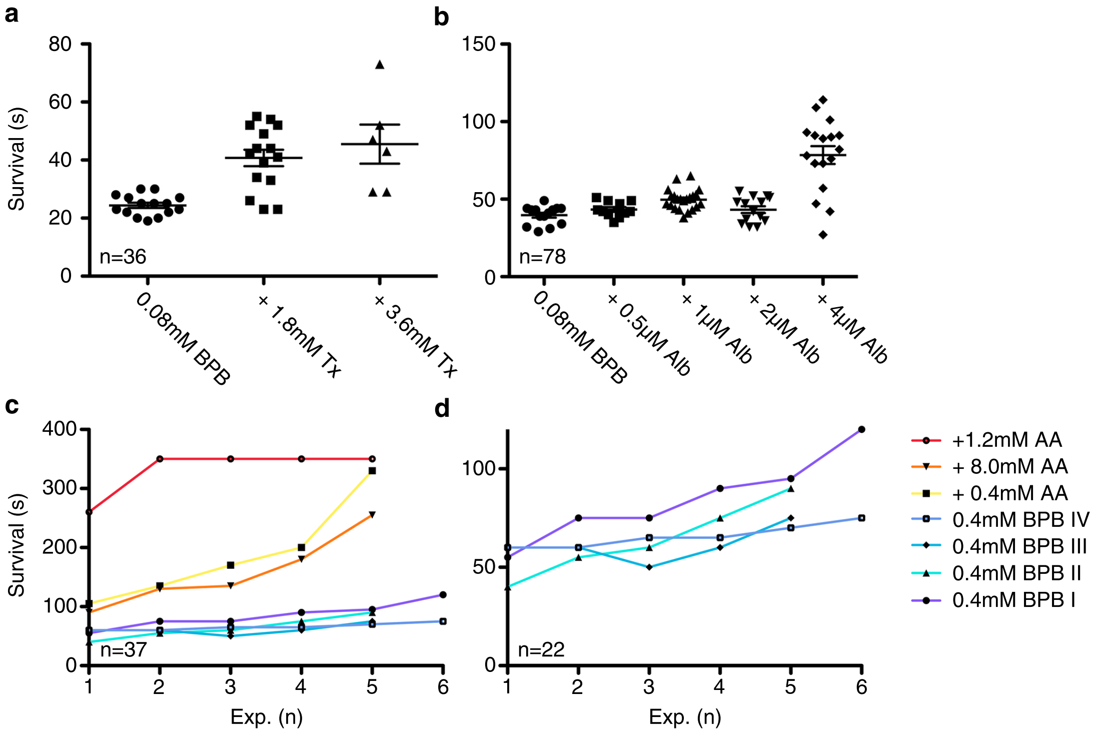

Figure 34 – Influence of antioxidants on the trypanocidal effect. a) Supplementing the BPB solution with 1.8 mM trolox improved survival times by 60 % from 24.4 ± 3.5 s to 40.7 ± 10.9 s, while further increasing the concentration to 3.6 mM resulted in a further improvement to 45.5 ± 16.4 s. b) Supplementing BPB with 4 µM albumin resulted in cell survival that increased from 39.6 ± 5.9 s to 78 ± 23.7 s. Further increasing concentrations resulted in background noise that outshone cell fluorescence and rendered cells immune to the TE. c) 0.4 - 0.8 mM ascorbic acid (AA) improved cell survival from 47.7 s to 95.7 s -340.5 s. Increasing the concentration to 1.2 mM improved cell survival to more than 360 s at which point the experiment was aborted. d) Cell survival improved from 47.7 s to up to 126.1 s even in the absence of antioxidants by pre-incubation of samples on glass slides.

4.3.4 Reversibility of cell photo-paralysis

During excitation at 560 nm, there is a short time frame of photo-paralysis prior to the fluorescence wave, when cells are completely immobile but not dead. To test whether this paralysis is reversible, cells were cultivated with 600 µM BPB (TDB) and 100 mM trolox. The high trolox concentration resulted in a delayed TE, separating paralysis and cell-death temporally. Turning off excitation or switching to a wavelength outside the excitation bandwidth of BPB allowed the paralysed cells to regain motility that was undistinguishable from non-excited cells within a few seconds, as judged by observation from bright-field microscopy.

4.4 Fluorescence of VSG'Y' mutants

In the endeavour to analyse the interactions between VSGs and TPMs, structural and fluorescence microscopic analyses were conducted and described in previous sections of this thesis. This section will describe VSG'Y' mutants that were constructed and analysed to identify the exact amino acids involved in these interactions. An alignment of the VSG'Y' sequence to the structure of MITat1.2 was used to identify individual amino acids that could be involved in the binding of TPMs. A likely mode of interaction is π-π-interaction of aromatic amino acids with the triphenyl-rings of the TPM dyes. Aromatic amino acids that are close to the surface and could interact with TPMs were identified and exchanged either conservatively with other aromatic amino acids or by alanine or isoleucine as described below. Once the mutants were generated, they were introduced into the inducible 13-90 cell line. This cell line is based on MITat1.2 and constitutively expresses the T7 RNA polymerase and a tetracycline repressor (Wirtz *et al.*, 1999). The cell line allows inducible expression of the introduced VSG'Y' mutants through the addition of 1 μg/ml tetracycline to cell cultures. The expression of the mutant VSG can then be monitored by a combination of VSG fluorescence, immunofluorescence and western blot analysis. Cells that lack VSG'Y' fluorescence but display unimpaired growth behaviour, while expressing and displaying VSG'Y' mutants on their surface, identify the exact location required in the binding of TPM compounds.

4.4.1 Generating mutants

For the generation of VSG mutants, the VSG'Y' gene was cloned into the pBluescript SK (+) cloning vector flanked by T7 and T3 promoters. Using the flanking T3 and T7 primers and the mutant primers resulted in two PCR fragments with different sizes for each of the mutants due to the position of the desired amino acid exchange. The initial PCR fragments were then used as template in a second PCR to assemble the complete VSG gene. The product was amplified and sequenced prior to transfection, and subcloned into transfection vector pLew82v4 that integrates into rRNA spacers of *T. b. brucei*. Mutations were performed for amino acid exchanges F8I, F8W, W11F, Y121A, W254F, Y269A, W329F and W475F (Fig. 35). It must be noted, that several primers were designed in incorrect orientation. Affected are primers F8WL, Y121AL and Y269AL which are directly complementary, instead of reverse complementary to the associated primers of the opposing strand. However, correct mutants could eventually be obtained before the error was noticed and all mutants were verified to correctly include the mutation of interest by sequencing. Primers for mutants W11A, F8IW11A, F107A and Y212A were prepared (including the lower primers (L) with wrong directionality) (Tab. 1), but mutants were not created, as is explained in the following sections.

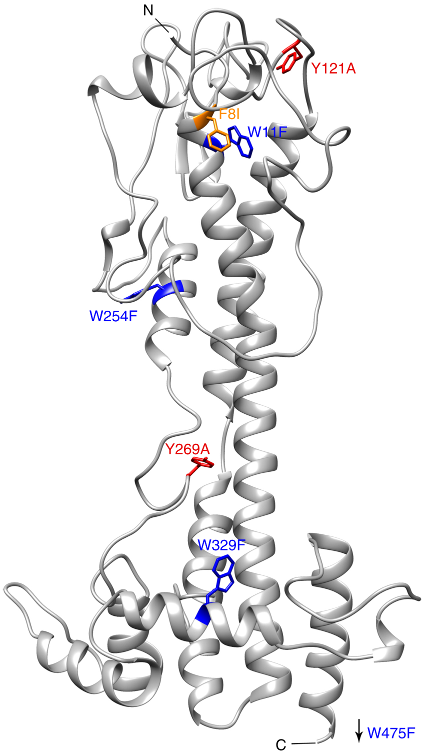

Figure 35 – Representation of all amino acid exchanges in VSG'Y'. Displayed is the VSG'Y' structure that is based on the alignment of the VSG'Y' amino acid sequence to the structure of MITat1.2 in monomeric form. Phenylalanine is displayed in orange, tryptophans in blue and tyrosines in red. Amino acid exchanges F8I/F8W and W11F may have a cumulative effect on TPM binding due to close proximity. W475F is part of the C-terminal domain and not displayed.

4.4.2 Western Blot analysis

Western blot analysis of mutant VSG cell lysates was conducted to test whether transfection was successful and protein expression levels of VSG'Y' mutants will reach that of wildtype levels, as described previously (Batram *et al.*, 2014). Cell lysates were harvested 24 h after induction and labelled using antibodies against MITat1.2 and VSG'Y' and displayed no VSG'Y' expression for F8I while all other mutants displayed strong expression levels (Fig. 36c).

4.4.3 Immunofluorescence

Immunofluorescence staining of fixed cells was performed to test whether the mutated VSGs are transported correctly to the trypanosomal cell surface. Fixed cells were labelled using antibodies against MITat1.2 and VSG'Y'. 24 h after induction all mutant cells showed a strong signal for MITat1.2, while the VSG'Y'signal was weak for mutants F8W and W11F and undetectable for mutant F8I (Fig 36b), which can be explained by a lack of protein expression identified by western blot analysis. Mutants Y121A - W475F displayed wildtype expression of VSG'Y' 24 h after induction.

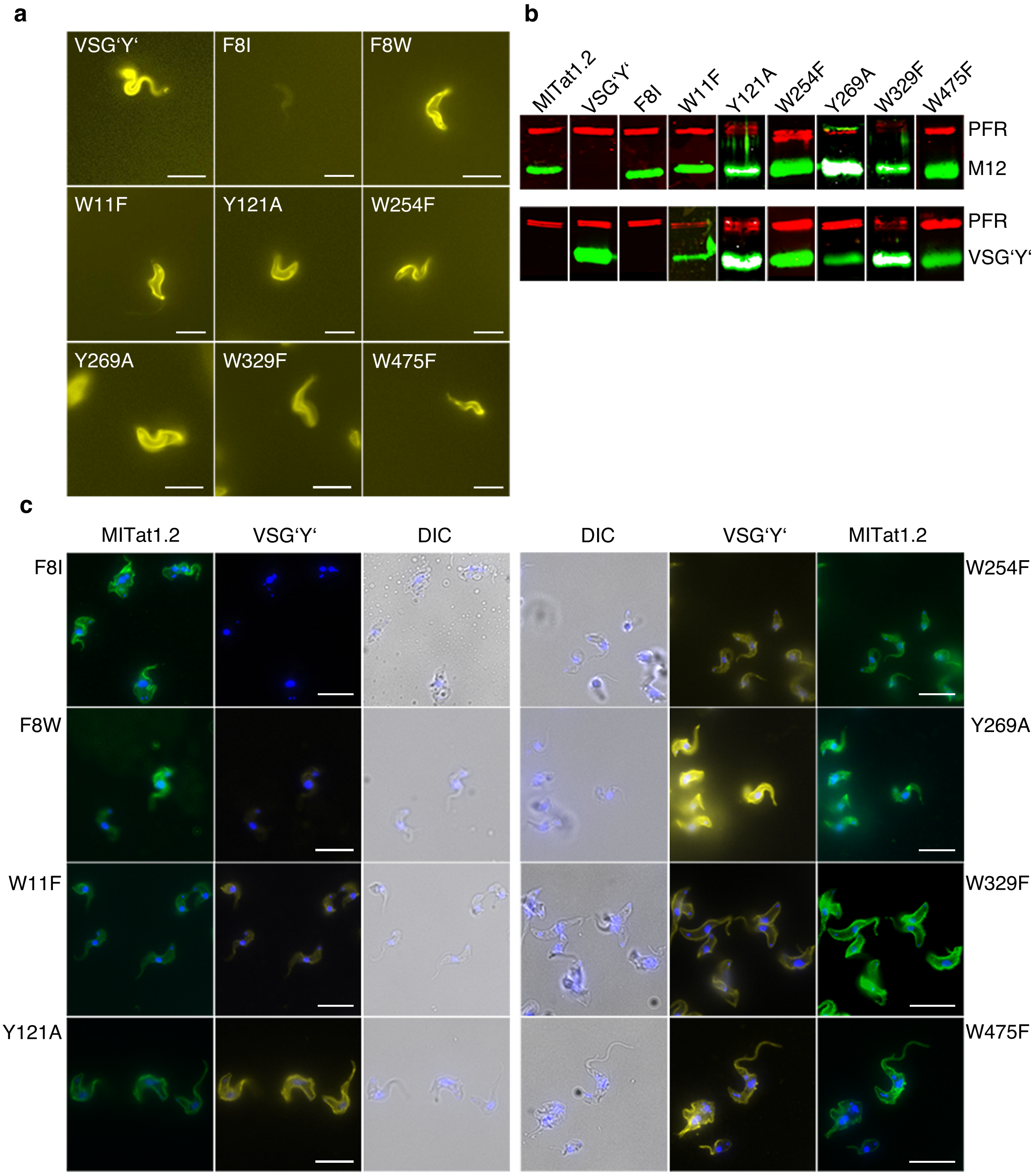

Figure 36 – Fluorescence analysis of VSG′Y′ mutants. a) All mutants except F8I displayed emissions on the cell surface with VSG′Y′ wildtype intensities. Maximum intensities were observed 24 h post induction. b) Cell lysates of all mutants were prepared and labelled for MITat1.2 (green (top)) and VSG′Y′ (green (bottom)). PFR (red) was used as a loading control. Mutant F8I displayed no signal for VSG′Y′ while the remaining mutants displayed unambiguous signals for both VSGs. c) 24 h post induction, all mutants were fixed and antibody-labelled against MITat1.2 (M1.2, green) and VSG′Y′ (yellow). Nuclei and kinetoplasts were labelled with DAPI (blue). Mutants F8W and W11F displayed only weak signals while F8I was negative for VSG′Y′. The remaining mutants displayed equally strong signals for both VSGs. Scale bar = 10 μm.

4.4.4 Cell cultivation

Following transfection, cells were cultivated in 24-well-plates until a stable population of at least 1 x 10^4 cells/ml was reached, at which point cultivation was continued in tissue culture flasks. Stable clones displaying exponential growth could be obtained for all mutants, even though some clones displayed slow growth (12 or more hours per duplication, compared to approximately 6 h for wildtype cells) within the initial 48 h of cultivation. Averaged cell growth, determined in intervals 6 - 16 h, fluctuated between 6.7 and 8.2 hours per duplication and cells were clearly sensitive towards antibiotic selection: Following dilution, cultures displayed increased duplication times of 8 - 12 h, while cultures that remained undisturbed for at least 24 h displayed growth of 6 h per duplication. This may have been caused by a population within the culture that is negative for the introduced VSG but may still show some antibiotic tolerance. When cells are diluted, some of the VSG-negative cells die upon contact with fresh selection, which is observable by slow population doubling times. After several hours of incubation the population of tolerant cells may increase in numbers once more, thus normalizing population doubling times. Upon induction of the VSG'Y' mutant by tetracycline addition, growth decreased noticeable to 9 - 15 h per duplication (Fig. 37).

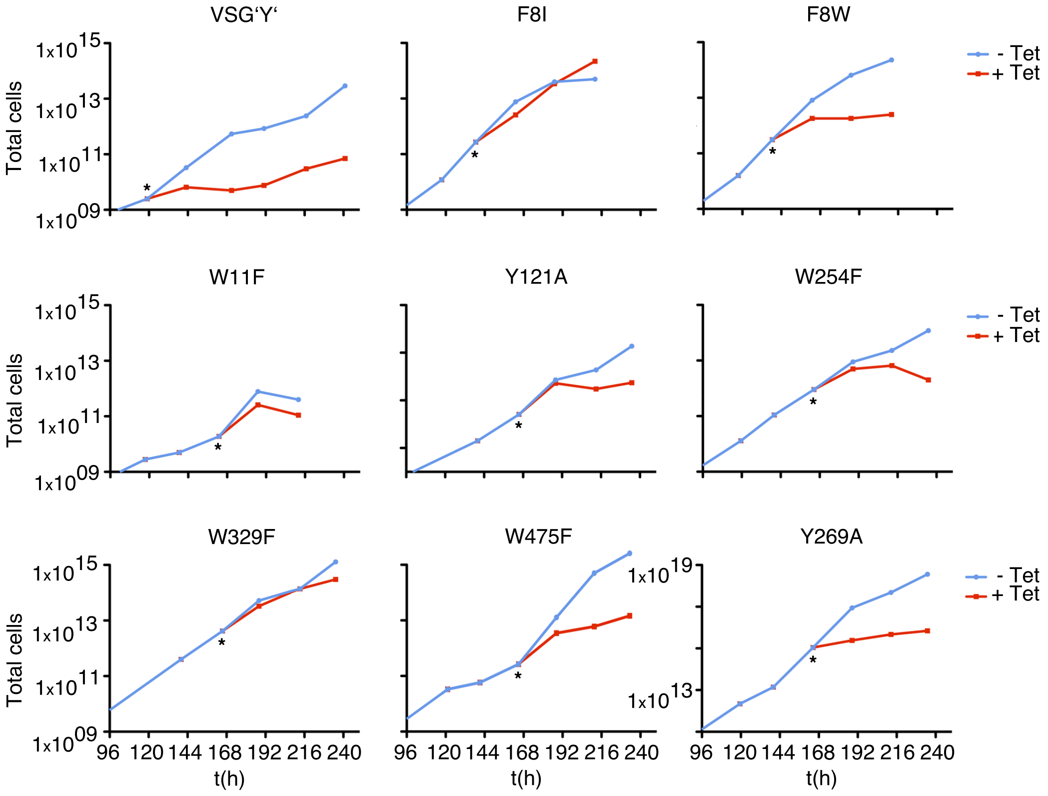

Figure 37 – Growth behaviour of individual mutants. Non-induced cultures are displayed in blue and induced cell lines in red. The time of induction is marked by an asterisk (*). Growth slows for all cell lines after induction except for mutant F8I. Cells displayed general sensitivity towards antibiotic selection and grew slower after dilution with fresh antibiotics.

4.4.5 Cell fluorescence analysis

VSG′Y′ mutants that are correctly expressed by the cells and transported to the cell surface were tested for fluorescence emission. Expression of the mutant forms of VSG′Y′ was induced by the addition of tetracycline to cultivation media. Emissions were monitored 0 - 48 h post induction using either the Leica DMI6000 B or DMI IRB fluorescence microscope at an excitation wavelength of 365 - 420 nm. The Till Photonics iMIC system was avoided during these experiments due to unreliable VSG′Y′ excitation in past experiments. With the exception of clone F8I, all of the generated mutants still expressed surface fluorescence at wildtype intensity (Fig. 36a). Mutant F8I only expressed $\leq 10\,\%$ of maximum intensity at all times, explained by lack of protein expression identified during western blot analysis.

4.4.6 TPM docking simulations

While it is valid to assume that TPM binding of VSG′Y′ is based on interaction of the TPM compound with aromatic acids of the protein, none of the performed mutations tested positive to this binding. To explore the possibility of alternatives to aromatic interaction, docking simulations were performed. These simulations can help to identify a potential binding position and mechanics. Docking studies were performed using MITat1.1, MITat1.2, ILTat1.24 and the VSG′Y′ alignment and were computed in SwissDock (Grosdidier *et al.*, 2011). Binding positions varied for most VSGs, however a single position was abundantly occupied in MITat1.2, ILTat1.24 and VSG′Y′ (Fig. 38). A pocket is formed in the dimerisation surface between monomers of the NTD in proximity to the N-terminal domain end. Simulations suggest interaction between PR and charged residues Lys, Arg, His, Glu and Asp (Fig. 38b), while no interaction with aromatic residues is shown. The same position is also occupied in docking studies of BPB. Positions F8 and W11 in VSG′Y′ were not occupied during simulations.

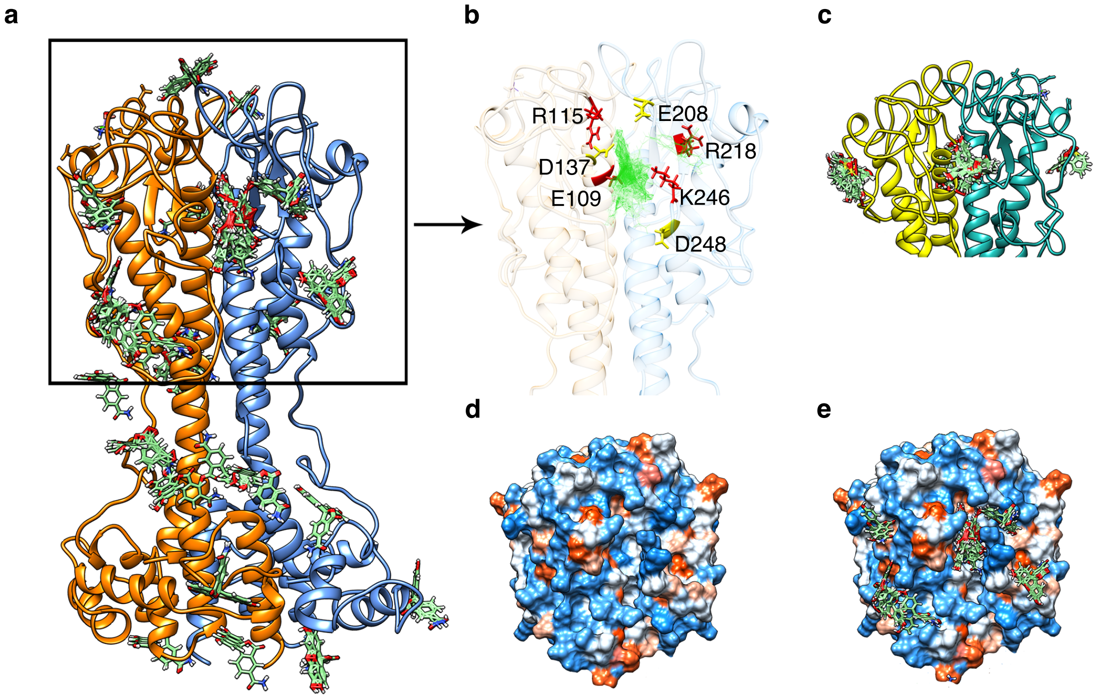

Figure 38 – Binding of PR in docking studies. a) Depicted is the computed NTD of VSG′Y′ (the alignment of the VSG′Y′ amino acid sequence to the MITat1.2 tertiary structure) with all simulated docking positions for PR (green). The most abundantly occupied position is a pocket in the dimerisation interface between NTD monomers (centre of box). b) Displayed are the anionic (red) and cationic (yellow) residues that may be involved in PR (green) binding. c) A similar position is occupied in MITat1.2 (displayed) and ILTat1.24 (not displayed). d) Hydrophobicity plot of the N-terminal end of the VSG′Y′ NTD with the central binding pocket. e) Hydrophobicity plot (d) with bound PR.

5 Discussion

The discovery of a fluorescent VSG protein, and subsequently of the trypanocidal effect, introduced a new perspective on VSGs. The prospect of a structural feature that may be conserved between different VSGs makes the protein a much more attractive drug target. Therefore, characterising the binding between VSGs and TPMs and identifying the conserved binding pocket were important goals in the course of this thesis. Applying fluorescence microscopy, protein mutagenesis and x-ray crystallography for the task was met with a varying degree of success. While the different approaches remained inconclusive in identifying a binding pocket and a binding mechanism, insights were gained in the potential working mechanisms of the unique VSG'Y' fluorescence and the trypanocidal effect. Furthermore, structural analysis of VSGs led to the solution of the first complete experimental VSG structure that represents a milestone for the research of the trypanosomal cell surface.

Some of the questions raised during this thesis could not be answered conclusively. The results of all conducted experiments that were presented in previous chapters, are discussed subsequently and function as a compendium for future research on VSG fluorescence, TPM binding and structural analysis of the VSG.

5.1 Structural analysis of VSGs

During cultivation, cell lines expressing different VSGs on their cell surface tend to have different population doubling times and maximum achievable densities even though they are genetically identical. However, while being genetically identical, the expression of certain proteins may vary between trypanosome cultures. In case of the activation of a new expression site during antigenic variation, the number and composition of expression-site associated genes (ESAGs) changes along with the VSG (Becker *et al.*, 2004), potentially influencing cell growth. An impaired cell growth was observed for MITat1.4 which could not be successfully cultivated in cell densities required for protein crystallography. MITat1.5 was also affected notably. While purification could be performed and crystals could be obtained, protein yield was inconsistent and at least 2-fold lower than for MITat1.1. Cell behaviour at high densities was also strongly dependent on the brand and batch of the FCS in use. During this thesis the original FCS batch was eventually changed, resulting in impaired cell growth for all but the most robust cell lines MITat1.1 and MITat1.2. Media for *in vitro* cultivation of *T. b. brucei* require the addition of serum, which is a complex solution that includes many unknown proteins and growth factors in a composition that varies between individual batches. Therefore, a change of the FCS batch may inevitably change growth behaviour of cultures. Trypanosome cultures that differ for the expressed VSG also express a different number and composition of ESAGs, some of which are known to code for cell surface receptors, e.g. ESAG 6 & ESAG 7 (Steverding *et al.*, 1994). So a difference in gene expression and receptor composition could explain how different trypanosome cultures react so differently to a change of the FCS batch. The reported cultivation parameters, including revolutions of orbital shaking, FCS concentration and maximum densities are optimized under current cultivation media conditions but will most likely change with further changes of the FCS batch. Expressing VSGs recombinantly in eukaryotic expression systems like *Pichia Pastoris* strain M5 (Roge *et al.*, 2013) would be insusceptible to the aforementioned cultivation difficulties. However, the expressed VSG would have to be carefully monitored for correct folding, dimerisation and glycosylation.

Once sufficient amounts of trypanosomes expressing the VSG of interest could be cultivated, protein purification could be performed. Purification parameters were adapted from previous protocols (Cross, 1984; Manthri *et al.*, 2008) to include multiple incubations for GPI-PLC release of sVSG (Fig. 10) and a different setup of protease-inhibitors. This had the strongest impact on protein yield, increasing VSG-yield 2-fold. Buffer-exchange and anion-exchange-chromatography could still be improved by the use of columns with higher loading-capacity to circumvent column overload or the requirement of multiple rounds of loading. Otherwise, the present protocol is state-of-the-art for the purification of soluble VSG from *in vitro* cultivated trypanosomes.

Once protein purity was confirmed chromatographically and electrophoretically, crystallisation experiments commenced. These experiments are generally performed by trial-and-error and are influenced by smallest differences in protein composition (e.g. single amino acid exchanges). This is exemplified by the relative ease with which MITat1.1 and MITat1.2 proteins form ordered crystals with high diffraction resolution, while extensive crystallographic efforts with VSG'Y' resulted in no evaluable diffraction data. So except for an educated guess, known crystallisation parameters for one VSG can give very little information towards the formulation of successful crystallisation parameters of another VSG. Electrophoretic comparison between crystallised and freshly purified VSGs illustrates the difficulty of VSG structure determination once more, since the crystallised proteins were degraded to approximately 40 kDa (Fig. 13a), corresponding to the size of the NTD. This is a common observation for the crystallisation of VSGs (D. M. Freymann *et al.*, 1984). Subsequent AFM analysis confirmed these results (Fig. 13b) and also implied protein flexibility. This flexibility could later be confirmed by the generation of the complete MITat1.1 and ILTat1.24 structures. The high flexibility of the CTD could hinder the formation of highly ordered crystals. Only once a sufficient amount of the VSG degraded to the compact NTD do orderly crystals form. This explains an earlier observation, where initial VSG'Y' crystals formed after approx. 120 days of crystallisation during which proteolytic cleavage decreased the size and flexibility of the protein. Once degraded (and crystals being accidentally destroyed), they could re-form within 5 - 10 days (Bartossek, 2011). Therefore, VSGs featuring a flexible CTD may always be subjected to prolonged crystallisation which only starts once a critical amount of the cleaved protein is available. A solution to this crystallographic problem could be a stabilization of the CTD. The VSG of interest could be cocrystallised with compounds binding to the CTD (e.g. stabilizing peptides bound to specific CTD antibodies) that reduce the flexibility and thus improve formation of ordered crystals. Similar methods were successfully used on the structural analysis of flexible domains of GPCRs (Ghosh *et al.*, 2015).

In contrast to the crystallisation of a crystallographically-unknown VSG, the crystallisation of MITat1.2 was straightforward, since successful crystallographic conditions are already published (D. Freymann *et al.,* 1990). Therefore, starting crystallisation trials with MITat1.2 had the advantage of yielding quick results and could prove that general protein quality was sufficient for x-ray crystallography and was a logical first choice for crystallisation trials. The resolution of the MITat1.2 structure was improved from the published 2.9 Å to 2.5 Å during this thesis. This improvement could result from either improved overall protein quality or the use of better x-ray facilities. The space group and resolution of the established MITat1.2 crystals changed in respect to the published ones (D. Freymann *et al.,* 1990), but the structure remained practically identical (Fig. 16), meaning that the crystal composition is different while the context of information is, as expected, of an identical structure.

Another advantage of the ease of MITat1.2 crystallisation was, that trials with cocrystallisation of TPM compounds could already be addressed without structural data of VSG′Y′. Cocrystallisation with TPM compounds resulted in reproducible growth of coloured crystals. However, these crystals lacked electron density data for the TPM compounds in all cases. Binding of the cofactor phenol red to the protein may be specific for VSG′Y′, which would also suggest a different mechanism for the trypanocidal effect. Furthermore, binding of TPMs to VSG could be too weak to occur during crystallisation or might be dependent on energy transfer induced by excitation. Excitation of soluble MITat1.2 and TPMs at the respective excitation wavelength prior to crystallisation might improve binding properties. However, the possibility remains that TPM compounds do not bind to MITat1.2 directly and that the interaction is specific for VSG′Y′ and phenol red.

The unsuccessful cocrystallisation trials with TPM compounds and MITat1.2 show, that a crystallographic structure of VSG′Y′ remains important for the identification of potential binding sites for TPM compounds. The best resolution for native VSG′Y′ crystals was in the range of 4 - 7 Å which is insufficient for evaluation. In the course of this thesis, no conditions were found that improved diffraction resolution of native VSG′Y′. A potential source for the lack of order was the heterogeneous glycosylation of the protein. Crystallisation of the deglycosylated variant of the protein indeed resulted in a resolution that improved to 1.6 Å but also suffered from twinning. This is insofar surprising, since the crystals of VSG′Y′ do not posses a CTD any more and the NTD of wild type VSG′Y′ and the deglycosylated form are identical. Residual N-glycans in the crystallisation-drop may have impaired the ordered aggregation of VSG′Y′. Conversely, the lack of a heterogeneously glycosylated CTD may have had a beneficial influence on crystal formation. Deglycosylated VSG′Y′ crystals grew under several similar conditions that all resulted in the same space group, resolution and twinning for crystals. However, it is possibly that the observed twinning was caused only indirectly by deglycosylation. It is also possibly that the deglycosylated form of VSG′Y′ was able to form crystals in a wider range of buffer compositions and that the composition that was found here is notorious to form twinned protein crystals. However, no exhaustive screening comparable to that of native VSG′Y′ was conducted. Since commercial screens for native VSG′Y′ were tested thoroughly without resulting in good diffracting crystals, the optimal course to pursue structure elucidation of VSG'Y' is thus rigorous screening for the deglycosylated variant of VSG'Y'. The resolution of 1.6 Å is already more than sufficient, and the pursuit of conditions that do not cause twinning of deglycosylated VSG'Y' may prove easier than the search for good diffracting native VSG'Y' crystals.

During crystallisation trials with MITat1.1, several condition were discovered that resulted in growth of protein crystals of high order and allowed structure determination of this VSG. The tertiary structure of the N-terminal domain of MITat1.1 shows resemblance to the published NTD structures of MITat1.2 (D. Freymann *et al.,* 1990) and ILTat1.24 (M. L. Blum *et al.,* 1993) (Fig. 15), including the structural features of the extended coiled coil, the unstructured membrane distal variable surface loops, an antiparallel β-sheet and a set of short helices close to the C-terminal end. Since the phase problem was solved by molecular replacement, which intrinsically leads to a bias towards the reference structure (Dodson, 2008), the model of MITat1.1 may be biased towards the structure of MITat1.2. A phase problem solved by isomorphous replacement (and thus independent of known protein structures) may provide a slightly different structure. Nonetheless, all three known A-type VSG structures (MITat1.1, MITat1.2 and ILTat1.24) show remarkable similarity and suggest that other A-type VSGs may be of similar composition. For future experiments, it may be of interest to crystallise a type-B VSG, or generally VSGs that vary in their distribution of cysteins, N-glycans and secondary structure elements. This would elucidate whether different VSG types share the same secondary- and tertiary motifs as described here, or if for example VSGs exist that form NTD homo-trimers or that could form hetero-dimers with different NTDs (similar to ESAGs 6 & 7). Such findings would have a strong impact in understanding the VSG coat.

The combination of high-resolution NMR and macromolecular crystallography domain structures with low-resolution SAXS structure prediction allowed to overcome problems of protein degradation that are common during crystallisation of proteins with flexible domains and that prevented determination of the complete VSG. While crystal growth is impaired by protein flexibility and requires a high amount of time for crystal growth during which proteins may degrade, SAXS experiments are conducted in a matter of minutes and are insusceptible to these problems. As a result the first complete structures of VSGs MITat1.1 and ILTat1.24 provide insight into the architecture of the protective VSG coat and display a high degree of conformational flexibility.

Additional SAXS experiments were performed with VSG'Y' even though high resolution structural data is not yet available. Sequencing data suggest that VSG'Y' is slightly larger than MITat1.1 and ILTat1.24, while the peak at lower angles in Fig. 23b + c, that refers to compact conformations, is higher for VSG'Y', suggesting that more of the protein is in a compact state than in MITat1.1 and ILTat1.24. The alignment with the two additional plateaus for ILTat1.24 in the *P(r)*-distribution suggests a conformation for VSG'Y' that is more closely related to ILTat1.24 than MITat1.1 and MITat1.2. This is unsurprising, since the distribution of cysteines and potential glycosylation-sites as well as the overall size of

VSG'Y' is more similar to ILTat1.24 as well. A more detailed analysis can be conducted with the SAXS data of VSG'Y' once high resolution domain information is available.

SAXS experiments are generally performed with the protein in solution and allow the protein to adopt to a variety of different conformations. Therefore, the extrinsic geometric constrains that influence the VSG in it's natural environment of the trypanosome cell membrane do not necessarily apply. For VSG modelling, two different approaches were taken to account for VSGs in solution and in the restrictive membrane environment. One method used modelling without restrictive protein symmetry to account for the unrestrained situation in solution. It was reassuring to see that models constructed without these restrictions always formed dimers of the NTD (Fig. 18b). The same models also possess highly asymmetric CTDs that display the high flexibility of this domain. The other method applied for VSG modelling included 2-fold protein symmetry that emulates the restrictions applied, for example by the GPI anchoring and the dimeric NTD of VSGs. This symmetry contributes significantly to the overall protein structure, which still remains highly flexible and produces multiple different conformations. The range of these conformations can be grouped into two main types. The first type extends perpendicular to the presumable membrane position and occupies a relatively small overall area, and is termed the *compact conformation* (Fig. 17, M1, M3 and M4). The second type is less extended but displays a wider footprint, extending further towards adjacent proteins and is termed *relaxed conformation* (Fig. 17, M2).

The average area that MITat1.1 and ILTat1.24 span for a non-hydrated and static model is 28 nm^2 and 30 nm^2, respectively, which is in agreement to previous calculations of 28 - 35 nm^2 (Grünfelder *et al.*, 2002; Jackson *et al.*, 1985). So despite a size difference of the CTD of more than 30 %, the average area that each VSG spans varies by only 7 % (Tab. 22 and 23) and seems to be strictly regulated on the cell surface. However, when considering the rotational freedom between CTD and NTD and the high mobile fraction of VSGs on the cell surface (Hartel *et al.*, 2016), the static model underestimates the actual area each VSG could occupy. Using the circular area and a theoretical hydration layer of 1 nm (derived as an average value from (Svergun, Richard, *et al.*, 1998) and (Merzel & Smith, 2002)) results in an average occupancy of 95 nm^2 and 118 nm^2 per VSG for MITat1.1 and ILTat1.24, respectively. The consideration of a highly dynamic VSG molecule results in an increased average area spanned by ILTat1.24 of 20 %, owing to the increased size of its CTD. This means that different VSGs can occupy different areas and that the total number of VSGs on the cell surface fluctuates with the expressed VSG. The only experimental analysis with respect to the number of VSG molecules on the trypanosome cell surface was published in 1985 by Jackson and Voorheis (Jackson *et al.*, 1985) and determined a total of 5×10^6 dimers per cell. This is in agreement with $4.2 - 5.7 \times 10^6$ dimers calculated from the MITat1.1 and ILTat1.24 models, but also suggest that the static area occupancy describes the situation on the cell surface more closely than the dynamic model. However, both methods to calculate the average area of a single VSG molecule are only approximations, based on the size of the VSG molecule and the cell surface, rather than *in vivo* experiments to actually "count" the VSG number and occupancy. The surface areas are subject to errors during calculation, since pleomorphic bloodstream form trypanosomes may vary greatly in size. Here, the static model represents the average size of a rigid protein and the dynamic model represents the maximum possible expansion of an unrestricted VSG molecule. On the highly dynamic cell surface, each VSG molecule will be subject to an individual environment that influences the degree of freedom of that molecule and therefore the area it can occupy. It is conceivable that each individual VSG can occupy the whole range of areas spanned by the static and dynamic occupancy models in dependency on its current environment.

VSGs may switch between compact and relaxed conformation types dynamically in response to the overall protein density on the cell surface and to maintain functionality in different environments, including the cell surface and endosomal apparatus. While on the cell surface, the protein is in a highly crowded environment. Once the protein is re-cycled and enters the endosomal system it is diluted up to 50-fold (Grünfelder *et al.*, 2002) and then re-concentrated before it is returned to the cell surface. Additionally, natural fluctuations in transcription rate and protein synthesis of VSGs occur, that further influence the protein density on the cell surface. During antigenic variation a new VSG is introduced that may occupy a different amount of space. During such events, the coat integrity must not be compromised, which displays the need for a protein that can adapt to a changing environment (Fig. 39). This is reflected by the fact that the total width of the VSG is always determined by the flexible CTD (Fig. 17 and 22), which spreads out furthest toward the surrounding protein coat. The removal of the C-terminal oligosaccharide drastically reduced the lateral mobility of VSG′Y′ in artificial bilayers (Hartel *et al.*, 2016), which agrees with the assumption that the spatial distribution of VSGs is regulated by the CTD. The reduced lateral mobility could be caused by attractive forces between VSG motifs that were previously insulated by the glycan's presence. In this case, removal of the glycan would not have made a difference if the spatial distribution were regulated by the NTD. Previously shielded residues could also interact with the surrounding medium, leading to the phenotype of reduced lateral mobility. Note however, that glycans on a VSG could also be a functional substitute, e.g. for an α-helix, since not all VSG CTDs require a glycan for functionality (Schwede *et al.*, 2015).

The N-linked glycan of MITat1.1, that is connected to Asn266 of the NTD may have an influence on VSG dynamics and flexibility similar to the observed influence of glycans in the CTD of VSG′Y′. However, the NTD glycan is not featured in all VSGs, e.g. ILTat1.24 which displays a helical motif at the same position (M. L. Blum *et al.*, 1993), or Buw2 and IL3298 that lack N-glycosylation completely (Schwede *et al.*, 2015). It was speculated before, that the N-glycan of MITat1.2 is a functional substitute of a missing helix (present in ILTat1.24), which is important for steric interaction and may shield hydrophobic residues from exposure (M. L. Blum *et al.*, 1993). However, the hydrophobic residues in MITat1.1 are buried in a pocket about 7.5 Å beneath the surface of the protein (Fig. 14c), which makes steric interactions improbable and monitoring of protein folding a more likely scenario for this oligosaccharide. The existence of VSGs that lack any form of N-glycosylation supports the idea that oligosaccharides are not generally necessary in VSG folding and

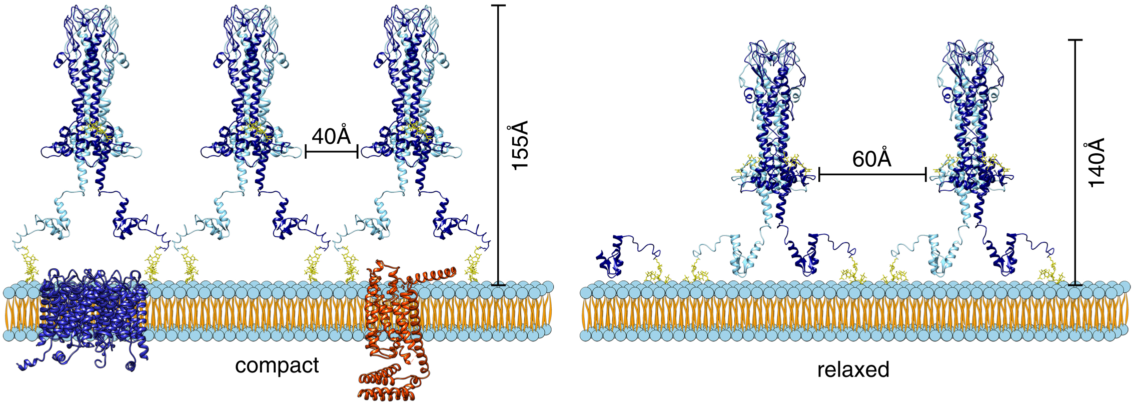

Figure 39 – Flexibility of VSGs within a surface coat. Side-view illustration of the cell surface occupied by VSGs at two different densities. A tightly packed conformation (left) can elevate the VSG above the transmembrane proteins (dark blue, red), while a relaxed conformation (right) could allow maintenance of a protective coat on the cell membrane even at reduced protein densities.

the formation of protective coats. Thus, N-glycans substitute existing functional elements such as α-helices in VSGs instead of introducing new ones.

While an individual VSG molecule can occupy a varying area, there are limitations to the degree that the VSG coat can be compacted on the cell surface. In previous work, the simultaneous expression of two independent VSGs from transgenic trypanosomes led to overexpresssion of up to 150 % total VSG (Batram *et al.*, 2014) which may force all VSGs on the cell surface into the compact conformation and prevents any further VSGs from entering the cell surface. This hypothesis is supported by the finding that the VSG density in artificial bilayers can be increased to 140 - 150 % before the molecular crowding threshold is reached and mobile fraction and diffusion coefficient break down (Hartel *et al.*, 2016). So once all VSGs have entered a compact conformation (at 150 % VSG density), the surface coat reaches its spacial limitations beyond which the protein may deform beyond the normal range of conformations that could sustain the required amount of mobility. Additionally to the VSG itself, other membrane proteins, including invariant receptors and channels that are important for sensing, communication and nutrient uptake of the parasite, act as obstacles that may affect the free diffusion of VSGs. However, the compact conformation lifts the protein far enough from the membrane surface to allow the VSG to float over obstacles unhindered. This includes obstacles up to the approximate size of a G-protein coupled receptor (Fig. 39). In this case, the CTD could be cushioning the influence of surface obstacles, similar in function to the suspension of a road vehicle, while the NTD remains unimpaired (Fig. 19 and 39). It is also possible that the binding of antibodies causes a deformation of the VSG. IgGs and IgMs tether together multiple VSGs, potentially impairing coat mobility. In response, the VSG could tilt along linker L1, bending the NTD in the direction of the drag forces that are applied to the coat during antibody clearance, while the remainder of the CTD maintains the necessary mobility.

Some invariant surface proteins, including the heterodimeric transferrin receptor (TfR) (Salmon *et al.*, 1997; Carrington & Boothroyd, 1996) and the trypanosomal haptoglobin-haemoglobin receptor (TbHpHbR) (Lane-Serff *et al.,* 2014) share a high structural similarity with VSG NTDS. These proteins share a three-helical core motif (Lane-Serff *et al.,* 2014; Higgins *et al.,* 2013), a GPI anchor and a similar overall size with the NTD. TfR models also form a dimer with resemblance to the VSG NTD tertiary structure (Salmon *et al.,* 1997; Carrington & Boothroyd, 1996) and connect to the membrane by a GPI anchor. However, the GPI anchor is attached only to one monomer (pESAG6) of the heterodimeric protein (Ligtenberg *et al.,* 1994). The unique feature of functional importance that sets VSGs apart from structurally similar proteins is the presence and flexibility of the C-terminal domain. TfR and TbHpHbR miss a flexible CTD and are composed of a rigid coiled-coil structure that closely resembles the VSG NTD. Both TfR and TbHpHbR need to bind their cargo while also not significantly exposing themselves to the host immune system. While TfR is only present in the secluded flagellar pocket, TbHpHbR is embedded and shielded within the VSG coat but still remains accessible for its ligands. A surrounding layer of VSGs in uniformly compact conformation could further help to shield the receptors from immune detection by reducing their accessibility. However, TfR and VSGs need to be in balance to maintain ligand binding without risking high accessibility to host antibodies. How this equilibrium is maintained remains unknown at this time, but could be closely linked to the different VSG conformations. A relaxed VSG conformation allows ligand accessibility while a compact conformation delivers higher protection.

In summary, the flexibility of the complete VSG structures presented in this work shed new light on the trypanosome VSG coat, which must be highly flexible and dynamic. The two main folds that VSGs can adopt appear to allow the shielding function to be maintained at varying protein densities, while enabling VSGs to maintain high mobility in the presence of obstacles and confinement on the cell surface. Only through this flexible coat topology can both mobility and a protective function be brought together in the complex and changing environment of the membrane surface.

These results could be complemented in several ways. Cryo-EM is improving to resolutions that match those of x-ray crystallography and could allow the structural analysis of VSGs in their membrane environment. Similarly, x-ray crystallography of the membrane form of VSGs, including lipid molecules, might be difficult to accomplish but could give important insight in the interaction between VSG and membrane. Dynamic *in silico* modelling of VSGs in membranes could supplement cryo-EM and crystallography of mfVSG in the context of protein-membrane-interaction. Diffusion experiments *in vivo* and in artificial bilayers could clarify the importance of the CTD for the overall VSG area occupancy. VSGs without a CTD should occupy a smaller area, but could also react differently to a change in coat density. Likewise, VSGs with a CTD that displays multiple N-glycans could react vastly different to changes in coat density. Finally, x-ray crystallography of B-type VSGs, or more generally of VSGs that are predicted to have a different secondary structure than the known A-type VSGs, would further the knowledge of the structural and functional understanding of VSG.

5.2 Characterization of VSG'Y' fluorescence

VSG fluorescence experiments were performed simultaneously to the structural analysis discussed in the previous section, since most of the experiments could be performed independent of structural knowledge of VSG'Y'. Ultimately, the structure of VSG'Y' remained elusive in the course of this thesis. While this did not hinder fluorescence analysis itself, experiments could not be designed with the same detail that structural knowledge about a binding domain would have provided. Fluorescence emission of the trypanosome cell surface requires VSG'Y' to be expressed by the cell and phenol red in the surrounding medium. However, due to the amount of factors that influence emission, elucidation of the fluorescence mechanism of VSG'Y' proved to be challenging. The basic emission of VSG'Y' was weak and low signal-to-noise ratios in the range of 1:1 - 1:5 were a common factor that complicated quantitative analysis of fluorescence intensities. In many cases repetition of experiments under identical conditions could not replicate identical results on a quantitative level. For example, in a set of identical experiments maximum fluorescence intensity varied, but the temporal progression of the emission was identical. Thus, in this example the experimental setup was focused on relative fluorescence kinetics and the temporal progression rather than quantitative intensities. This way, the influence of each factor under analysis can be described, even though other, potentially yet undiscovered factors, could inadvertently remain variable. Experiments would be less susceptible to influence by parameter fluctuations if the overall fluorescence intensity were stronger, e.g. in the range of commercial fluorophores like GFP. While minor fluctuations (e.g. from medium composition) will lead to huge errors if the initial signal-to-noise ratio is only 1:1 - 1:5, it would be insignificant if the fluorophores (and the signal-to-noise ratio) were stronger (e.g. ≥1:10). The key for more robust results is therefore an improvement of the VSG'Y' fluorescence emission, which was partly successful in the formulation of the FMix solution that increased signal intensity, reduced background noise and improved cell viability during fluorescence excitation. Knowledge of the mechanisms that govern VSG'Y' fluorescence could help to refine the FMix solution and to further increase fluorescence emission. In addition to a more robust signal, this would also allow to test the influence that different emission intensities could have for example on cell viability and fluorescence kinetics.

The emission that follows excitation of VSG'Y' in the presence of phenol red, displays unique kinetics. While common fluorophores have an excited-state half-life of a few nanoseconds until linear or exponential emissions can be detected, VSG'Y' displays an initial delay of up to several seconds during which only weak or no emission could be detected. Subsequently, fluorescence kinetics rise sigmoidally (Fig. 24a). Following peak emission at the end of this sigmoidal rise of fluorescence, emission started to decrease linearly and eventually quenched completely. Quenching was reversible and fluorescence emission could be recovered after a short pause. It was the endeavour of this thesis to characterize these unique emission kinetics, by first identifying all factors from cultivation that exerted an influence on the fluorescence emission. Exchanging the HMI-9 cultivation medium with TDB extinguished fluorescence emission, which revealed that the HMI-9 medium contained a cofactor that was required for VSG'Y' fluorescence. Previous studies by Markus Engstler have shown that the required cofactor was the pH indicator phenol red and that HMI-9 medium that lacks phenol red could not trigger fluorescence emission of VSG'Y'. At the start of this thesis, a minimum medium that was less complex than HMI-9 was used to start fluorescence analysis of VSG'Y'. While this minimum medium, composed of phenol red solubilised in TDB (TDB-PR) was sufficient to produce VSG'Y' fluorescence, the signal was different from the signal obtained for HMI-9. Although only VSG'Y' and PR were required to trigger the emission, the delay until fluorescence could be detected was relatively long, with slowly progressing kinetics and a low maximum intensity. It was also observed that TDB-PR medium triggered cell-toxicity upon excitation and even during cultivation of trypanosomes. Experiments using the standard cultivation medium HMI-9 instead of TDB-PR increased cell viability, maximum intensities and fluorescence kinetics notably. This indicated that some component of the more complex medium had an amplifying effect on emission while the same or a different component inhibited cell-toxicity. Subsequently, TDB-PR was supplemented with individual components of HMI-9 medium to identify the beneficial factors. Trolox, the water-soluble derivative of the antioxidant vitamin E improved cell viability in TDB-PR and TDB-BPB 2 - 3-fold, while the antioxidant ascorbic acid had no detectable effect on cell viability or fluorescence kinetics. While ascorbic acid typically reacts with reactive oxygen species including hydroxyl radicals, α-tocopherols like trolox are known to react with lipid radicals, produced during a lipid peroxidation chain reaction. This chain reaction is in turn often produced by other radicals such as hydroxyls. The fact that trolox, but not ascorbic acid shows an effect indicates, that VSG'Y' excitation produces lipid radicals, without depending on other reactive oxygen species. Another HMI-9 component influencing VSG'Y' fluorescence was FCS/BSA. Addition of albumin to TDB-PR resulted in a 2-fold increase in surface fluorescence while also drastically increasing background noise. Albumin is known to bind phenol red (Kragh-Hansen, 1981) and could catalyse PR fluorescence in the cultivation medium. *Vice versa*, phenol red could catalyse the characteristic albumin fluorescence at 281 nm. This observation implicates the possibility that the detectable VSG'Y' fluorescence may actually be emitted by phenol red, which is known to fluoresce at 440 nm. Through binding to VSG'Y' the emission could become blue-shifted from 440 nm to 365 - 420 nm and localized to the cell surface. In a scenario where phenol red is the fluorophore, the exclusive factor that allows emission only in the presence of VSG'Y' is either the binding of phenol red to VSG'Y' or the influence that VSG'Y' exerts on the emission characteristics of the bound phenol red. So other VSGs either bind phenol red without triggering the emission of a detectable fluorescence or do not bind phenol red at all. The counter-scenario is that the observed fluorescence is emitted by VSG'Y' while the restrictions that make fluorescence emission unique to phenol red + VSG'Y' remain the same. It remains unknown at this point which of the two components is emitting the fluorescence and whether phenol red can bind to other VSGs while not expressing fluorescence.

The factors with the strongest impact on VSG'Y' fluorescence, judged by decreased emission delays and increased fluorescence intensities, were the cell density and the cell equilibration period on slides (Fig. 24 and 25). The emission delay decreased linearly with increasing cell densities. While the protein-to-cofactor ratio changed towards higher protein abundance at higher cell densities, counter regulation with increased amounts of PR had no influence. The more likely cause of improved emission is an increased metabolism of a medium component by higher cell numbers. A factor, which is yet to be identified, may have to be metabolised by cells in order to amplify fluorescence emission. Therefore, more cells can produce the required factor quicker and display shorter emission delays. Similarly, prolonged equilibration periods by cells on slides may lead to a similar result. Both factors had cumulative effects on emission and could compensate each other. It remains unknown, whether part of the cultivation medium is metabolised or if a metabolite is excreted from the cells that amplifies VSG fluorescence. Fluorescence experiments with medium depleted and acidified by long-term cell cultivation displayed faster fluorescence responses but also quicker quenching (Fig. 26). HPLC analysis of the depleted medium could not indicate phenol red metabolism (Fig. 28) since the experiment lacked the required sensitivity to detect the components of the cultivation medium and it should be considered to repeat the experiment with more sensitive detectors and concentrated medium samples. Acidification of depleted medium was reported by colour change of the pH indicator phenol red and could have influenced emission kinetics through a change of protonation of the pH indicator. Subsequent experiments with varying medium pH expressed individual kinetics for basic, neutral and acidic medium pH (Fig. 27). At very low pH values, phenol red exists as a zwitterion with a protonated ketone and a negatively charged sulphate group. With increasing pH values the net charge of the dye becomes more negative. The ketone is deprotonated when pH >1.2 is reached and the phenol's hydroxide group is deprotonated at pH >7.7. Kinetics are quickest at pH 6.0, meaning that phenol red binds and releases quickest with a single negative charge, followed by pH 9.0 with a net charge of -2. Considering that binding of PR to VSG'Y' may occur through interaction with charged residues, changing the PR protonation species can explain the different binding constants and thus different fluorescence kinetics, similar to those observed for the binding between albumin and PR (M. Lee & Debro, 1963). This is supported by the observation that a pH which promoted quick binding (indicated by faster kinetics) also led to earlier quenching and *vice versa* (Fig. 27). It should be noted however, that different kinetics were observed for pH 5.0, 6.0 and 7.5 even though the protonation species for phenol red at these pH values is the same. A change of the pH, especially towards strong basic and acidic values (5.0 and 9.0) may influence not only phenol red but the cell surface, the protonation of VSG'Y' (pI ≈ 6.9) and other components of the cultivation medium as well. Testing the pH influence with a simplified setup, e.g. purified VSG'Y' in an aqueous solution of phenol red may help to achieve clearer results.

High concentrations (≥20 mg/ml) of soluble VSG'Y' were able to generate fluorescence emission (Fig. 30). The signal increased semi-parabolically in a period of several seconds, similar to the time VSG'Y' expressing cells require to establish emission. Denaturation of protein samples extinguished emission, further showing that protein folding is important for fluorescence emission. Excitation of soluble VSG'Y' was accomplished both in FMix solution and HMI-9, albeit with sigmoidal kinetics for HMI-9 and semi-parabolic kinetics for FMix. Fluorescent components of HMI-9 (albumin and/or PR) express linear fluorescence kinetics in isolation. Sigmoidal kinetics indicate positive cooperative binding, where the affinity for a second substrate is improved by binding of the initial substrate. Non-sigmoidal kinetics were only observed for TDB-PR or the combination of FMix and either soluble VSG'Y', deceased trypanosomes or trypanosomes in 96-well-plates (Fig. 24, 26 and 30), with the latter potentially being an artefact by the combination of strong noise and a diffuse signal. Thus, a potential cooperative binding partner must be a component of HMI-9 other than PR and albumin. Non-sigmoidal kinetics for deceased cells and soluble VSG show, that the condition of the cell surface influences kinetics but is not required for fluorescence emission. Another possibility is, that an antagonistic effect instead of the cooperative binding is causing both the sigmoidal kinetics and the initial delay. This is indicated by the progression of fluorescence kinetics prior to the half-maximal intensity, which displays higher intensities for linear or semi-parabolic emission (see Fig. 30c) than for sigmoidal signals. In other words, the first half of a sigmoidal signal is weaker than other signal forms, and therefore has to represent an effect that antagonises fluorescence emission. A potential source for this effect could be the intact cell membrane, which quenches the initial signal through non-radiative energy transfer. Only once the constant excitation surpasses the quenching-capacity of the membrane, does fluorescence emission, and also photo-toxicity of unprotected samples occur. This would explain non-sigmoidal kinetics for soluble VSGs and dead cells and a lack of reproducibility through the use of pulsed excitation light.

In contrast to soluble VSG'Y', incorporation of VSG'Y' in artificial bilayers in cell surface densities led to no detectable fluorescence emission, independent of the used cultivation medium. A lack of detectable emission could have been caused by the combination of suboptimal excitation by the pulsed iMIC light source used for this experiment and a fluorescence emission that may be weaker than on the cell surface of trypanosomes. However, to confirm the correct incorporation of VSGs at cell surface concentrations into the artificial bilayer (by measuring VSG mobility), FRAP experiments were performed, that require the IMIC microscope setup. At this point it remains unknown whether VSGs can emit fluorescence from artificial bilayers, or which influence either the natural or artificial membrane has on emission. Meanwhile, fluorescence emission of soluble VSG could be detected with the more suitable Leica DMI 6000B setup and at substantially increased protein concentrations, leading to the conclusion that VSG'Y' should display emission independent of the chosen membrane system. Further experiments with artificial bilayers should be considered for the Leica microscope and at potentially higher protein concentrations.

Pre-excitation of cultivation medium did not influence fluorescence kinetics notably, unless excessive photon energy was applied. Prolonged exposure of HMI-9 and trypanosomes to unfiltered light from a mercury lamp resulted in a base fluorescence which could be excited immediately, but the excessive energy also resulted in the death of ≥90 % of cells and bleaching of the medium. In conclusion, the cultivation medium can not be charged by photon-energy to improve VSG'Y' emissions. Subsequent use of the bleached medium resulted in emission at approximately 20 % of the original intensity with normal kinetics. Pre-excitation with daylight or a desk lamp had no detectable influence on kinetics. The earlier observation of improved kinetics for on-slide cultivated trypanosomes was therefore not caused by pre-excitation, but some form of equilibration on slides during exposure with the surrounding atmosphere. A volume of approximately 1.8 μl may equilibrate relatively quickly to conditions of the surrounding atmosphere even when compressed between cover slip and microscopic slide. Additionally, settling of cells on the slide may have improved the fluorescence emission as well.

It is conceivable that the initial delay of the VSG'Y' emission is caused by phosphorescence. The photon energy that is taken up by the protein during excitation could cause a change of energy of a hull electron into a triplet state which radiates its phosphorescence with a substantial delay when it returns to the ground state. This could explain the initial delay and would also result in emissions that are detectable after excitation has been terminated. Recording of VSG'Y' emission at very high frame rates displayed a weak surface fluorescence that extinguished at the same frame at which excitation was stopped (Fig. 29). These recordings were conducted at 500 frames/s resulting in a frame time of 2 ms during which emission extinguished. Phosphorescence lifetimes usually range from milliseconds to hours rendering phosphorescence as a mechanism of VSG'Y' luminescence and as an explanation for emission delays unlikely.

Labelling of VSGs with molecules that attach to specific amino acids covalently may block the binding motif from TPM contact and could help to pinpoint the exact position of VSG-TPM-interaction. Sulfo-NHS compounds bind primary amines, e.g. in the side chain of lysine. Successful labelling of VSG'Y' with Sulfo-NHS-Biotin and -Atto labels was confirmed by surface localization of the fluorescent ATTO-488 label but had no influence on VSG'Y' emission. Thus the binding motif for TPMs could not be blocked by the attachment, suggesting that lysines and arginines are not involved in TPM binding. However, covalent binding of specific amino acids remains a sensible option to identify the region of VSG-TPM-interaction. For example, maleimide or pyridyl disulphides can be attached to cysteines and methionines and carbodiimides like EDC can be used to tag glutamic acid and aspartic acid.

Calorimetric analysis of the binding between PR and soluble VSG'Y' by isothermal titration calorimetry (ITC) should provide binding constants for the binding between PR and VSG'Y'. However, calorimetric analysis remained inconclusive, since no thermodynamic changes were detected by the successive addition of a 5-fold molar excess of PR to VSG'Y' (Fig. 31). The initial concentration of PR could have been chosen too high, resulting in immediate saturation. However, since initial molar ratios of below 1.0 were chosen, this seems unlikely, since fewer PR than VSG molecules were present. Alternatively, the binding of PR may require photo-activation of the binding-site, which may also explain the lack of TPM binding in MITat1.2 cocrystallisation trials even though a potential binding site was identified for this VSG during docking studies (Fig. 38). Further calorimetric studies and additional surface plasmon resonance energy transfer (PRET), which can identify cofactor binding and binding strength should be performed on a broader concentration range of TPM compounds and should include pre-excitation of proteins and cofactors. Both experiments should provide binding constants if applicable, thus unequivocally confirming or dismissing TPM binding. Additionally, cocrystallisation setups could be adapted to include fluorescence excitation to test for improved cofactor binding.

In summary, VSG fluorescence is based on the interaction between VSG'Y' and phenol red. Fluorescence emission can only be detected for the combination of VSG'Y' and PR and may involve specific non-radiative energy transfer between protein and cofactor, where the cofactor absorbs radiation energy, transfers this energy via resonance energy transfer to the protein which then emits fluorescence emission or *vice versa*. Neither live cells or intact cell membranes are required but improve intensities and change kinetics to progress sigmoidally, suggesting a cooperative binding with the outer surface of intact trypanosomes and components of HMI-9. However, it is possible that the same sigmoidal progression, and thus the initial emission delay, is caused by emission quenching, induced by non-radiative energy transfer through the cell membrane. The same energy transfer could also cause direct lipid peroxidation, resulting in cell damage. It still remains unclear whether the observed emission originates from protein fluorescence or, for example a blue-shift of PR fluorescence. It further remains unclear which factor is metabolised in the medium during experiments and whether it influences emission. Additional mass spectrometric analysis could shed light on the changes that occur in the medium during cultivation. The cause of the emission delay may involve complex interaction between protein, TPM and additional factors. Photo-excitation could be a prerequisite of TPM binding to VSGs which is further influenced by the present protonation states of PR. Further research should focus on a precise structural basis for VSG'Y' with support by mass spectrometric analysis of the changes in medium composition that accompany improved emission and by ITC and PRET binding studies.

5.3 The trypanocidal effect

Observation of the trypanocidal effect raised the questions whether BPB-binding and fluorescence emission use the same mechanisms as the fluorescence of VSG'Y' and phenol red. A major difference was the observation that no specific VSG was required on the cell surface to excite BPB-dependent fluorescence and to trigger the TE. Another indicator for a different working mechanisms was the difference in emission kinetics observed for BPB and PR. While the VSG'Y'fluorescence expressed a sigmoidal progression during excitation and eventual loss of intensity, the BPB induced emission increased linearly in the course of time with a quick fluorescence burst during the TE wave (Fig. 32). While the complex emission of VSG'Y' could be enhanced by multiple components, BPB emission was amplified only by BPB itself. Increasing the BPB concentration resulted in stronger emission and a quicker progression of the TE, while most of the typical factors for VSG'Y' emission, including cofactor concentration, cell density and TPM competition had no influence. This could be the case if the TE itself is independent of VSG binding. BPB in proximity to the cell surface may transfer absorbed photo-energy to H_2O molecules directly, forming hydroxyl radical that damage the cell membrane.

The characteristic fluorescence wave of the TE initiated mostly non-specifically at one spot along the cell surface with a minor tendency towards the flagellar pocket and spread evenly through the cell. The spot where the wave initiates is likely the point where most of the surface damage accumulated, which in turn could be influenced by local VSG- and BPB-density and the membrane environment. Proliferation of the wave was temporally separated between flagellum and cytoplasm, indicating a physical barrier for the wave formed by the cell membrane. When the cell membrane is ruptured, spots of fluorescent particles escape the cell surface of deceased cells (x in Fig. 32). This indicates that the fluorescence wave is not only produced along the cell membrane but involves particles within the cytosol. Cytosolic components are influenced by the initial rupture of the cell membrane, for example through the sudden breakdown of the membrane potential and produce a fluorescence wave that spreads outwards from the initial damage. Once the membrane damage is severe enough, fluorescent particles may leak through the ruptured membrane to the surrounding medium as observed in Fig. 32.

Increasing concentrations of the antioxidants trolox and ascorbic acid increased the delay between excitation of cells and the initiation of the fluorescence wave (Fig. 34). This suggests that oxidative stress caused the membrane damage that led to the TE. BPB particles could be excited by photon energy, producing hydroxyl radicals by non-radiative energy transfer, which in turn lead to fatty acid peroxidation of the cell membrane. Similar mechanisms that lead to lipid peroxidation and cell-toxicity are published for malachite green, which is a triphenylmethane compound similar to BPB (Panandiker *et al.*, 1992; Michaels & Lewis, 1985). Prolonged cultivation of cells on slides prior to experiments also led to an increased delay between excitation and TE (Fig. 34c). Equilibration of the medium may have led to increased antioxidative capacities and emission could have improved as observed for VSG'Y' (Fig. 24d), shifting energy transfer slightly from non-radiating to radiating exchanges. Addition of albumin led to a similar delay, but could also inhibit the TE completely. At high concentrations the fluorescence of albumin resulted in a strong signal in the surrounding medium that outshone cell fluorescence. The excess albumin quenched BPB excitation and thus radical formation and lipid peroxidation, while emitting strong fluorescence emission itself. This albumin fluorescence was in turn not sufficient to produce any detectable cell damage.

Cell motility diminished in the course of excitation until movement ceased during the onset of the TE. By supplementing the cell medium with antioxidants, the complete standstill of cells could be temporally separated from the TE, effectively inducing a photo-paralysis of irradiated cells. Upon switching to light outside the excitation wavelength of BPB, cells recovered motility that was indistinguishable from untreated cells after a short time. Possible explanations for the change of motility are phospholipid oxidation induced receptor inhibition (Erridge *et al.,* 2008) that could inhibit signal transduction along the flagellum or a loss of fatty acid fluidity (Alvarez & Storey, 1982; Sharma & Agarwal, 1996). Furthermore, uncoupling of the membrane potential or of oxidative phosphorylation, similar to the effects described for the TPM crystal violet (Docampo *et al.,* 1993; Moreno *et al.,* 1988) could cause the temporary loss of motility. The recovery of unimpaired motility within 10 s implies that no permanent damage is caused until membrane rupture and the subsequent TE are induced.

In summary, the TE seems to be functionally distinctive from VSG'Y' fluorescence due to significant differences in fluorescence kinetics and it's influencing factors. The damage that is caused to the cell can most likely be attributed to excitation-induced radical formation and subsequent damage to the cell membrane, while the fluorescence wave could be induced by a breakdown of the membrane potential during membrane rupture. Radical formation and subsequent membrane damage could be caused by non-radiative energy transfer from BPB molecules in membrane proximity that are not necessarily bound to VSG molecules, which would also explain the independence of the TE for a specific VSG on the cell surface. Until the membrane ruptures, damage seems to be reversible. The open questions that remain are, whether the TE and VSG'Y' fluorescence share mechanisms for binding and energy transfer. Further research needs to focus on the identification of the exact mechanism of BPB energy transfer and whether binding between BPB and VSGs takes place. This can be achieved, for example by testing of procyclic cells for the TE, which do not express VSGs on their cell surface. Additionally, cocrystallisation of VSGs and TPMs remains important in identifying potential binding.

5.4 Fluorescence of VSG'Y' mutants

The fact that both phenol red and the protein VSG'Y' are required for VSG fluorescence emission suggest direct interaction between the pH indicator and the protein. In the course of this thesis, two possible mechanisms were formulated to describe this interaction: Due to the poly-aromatic structure of TPMs it is plausible that phenol red binds to aromatic amino acids in VSG'Y' via π-stacking. And since no other combination of TPMs and VSGs expresses similar fluorescence emission, the binding motif has to be highly specific, further indicating aromatic interaction rather than unspecific electrostatic interaction of charged residues. The second potential mechanism involves interaction with charged residues in a specific binding motif located in the dimerisation surface of the NTD dimer. It should be noted, that the later mechanism was formulated at a time point when mutational analysis was already concluded and was not considered in the experiments discussed here.

To identify potential targets in VSG'Y' for TPM binding, homology modelling of the VSG'Y' sequence and the structure of MITat1.2 was done. Even though the sequence identities betweens VSGs of known structure are low, their models suggest that the tertiary structure between VSGs, or at least type A NTDs, is highly conserved (D. Freymann *et al.,* 1990; M. L. Blum *et al.*, 1993). Aromatic residues with surface access along the NTD of VSG'Y' were chosen from the alignment and changed conservatively into phenylalanine or tryptophan or non-conservatively into alanine or isoleucine (Fig. 35) to remove the aromatic character of that position.

Following transfection, VSG mutant cell lines expressed severe sensitivity during cultivation that resulted in impaired cell growth (Fig. 37). While most individual cells still appeared vital, judged by cell motility, cultures displayed population doubling times that increased by several hours. This effect was most severe following culture dilution with fresh medium and antibiotics and normalized after approximately 24 h of cultivation. This sensitivity was still observed after 10 days of cultivation. Whether this sensitivity was caused by antibiotics or a late effect of cell electroporation could not be identified. Reducing concentrations of antibiotic selection might restore cell growth but also reduces selectivity towards successful transfectants and was not considered an option. It should be noted that the pLew82v4 construct was used by other members of the lab without similar recurring signs of growth retardation. Additionally, following induction, many of the clones that display growth impairment displayed VSG'Y' expression, which was determined by surface fluorescence, indicating that insertion of the construct worked as expected and was not a cause for the delay in cell growth. It was observed during the time of this thesis that *in vitro* cultivated trypanosomes tend to react sensitive to changes in medium composition, mostly originating from a variance between FCS batches. A change of FCS batches had a major impact in high-density cultivation of trypanosomes and may also explain the early growth-retardation of freshly cultivated VSG'Y' mutants and the sensitivity following cell dilutions. However, cultures should eventually adapt to the fresh batch of FCS, resulting in doubling times of approx. 8 h, which was not always the case. The display of surface fluorescence of most mutants suggest that the problem is caused during cell cultivation rather than transfection.

Initial identification of transfectants was conducted by the detection of fluorescence emission of the expressed VSG'Y' mutants. If emission could still be detected the mutation was non-relevant for TPM binding and had no influence on protein expression. Subsequently, and in the absence of emission, western-blot and immunofluorescence staining were conducted to make sure that protein mutants were expressed and that the lack of fluorescence was a result of a loss-of-function-mutation of the TPM binding site. Mutants F8W, W11F, Y121A, W254F, Y269A, W329F and W475F still displayed normal fluorescence emission 24 h after induction of the exogenous VSG (Fig. 36a), identifying each of the original residues as non-relevant for the binding of phenol red. Mutant F8I displayed no emission, which resulted from untraceable VSG'Y' expression, identified by western-blot analysis of the induced mutant cell line (Fig. 36c). As a consequence no VSG'Y' could be detected by immunofluorescence staining of the cell surface (Fig. 36b). Thus, the lack of emission from F8I is a result of missing protein expression. In comparison, the conservative exchange of phenylalanine into tryptophan in mutant F8W resulted in normal fluorescence emission. This shows that position 8 can readily be modified and a conservative amino acid exchange retains normal protein function, whereas removal of the aromatic character could exert detrimental effects on either TPM binding or protein folding. However, the lack of signal during western-blot suggests that transfection was unsuccessful.

Docking studies conducted with SwissDock and the alignment of the VSG'Y' sequence to the MITat1.2 structure suggest that potential binding occurs between PR and charged residues Lys, Arg, His, Glu and Asp (Fig. 38). The most abundantly occupied position is a pocket formed between residues Glu109, Arg115 and Lys246 along the dimerisation surface of the NTD. Thus binding of PR to this pocket may require the formation of intact VSG dimers, which is naturally the case on the cell surface but which can be compromised, for example by denaturation of the VSG. Simulations also indicated that aromatic amino acids are not involved in PR binding and that the motif formed by F8 and W11 is sterically inaccessible for phenol red. This inaccessibility was indicated by the size of the TPM compound and the compact structure of the VSG NTD (Fig. 38), which would require protein deformation to enable contact. Additional studies with BPB indicate binding to the same motif as PR in VSG'Y'. The observed diminishing of VSG'Y' emission during coincubation of PR with BPB (Fig. 29a) supports the idea of a shared binding motif, which is competitively blocked by BPB. Docking studies conducted with published VSG structures reveal no binding for MITat1.1, while ILTat1.24 and MITat1.2 show PR binding to a motif at the dimerisation surface close to the N-terminal domain end that is similar to the position in VSG'Y'. These findings suggest that binding of TPMs is not exclusive for VSG'Y'. However, binding of TPMs alone is not sufficient to establish fluorescence emission and requires energy transfer that may be unique for VSG'Y' and PR. Also, while BPB may competitively bind to VSGs, the trypanocidal effect may work independently, since trypanosomes expressing MITat1.1 display the trypanocidal effect while not indicating TPM binding during docking. Non-radiative energy transfer does not require direct binding between donor and acceptor and bromophenol blue may cause direct lipid peroxidation from the membrane vicinity without necessarily binding to a VSG.

26 aromatic amino acids are available for mutation in VSG'Y' in addition to the 7 positions that were tested in this thesis. Production and testing of the remaining mutants may be sensible, but would be time- and resource-consuming without a more educated guess about the residues involved in binding. Additionally, no binding of TPMs to VSGs could be detected in either crystallographic trials or isothermal titration calorimetry, which were conducted in parallel. As stated before, this could be explained by the requirement of photo-excitation to enable binding between TPMs and VSGs. This would also explain the delay that is observed in fluorescence emission of VSG'Y'. Docking studies with SwissDock also suggest ionic- or Van-der-Waals interaction instead of π-stacking. If this were the case, mutation of aromatic amino acids could influence protein folding, but would exert no influence on TPM binding otherwise. Additionally, the homology modelling of VSG'Y' is only a structural approximation. A difference in protein folding caused by single amino acid exchanges could already result in side chains that are not exposed to the surface of the protein but buried within the protein structure

and thus inaccessible. At this point the construction of additional VSG'Y' mutants was postponed until more solid information about the potential binding motif in VSG'Y' could be acquired.

The results of the docking experiments would explain why none of the mutants influenced protein fluorescence. While these simulations are used frequently, e.g. in drug screening, they are completely *in silico* based and should be cross referenced with additional docking tools and experimental approaches including mutational analysis. Future mutational experiments of VSG'Y' should include residues that are involved in the formation of the binding motif in the dimerisation surface of the NTD, which was identified in docking studies.

In Summary, while analysis of VSG'Y' mutants was affected by impaired cultivation of individual clones, the combination of cell fluorescence, western-blot and immunofluorescence analysis has shown that the chosen mutations do not affect TPM binding. It remains uncertain whether aromatic amino acids are key in TPM binding, or whether other mechanisms, including electrostatic interactions are involved. However, so long as binding involves specific motifs, it should be identifiable by means of single amino acid exchange. A prerequisite for further mutational analysis is a confirmation of TPM binding, for example by means of ITC or PRET and a better understanding of the location and mechanism of the binding through structural analysis.

6 Abbreviations

AEC	anion exchange chromatography
AFM	atomic force microscopy
BCG	bromocresol green
BCP	bromocresol purple
BESSY	Berliner Elektronenspeicherring-Gesellschaft für Synchrotronstrahlung
BPB	bromophenol blue
BPR	bromophenol red
BSA	bovine serum albumin
BSF	bloodstream form
cm^2	square centimeter
CPR	chlorophenol red
CR	cresol red
CTD	C-terminal domain
DAPI	4′,6-Diamidin-2-phenylindol
ddH_2O	double distilled water
D_{max}	maximum dimension
ESRF	European Sychrotron Radiation Facility
FCS	fetal calf serum
g	acceleration relative to earth gravitation
GFP	green fluorescent protein
GPI	glycophosphatidylinositol
GPI-PLC	GPI-specific phospholipase C
h	hours
HAT	Human african trypanosomiasis
HMI-9	Hirumi's modified Iscove's medium 9
HPLC	high precision liquid chromatography
ILTat	ILRAD Trypanozoon antigen type
IMR	isomorphus replacement
$I(0)$	zero-angle scattering intensity
kDa	kilodalton
LB	Luria Bertani
M	molar
mA	miliampere
mAU	milliabsorbance units
mfVSG	membane form variant surface glycoprotein
min	minute
MITat	Molteno Institute Trypanozoon antigen type
MR	molecular replacement
MW	megawatt
NHS	N-hydroxysulfosuccinimide

nl	nanoliter
NMR	nuclear magnetic resonance
NTD	N-terminal domain
PAGE	polyacrylamide gel electrophoresis
PBS	phosphate buffered saline
PCF	procyclic form
pdb	protein database
PEG	polyethylene glycol
PFR	paraflagellar rod
POI	protein of interest
PR	phenol red
$P(r)$	pair-distance distribution function
R_g	radius of gyration
rpm	revolutions per minute
RVZ	Rudolf-Virchov-Zentrum
SAS	saturated ammonium sulfate
SAXS	small angle x-ray scattering
SDS	sodium dodecyle sulfate
SEC	size exclusion chromatography
sVSG	soluble form variant surface glycoprotein
TB	thymol blue
TDB	trypanosome dilution buffer
TE	trypanocidal effect
TFA	trifluor acetic acid
TLCK	Nα-Tosyl-L-lysinchlormethylketon-Hydrochlorid
TPM	triphenylmethane
T.b.	Trypanosoma brucei
V	volt
v/v	volume per colume
VMD	visual molecular dynamics
VSG	variant surface glycoprotein
VSG'Y'	yellow fluorescent variant surface glycoprotein
w/v	weight per volume
Å	angstroms
μg	microgram
μm	micrometer
°C	degree celsius

7 References

References

1. Adams, P. D. *et al.* PHENIX: a comprehensive Python-based system for macromolecular structure solution. *Acta Crystallogr. D Biol. Crystallogr.* **66,** 213–221 (Feb. 2010).
2. Aitcheson, N. *et al.* VSG switching in *Trypanosoma brucei*: antigenic variation analysed using RNAi in the absence of immune selection. *Mol. Microbiol.* **57,** 1608–1622 (Sept. 2005).
3. Alvarez, J. G. & Storey, B. T. Spontaneous lipid peroxidation in rabbit epididymal spermatozoa: its effect on sperm motility. *Biol. Reprod.* **27,** 1102–1108 (Dec. 1982).
4. Auffret, C. A. & Turner, M. J. Variant specific antigens of *Trypanosoma brucei* exist in solution as glycoprotein dimers. *Biochem. J.* **193,** 647–650 (Feb. 1981).
5. Bangs, J. D., Doering, T. L., Englund, P. T. & Hart, G. W. Biosynthesis of a variant surface glycoprotein of *Trypanosoma brucei*. Processing of the glycolipid membrane anchor and N-linked oligosaccharides. *J. Biol. Chem.* **263,** 17697–17705 (Nov. 1988).
6. Bartossek, T. *Structural analysis of* Trypanosoma brucei *variant surface glycoprotein MITat1.6 by X-ray crystallography.* Diploma thesis (Lehrstuhl für Zell- und Entwicklungsbiologie, Universität Würzburg, May 2011).
7. Batram, C., Jones, N. G., Janzen, C. J., Markert, S. M. & Engstler, M. Expression site attenuation mechanistically links antigenic variation and development in *Trypanosoma brucei*. *Elife* **3,** e02324 (2014).
8. Becker, M. *et al.* Isolation of the repertoire of VSG expression site containing telomeres of *Trypanosoma brucei* 427 using transformation-associated recombination in yeast. *Genome Res.* **14,** 2319–2329 (Nov. 2004).
9. Bernadó, P., Mylonas, E., Petoukhov, M. V., Blackledge, M. & Svergun, D. I. Structural characterization of flexible proteins using small-angle X-ray scattering. *J. Am. Chem. Soc.* **129,** 5656–5664 (May 2007).
10. Berriman, M. *et al.* The genome of the African trypanosome *Trypanosoma brucei*. *Science* **309,** 416–422 (July 2005).
11. Blum, M. L. *et al.* A structural motif in the variant surface glycoproteins of *Trypanosoma brucei*. *Nature* **362,** 603–609 (Apr. 1993).
12. Böhme, U. & Cross, G. A. Mutational analysis of the variant surface glycoprotein GPI-anchor signal sequence in *Trypanosoma brucei*. *J. Cell. Sci.* **115,** 805–816 (Feb. 2002).
13. Bruce, D. *Preliminary report on the tsetse fly disease or nagana in Zululand* 1895.
14. Brun, R. & Blum, J. Human African trypanosomiasis. *Infect. Dis. Clin. North. Am.* **26,** 261–273 (June 2012).
15. Caffrey, M. & Cherezov, V. Crystallizing membrane proteins using lipidic mesophases. *Nat. Protoc.* **4,** 706–731 (2009).

16. Cardoso de Almeida, M. L. & Turner, M. J. The membrane form of variant surface glycoproteins of *Trypanosoma brucei*. *Nature* **302,** 349–352 (1983).

17. Carrington, M. & Boothroyd, J. Implications of conserved structural motifs in disparate trypanosome surface proteins. *Mol. Biochem. Parasitol.* **81,** 119–126 (Oct. 1996).

18. Carrington, M., Miller, N., *et al.* Variant specific glycoprotein of *Trypanosoma brucei* consists of two domains each having an independently conserved pattern of cysteine residues. *J. Mol. Biol.* **221,** 823–835 (Oct. 1991).

19. Chattopadhyay, A. *et al.* Structure of the C-terminal domain from *Trypanosoma brucei* variant surface glycoprotein MITat1.2. *J. Biol. Chem.* **280,** 7228–7235 (Feb. 2005).

20. Cowtan, K. The Buccaneer software for automated model building. 1. Tracing protein chains. *Acta Crystallogr. D Biol. Crystallogr.* **62,** 1002–1011 (Sept. 2006).

21. Cross, G. A. Identification, purification and properties of clone-specific glycoprotein antigens constituting the surface coat of *Trypanosoma brucei*. *Parasitology* **71,** 393–417 (Dec. 1975).

22. Cross, G. A. Release and purification of *Trypanosoma brucei* variant surface glycoprotein. *J. Cell. Biochem.* **24,** 79–90 (1984).

23. De Maria Antolinos, A. *et al.* ISPyB for BioSAXS, the gateway to user autonomy in solution scattering experiments. *Acta Crystallogr. D Biol. Crystallogr.* **71,** 76–85 (Jan. 2015).

24. Docampo, R. *et al.* Disruption of Ca2+ homeostasis in *Trypanosoma cruzi* by crystal violet. *J. Eukaryot. Microbiol.* **40,** 311–316 (1993).

25. Dodson, E. The befores and afters of molecular replacement. *Acta Crystallogr. D Biol. Crystallogr.* **64,** 17–24 (Jan. 2008).

26. *Crystallization of Nucleic Acids and Proteins: A Practical Approach (Practical Approach Series)* 2nd ed. (eds Ducruix, A. & Giegé, R.) ISBN: 9780199636785 (Oxford University Press, USA, Jan. 2000).

27. Emsley, P., Lohkamp, B., Scott, W. G. & Cowtan, K. Features and development of Coot. *Acta Crystallogr. D Biol. Crystallogr.* **66,** 486–501 (Apr. 2010).

28. Engstler, M. *et al.* Hydrodynamic flow-mediated protein sorting on the cell surface of trypanosomes. *Cell* **131,** 505–515 (Nov. 2007).

29. Erb, E. M., Tangemann, K., Bohrmann, B., Müller, B. & Engel, J. Integrin alphaIIb beta3 reconstituted into lipid bilayers is nonclustered in its activated state but clusters after fibrinogen binding. *Biochemistry* **36,** 7395–7402 (June 1997).

30. Erridge, C., Kennedy, S., Spickett, C. M. & Webb, D. J. Oxidized phospholipid inhibition of toll-like receptor (TLR) signaling is restricted to TLR2 and TLR4: roles for CD14, LPS-binding protein, and MD2 as targets for specificity of inhibition. *J. Biol. Chem.* **283,** 24748–24759 (Sept. 2008).

31. Evans, P. R. Scaling and assessment of data quality. *Acta Crystallogr. D Biol. Crystallogr.* **62,** 72–82 (Jan. 2006).

32. Evans, P. R. An introduction to data reduction: space-group determination, scaling and intensity statistics. *Acta Crystallogr. D Biol. Crystallogr.* **67,** 282–292 (Apr. 2011).

33. Ewald, P. P. Zur Theorie der Interferenzen der Röntgentstrahlen in Kristallen. *Physik. Z.* **14,** 465–472 (1913).

34. Ferguson, M. A., Haldar, K. & Cross, G. A. *Trypanosoma brucei* variant surface glycoprotein has a sn-1,2-dimyristyl glycerol membrane anchor at its COOH terminus. *J. Biol. Chem.* **260,** 4963–4968 (Apr. 1985).

35. Freymann, D. M., Metcalf, P., Turner, M. & Wiley, D. C. 6 Å-resolution X-ray structure of a variable surface glycoprotein from *Trypanosoma brucei*. *Nature* **311,** 167–169 (1984).

36. Freymann, D. *et al.* 2.9 Å resolution structure of the N-terminal domain of a variant surface glycoprotein from *Trypanosoma brucei*. *J. Mol. Biol.* **216,** 141–160 (Nov. 1990).

37. Ghosh, E., Kumari, P., Jaiman, D. & Shukla, A. K. Methodological advances: the unsung heroes of the GPCR structural revolution. *Nat. Rev. Mol. Cell Biol.* **16,** 69–81 (Feb. 2015).

38. Grosdidier, A., Zoete, V. & Michielin, O. SwissDock, a protein-small molecule docking web service based on EADock DSS. *Nucleic Acids Res.* **39,** W270–277 (July 2011).

39. Grünfelder, C. G. *et al.* Accumulation of a GPI-anchored protein at the cell surface requires sorting at multiple intracellular levels. *Traffic* **3,** 547–559 (Aug. 2002).

40. Hartel, A. J. *et al.* N-glycosylation enables high lateral mobility of GPI-anchored proteins at a molecular crowding threshold. *Nat. Commun.* **7,** 12870 (Sept. 2016).

41. Henikoff, S. & Henikoff, J. G. Amino acid substitution matrices from protein blocks. *Proc. Natl. Acad. Sci. U S A* **89,** 10915–10919 (Nov. 1992).

42. Hermann, A. *Optimisation of* Trypanosoma brucei *cell cultivation.* Diploma thesis (Institut für Mikrobiologie und Genetik, Technische Universität Darmstadt, Aug. 2008).

43. Hertz-Fowler, C. *et al.* Telomeric expression sites are highly conserved in *Trypanosoma brucei*. *PLoS ONE* **3,** e3527 (2008).

44. Higgins, M. K. *et al.* Structure of the trypanosome haptoglobin-hemoglobin receptor and implications for nutrient uptake and innate immunity. *Proc. Natl. Acad. Sci. U S A* **110,** 1905–1910 (Jan. 2013).

45. Hirumi, H. & Hirumi, K. Continuous cultivation of *Trypanosoma brucei* blood stream forms in a medium containing a low concentration of serum protein without feeder cell layers. *J. Parasitol.* **75,** 985–989 (Dec. 1989).

46. Holton, J. M. & Frankel, K. A. The minimum crystal size needed for a complete diffraction data set. *Acta Crystallogr. D Biol. Crystallogr.* **66,** 393–408 (Apr. 2010).

47. Hu, B. *et al.* Intervesicle cross-linking with integrin alpha IIb beta 3 and cyclic-RGD-lipopeptide. A model of cell-adhesion processes. *Biochemistry* **39,** 12284–12294 (Oct. 2000).

48. Humphrey, W., Dalke, A. & Schulten, K. VMD: visual molecular dynamics. *J. Mol. Graph.* **14,** 33–38 (Feb. 1996).

49. Jackson, D. G., Owen, M. J. & Voorheis, H. P. A new method for the rapid purification of both the membrane-bound and released forms of the variant surface glycoprotein from *Trypanosoma brucei*. *Biochem. J.* **230,** 195–202 (Aug. 1985).

50. Jauncey, G. E. The Scattering of X-Rays and Bragg's Law. *Proc. Natl. Acad. Sci. U S A* **10,** 57–60 (Feb. 1924).

51. Jones, N. G. *et al.* Structure of a glycosylphosphatidylinositol-anchored domain from a trypanosome variant surface glycoprotein. *J. Biol. Chem.* **283,** 3584–3593 (Feb. 2008).

52. Kennedy, P. G. Human African trypanosomiasis: in and out of Africa. *Neurology* **66,** 962–963 (Apr. 2006).

53. Kikhney, A. G. & Svergun, D. I. A practical guide to small angle X-ray scattering (SAXS) of flexible and intrinsically disordered proteins. *FEBS Lett.* **589,** 2570–2577 (Sept. 2015).

54. Konarev, p. V. & Petoukhov M. V. amd Svergun, D. I. MASSHA - a graphics system for rigid-body modelling of macromolecular complexes against solution scattering data. *J. Appl. Crystallogr.* **34,** 527–532 (2001).

55. Konarev, P. V., Volkov, V. V., Sokolova, A. V., Koch, M. H. J. & Svergun, D. I. PRIMUS: a Windows PC-based system for small-angle scattering data analysis. *J. Appl. Crystallogr.* **36,** 1277–1282 (2003).

56. Kragh-Hansen, U. Effects of aliphatic fatty acids on the binding of Phenol Red to human serum albumin. *Biochem. J.* **195,** 603–613 (June 1981).

57. Krug, M., Weiss, M. S., Heinemann, U. & Mueller, U. XDSAPP: a graphical user interface for the convenient processing of diffraction data using XDS. *J. Appl. Crystallogr.* **45,** 568–572 (2012).

58. Kyte, J. & Doolittle, R. F. A simple method for displaying the hydropathic character of a protein. *J. Mol. Biol.* **157,** 105–132 (May 1982).

59. Laemmli, U. K. Cleavage of structural proteins during the assembly of the head of bacteriophage T4. *Nature* **227,** 680–685 (Aug. 1970).

60. Lane-Serff, H., MacGregor, P., Lowe, E. D., Carrington, M. & Higgins, M. K. Structural basis for ligand and innate immunity factor uptake by the trypanosome haptoglobin-haemoglobin receptor. *Elife* **3,** e05553 (2014).

61. Langer, G., Cohen, S. X., Lamzin, V. S. & Perrakis, A. Automated macromolecular model building for X-ray crystallography using ARP/wARP version 7. *Nat. Protoc.* **3,** 1171–1179 (2008).

62. Lee, M. & Debro, J. R. The application of gel filtration to the measurement of the binding of phenol red by human serum proteins. *J. Chromatogr.* **10,** 68–72 (Jan. 1963).

63. Lee, Y. C. & Montgomery, R. Glycopeptides from ovalbumin: the structure of the peptide chains. *Arch. Biochem. Biophys.* **97,** 9–17 (Apr. 1962).

64. Leslie, A. G. & Powell, H. R. Processing diffraction data with mosflm. *Evolving Methods for Macromolecular Crystallography* **245,** 41–51 (2007).

65. Ligtenberg, M. J. *et al.* Reconstitution of a surface transferrin binding complex in insect form *Trypanosoma brucei*. *EMBO J.* **13,** 2565–2573 (June 1994).

66. *Bioanalytik (German Edition)* 2nd ed. (eds Lottspeich, F., Engels, J. W. & Lay, S. Z.) ISBN: 9783827415202 (Spektrum Akademischer Verlag, Dec. 2008).

67. Macaskill, J. A., Holmes, P. H., Jennings, F. W. & Urquhart, G. M. Immunological clearance of 75Se-labelled *Trypanosoma brucei* in mice. III. Studies in animals with acute infections. *Immunology* **43,** 691–698 (Aug. 1981).

68. MacGregor, P., Savill, N. J., Hall, D. & Matthews, K. R. Transmission stages dominate trypanosome within-host dynamics during chronic infections. *Cell Host Microbe* **9,** 310–318 (Apr. 2011).

69. Manthri, S., Güther, M. L., Izquierdo, L., Acosta-Serrano, A. & Ferguson, M. A. Deletion of the TbALG3 gene demonstrates site-specific N-glycosylation and N-glycan processing in *Trypanosoma brucei*. *Glycobiology* **18,** 367–383 (May 2008).

70. Marcello, L. & Barry, J. D. Analysis of the VSG gene silent archive in *Trypanosoma brucei* reveals that mosaic gene expression is prominent in antigenic variation and is favored by archive substructure. *Genome Res.* **17,** 1344–1352 (Sept. 2007).

71. McCoy, A. J. *et al.* Phaser crystallographic software. *J. Appl. Crystallogr.* **40,** 658–674 (Aug. 2007).

72. McLintock, L. M., Turner, C. M. & Vickerman, K. Comparison of the effects of immune killing mechanisms on *Trypanosoma brucei* parasites of slender and stumpy morphology. *Parasite Immunol.* **15,** 475–480 (Aug. 1993).

73. Mehlert, A., Zitzmann, N., Richardson, J. M., Treumann, A. & Ferguson, M. A. The glycosylation of the variant surface glycoproteins and procyclic acidic repetitive proteins of *Trypanosoma brucei*. *Mol. Biochem. Parasitol.* **91,** 145–152 (Mar. 1998).

74. Merzel, F. & Smith, J. C. Is the first hydration shell of lysozyme of higher density than bulk water? *Proc. Natl. Acad. Sci. U.S.A.* **99,** 5378–5383 (Apr. 2002).

75. Michaels, G. B. & Lewis, D. L. Sorption and toxicity of azo and triphenylmethane dyes to aquatic microbial populations. *Environ. Toxicol. Chem.* **4,** 45–50 (Feb. 1985).

76. Moreno, S. N., Gadelha, F. R. & Docampo, R. Crystal violet as an uncoupler of oxidative phosphorylation in rat liver mitochondria. *J. Biol. Chem.* **263,** 12493–12499 (Sept. 1988).

77. Murshudov, G. N., Vagin, A. A. & Dodson, E. J. Refinement of macromolecular structures by the maximum-likelihood method. *Acta Crystallogr. D Biol. Crystallogr.* **53,** 240–255 (May 1997).

78. Navarro, M. & Cross, G. A. DNA rearrangements associated with multiple consecutive directed antigenic switches in *Trypanosoma brucei*. *Mol. Cell. Biol.* **16,** 3615–3625 (July 1996).

79. Needleman, S. B. & Wunsch, C. D. A general method applicable to the search for similarities in the amino acid sequence of two proteins. *J. Mol. Biol.* **48,** 443–453 (Mar. 1970).

80. Panandiker, A., Fernandes, C. & Rao, K. V. The cytotoxic properties of malachite green are associated with the increased demethylase, aryl hydrocarbon hydroxylase and lipid peroxidation in primary cultures of Syrian hamster embryo cells. *Cancer Lett.* **67,** 93–101 (Dec. 1992).

81. Penchenier, L. *et al.* Spontaneous cure of domestic pigs experimentally infected by *Trypanosoma brucei gambiense*. Implications for the control of sleeping sickness. *Vet. Parasitol.* **133,** 7–11 (Oct. 2005).

82. Petoukhov, M. V., Franke, D., *et al.* New developments in the ATSAS program package for small-angle scattering data analysis. *J. Appl. Crystallogr.* **45,** 342–350 (Apr. 2012).

83. Petoukhov, M. V., Konarev, P. V., Kikhney, A. G. & Svergun, D. I. ATSAS 2.1 - towards automated and web-supported small-angle scattering data analysis. *J. Appl. Crystallogr.* **40,** 223–228 (2007).

84. Petoukhov, M. V. & Svergun, D. I. Global rigid body modeling of macromolecular complexes against small-angle scattering data. *Biophys. J.* **89,** 1237–1250 (Aug. 2005).

85. Pettersen, E. F. *et al.* UCSF Chimera–a visualization system for exploratory research and analysis. *J. Comput. Chem.* **25,** 1605–1612 (Oct. 2004).

86. Roge, S. *et al.* Recombinant expression of trypanosome surface glycoproteins in *Pichia pastoris* for the diagnosis of *Trypanosoma evansi* infection. *Vet. Parasitol.* **197,** 571–579 (Nov. 2013).

87. Ross, R. & Thomason, D. A Case of Sleeping Sickness Studied by Precise Enummerative Methods: Regular Periodical Increase of the Parasites Disclosed. *Proc. Biol. Sci.* **82,** 411–415 (July 1910).

88. Rotureau, B., Subota, I., Buisson, J. & Bastin, P. A new asymmetric division contributes to the continuous production of infective trypanosomes in the tsetse fly. *Development* **139,** 1842–1850 (May 2012).

89. Round, A. R. *et al.* Automated sample-changing robot for solution scattering experiments at the EMBL Hamburg SAXS station X33. *J. Appl. Crystallogr.* **41,** 913–917 (Oct. 2008).

90. Russell, R. B. & Barton, G. J. Multiple protein sequence alignment from tertiary structure comparison: assignment of global and residue confidence levels. *Proteins* **14,** 309–323 (Oct. 1992).

91. Salmon, D. *et al.* Characterization of the ligand-binding site of the transferrin receptor in *Trypanosoma brucei* demonstrates a structural relationship with the N-terminal domain of the variant surface glycoprotein. *EMBO J.* **16,** 7272–7278 (Dec. 1997).
92. Schwede, A., Macleod, O. J., MacGregor, P. & Carrington, M. How Does the VSG Coat of Bloodstream Form African Trypanosomes Interact with External Proteins? *PLoS Pathog.* **11,** e1005259 (Dec. 2015).
93. Seyfang, A., Mecke, D. & Duszenko, M. Degradation, recycling, and shedding of *Trypanosoma brucei* variant surface glycoprotein. *J. Protozool.* **37,** 546–552 (1990).
94. Sharma, R. K. & Agarwal, A. Role of reactive oxygen species in male infertility. *Urology* **48,** 835–850 (Dec. 1996).
95. Steverding, D. *et al.* ESAG 6 and 7 products of *Trypanosoma brucei* form a transferrin binding protein complex. *Eur. J. Cell Biol.* **64,** 78–87 (June 1994).
96. Strang, A. M., Allen, A. K., Holder, A. A. & van Halbeek, H. The carbohydrate structures of *Trypanosoma brucei brucei* MITat 1.6 variant surface glycoprotein. A re-investigation of the C-terminal glycan. *Biochem. Biophys. Res. Commun.* **196,** 1430–1439 (Nov. 1993).
97. Sullivan, L., Wall, S. J., Carrington, M. & Ferguson, M. A. Proteomic selection of immunodiagnostic antigens for human African trypanosomiasis and generation of a prototype lateral flow immunodiagnostic device. *PLoS Negl. Trop. Dis.* **7,** e2087 (2013).
98. Svergun, D. I. Determination of the regularization parameter in indirect-transform methods using perceptual criteria. *J. Appl. Crystallogr.* **25,** 495–503 (1992).
99. Svergun, D. I. Restoring low resolution structure of biological macromolecules from solution scattering using simulated annealing. *Biophys. J.* **76,** 2879–2886 (June 1999).
100. Svergun, D. I., Barberato, C. & Koch, M. H. J. CRYSOL - a Program to Evaluate X-ray Solution Scattering of Biological Macromolecules from Atomic Coordinates. *J. Appl. Crystallogr.* **28,** 768–773 (1995).
101. Svergun, D. I., Richard, S., *et al.* Protein hydration in solution: experimental observation by x-ray and neutron scattering. *Proc. Natl. Acad. Sci. U.S.A.* **95,** 2267–2272 (Mar. 1998).
102. Tria, G., Mertens, H. D., Kachala, M. & Svergun, D. I. Advanced ensemble modelling of flexible macromolecules using X-ray solution scattering. *IUCrJ.* **2,** 207–217 (Mar. 2015).
103. Van Den Abbeele, J., Claes, Y., van Bockstaele, D., Le Ray, D. & Coosemans, M. *Trypanosoma brucei* spp. development in the tsetse fly: characterization of the post-mesocyclic stages in the foregut and proboscis. *Parasitology* **118 (Pt 5),** 469–478 (May 1999).

104. Vanhamme, L., Lecordier, L. & Pays, E. Control and function of the bloodstream variant surface glycoprotein expression sites in *Trypanosoma brucei*. *Int. J. Parasitol.* **31,** 523–531 (May 2001).

105. Vassella, E. & Boshart, M. High molecular mass agarose matrix supports growth of bloodstream forms of pleomorphic Trypanosoma brucei strains in axenic culture. *Mol. Biochem. Parasitol.* **82,** 91–105 (Nov. 1996).

106. Vickerman, K. On the surface coat and flagellar adhesion in trypanosomes. *J. Cell. Sci.* **5,** 163–193 (July 1969).

107. Volkov, V. V. & Svergun, D. I. Uniqueness of ab initio shape determination in small-angle scattering. *J. Appl. Crystallogr.* **36,** 860–864 (2003).

108. Vonrhein, C. *et al.* Data processing and analysis with the autoPROC toolbox. *Acta Crystallogr. D Biol. Crystallogr.* **67,** 293–302 (Apr. 2011).

109. Winn, M. D. *et al.* Overview of the CCP4 suite and current developments. *Acta Crystallogr. D Biol. Crystallogr.* **67,** 235–242 (Apr. 2011).

110. Wirtz, E., Leal, S., Ochatt, C. & Cross, G. A. A tightly regulated inducible expression system for conditional gene knock-outs and dominant-negative genetics in *Trypanosoma brucei*. *Mol. Biochem. Parasitol.* **99,** 89–101 (Mar. 1999).

111. Wriggers, W. Using Situs for the integration of multi-resolution structures. *Biophys. Rev.* **2,** 21–27 (Feb. 2010).

112. Zamze, S. E. *et al.* Characterisation of the asparagine-linked oligosaccharides from *Trypanosoma brucei* type-I variant surface glycoproteins. *Eur. J. Biochem.* **187,** 657–663 (Feb. 1990).

113. Ziegelbauer, K. & Overath, P. Organization of two invariant surface glycoproteins in the surface coat of *Trypanosoma brucei*. *Infect. Immun.* **61,** 4540–4545 (Nov. 1993).

8 Appendix

8.1 Composition of x-ray screens

Table 1 – Definition of Hampton Research HT HR2-130 crystal screen 1/2.

Well no.	Crystallisation parameters
A1	0.02 M calcium chloride dihydrate, 0.1 M na-acetate trihydrate pH 4.6, 30 % (v/v) (+/-)-2-methyl-2,4-pentanediol
A2	0.4 M potassium sodium tartrate tetrahydrate
A3	0.4 M ammonium phosphate monobasic
A4	0.1 M tris hydrochloride, pH 8.5, 2.0 M ammonium sulfate
A5	0.2 M sodium citrate tribasic dihydrate, 0.1 M HEPES sodium, pH 7.5, 30 % (v/v) (+/-)-2-methyl-2,4-pentanediol
A6	0.2 M magnesium chloride hexahydrate, 0.1 M tris hydrochloride, pH 8.5, 30 % (w/v) polyethylene glycol 4,000
A7	0.1 M sodium cacodylate trihydrate, pH 6.5, 1.4 M sodium acetate trihydrate
A8	0.2 M sodium citrate tribasic dihydrate, 0.1 M sodium cacodylate trihydrate, pH 6.5, 30 % (v/v) 2-propanol
A9	0.2 M ammonium acetate, 0.1 M sodium citrate tribasic dihydrate, pH 5.6, 30 % (w/v) polyethylene glycol 4,000
A10	0.2 M ammonium acetate, 0.1 M sodium acetate trihydrate, pH 4.6, 30 % (w/v) polyethylene glycol 4,000
A11	0.1 M sodium citrate tribasic dihydrate, pH 5.6, 1.0 M ammonium phosphate monobasic
A12	0.2 M magnesium chloride hexahydrate, 0.1 M HEPES sodium, pH 7.5, 30 % (v/v) 2-propanol
B1	0.2 M sodium citrate tribasic dihydrate, 0.1 M tris hydrochloride, pH 8.5, 30 % (v/v) polyethylene glycol 400
B2	0.2 M calcium chloride dihydrate, 0.1 M HEPES sodium, pH 7.5, 28 % (v/v) polyethylene glycol 400
B3	0.2 M ammonium sulfate, 0.1 M sodium cacodylate trihydrate, pH 6.5, 30 % (w/v) polyethylene glycol 8,000
B4	0.1 M HEPES sodium, pH 7.5, 1.5 M lithium sulfate monohydrate
B5	0.2 M lithium sulfate monohydrate, 0.1 M tris hydrochloride, pH 8.5, 30 % (w/v) polyethylene glycol 4,000
B6	0.2 M magnesium acetate tetrahydrate, 0.1 M sodium cacodylate trihydrate, pH 6.5, 20 % (w/v) PEG 8,000
B7	0.2 M ammonium acetate, 0.1 M tris hydrochloride, pH 8.5, 30 % (v/v) 2-propanol
B8	0.2 M ammonium sulfate, 0.1 M sodium acetate trihydrate, pH 4.6, 25 % (w/v) polyethylene glycol 4,000
B9	0.2 M magnesium acetate tetrahydrate, 0.1 M na-cacodylate trihydrate, pH 6.5, 30 % (v/v) (+/-)-2-methyl-2,4-pentanediol
B10	0.2 M sodium acetate trihydrate, 0.1 M tris hydrochloride, pH 8.5, 30 % (w/v) polyethylene glycol 4,000
B11	0.2 M magnesium chloride hexahydrate, 0.1 M HEPES sodium, pH 7.5, 30 % (v/v) polyethylene glycol 400
B12	0.2 M calcium chloride dihydrate, 0.1 M sodium acetate trihydrate, pH 4.6, 20 % (v/v) 2-propanol
C1	0.1 M imidazole, pH 6.5, 1.0 M sodium acetate trihydrate
C2	0.2 M ammonium acetate, 0.1 M sodium citrate tribasic dihydrate, pH 5.6, 30 % (v/v) (+/-)-2-methyl-2,4-pentanediol
C3	0.2 M sodium citrate tribasic dihydrate, 0.1 M HEPES sodium, pH 7.5, 20 % (v/v) 2-propanol
C4	0.2 M sodium acetate trihydrate, 0.1 M sodium cacodylate trihydrate, pH 6.5, 30 % (w/v) polyethylene glycol 8,000
C5	0.1 M HEPES sodium, pH 7.5, 0.8 M potassium sodium tartrate tetrahydrate
C6	0.2 M ammonium sulfate, 30 % (w/v) polyethylene glycol 8,000
C7	0.2 M ammonium sulfate, 30 % (w/v) polyethylene glycol 4,000
C8	2.0 M ammonium sulfate
C9	4.0 M sodium formate
C10	0.1 M sodium acetate trihydrate, pH 4.6, 2.0 M sodium formate
C11	0.1 M HEPES sodium, pH 7.5, 0.8 M na-phosphate monobasic monohydrate, 0.8 M potassium phosphate monobasic
C12	0.1 M tris hydrochloride, pH 8.5, 8 % (w/v) polyethylene glycol 8,000
D1	0.1 M sodium acetate trihydrate, pH 4.6, 8 % (w/v) polyethylene glycol 4,000
D2	0.1 M HEPES sodium, pH 7.5, 1.4 M sodium citrate tribasic dihydrate
D3	0.1 M HEPES sodium, pH 7.5, 2 % (v/v) polyethylene glycol 400, 2.0 M ammonium sulfate
D4	0.1 M sodium citrate tribasic dihydrate, pH 5.6, 20 % (v/v) 2-propanol, 20 % (w/v) polyethylene glycol 4,000
D5	0.1 M HEPES sodium, pH 7.5, 10 % (v/v) 2-propanol, 20 % (w/v) polyethylene glycol 4,000
D6	0.05 M potassium phosphate monobasic, 20 % (w/v) polyethylene glycol 8,000
D7	30 % (w/v) polyethylene glycol 1,500
D8	0.2 M magnesium formate dihydrate
D9	0.2 M zinc acetate dihydrate, 0.1 M sodium cacodylate trihydrate, pH 6.5, 18 % (w/v) polyethylene glycol 8,000
D10	0.2 M calcium acetate hydrate, 0.1 M sodium cacodylate trihydrate, pH 6.5, 18 % (w/v) polyethylene glycol 8,000
D11	0.1 M sodium acetate trihydrate, pH 4.6, 2.0 M ammonium sulfate
D12	0.1 M tris hydrochloride, pH 8.5, 2.0 M ammonium phosphate monobasic

Table 2 – Definition of Hampton Research HT HR2-130 crystal screen 2/2.

Well no.	Crystallisation parameters
E1	2.0 M sodium chloride, 10 % (w/v) polyethylene glycol 6,000
E2	0.5 M sodium chloride, 0.01 M magnesium chloride hexahydrate, 0.01 M hexadecyltrimethylammonium bromide
E3	25 % (v/v) ethylene glycol
E4	35 % (v/v) 1,4-dioxane
E5	2.0 M ammonium sulfate, 5 % (v/v) 2-propanol
E6	1.0 M imidazole, pH 7.0
E7	10 % (w/v) polyethylene glycol 1,000, 10 % (w/v) polyethylene glycol 8,000
E8	1.5 M sodium chloride, 10 % (v/v) ethanol
E9	0.1 M sodium acetate trihydrate, pH 4.6, 2.0 M sodium chloride
E10	0.2 M sodium chloride, 0.1 M sodium acetate trihydrate, pH 4.6, 30 % (v/v) (+/-)-2-methyl-2,4-pentanediol
E11	0.01 M cobalt(II) chloride hexahydrate, 0.1 M sodium acetate trihydrate, pH 4.6, 1.0 M 1,6-hexanediol
E12	0.1 M cadmium chloride hydrate, 0.1 M sodium acetate trihydrate, pH 4.6, 30 % (v/v) polyethylene glycol 400
F1	0.2 M ammonium sulfate, 0.1 M sodium acetate trihydrate, pH 4.6, 30 % (w/v) polyethylene glycol monomethyl ether 2,000
F2	0.2 M potassium sodium tartrate tetrahydrate, 0.1 M sodium citrate tribasic dihydrate, pH 5.6, 2.0 M ammonium sulfate
F3	0.5 M ammonium sulfate, 0.1 M sodium citrate tribasic dihydrate, pH 5.6, 1.0 M lithium sulfate monohydrate
F4	0.5 M sodium chloride, 0.1 M sodium citrate tribasic dihydrate, pH 5.6, 2 % (v/v) ethylene imine polymer
F5	0.1 M sodium citrate tribasic dihydrate, pH 5.6, 35 % (v/v) tert-butanol
F6	0.01 M iron(III) chloride hexahydrate, 0.1 M sodium citrate tribasic dihydrate, pH 5.6, 10 % (v/v) Jeffamine M600
F7	0.1 M sodium citrate tribasic dihydrate, pH 5.6, 2.5 M 1,6-hexanediol
F8	0.1 M MES monohydrate, pH 6.5, 1.6 M magnesium sulfate heptahydrate
F9	0.1 M sodium phosphate monobasic monohydrate, 0.1 M potassium phosphate monobasic, 0.1 M MES monohydrate, pH 6.5, 2.0 M sodium chloride
F10	0.1 M MES monohydrate, pH 6.5, 12 % (w/v) polyethylene glycol 20,000
F11	1.6 M ammonium sulfate, 0.1 M MES monohydrate, pH 6.5, 10 % (v/v) 1,4-dioxane
F12	0.05 M cesium chloride, 0.1 M MES monohydrate, pH 6.5, 30 % (v/v) Jeffamine M600
G1	0.01 M cobalt(II) chloride hexahydrate, 0.1 M MES monohydrate, pH 6.5, 1.8 M ammonium sulfate
G2	0.2 M ammonium sulfate, 0.1 M MES monohydrate, pH 6.5, 30 % (w/v) polyethylene glycol monomethyl ether 5,000
G3	0.01 M zinc sulfate heptahydrate, 0.1 M MES monohydrate, pH 6.5, 25 % (v/v) polyethylene glycol monomethyl ether 550
G4	1.6 M sodium citrate tribasic dihydrate, pH 6.5
G5	0.5 M ammonium sulfate, 0.1 M HEPES, pH 7.5, 30 % (v/v) (+/-)-2-methyl-2,4-pentanediol
G6	0.1 M HEPES, pH 7.5, 10 % (w/v) polyethylene glycol 6,000, 5 % (v/v) (+/-)-2-methyl-2,4-pentanediol
G7	0.1 M HEPES, pH 7.5, 20 % (v/v) Jeffamine M600
G8	0.1 M sodium chloride, 0.1 M HEPES, pH 7.5, 1.6 M ammonium sulfate
G9	0.1 M HEPES, pH 7.5, 2.0 M ammonium formate
G10	0.05 M cadmium sulfate hydrate, 0.1 M HEPES, pH 7.5, 1.0 M sodium acetate trihydrate
G11	0.1 M HEPES, pH 7.5, 70 % (v/v) (+/-)-2-methyl-2,4-pentanediol
G12	0.1 M HEPES, pH 7.5, 4.3 M sodium chloride
H1	0.1 M HEPES, pH 7.5, 10 % (w/v) polyethylene glycol 8,000, 8 % (v/v) ethylene glycol
H2	0.1 M HEPES, pH 7.5, 20 % (w/v) polyethylene glycol 10,000
H3	0.2 M magnesium chloride hexahydrate, 0.1 M tris, pH 8.5, 3.4 M 1,6-hexanediol
H4	0.1 M tris, pH 8.5, 25 % (v/v) tert-butanol
H5	0.01 M nickel(II) chloride hexahydrate, 0.1 M tris, pH 8.5, 1.0 M lithium sulfate monohydrate
H6	1.5 M ammonium sulfate, 0.1 M tris, pH 8.5, 12 % (v/v) glycerin
H7	0.2 M ammonium phosphate monobasic, 0.1 M tris, pH 8.5, 50 % (v/v) (+/-)-2-methyl-2,4-pentanediol
H8	0.1 M tris, pH 8.5, 20 % (v/v) ethanol
H9	0.01 M nickel(II) chloride hexahydrate, 0.1 M tris pH 8.5, 20 % (w/v) polyethylene glycol monomethyl ether 2,000
H10	0.1 M sodium chloride, 0.1 M bicine, pH 9.0, 20 % (v/v) polyethylene glycol monomethyl ether 550
H11	0.1 M bicine, pH 9.0, 2.0 M magnesium chloride hexahydrate
H12	0.1 M bicine, pH 9.0, 2 % (v/v) 1,4-dioxane, 10 % (w/v) polyethylene glycol 20,000

Table 3 – Definition of Hampton Research HR2-134 Index screen 1/2.

Well no.	Crystallisation parameters
A1	0.1 M citric acid, pH 3.5, 2.0 M ammonium sulfate
A2	0.1 M sodium acetate trihydrate, pH 4.5, 2.0 M ammonium sulfate
A3	0.1 M bis-tris, pH 5.5, 2.0 M ammonium sulfate
A4	0.1 M bis-tris, pH 6.5, 2.0 M ammonium sulfate
A5	0.1 M HEPES, pH 7.5, 2.0 M ammonium sulfate
A6	0.1 M tris, pH 8.5, 2.0 M ammonium sulfate
A7	0.1 M citric acid, pH 3.5, 3.0 M sodium chloride
A8	0.1 M sodium acetate trihydrate, pH 4.5, 3.0 M sodium chloride
A9	0.1 M bis-tris, pH 5.5, 3.0 M sodium chloride
A10	0.1 M bis-tris, pH 6.5, 3.0 M sodium chloride
A11	0.1 M HEPES, pH 7.5, 3.0 M sodium chloride
A12	0.1 M tris, pH 8.5, 3.0 M sodium chloride
B1	0.1 M bis-tris, pH 5.5, 0.3 M magnesium formate dihydrate
B2	0.1 M bis-tris, pH 6.5, 0.5 M magnesium formate dihydrate
B3	0.1 M HEPES, pH 7.5, 0.5 M magnesium formate dihydrate
B4	0.1 M tris, pH 8.5, 0.3 M magnesium formate dihydrate
B5	1.26 M sodium phosphate monobasic monohydrate, 0.14 M potassium phosphate dibasic
B6	0.49 M sodium phosphate monobasic monohydrate, 0,91 M potassium phosphate dibasic
B7	0.06 M sodium phosphate monobasic monohydrate, 1.34 M potassium phosphate dibasic
B8	0.1 M HEPES, pH 7.5, 1.4 M sodium citrate tribasic dihydrate
B9	1.8 M ammonium citrate tribasic, pH 7.0
B10	0.8 M succinic acid, pH 7.0
B11	2.1 M DL-malic acid, pH 7.0
B12	2.8 M sodium acetate trihydrate, pH 7.0
C1	3.5 M sodium formate, pH 7.0
C2	1.1 M ammonium tartrate dibasic, pH 7.0
C3	2.4 M sodium malonate, pH 7.0
C4	35 % (v/v) Tacsimate, pH 7.0
C5	60 % (v/v) Tacsimate, pH 7.0
C6	0.1 M sodium chloride, 0.1 M bis-tris, pH 6.5, 1.5 M ammonium sulfate
C7	0.8 M potassium sodium tartrate tetrahydrate, 0.1 M tris, pH 8.5, 0,5 % (w/v) polyethylene glycol monomethyl ether 5,000
C8	1.0 M ammonium sulfate, 0.1 M bis-tris, pH 5.5, 1 % (w/v) polyethylene glycol 3,350
C9	1.1 M sodium malonate pH 7.0, 0.1 M HEPES, pH 7.0, 0.5 % (v/v) jeffamine ED-2001 pH 7.0
C10	1.0 M succinic acid pH 7.0, 0.1 M HEPES, pH 7.0, 1 % (w/v) polyethylene glycol monomethyl ether 2,000
C11	1.0 M ammonium sulfate, 0.1 M HEPES, pH 7.0, 0.5 % (w/v) polyethylene glycol 8,000
C12	15 % (v/v) tacsimate pH 7.0, 0.1 M HEPES, pH 7.0, 2 % (w/v) polyethylene glycol 3,350
D1	25 % (w/v) polyethylene glycol 1,500
D2	0.1 M HEPES, pH 7.0, 30 % (v/v) Jeffamine M600. pH 7.0
D3	0.1 M HEPES, pH 7.0, 30 % (v/v) Jeffamine ED-2001 pH 7.0
D4	0.1 M citric acid, pH 3.5, 25 % (w/v) polyethylene glycol 3,350
D5	0.1 M sodium acetate trihydrate, pH 4.5, 25 % (w/v) polyethylene glycol 3,350
D6	0.1 M bis-tris, pH 5.5, 25 % (w/v) polyethylene glycol 3,350
D7	0.1 M bis-tris, pH 6.5, 25 % (w/v) polyethylene glycol 3,350
D8	0.1 M HEPES, pH 7.5, 25 % (w/v) polyethylene glycol 3,350
D9	0.1 M tris, pH 8.5, 25 % (w/v) polyethylene glycol 3,350
D10	0.1 M bis-tris, pH 6.5, 20 % (w/v) polyethylene glycol monomethyl ether 5,000
D11	0.1 M bis-tris, pH 6.5, 28 % (w/v) Polyethylene glycol monomethyl ether 2,000
D12	0.2 M calcium chloride dihydrate, 0.1 M bis-tris, pH 5.5, 45 % (v/v) (+/-)-2-methyl-2,4-pentanediol

Table 4 – Definition of Hampton Research HR2-134 Index screen 2/2.

Well no.	Crystallisation parameters
E1	0.2 M calcium chloride dihydrate, 0.1 M bis-tris, pH 6.5, 45 % (v/v) (+/-)-2-methyl-2,4-pentanediol
E2	0.2 M ammonium acetate, 0.1 M bis-tris, pH 5.5, 45 % (v/v) (+/-)-2-methyl-2,4-pentanediol
E3	0.2 M ammonium acetate, 0.1 M bis-tris, pH 6.5, 45 % (v/v) (+/-)-2-methyl-2,4-pentanediol
E4	0.2 M ammonium acetate, 0.1 M HEPES, pH 7.5, 45 % (v/v) (+/-)-2-Methyl-2,4-pentanediol
E5	0.2 M ammonium acetate, 0.1 M tris, pH 8.5, 45 % (v/v) (+/-)-2-Methyl-2,4-pentanediol
E6	0.05 M calcium chloride dihydrate, 0.1 M bis-tris, pH 6.5, 30 % (v/v) polyethylene glycol monomethyl ether 550
E7	0.05 M magnesium chloride hexahydrate, 0.1 M HEPES, pH 7.5, 30 % (v/v) polyethylene glycol monomethyl ether 550
E8	0.2 M potassium chloride, 0.05 M HEPES, pH 7.5, 35 % (v/v) pentaerythritol propoxylate (5/4 PO/OH)
E9	0.05 M ammonium sulfate, 0.05 M bis-tris, pH 6.5, 30 % (v/v) pentaerythritol ethoxylate (15/4 EO/OH)
E10	0.1 M bis-tris, pH 6.5, 45 % (v/v) polypropylene glycol P 400
E11	0.02 M magnesium chloride hexahydrate, 0.1 M HEPES, pH 7.5, 22 % (w/v) polyacrylic acid sodium salt 5,100
E12	0.01 M cobalt(II) chloride hexahydrate, 0.1 M tris, pH 8.5, 20 % (w/v) polyvinylpyrrolidone K 15
F1	0.2 M L-proline, 0.1 M HEPES, pH 7.5, 10 % (w/v) polyethylene glycol 3,350
F2	0.2 M trimethylamine N-oxide dihydrate, 0.1 M tris, pH 8.5, 20 % (w/v) polyethylene glycol monomethyl ether 2,000
F3	5 % (v/v) Tacsimate pH 7.0, 0.1 M HEPES, pH 7.0, 10 % (w/v) polyethylene glycol monomethyl ether 5,000
F4	0.005 M cobalt(II) chloride hexahydrate, 0.1 M HEPES, pH 7.5, 12 % (w/v) polyethylene glycol 3,350 0.005 M nickel(II) chloride hexahydrate, 0.005 M cadmium chloride hydrate, 0.005 M magnesium chloride hexahydrate
F5	0.1 M ammonium acetate 0.1 M bis-tris, pH 5.5, 17 % (w/v) polyethylene glycol 10,000
F6	0.2 M ammonium sulfate 0.1 M bis-tris, pH 5.5, 25 % (w/v) polyethylene glycol 3,350
F7	0.2 M ammonium sulfate 0.1 M bis-tris, pH 6.5, 25 % (w/v) polyethylene glycol 3,350
F8	0.2 M ammonium sulfate 0.1 M HEPES, pH 7.5, 25 % (w/v) polyethylene glycol 3,350
F9	0.2 M ammonium sulfate 0.1 M tris, pH 8.5, 25 % (w/v) polyethylene glycol 3,350
F10	0.2 M sodium chloride, 0.1 M bis-tris, pH 5.5, 25 % (w/v) polyethylene glycol 3,350
F11	0.2 M sodium chloride, 0.1 M bis-tris, pH 6.5, 25 % (w/v) polyethylene glycol 3,350
F12	0.2 M sodium chloride, 0.1 M HEPES, pH 7.5, 25 % (w/v) polyethylene glycol 3,350
G1	0.2 M sodium chloride, 0.1 M tris, pH 8.5, 25 % (w/v) polyethylene glycol 3,350
G2	0.2 M lithium sulfate monohydrate, 0.1 M bis-tris, pH 5.5, 25 % (w/v) polyethylene glycol 3,350
G3	0.2 M lithium sulfate monohydrate, 0.1 M bis-tris, pH 6.5, 25 % (w/v) polyethylene glycol 3,350
G4	0.2 M lithium sulfate monohydrate, 0.1 M HEPES, pH 7.5, 25 % (w/v) polyethylene glycol 3,350
G5	0.2 M lithium sulfate monohydrate, 0,1 M tris, pH 8.5, 25 % (w/v) polyethylene glycol 3,350
G6	0.2 M ammonium acetate, 0.1 M bis-tris, ph 5.5, 25 % (w/v) polyethylene glycol 3,350
G7	0.2 M ammonium acetate, 0.1 M bis-tris, pH 6.5, 25 % (w/v) polyethylene glycol 3,350
G8	0.2 M ammonium acetate, 0.1 M HEPES, 7.5, 25 % (w/v) polyethylene glycol 3,350
G9	0.2 M ammonium acetate, 0.1 M tris, 8.5, 25 % (w/v) polyethylene glycol 3,350
G10	0.2 M magnesium chloride hexahydrate, 0.1 M bis-tris, pH 5.5, 25 % (w/v) polyethylene glycol 3,350
G11	0.2 M magnesium chloride hexahydrate, 0.1 M bis-tris, pH 6.5, 25 % (w/v) polyethylene glycol 3,350
G12	0.2 M magnesium chloride hexahydrate, 0.1 M HEPES, pH 7.5, 25 % (w/v) polyethylene glycol 3,350
H1	0.2 M magnesium chloride hexahydrate, 0.1 M tris, pH 8.5, 25 % (w/v) polyethylene glycol 3,350
H2	0.2 M potassium sodium tartrate tetrahydrate, 20 % (w/v) polyethylene glycol 3,350
H3	0.2 M sodium malonate, pH 7.0, 20 % (w/v) polyethylene glycol 3,350
H4	0.2 M ammonium citrate tribasic, pH 7.0, 20 % (w/v) polyethylene glycol 3,350
H5	0,1 M succinic acid, pH 7.0, 15 % (w/v) polyethylene glycol 3,350
H6	0.2 M sodium formate, 20 % (w/v) polyethylene glycol 3,350
H7	0.15 M DL-malic acid, pH 7.0, 20 % (w/v) polyethylene glycol 3,350
H8	0.1 M magnesium formate dihydrate, 15 % (w/v) polyethylene glycol 3,350
H9	0.05 M zinc acetate dihydrate, 20 % (w/v) polyethylene glycol 3,350
H10	0.2 M sodium citrate tribasic dihydrate, 20 % (w/v) polyethylene glycol 3,350
H11	0.1 M potassium thiocyanate, 30 % (w/v) polyethylene glycol monomethyl ether 2,000
H12	0.15 M potassium bromide, 30 % (w/v) polyethylene glycol monomethyl ether 2,000

Table 5 – Definition of the QIAGEN Nextal PEG screen.

Well no.	Crystallisation parameters	Well no.	Crystallisation parameters
A1	0.1 M sodium acetate, pH 4.6, 40 % (v/v) PEG 200	E1	0.2 M sodium fluoride, 20 % (w/v) PEG 3,350
A2	0.1 M sodium acetate, pH 4.6, 30 % (v/v) PEG 300	E2	0.2 M potassium fluoride, 20 % (w/v) PEG 3,350
A3	0.1 M sodium acetate, pH 4.6, 30 % (v/v) PEG 400	E3	0.2 M ammonium fluoride, 20 % (w/v) PEG 3,350
A4	0.1 M sodium acetate, pH 4.6 25 % (v/v) PEG 550 MME	E4	0.2 M lithium chloride, 20 % (w/v) PEG 3,350
A5	0.1 M sodium acetate, pH 4.6 25 % (w/v) PEG 1,000	E5	0.2 M magnesium chloride, 20 % (w/v) PEG 3,350
A6	0.1 M sodium acetate, pH 4.6 25 % (w/v) PEG 2,000 MME	E6	0.2 M sodium chloride, 20 % (w/v) PEG 3,350
A7	0.1 M MES, pH 6.5, 40 % (v/v) PEG 200	E7	0.2 M calcium chloride, 20 % (w/v) PEG 3,350
A8	0.1 M MES, pH 6.5, 30 % (v/v) PEG 300	E8	0.2 M potassium chloride, 20 % (w/v) PEG 3,350
A9	0.1 M MES, pH 6.5, 30 % (v/v) PEG 400	E9	0.2 M ammonium chloride, 20 % (w/v) PEG 3,350
A10	0.1 M MES, pH 6.5, 25 % (v/v) PEG 550 MME	E10	0.2 M sodium iodide, 20 % (w/v) PEG 3,350
A11	0.1 M MES, pH 6.5, 25 % (w/v) PEG 1,000	E11	0.2 M potassium iodide, 20 % (w/v) PEG 3,350
A12	0.1 M MES, pH 6.5, 25 % (w/v) PEG 2,000 MME	E12	0.2 M ammonium iodide, 20 % (w/v) PEG 3,350
B1	0.1 M sodium HEPES, pH 7.5, 40 % (v/v) PEG 200	F1	0.2 M sodium thiocyanate, 20 % (w/v) PEG 3,350
B2	0.1 M sodium HEPES, pH 7.5, 30 % (v/v) PEG 300	F2	0.2 M potassium thiocyanate, 20 % (w/v) PEG 3,350
B3	0.1 M sodium HEPES, pH 7.5, 30 % (v/v) PEG 400	F3	0.2 M lithium nitrate, 20 % (w/v) PEG 3,350
B4	0.1 M sodium HEPES, pH 7.5, 25 % (v/v) PEG 550 MME	F4	0.2 M magnesium nitrate, 20 % (w/v) PEG 3,350
B5	0.1 M sodium HEPES, pH 7.5, 25 % (w/v) PEG 1,000	F5	0.2 M sodium nitrate, 20 % (w/v) PEG 3,350
B6	0.1 M sodium HEPES, pH 7.5, 25 % (w/v) PEG 2,000 MME	F6	0.2 M potassium nitrate, 20 % (w/v) PEG 3,350
B7	0.1 M tris, pH 8.5 40 % (v/v) PEG 200	F7	0.2 M ammonium nitrate, 20 % (w/v) PEG 3,350
B8	0.1 M tris, pH 8.5 30 % (v/v) PEG 300	F8	0.2 M magnesium formate, 20 % (w/v) PEG 3,350
B9	0.1 M tris, pH 8.5 30 % (v/v) PEG 400	F9	0.2 M sodium formate, 20 % (w/v) PEG 3,350
B10	0.1 M tris, pH 8.5 25 % (v/v) PEG 550 MME	F10	0.2 M potassium formate, 20 % (w/v) PEG 3,350
B11	0.1 M tris, pH 8.5 25 % (w/v) PEG 1,000	F11	0.2 M ammonium formate, 20 % (w/v) PEG 3,350
B12	0.1 M tris, pH 8.5 25 % (w/v) PEG 2,000 MME	F12	0.2 M lithium acetate, 20 % (w/v) PEG 3,350
C1	0.1 M sodium acetate, pH 4.6, 25 % (w/v) PEG 3,000	G1	0.2 M magnesium acetate, 20 % (w/v) PEG 3,350
C2	0.1 M sodium acetate, pH 4.6, 25 % (w/v) PEG 4,000	G2	0.2 M zinc acetate, 20 % (w/v) PEG 3,350
C3	0.1 M sodium acetate, pH 4.6, 25 % (w/v) PEG 6,000	G3	0.2 M sodium acetate, 20 % (w/v) PEG 3,350
C4	0.1 M sodium acetate, pH 4.6, 25 % (w/v) PEG 8,000	G4	0.2 M calcium acetate, 20 % (w/v) PEG 3,350
C5	0.1 M sodium acetate, pH 4.6, 20 % (w/v) PEG 10,000	G5	0.2 M potassium acetate, 20 % (w/v) PEG 3,350
C6	0.1 M sodium acetate, pH 4.6, 15 % (w/v) PEG 20,000	G6	0.2 M ammonium acetate, 20 % (w/v) PEG 3,350
C7	0.1 M MES, pH 6.5, 25 % (w/v) PEG 3,000	G7	0.2 M lithium sulfate, 20 % (w/v) PEG 3,350
C8	0.1 M MES, pH 6.5, 25 % (w/v) PEG 4,000	G8	0.2 M magnesium sulfate, 20 % (w/v) PEG 3,350
C9	0.1 M MES, pH 6.5, 25 % (w/v) PEG 6,000	G9	0.2 M sodium sulfate, 20 % (w/v) PEG 3,350
C10	0.1 M MES, pH 6.5, 25 % (w/v) PEG 8,000	G10	0.2 M potassium sulfate, 20 % (w/v) PEG 3,350
C11	0.1 M MES, pH 6.5, 20 % (w/v) PEG 10,000	G11	0.2 M ammonium sulfate, 20 % (w/v) PEG 3,350
C12	0.1 M MES, pH 6.5, 15 % (w/v) PEG 20,000	G12	0.2 M di-sodium tartrate, 20 % (w/v) PEG 3,350
D1	0.1 M sodium HEPES, pH 7.5, 25 % (w/v) PEG 3,000	H1	0.2 M K/Na tartrate, 20 % (w/v) PEG 3,350
D2	0.1 M sodium HEPES, pH 7.5, 25 % (w/v) PEG 4,000	H2	0.2 M di-ammonium tartrate, 20 % (w/v) PEG 3,350
D3	0.1 M sodium HEPES, pH 7.5, 25 % (w/v) PEG 6,000	H3	0.2 M sodium phosphate, 20 % (w/v) PEG 3,350
D4	0.1 M sodium HEPES, pH 7.5, 25 % (w/v) PEG 8,000	H4	0.2 M di-sodium phosphate, 20 % (w/v) PEG 3,350
D5	0.1 M sodium HEPES, pH 7.5, 20 % (w/v) PEG 10,000	H5	0.2 M potassium phosphate, 20 % (w/v) PEG 3,350
D6	0.1 M sodium HEPES, pH 7.5, 15 % (w/v) PEG 20,000	H6	0.2 M di-potassium phosphate, 20 % (w/v) PEG 3,350
D7	0.1 M tris, pH 8.5, 25 % (w/v) PEG 3,000	H7	0.2 M ammonium phosphate, 20 % (w/v) PEG 3,350
D8	0.1 M tris, pH 8.5, 25 % (w/v) PEG 4,000	H8	0.2 M di-ammonium phosphate, 20 % (w/v) PEG 3,350
D9	0.1 M tris, pH 8.5, 25 % (w/v) PEG 6,000	H9	0.2 M tri-lithium citrate, 20 % (w/v) PEG 3,350
D10	0.1 M tris, pH 8.5, 25 % (w/v) PEG 8,000	H10	0.2 M tri-sodium citrate, 20 % (w/v) PEG 3,350
D11	0.1 M tris, pH 8.5, 20 % (w/v) PEG 10,000	H11	0.2 M tri-potassium citrate, 20 % (w/v) PEG 3,350
D12	0.1 M tris, pH 8.5, 15 % (w/v) PEG 20,000	H12	0.18 M tri-ammonium citrate, 20 % (w/v) PEG 3,350

Table 6 – Definition of the Molecular Dimensions MIDAS HT-96 screen 1/2.

Well no.	Crystallisation parameters
A1	50 % (v/v) polypropylene glycol 400, 5 % (v/v) dimethyl sulfoxide, 0,1 M HEPES NaOH, pH 6.0
A2	12 % (w/v) polyvinyl pyrrolidone K15, 0.1 M MES NaOH, pH 5.5
A3	45 % (w/v) polyacrylate 2,100, sodium salt, 0.1 M HEPES NaOH, pH 6.5
A4	14 % (v/v) acrylic acid/maleic acid copolymer (50:50), sodium salt
A5	12.5 % (w/v) polyacrylate 2,100, sodium salt, 0.5 M ammonium phosphate
A6	19 % (v/v) acrylic acid/maleic acid copolymer (50:50), sodium salt, 0.1 M tris HCl, pH 8.5
A7	10 % (v/v) polypropylene glycol 400
A8	5 % (w/v) polyacrylate 2,100, sodium salt
A9	25 % (v/v) pentaerythritol propoxylate (5/4 PO/OH), 0.1 M MES NaOH, pH 6.0
A10	24 % (w/v) polyvinyl pyrrolidone K15, 0.1 M sodium sulfate
A11	35 % (v/v) pentaerythritol ethoxylate (15/4 EO/OH), 0.2 M calcium chloride, 0.1 M HEPES NaOH, pH 6.5
A12	3 % (v/v) polypropylene glycol 400, 0.1 M K/Na phosphate
B1	20 % (v/v) Jeffamine D2000, 10 % (v/v) Jeffamine M2005, 0.2 M sodium chloride, 0.1 M MES NaOH, pH 5.5
B2	15 % (v/v) pentaerythritol propoxylate (5/4 PO/OH, 0.2 M sodium thiocyanate, 0.1 M HEPES NaOH, pH 7.0
B3	5 % (w/v) polyvinyl alcohol type II, 10 % (v/v) Jeffamine T403, 0.2 M potassium acetate, 0.1 M HEPES NaOH, pH 7.0
B4	45 % (v/v) pentaerythritol propoxylate (5/4 PO/OH), 0.2 M sodium chloride, 0.1 M MES NaOH, pH 6.0
B5	8 % (w/v) polyvinyl alcohol type II, 10 % (v/v) 1-propanol, 0.1 M HEPES NaOH, pH 7.0
B6	30 % (w/v) polyvinyl pyrrolidone K15, 0.1 M lithium sulfate, 0.1 M HEPES NaOH, pH 7.0
B7	40 % (v/v) polypropylene glycol 400, 0.2 M imidazole, pH 7.0
B8	8 % (w/v) acrylic acid/maleic acid copolymer (50:50), sodium salt, 3 % (v/v) pentaerythritol ethoxylate (3/4 EO/OH), 0.06 M lithium sulfate, 0.1 M HEPES NaOH, pH 7.5
B9	35 % (v/v) Jeffamine SD2001, 0.1 M sodium chloride, 0.1 M tris HCl, pH 8.0
B10	30 % (v/v) Jeffamine M600, 10 % (v/v) dimethyl sulfoxide
B11	20 % (v/v) polypropylene glycol 400, 10 % (v/v) 1-propanol
B12	28 % (w/v) acrylic acid/maleic acid copolymer (50:50), sodium salt, 0.1 M HEPES NaOH, pH 6.5
C1	15 % (w/v) Jeffamine ED2003, 10 % (v/v) ethanol
C2	30 % (w/v) Jeffamine ED2003, 0.2 M sodium chloride, 0.1 M MES NaOH, pH 6.0
C3	25 % (v/v) Jeffamine SD2001, 0.1 M sodium malonate, 0.1 M MES NaOH, pH 5.5
C4	15 % (v/v) pentaerythritol propoxylate (5/4 PO/OH), 0.2 M sodium chloride, 0.1 M MES NaOH, pH 6.0
C5	35 % (v/v) pentaerythritol propoxylate (3/4 PO/OH), 0.2 M magnesium chloride
C6	40 % (v/v) pentaerythritol propoxylate (5/4 PO/OH), 15 % (v/v) ethanol
C7	50 % (v/v) pentaerythritol propoxylate (5/4 PO/OH), 0.1 M tris HCl, pH 8.0
C8	12.5 % (w/v) polyvinyl pyrrolidone K15, 10 % (w/v) PEG 4,000, 0.2 M sodium chloride, 0.1 M tris HCl, pH 8.0
C9	25 % (v/v) pentaerythritol propoxylate (5/4 PO/OH), 10 % (v/v) dimethyl sulfoxide, 0.1 M sodium chloride
C10	35 % (w/v) polyacrylate 2,100, sodium salt, 0.2 M ammonium sulfate, 0.1 M HEPES NaOH, pH 7.5
C11	30 % (v/v) pentaerythritol ethoxylate (15/4 EO/OH), 0.1 M magnesium formate, 0.1 M tris HCl, pH 8.5
C12	20 % (v/v) Glascol W13, 0.2 M sodium sulfate, 0.1 M HEPES NaOH, pH 7.5
D1	60 % (v/v) polypropylene glycol 400, 0.1 M tris HCl, pH 8.0
D2	30 % (v/v) pentaerythritol ethoxylate (15/4 EO/OH), 6 % (w/v) polyvinyl pyrrolidone K15, 0.1 M HEPES NaOH, pH 7.5
D3	45 % (v/v) polypropylene glycol 400, 10 % (v/v) ethanol
D4	10 % (v/v) pentaerythritol ethoxylate (3/4 EO/OH), 10 % (v/v) 1-butanol
D5	12.5 % (w/v) polyacrylate 2,100, sodium salt, 6 % (v/v) Jeffamine SD2001, 0.1 M HEPES NaOH, pH 7.0
D6	6 % (w/v) polyvinyl pyrrolidone K15, 0.1 M HEPES NaOH, pH 6.5
D7	20 % (w/v) Jeffamine ED2003, 0.1 M HEPES NaOH, pH 6.5
D8	20 % (v/v) glycerol ethoxylate, 10 % (v/v) tetrahydrofuran, 0.1 M tris HCl, pH 8.0
D9	25 % (v/v) Jeffamine D2000, 0.2 M imidazole, pH 7.0
D10	30 % (v/v) Jeffamine SD2001, 0.2 M potassium chloride, 0.1 M HEPES NaOH, pH 6.5
D11	30 % (v/v) polypropylene glycol 400, 0.1 M sodium chloride
D12	20 % (v/v) Jeffamine SD2001, 15 % 1-propanol

Table 7 – Definition of the Molecular Dimensions MIDAS HT-96 screen 2/2.

Well no.	Crystallisation parameters
E1	25 % (v/v) Jeffamine T403, 0.2 M lithium sulfate, 0.1 M tris HCl, pH 8.0
E2	35 % (v/v) pentaerythritol propoxylate (5/4 PO/OH), 0.2 M potassium acetate
E3	20 % (v/v) pentaerythritol ethoxylate (15/4 EO/OH), 0.2 M potassium chloride, 0.1 M glycine, pH 9.5
E4	40 % (v/v) pentaerythritol propoxylate (5/4 PO/OH), 0.2 M sodium thiocyanate, 0.1 M HEPES NaOH, pH 7.0
E5	15 % (v/v) Jeffamine T403, 15 % (w/v) Jeffamine ED2003, 0.2 M potassium chloride, 0.1 M HEPES NaOH, pH 6.5
E6	15 % (v/v) pentaerythritol ethoxylate (15/4 EO/OH), 3 % (v/v) Jeffamine T403, 0,2 M potassium acetate, 0.1 M MES NaOH, pH 6.0
E7	30 % (w/v) polyacrylate 2100, sodium salt, 0.1 M sodium malonate, 0.1 M HEPES NaOH, pH 7.0
E8	10 % (v/v) Jeffamine D2000, 10 % (v/v) Jeffamine M2005, 10 % (v/v) ethanol
E9	25 % (w/v) Jeffamine ED2003, 0.1 M lithium sulfate, 0.1 M tris HCl, pH 8.0
E10	10 % (v/v) Jeffamine T403, 10 % (w/v) Jeffamine ED2003, 0.1 M tris HCl, pH 8.0
E11	25 % (w/v) polyacrylate 2100, sodium salt, 0.1 M lithium sulfate, 0.1 M HEPES NaOH, pH 6.5
E12	15 % (w/v) polyacrylate 2100, sodium salt, 0.2 M magnesium chloride, 0.1 M HEPES NaOH, pH 7.5
F1	40 % (v/v) Jeffamine D2000, 0.1 M HEPES NaOH, pH 6.5
F2	10 % (v/v) polyacrylate 2100, sodium salt, 0.5 M sodium chloride, 0.1 M tris HCl, pH 8.0
F3	14 % (v/v) Jeffamine ED900, 11 % (v/v) Jeffamine SD2001, 0.1 M K/Na phosphate, pH 7.0
F4	20 % (v/v) polyacrylate 2100, sodium salt, 0.2 M sodium chloride, 0.1 M bicine, pH 9.0
F5	20 % (v/v) Jeffamine D2000, 0.2 M sodium malonate, 0.1 M MES NaOH, pH 5.5
F6	30 % (v/v) Jeffamine M2070, 0.2 M potassium chloride, 0.1 M tris HCl, pH 8.0
F7	20 % (v/v) Jeffamine M2070, 20 % (v/v) dimethyl sulfoxide
F8	40 % (w/v) pentaerythritol propoxylate (17/8 PO/OH), 0.2 M magnesium chloride, 0.1 M MES NaOH, pH 5.5
F9	20 % (w/v) polyacrylate 5100, sodium salt, 0.1 M tris HCl, pH 8.0
F10	28 % (v/v) poly(ethylene imine), branched, 0.1 M HEPES NaOH, pH 7.0
F11	20 % (v/v) Sokalan CP 7, 0.1 M ammonium formate, 0.1 M HEPES NaOH, pH 7.0
F12	20 % (w/v) Sokalan HP 56, 0.2 M sodium sulfate, 0.1 M tris HCl, pH 8.0
G1	25 % (v/v) Sokalan CP 7, 0.1 M potassium chloride, 0.1 M HEPES NaOH, pH 7.0
G2	20 % (v/v) Sokalan CP 5, 0.3 M ammonium formate, 0.1 M HEPES NaOH, pH 7.0
G3	40 % (v/v) glycerol ethoxylate
G4	30 % (v/v) glycerol ethoxylate, 0.1 M tris HCl, pH 8.5
G5	15 % (v/v) Sokalan HP 66 K, 3 % (v/v) poly(ethylene imine), 0.1 M HEPES NaOH, pH 7.0
G6	35 % (v/v) glycerol ethoxylate, 0.2 M lithium citrate
G7	30 % (v/v) glycerol ethoxylate, 0.2 M ammonium acetate, 0.1 M MES NaOH, pH 6.5
G8	20 % (v/v) Sokalan CP 42, 5 % (v/v) methanol, 0.1 M tris HCl, pH 8.0
G9	25 % (v/v) Sokalan CP 42, 10 % (v/v) tetrahydrofuran, 0.1 M tris HCl, pH 7.0
G10	20 % (v/v) Sokalan CP 42, 0.1 M lithium acetate, 0.1 M bis-tris NaOH, pH 6.0
G11	15 % (v/v) Sokalan CP 12 S, 0.1 M lithium citrate, 0.1 M bis-tris NaOH, pH 5.5
G12	15 % (v/v) Sokalan CP 5, 0.1 M bis-tris NaOH, pH 6.0
H1	25 % (v/v) Sokalan CP 42, 0.1 M bis-tris NaOH, pH 6.0
H2	25 % (v/v) Sokalan HP 66 K, 0.2 M ammonium acetate, 0.1 M HEPES NaOH, pH 7.0
H3	20 % (v/v) glycerol ethoxylate, 3 % (v/v) poly(ethylene imine) 0.1 M tris HCl, pH 8.5
H4	25 % (v/v) glycerol ethoxylate, 0.2 M ammonium chloride, 0.1 M HEPES NaOH, pH 7.5
H5	40 % (v/v) Glascol W13, 0.2 M potassium citrate
H6	30 % (w/v) polyacrylate 5100, sodium salt, 10 % (v/v) ethanol, 0.1 M MES NaOH, pH 6.0
H7	15 % (v/v) Sokalan CP 42, 0.2 M potassium citrate
H8	30 % (v/v) Sokalan CP 42, 0.1 M tris HCl, pH 8.5
H9	25 % (w/v) Sokalan HP 56, 0.2 M ammonium acetate, 0.1 M HEPES NaOH, pH 7.0
H10	25 % (v/v) Sokalan CP 5, 0.1 M tris HCl, pH 8.5
H11	10 % (w/v) poly(vinyl pyrrolidone) K15, 20 % (w/v) PEG 4,000, 0.2 M ammonium formate
H12	15 % (w/v) poly(vinyl pyrrolidone) K15, 25 % (w/v) PEG MME 5,000, 0.1 M tris HCl, pH 8.0

Table 8 – Definition of the Fluidigm Topaz Optimix PEG screen 1/2.

Well no.	Crystallisation parameters
A1	0.9 M magnesium acetate, 0.1 M tris HCl, pH 8.5, 23 % (w/v) polyethylene glycol 4,000
A2	1.0 M lithium chloride, 23 % (w/v) polyethylene glycol 4,000
A3	0.4 M lithium sulfate, 0.1 M bis-tris propane, pH 7.0, 27 % (w/v) polyethylene glycol 4,000
A4	1.0 M ammonium formate, 0.1 M sodium citrate, pH 5.6, 23 % (w/v) polyethylene glycol 4,000
A5	15 % (v/v) Tacsimate 0.1 M sodium cacodylate, pH 6.5, 27 % (w/v) polyethylene glycol 4,000
A6	0.6 M magnesium acetate, 0.1 M sodium cacodylate, pH 6.5, 27 % (w/v) polyethylene glycol 4,000
A7	0.8 M ammonium chloride, 0.1 M sodium cacodylate, pH 6.5, 23 % (w/v) polyethylene glycol 4,000
A8	0.8 M sodium formate, 0.1 M sodium citrate, pH 5.6, 23 % (w/v) polyethylene glycol 4,000
A9	0.5 M ammonium citrate, 0.1 M HEPES, pH 7.5, 23 % (w/v) polyethylene glycol 4,000
A10	0.5 M magnesium chloride, 23 % (w/v) polyethylene glycol 4,000
A11	0.8 M potassium nitrate, 0.1 M sodium acetate, pH 4.6, 27 % (w/v) polyethylene glycol 4,000
A12	1.0 M ammonium formate, 18 % (w/v) polyethylene glycol 4,000
B1	0.6 M sodium acetate, 0.1 M HEPES, pH 7.5, 18 % (w/v) polyethylene glycol 4,000
B2	0.8 M sodium formate, 0.1 M imidazole, pH 8.0, 18 % (w/v) polyethylene glycol 4,000
B3	0.8 M potassium chloride, 18 % (w/v) polyethylene glycol 4,000
B4	0.6 M ammonium tartrate, dibasic, 18 % (w/v) polyethylene glycol 4,000
B5	0.5 M ammonium citrate, 0.1 M sodium citrate, pH 5.6, 18 % (w/v) polyethylene glycol 4,000
B6	0.5 M sodium acetate, 27 % (w/v) polyethylene glycol 4,000
B7	0.3 M magnesium formate, 0.1 M sodium acetate, pH 4.6, 27 % (w/v) polyethylene glycol 4,000
B8	1.0 M ammonium iodide, 0.1 M bicine, pH 9.0, 18 % (w/v) polyethylene glycol 4,000
B9	0.4 M lithium sulfate, 18 % (w/v) polyethylene glycol 4,000
B10	0.4 M sodium acetate, 0.1 M sodium citrate, pH 5.6, 18 % (w/v) polyethylene glycol 4,000
B11	0.5 M potassium acetate, 27 % (w/v) polyethylene glycol 4,000
B12	0.4 M sodium malonate, 0.1 M tris HCl, pH 8.5 18 % (w/v) polyethylene glycol 4,000
C1	0.4 M magnesium nitrate, 0.1 M HEPES, pH 7.5, 23 % (w/v) polyethylene glycol 4,000
C2	0.6 M sodium iodide, 0.1 M sodium citrate, pH 5.6, 27 % (w/v) polyethylene glycol 4,000
C3	0.4 M magnesium formate, 0.1 M MES, pH 6.0, 18 % (w/v) polyethylene glycol 4,000
C4	0.4 M potassium nitrate, 0.1 M HEPES, pH 7.5, 23 % (w/v) polyethylene glycol 4,000
C5	0.4 M magnesium nitrate, 27 % (w/v) polyethylene glycol 4,000
C6	0.4 M cesium chloride, 0.1 M sodium citrate, pH 5.6, 23 % (w/v) polyethylene glycol 4,000
C7	0.4 M calcium chloride, 0.1 M sodium acetate, pH 4.6, 18 % (w/v) polyethylene glycol 4,000
C8	0.3 M magnesium formate, 23 % (w/v) polyethylene glycol 4,000
C9	0.5 M potassium thiocyanate, 0.1 M HEPES, pH 7.5, 18 % (w/v) polyethylene glycol 4,000
C10	0.4 M ammonium chloride, 0.1 M imidazole, pH 6.5, 18 % (w/v) polyethylene glycol 4,000
C11	0.2 M calcium acetate, 0.1 M HEPES, pH 7.5, 27 % (w/v) polyethylene glycol 4,000
C12	0.1 M magnesium chloride, 0.1 M sodium citrate, pH 5.6, 25 % (w/v) polyethylene glycol 4,000
D1	0.1 M potassium sulfate, 27 % (w/v) polyethylene glycol 4,000
D2	0.1 M glycyl-glycine, pH 8.5, 27 % (w/v) polyethylene glycol 4,000
D3	0.1 M tris HCl, pH 8.0, 23 % (w/v) polyethylene glycol 4,000
D4	0.1 M TAPS, pH 9.0, 23 % (w/v) polyethylene glycol 4,000
D5	0.1 M magnesium chloride, 0.1 M tris HCl, pH 8.5, 18 % (w/v) polyethylene glycol 4,000
D6	0.1 M potassium sulfate, 0.1 M tris HCl, pH 8.5, 18 % (w/v) polyethylene glycol 4,000
D7	0.1 M ADA, pH 6.5, 23 % (w/v) polyethylene glycol 4,000
D8	0.1 M MOPS, pH 7.0, 18 % (w/v) polyethylene glycol 4,000
D9	0.1 M tris HCl, pH 8.5, 18 % (w/v) polyethylene glycol 4,000
D10	23 % (w/v) polyethylene glycol 4,000
D11	0. M HEPES, pH 7.5, 18 % (w/v) polyethylene glycol 4,000
D12	10 % (w/v) polyethylene glycol 1,500 18 % (w/v) polyethylene glycol 4,000

Table 9 – Definition of the Fluidigm Topaz Optimix PEG screen 2/2.

Well no.	Crystallisation parameters
E1	8 % (w/v) polyethylene glycol 8,000, 18 % (w/v) polyethylene glycol 4,000
E2	5 % (w/v) polyethylene glycol 10,000, 18 % (w/v) polyethylene glycol 4,000
E3	10 % (w/v) polyethylene glycol 1,000, 18 % (w/v) polyethylene glycol 4,000
E4	0.2 M succinic acid, sodium salt, 23 % (w/v) polyethylene glycol 4,000
E5	18 % (w/v) polyethylene glycol 4,000
E6	25 % (w/v) polyethylene glycol 4,000
E7	27 % (w/v) polyethylene glycol 4,000
E8	0.4 M DL-malic acid, 23 % (w/v) polyethylene glycol 4,000
E9	0.2 M potassium fluoride, 18 % (w/v) polyethylene glycol 4,000
E10	0.1 M zinc acetate, 0.1 M sodium cacodylate, pH 6.5, 18 % (w/v) polyethylene glycol 4,000
E11	0.1 M tris HCl, pH 7.5, 27 % (w/v) polyethylene glycol 4,000
E12	10 % (w/v) polyethylene glycol 6,000, 18 % (w/v) polyethylene glycol 4,000
F1	0.4 M potassium chloride, 23 % (w/v) polyethylene glycol 4,000
F2	0.5 M ammonium iodide, 0.1 M MES, pH 6.0, 23 % (w/v) polyethylene glycol 4,000
F3	0.4 M ammonium chloride, 0.1 M tris HCl, pH 8.5, 27 % (w/v) polyethylene glycol 4,000
F4	0.8 M ammonium nitrate, 0.1 M CHES, pH 9.5, 18 % (w/v) polyethylene glycol 4,000
F5	0.2 M calcium acetate, 27 % (w/v) polyethylene glycol 4,000
F6	0.2 M potassium formate, 0.1 M sodium cacodylate, pH 6.5, 23 % (w/v) polyethylene glycol 4,000
F7	0.3 M sodium formate, 23 % (w/v) polyethylene glycol 4,000
F8	0.5 M sodium nitrate, 0.1 M sodium acetate, pH 4.6, 23 % (w/v) polyethylene glycol 4,000
F9	0.5 M potassium iodide, 0.1 M sodium citrate, pH 5.6, 18 % (w/v) polyethylene glycol 4,000
F10	0.5 M lithium acetate, 0.1 M HEPES, pH 7.5, 18 % (w/v) polyethylene glycol 4,000
F11	0.2 M sodium malonate, 0.1 M sodium citrate, pH 5.6, 23 % (w/v) polyethylene glycol 4,000
F12	0.4 M potassium acetate, 0.1 M MES, pH 6.0, 18 % (w/v) polyethylene glycol 4,000
G1	0.3 M magnesium chloride, 0.1 M sodium acetate, pH 4.6, 27 % (w/v) polyethylene glycol 4,000
G2	0.3 M sodium tartrate, 0.1 M sodium cacodylate, pH 6.5, 23 % (w/v) polyethylene glycol 4,000
G3	0.3 M sodium tartrate, 0.1 M bis-tris propane, pH 7.0, 27 % (w/v) polyethylene glycol 4,000
G4	0.5 M potassium sodium tartrate, 18 % (w/v) polyethylene glycol 4,000
G5	0.5 M lithium nitrate, 0.1 M MES, pH 6.0, 27 % (w/v) polyethylene glycol 4,000
G6	0.6 M potassium thiocyanate, 0.1 M sodium citrate, pH 5.6, 27 % (w/v) polyethylene glycol 4,000
G7	0.5 M L-proline, 0.1 M sodium cacodylate, pH 6.5, 27 % (w/v) polyethylene glycol 4,000
G8	0.6 M sodium nitrate, 0.1 M MES, pH 6.0, 27 % (w/v) polyethylene glycol 4,000
G9	0.5 M potassium formate, 0.1 M tris HCl, pH 8.5, 27 % (w/v) polyethylene glycol 4,000
G10	0.8 M potassium nitrate, 27 % (w/v) polyethylene glycol 4,000
G11	0.4 M sodium malonate, 0.1 M sodium cacodylate, pH 6.5, 18 % (w/v) polyethylene glycol 4,000
G12	0.8 M potassium nitrate, 0.1 M bis-tris propane, pH 7.0, 18 % (w/v) polyethylene glycol 4,000
H1	0.6 M calcium chloride, 18 % (w/v) polyethylene glycol 4,000
H2	0.8 M potassium nitrate, 0.1 M bicine, pH 9.0, 23 % (w/v) polyethylene glycol 4,000
H3	0.5 M potassium bromide, 23 % (w/v) polyethylene glycol 4,000
H4	1.0 M lithium nitrate, 23 % (w/v) polyethylene glycol 4,000
H5	0.6 M sodium acetate, 23 % (w/v) polyethylene glycol 4,000
H6	0.5 M ammonium tartrate, dibasic, 0.1 M sodium cacodylate, pH 6.5, 23 % (w/v) polyethylene glycol 4,000
H7	0.5 M lithium sulfate, 0.1 M sodium acetate, pH 4.6, 18 % (w/v) polyethylene glycol 4,000
H8	0.6 M sodium iodide, 0.1 M sodium acetate, pH 4.6, 18 % (w/v) polyethylene glycol 4,000
H9	0.6 M magnesium acetate, 0.1 M sodium citrate, pH 5.6, 18 % (w/v) polyethylene glycol 4,000
H10	0.8 M potassium chloride, 0.1 M sodium cacodylate, pH 6.5, 27 % (w/v) polyethylene glycol 4,000
H11	0.8 M lithium acetate, 27 % (w/v) polyethylene glycol 4,000
H12	0.8 M ammonium acetate, 0.1 M MES, pH 6.0, 27 % (w/v) polyethylene glycol 4,000

Table 10 – Definition of the QIAGEN Nextal protein complex screen 1/2.

Well no.	Crystallisation parameters
A1	0.1 M tris, pH 8.0, 25 % (w/v) PEG 350 MME
A2	0.1 M calcium acetate, 0.1 M MES, pH 6.0, 15 % (v/v) PEG 400
A3	0.1 M lithium chloride, 0.1 M HEPES, pH 7.5, 20 % (v/v) PEG 400
A4	0.1 M tris, pH 8.0, 25 % (v/v) PEG 400
A5	0.1 M MES, pH 6.5, 15 % (w/v) PEG 550 MME
A6	0.2 M sodium chloride, 0.1 M Na/K phosphate, pH 6.5, 25 % (w/v) PEG 1,000
A7	0.1 M ammonium sulfate, 0.1 M tris, pH 7.5, 20 % (w/v) PEG 1,500
A8	0.2 M ammonium sulfate, 0.1 M sodium acetate, pH 5.5, 10 % (w/v) PEG 2,000 MME
A9	0.2 M sodium chloride, 0.1 M MES, pH 6.0, 20 % (w/v) PEG 2,000 MME
A10	0.1 M potassium chloride, 0.1 M tris, pH 8.0, 15 % (w/v) PEG 2,000 MME
A11	0.1 M HEPES, pH 7.5, 25 % (w/v) PEG 2,000 MME
A12	0.2 M sodium acetate, 0.1 M sodium citrate, pH 5.5, 5 % (w/v) PEG 4,000
B1	0.2 M lithium sulfate, 0.1 M tris, pH 7.5, 5 % (w/v) PEG 4,000
B2	0.1 M calcium acetate, 0.1 M sodium acetate, pH 4.5, 10 % (w/v) PEG 4,000
B3	0.2 M sodium acetate, 0.1 M sodium citrate, pH 5.5, 10 % (w/v) PEG 4,000
B4	0.2 M sodium chloride, 0.1 M MES, pH 6.5, 10 % (w/v) PEG 4,000
B5	0.1 M magnesium chloride, 0.1 M HEPES, pH 7.5, 10 % (w/v) PEG 4,000
B6	0.1 M HEPES, pH 7.0, 10 % (w/v) PEG 4,000, 10 % (v/v) isopropanol
B7	0.2 M ammonium acetate, 0.1 M sodium acetate, pH 4.0, 15 % (w/v) PEG 4,000
B8	0.1 M magnesium chloride, 0.1 M sodium citrate, pH 5.0, 15 % (w/v) PEG 4,000
B9	0.1 M sodium cacodylate, pH 6.0, 15 % (w/v) PEG 4,000
B10	0.15 M ammonium sulfate, 0.1 M MES, pH 6.0, 15 % (w/v) PEG 4,000
B11	0.1 M HEPES, pH 7.0, 15 % (w/v) PEG 4,000
B12	0.1 M magnesium chloride, 0.1 M HEPES, pH 7.0, 15 % (w/v) PEG 4,000
C1	0.15 M ammonium sulfate, 0.1 M tris, pH 8.0, 15 % (w/v) PEG 4,000
C2	0.1 M sodium citrate, pH 4.5, 20 % (w/v) PEG 4,000
C3	0.2 M ammonium acetate, 0.1 M sodium acetate, pH 5.0, 20 % (w/v) PEG 4,000
C4	0.2 M lithium sulfate, 0.1 M MES, pH 6.0, 20 % (w/v) PEG 4,000
C5	0.1 M tris pH 8.0, 20 % (w/v) PEG 4,000
C6	0.15 M ammonium sulfate, 0.1 M HEPES, pH 7.0, 20 % (w/v) PEG 4,000
C7	0.1 M sodium citrate, pH 5.6, 20 % (w/v) PEG 4,000, 20 % (v/v) isopropanol
C8	0.2 M sodium chloride, 0.1 M tris, pH 8.0, 20 % (w/v) PEG 4,000
C9	0.1 M sodium cacodylate, pH 5.5, 25 % (w/v) PEG 4,000
C10	0.15 M ammonium sulfate, 0.1 M MES, pH 5.5, 25 % (w/v) PEG 4,000
C11	0.1 M sodium cacodylate, pH 6.5, 25 % (w/v) PEG 4,000
C12	0.2 M potassium iodide, 0.1 M MES, pH 6.5, 25 % (w/v) PEG 4,000
D1	0.2 M sodium chloride, 0.1 M HEPES, pH 7.5, 25 % (w/v) PEG 4,000
D2	0.1 M MES, pH 6.5, 10 % (w/v) PEG 5,000 MME, 12 % (v/v) 1-propanol
D3	0.1 M potassium chloride, 0.1 M HEPES, pH 7.0, 15 % (w/v) PEG 5,000 MME
D4	0.2 M ammonium sulfate, 0.1 M tris, pH 7.5, 20 % (w/v) PEG 5,000 MME
D5	0.1 M magnesium chloride, 0.1 M MES, pH 6.0, 8 % (w/v) PEG 6,000
D6	0.15 M sodium chloride, 0.1 M tris, pH 8.0, 8 % (w/v) PEG 6,000
D7	0.1 M sodium citrate, pH 5.5, 15 % (w/v) PEG 6,000
D8	0.1 M magnesium acetate, 0.1 M sodium cacodylate, pH 6.5, 15 % (w/v) PEG 6,000
D9	0.1 M MES, pH 6.5, 15 % (w/v) PEG 6,000, 5 % (v/v) MPD
D10	0.1 M potassium chloride, 0.1 M HEPES, pH 7.5, 15 % (w/v) PEG 6,000
D11	0.1 M tris, pH 7.5, 15 % (w/v) PEG 6,000
D12	0.1 M tris, pH 8.5, 20 % (w/v) PEG 6,000

Table 11 – Definition of the QIAGEN Nextal protein complex screen 2/2.

Well no.	Crystallisation parameters
E1	0.1 M magnesium acetate, 0.1 M sodium acetate, pH 4.5, 8 % (w/v) PEG 8,000
E2	0.1 M sodium citrate, pH 5.0, 8 % (w/v) PEG 8,000
E3	0.2 M sodium chloride, 0.1 M sodium cacodylate, pH 6.0, 8 % (w/v) PEG 8,000
E4	0.1 M HEPES, pH 7.0, 8 % (w/v) PEG 8,000
E5	0.1 M tris, pH 8.0, 8 % (w/v) PEG 8,000
E6	0.1 M calcium acetatec 0.1 M sodium cacodylate, pH 5.5, 12 % (w/v) PEG 8,000
E7	0.1 M sodium dihydrogen phosphate, pH 6.5, 12 % (w/v) PEG 8,000
E8	0.1 M magnesium acetate, 0.1 M MOPS, pH 7.5, 12 % (w/v) PEG 8,000
E9	0.2 M sodium chloride, 0.1 M HEPES, pH 7.5, 12 % (w/v) PEG 8,000
E10	0.2 M ammonium sulfate, 0.1 M tris, pH 8.5, 12 % (w/v) PEG 8,000
E11	0.1 M sodium citrate, pH 5.0, 20 % (w/v) PEG 8,000
E12	0.2 M ammonium sulfate, 0.1 M MES, pH 6.5, 20 % (w/v) PEG 8,000
F1	0.1 M HEPES, pH 7.0, 20 % (w/v) PEG 8,000
F2	0.2 M lithium chloride, 0.1 M tris, pH 80, 20 % (w/v) PEG 8,000
F3	0.1 M magnesium acetate, 0.1 M MES, pH 6.5, 10 % (w/v) PEG 10,000
F4	0.1 M HEPES, pH 7.0, 18 % (w/v) PEG 12,000
F5	0.1 M sodium chloride, 0.1 M tris, pH 8.0, 8 % (w/v) PEG 20,000
F6	0.1 M HEPES, pH 7.0, 15 % (w/v) PEG 20,000
F7	0.1 M MES, pH 6.5, 0.5 M ammonium sulfate
F8	0.1 M sodium acetate, pH 5.0, 1.0 M ammonium sulfate
F9	0.1 M MES, pH 6.5, 1.0 M ammonium sulfate
F10	0.1 M tris, pH 8.0, 1.0 M ammonium sulfate
F11	0.1 M sodium acetate, pH 5.0, 1.5 M ammonium sulfate
F12	0.1 M HEPES, pH 7.0, 1.5 M ammonium sulfate
G1	0.1 M tris, pH 8.0, 1.5 M ammonium sulfate
G2	0.1 M sodium acetate, pH 5.0, 2.0 M ammonium sulfate
G3	0.1 M HEPES, pH 7.0, 2.0 M ammonium sulfate
G4	0.1 M tris, pH 8.0, 2.0 M ammonium sulfate
G5	1.0 M potassium chloride, 0.1 M HEPES, pH 7.0, 1.0 M ammonium sulfate
G6	0.1 M sodium acetate, pH 5.0, 2.0 M sodium formate
G7	0.1 M tris, pH 7.5, 3.0 M sodium formate
G8	0.8 M potassium/sodium phosphate, pH 7.5
G9	1.3 M potassium/sodium phosphate, pH 7.0
G10	1.6 M potassium/sodium phosphate, pH 6.5
G11	0.1 M HEPES, pH 7.5, 1.0 M sodium acetate
G12	0.1 M HEPES, pH 7.0, 1.0 M sodium citrate
H1	0.1 M sodium citrate, pH 6.0, 2.0 M sodium chloride
H2	0.1 M MES, pH 6.5, 1.0 M lithium sulfate
H3	0.1 M tris, pH 8.0, 1.6 M lithium sulfate
H4	1.4 M sodium malonate, pH 6.0
H5	0.1 M tris, pH 8.0, 1.2 M sodium/potassium tartrate
H6	0.1 M MES, pH 6.5, 1.6 M magnesium sulfate
H7	0.1 M sodium acetate, pH 5.0, 15 % (v/v) MPD, 2 % (w/v) PEG 4,000
H8	0.05 M calcium acetate, 0.1 M sodium cacodylate, pH 6.0, 25 % (v/v) MPD
H9	0.1 M imidazole, pH 7.0, 50 % (v/v) MPD
H10	0.05 M magnesium chloride 0.1 M MES, pH 6.5, 10 % (v/v) isopropanol, 5 % (w/v) PEG 4,000
H11	0.2 M ammonium acetate, 0.1 M HEPES, pH 7.5, 25 % (v/v) isopropanol
H12	0.1 M sodium chloride, 0.1 M tris, pH 8.0, 15 % (v/v) ethanol, 5 %(v/v) MPD

Table 12 – Definition of the QIAGEN Nextal pH clear screen.

Well no.	Crystallisation parameters	Well no.	Crystallisation parameters
A1	0.1 M citric acid, pH 4.0, 1.0 M sodium chloride	E1	0.1 M citric acid, pH 4.0, 0.8 M ammonium sulfate
A2	0.1 M citric acid, pH 5.0, 1.0 M sodium chloride	E2	0.1 M citric acid, pH 5.0, 0.8 M ammonium sulfate
A3	0.1 M MES, pH 6.0, 1.0 M sodium chloride	E3	0.1 M MES, pH 6.0, 0.8 M ammonium sulfate
A4	0.1 M HEPES, pH 7.0, 1.0 M sodium chloride	E4	0.1 M HEPES, pH 7.0, 0.8 M ammonium sulfate
A5	0.1 M tris, pH 8.0, 1.0 M sodium chloride	E5	0.1 M tris, pH 8.0, 0.8 M ammonium sulfate
A6	0.1 M bicine, pH 9.0, 1.0 M sodium chloride	E6	0.1 M bicine, pH 9.0, 0.8 M ammonium sulfate
A7	0.1 M citric acid, pH 4.0, 2.0 M sodium chloride	E7	0.1 M citric acid, pH 4.0, 1.6 M ammonium sulfate
A8	0.1 M citric acid, pH 5.0, 2.0 M sodium chloride	E8	0.1 M citric acid, pH 5.0, 1.6 M ammonium sulfate
A9	0.1 M MES, pH 6.0, 2.0 M sodium chloride	E9	0.1 M MES, pH 6.0, 1.6 M ammonium sulfate
A10	0.1 M HEPES, pH 7.0, 2.0 M sodium chloride	E10	0.1 M HEPES, pH 7.0, 1.6 M ammonium sulfate
A11	0.1 M tris, pH 8.0, 2.0 M sodium chloride	E11	0.1 M tris, pH 8.0, 1.6 M ammonium sulfate
A12	0.1 M bicine, pH 9.0, 2.0 M sodium chloride	E12	0.1 M bicine, pH 9.0, 1.6 M ammonium sulfate
B1	0.1 M citric acid, pH 4.0, 3.0 M sodium chloride	F1	0.1 M citric acid, pH 4.0, 2.4 M ammonium sulfate
B2	0.1 M citric acid, pH 5.0, 3.0 M sodium chloride	F2	0.1 M citric acid, pH 5.0, 2.4 M ammonium sulfate
B3	0.1 M MES, pH 6.0, 3.0 M sodium chloride	F3	0.1 M MES, pH 6.0, 2.4 M ammonium sulfate
B4	0.1 M HEPES, pH 7.0, 3.0 M sodium chloride	F4	0.1 M HEPES, pH 7.0, 2.4 M ammonium sulfate
B5	0.1 M tris, pH 8.0, 3.0 M sodium chloride	F5	0.1 M tris, pH 8.0, 2.4 M ammonium sulfate
B6	0.1 M bicine, pH 9.0, 3.0 M sodium chloride	F6	0.1 M bicine, pH 9.0, 2.4 M ammonium sulfate
B7	0.1 M citric acid, pH 4.0, 4.0 M sodium chloride	F7	0.1 M citric acid, pH 4.0, 3.2 M ammonium sulfate
B8	0.1 M citric acid, pH 5.0, 4.0 M sodium chloride	F8	0.1 M citric acid, pH 5.0, 3.2 M ammonium sulfate
B9	0.1 M MES, pH 6.0, 4.0 M sodium chloride	F9	0.1 M MES, pH 6.0, 3.2 M ammonium sulfate
B10	0.1 M HEPES, pH 7.0, 4.0 M sodium chloride	F10	0.1 M HEPES, pH 7.0, 3.2 M ammonium sulfate
B11	0.1 M tris, pH 8.0, 4.0 M sodium chloride	F11	0.1 M tris, pH 8.0, 3.2 M ammonium sulfate
B12	0.1 M bicine, pH 9.0, 4.0 M sodium chloride	F12	0.1 M bicine, pH 9.0, 3.2 M ammonium sulfate
C1	0.1 M citric acid, pH 4.0, 5 % (w/v) PEG 6,000	G1	0.1 M citric acid, pH 4.0, 10 % (v/v) MPD
C2	0.1 M citric acid, pH 5.0, 5 % (w/v) PEG 6,000	G2	0.1 M sodium acetate, pH 5.0, 10 % (v/v) MPD
C3	0.1 M MES, pH 6.0, 5 % (w/v) PEG 6,000	G3	0.1 M MES, pH 6.0, 10 % (v/v) MPD
C4	0.1 M HEPES, pH 7.0, 5 % (w/v) PEG 6,000	G4	0.1 M HEPES, pH 7.0, 10 % (v/v) MPD
C5	0.1 M tris, pH 8.0, 5 % (w/v) PEG 6,000	G5	0.1 M tris, pH 8.0, 10 % (v/v) MPD
C6	0.1 M bicine, pH 9.0, 5 % (w/v) PEG 6,000	G6	0.1 M bicine, pH 9.0, 10 % (v/v) MPD
C7	0.1 M citric acid, pH 4.0, 10 % (w/v) PEG 6,000	G7	0.1 M citric acid, pH 4.0, 20 % (v/v) MPD
C8	0.1 M citric acid, pH 5.0, 10 % (w/v) PEG 6,000	G8	0.1 M sodium acetate, pH 5.0, 20 % (v/v) MPD
C9	0.1 M MES, pH 6.0, 10 % (w/v) PEG 6,000	G9	0.1 M MES, pH 6.0, 20 % (v/v) MPD
C10	0.1 M HEPES, pH 7.0, 10 % (w/v) PEG 6,000	G10	0.1 M HEPES, pH 7.0, 20 % (v/v) MPD
C11	0.1 M tris, pH 8.0, 10 % (w/v) PEG 6,000	G11	0.1 M tris, pH 8.0, 20 % (v/v) MPD
C12	0.1 M bicine, pH 9.0, 10 % (w/v) PEG 6,000	G12	0.1 M bicine, pH 9.0, 20 % (v/v) MPD
D1	0.1 M citric acid, pH 4.0, 20 % (w/v) PEG 6,000	H1	0.1 M citric acid, pH 4.0, 40 % (v/v) MPD
D2	0.1 M citric acid, pH 5.0, 20 % (w/v) PEG 6,000	H2	0.1 M sodium acetate, pH 5.0, 40 % (v/v) MPD
D3	0.1 M MES, pH 6.0, 20 % (w/v) PEG 6,000	H3	0.1 M MES, pH 6.0, 40 % (v/v) MPD
D4	0.1 M HEPES, pH 7.0, 20 % (w/v) PEG 6,000	H4	0.1 M HEPES, pH 7.0, 40 % (v/v) MPD
D5	0.1 M tris, pH 8.0, 20 % (w/v) PEG 6,000	H5	0.1 M tris, pH 8.0, 40 % (v/v) MPD
D6	0.1 M bicine, pH 9.0, 20 % (w/v) PEG 6,000	H6	0.1 M bicine, pH 9.0, 40 % (v/v) MPD
D7	0.1 M citric acid, pH 4.0, 30 % (w/v) PEG 6,000	H7	0.1 M citric acid, pH 4.0, 65 % (v/v) MPD
D8	0.1 M citric acid, pH 5.0, 30 % (w/v) PEG 6,000	H8	0.1 M sodium acetate, pH 5.0, 65 % (v/v) MPD
D9	0.1 M MES, pH 6.0, 30 % (w/v) PEG 6,000	H9	0.1 M MES, pH 6.0, 65 % (v/v) MPD
D10	0.1 M HEPES, pH 7.0, 30 % (w/v) PEG 6,000	H10	0.1 M HEPES, pH 7.0, 65 % (v/v) MPD
D11	0.1 M tris, pH 8.0, 30 % (w/v) PEG 6,000	H11	0.1 M tris, pH 8.0, 65 % (v/v) MPD
D12	0.1 M bicine, pH 9.0, 30 % (w/v) PEG 6,000	H12	0.1 M bicine, pH 9.0, 65 % (v/v) MPD

Table 13 – Definition of the Fluidigm Topaz Optimix 3 screen.

Well no.	Crystallisation parameters	Well no.	Crystallisation parameters
A1	2.5 M ammonium sulfate, 0.1 M HEPES, pH 7.5	E1	0.6 M potassium thiocyanate, 0.1 M sodium citrate, pH 5.6
A2	4.0 M ammonium nitrate, 0.1 M bicine, pH 9.0	E2	1.0 M magnesium sulfate, 0.1 M MES, pH 6.0
A3	2.5 M ammonium sulfate, 0.1 M bicine, pH 9.0	E3	1.5 M magnesium sulfate, 0.1 M tris HCl, pH 8.5
A4	3.0 M potassium formate, 0.1 M sodium acetate, pH 4.6	E4	0.8 M sodium acetate, 0.1 M sodium citrate, pH 5.6
A5	3.5 M ammonium chloride, 0.1 M sodium acetate, pH 4.6	E5	0.5 M sodium chloride, 0.1 M HEPES, pH 7.5
A6	2.5 M ammonium sulfate, 0.1 M sodium acetate, pH 4.6	E6	0.5 M sodium malonate, 0.1 M HEPES, pH 7.5
A7	3.0 M sodium nitrate, 0.1 M MES, pH 6.0	E7	0.8 M potassium sodium tartrate
A8	3.0 M lithium nitrate, 0.1 M bicine, pH 9.0	E8	0.8 M sodium tartrate, 0.1 M sodium acetate, pH 4.6
A9	3.0 M ammonium acetate	E9	1.0 M ammonium acetate, 0.1 M sodium cacodylate, pH 6.5
A10	1.5 M magnesium acetate, 0.1 M bis-tris, pH 6.0	E10	0.8 M sodium tartrate, 0.1 M tris HCl, pH 8.5
A11	3.0 M sodium formate, 0.1 M imidazole, pH 8.0	E11	1.0 M potassium phosphate, dibasic
A12	3.0 M potassium acetate, 0.1 M sodium cacodylate, pH 6.5	E12	1.0 M sodium phosphate monobasic
B1	2.0 M potassium sodium tartrate	F1	1.0 M ammonium sulfate, 0.1 M MES, pH 6.0
B2	2.0 M ammonium sulfate, 0.1 M MES, pH 6.0	F2	1.0 M potassium formate, 0.1 M sodium cacodylate, pH 6.5
B3	1.5 M sodium malonate, 0.1 M HEPES, pH 7.5	F3	1.5 M ammonium nitrate, 0.1 M sodium acetate, pH 4.6
B4	2.0 M potassium phosphate, dibasic	F4	1.0 M sodium malonate, 0.1 M tris HCl, pH 8.5
B5	2.0 M ammonium sulfate, 0.1 M sodium acetate, pH 4.6	F5	1.0 M potassium sodium tartrate
B6	2.0 M ammonium sulfate, 0.1 M HEPES, pH 7.5	F6	0.9 M sodium tartrate, 0.1 M HEPES, pH 7.5
B7	1.5 M sodium malonate, 0.1 M tris HCl, pH 8.5	F7	1.0 M ammonium sulfate, 0.1 M bicine, pH 9.0
B8	1.8 M sodium acetate, 0.1 M imidazole, pH 8.0	F8	1.5 M potassium formate, 0.1 M bis-tris propane, pH 7.0
B9	1.2 M potassium thiocyanate, 0.1 M HEPES, pH 7.5	F9	1.5 M ammonium acetate
B10	1.5 M potassium sodium tartrate	F10	1.0 M sodium malonate, 0.1 M sodium citrate, pH 5.6
B11	2.0 M sodium nitrate, 0.1 M sodium acetate, pH 4.6	F11	2.0 M sodium phosphate monobasic
B12	2.0 M ammonium chloride, 0.1 M sodium cacodylate,pH 6.5	F12	1.8 M potassium thiocyanate, 0.1 M tris HCl, pH 8.5
C1	1.5 M lithium acetate, 0.1 M sodium acetate, pH 4.6	G1	2.0 M ammonium nitrate, 0.1 M HEPES, pH 7.5
C2	1.5 M potassium phosphate, dibasic	G2	1.5 M lithium nitrate, 0.1 M sodium acetate, pH 4.6
C3	1.0 M sodium malonate, 0.1 M sodium acetate, pH 4.6	G3	1.5 M sodium malonate, 0.1 M sodium acetate, pH 4.6
C4	1.0 M sodium malonate, 0.1 M HEPES, pH 7.5	G4	2.0 M sodium formate, 0.1 M sodium cacodylate, pH 6.5
C5	1.0 M magnesium acetate, 0.1 M tris HCl, pH 8.5	G5	1.5 M sodium acetate, 0.1 M HEPES, pH 7.0
C6	1.0 M ammonium citrate, 0.1 M sodium citrate, pH 5.6	G6	1.8 M potassium thiocyanate, 0.1 M sodium acetate, pH 4.6
C7	1.2 M potassium thiocyanate, 0.1 M bis-tris propane, pH 7.0	G7	2.0 M ammonium formate, 0.1 M sodium cacodylate, pH 6.5
C8	0.9 M sodium tartrate, 0.1 M bicine, pH 9.0	G8	2.0 M ammonium sulfate, 0.1 M bicine, pH 9.0
C9	1.0 M sodium acetate, 0.1 M sodium cacodylate, pH 6.5	G9	1.5 M sodium malonate, 0.1 M sodium citrate, pH 5.6
C10	1.0 M ammonium sulfate, 0.1 M tris HCl, pH 8.5	G10	2.0 M sodium chloride, 0.1 M sodium cacodylate, pH 6.5
C11	1.0 M ammonium sulfate, 0.1 M sodium acetate, pH 4.6	G11	2.0 M ammonium sulfate, 0.1 M tris HCl, pH 8.5
C12	1.0 M ammonium sulfate, 0.1 M HEPES, pH 7.5	G12	2.0 M ammonium acetate
D1	0.8 M sodium tartrate, 0.1 M bis-tris propane, pH 7.0	H1	3.0 M lithium acetate, 0.1 M bis-tris propane, pH 7.0
D2	1.0 M sodium chloride, 0.1 M tris HCl, pH 8.5	H2	2.0 M potassium acetate, 0.1 M tris HCl, pH 8.5
D3	0.7 M sodium tartrate, 0.1 M sodium citrate, pH 5.6	H3	3.0 M sodium chloride, 0.1 M bis-tris propane, pH 7.0
D4	1.0 M sodium formate, 0.1 M HEPES, pH 7.5	H4	3.5 M sodium formate, 0.1 M sodium citrate, pH 5.6
D5	1.0 M ammonium chloride, 0.1 M sodium acetate, pH 4.6	H5	1.5 M ammonium citrate, 0.1 M HEPES, pH 7.5
D6	0.8 M sodium tartrate, 0.1 M sodium cacodylate, pH 6.5	H6	3.0 M ammonium nitrate, 0.1 M MES, pH 6.0
D7	1.0 M ammonium nitrate, 0.1 M MES, pH 6.0	H7	3.0 M lithium nitrate, 0.1 M sodium cacodylate, pH 6.5
D8	0.5 M sodium malonate, 0.1 M sodium citrate, pH 5.6	H8	2.5 M ammonium sulfate, 0.1 M MES, pH 6.0
D9	0.5 M sodium malonate, 0.1 M tris HCl, pH 8.5	H9	4.0 M ammonium formate, 0.1 M bis-tris propane, pH 7.0
D10	0.6 M potassium thiocyanate, 0.1 M sodium cacodylate, pH 6.5	H10	4.0 M potassium acetate, 0.1 M bicine, pH 9.0
D11	0.5 M sodium malonate, 0.1 M sodium acetate, pH 4.6	H11	2.5 M ammonium sulfate, 0.1 M tris HCl, pH 8.5
D12	0.7 M sodium tartrate, 0.1 M MES, pH 6.0	H12	2.5 M potassium formate, 0.1 M sodium cacodylate, pH 6.5

Table 14 – Definition of the Nextal C12 fine-screen.

Well no.	Crystallisation parameters	Well no.	Crystallisation parameters
A1	0.1 M citric acid pH 5.5, 18 % PEG 10,000	E1	0.1 M tris pH 7.0, 18 % PEG 10,000
A2	0.1 M citric acid pH 5.5, 19 % PEG 10,000	E2	0.1 M tris pH 7.0, 19 % PEG 10,000
A3	0.1 M citric acid pH 5.5, 20 % PEG 10,000	E3	0.1 M tris pH 7.0, 20 % PEG 10,000
A4	0.1 M citric acid pH 5.5, 21 % PEG 10,000	E4	0.1 M tris pH 7.0, 21 % PEG 10,000
A5	0.1 M citric acid pH 5.5, 22 % PEG 10,000	E5	0.1 M tris pH 7.0, 22 % PEG 10,000
A6	0.1 M citric acid pH 5.5, 23 % PEG 10,000	E6	0.1 M tris pH 7.0, 23 % PEG 10,000
A7	0.1 M citric acid pH 5.5, 13 % PEG 20,000	E7	0.1 M tris pH 7.0, 13 % PEG 20,000
A8	0.1 M citric acid pH 5.5, 14 % PEG 20,000	E8	0.1 M tris pH 7.0, 14 % PEG 20,000
A9	0.1 M citric acid pH 5.5, 15 % PEG 20,000	E9	0.1 M tris pH 7.0, 15 % PEG 20,000
A10	0.1 M citric acid pH 5.5, 16 % PEG 20,000	E10	0.1 M tris pH 7.0, 16 % PEG 20,000
A11	0.1 M citric acid pH 5.5, 17 % PEG 20,000	E11	0.1 M tris pH 7.0, 17 % PEG 20,000
A12	0.1 M citric acid pH 5.5, 18 % PEG 20,000	E12	0.1 M tris pH 7.0, 18 % PEG 20,000
B1	0.1 M MES pH 5.5, 18 % PEG 10,000	F1	0.1 M tris pH 7.5, 18 % PEG 10,000
B2	0.1 M MES pH 5.5, 19 % PEG 10,000	F2	0.1 M tris pH 7.5, 19 % PEG 10,000
B3	0.1 M MES pH 5.5, 20 % PEG 10,000	F3	0.1 M tris pH 7.5, 20 % PEG 10,000
B4	0.1 M MES pH 5.5, 21 % PEG 10,000	F4	0.1 M tris pH 7.5, 21 % PEG 10,000
B5	0.1 M MES pH 5.5, 22 % PEG 10,000	F5	0.1 M tris pH 7.5, 22 % PEG 10,000
B6	0.1 M MES pH 5.5, 23 % PEG 10,000	F6	0.1 M tris pH 7.5, 23 % PEG 10,000
B7	0.1 M MES pH 5.5, 13 % PEG 20,000	F7	0.1 M tris pH 7.5, 13 % PEG 20,000
B8	0.1 M MES pH 5.5, 14 % PEG 20,000	F8	0.1 M tris pH 7.5, 14 % PEG 20,000
B9	0.1 M MES pH 5.5, 15 % PEG 20,000	F9	0.1 M tris pH 7.5, 15 % PEG 20,000
B10	0.1 M MES pH 5.5, 16 % PEG 20,000	F10	0.1 M tris pH 7.5, 16 % PEG 20,000
B11	0.1 M MES pH 5.5, 17 % PEG 20,000	F11	0.1 M tris pH 7.5, 17 % PEG 20,000
B12	0.1 M MES pH 5.5, 18 % PEG 20,000	F12	0.1 M tris pH 7.5, 18 % PEG 20,000
C1	0.1 M MES pH 6.0, 18 % PEG 10,000	G1	0.1 M sodium phosphate pH 6.0, 18 % PEG 10,000
C2	0.1 M MES pH 6.0, 19 % PEG 10,000	G2	0.1 M sodium phosphate pH 6.0, 19 % PEG 10,000
C3	0.1 M MES pH 6.0, 20 % PEG 10,000	G3	0.1 M sodium phosphate pH 6.0, 20 % PEG 10,000
C4	0.1 M MES pH 6.0, 21 % PEG 10,000	G4	0.1 M sodium phosphate pH 6.0, 21 % PEG 10,000
C5	0.1 M MES pH 6.0, 22 % PEG 10,000	G5	0.1 M sodium phosphate pH 6.0, 22 % PEG 10,000
C6	0.1 M MES pH 6.0, 23 % PEG 10,000	G6	0.1 M sodium phosphate pH 6.0, 23 % PEG 10,000
C7	0.1 M MES pH 6.0, 13 % PEG 20,000	G7	0.1 M sodium phosphate pH 6.0, 13 % PEG 20,000
C8	0.1 M MES pH 6.0, 14 % PEG 20,000	G8	0.1 M sodium phosphate pH 6.0, 14 % PEG 20,000
C9	0.1 M MES pH 6.0, 15 % PEG 20,000	G9	0.1 M sodium phosphate pH 6.0, 15 % PEG 20,000
C10	0.1 M MES pH 6.0, 16 % PEG 20,000	G10	0.1 M sodium phosphate pH 6.0, 16 % PEG 20,000
C11	0.1 M MES pH 6.0, 17 % PEG 20,000	G11	0.1 M sodium phosphate pH 6.0, 17 % PEG 20,000
C12	0.1 M MES pH 6.0, 18 % PEG 20,000	G12	0.1 M sodium phosphate pH 6.0, 18 % PEG 20,000
D1	0.1 M MES pH 6.5, 18 % PEG 10,000	H1	0.1 M sodium phosphate pH 6.5, 18 % PEG 10,000
D2	0.1 M MES pH 6.5, 19 % PEG 10,000	H2	0.1 M sodium phosphate pH 6.5, 19 % PEG 10,000
D3	0.1 M MES pH 6.5, 20 % PEG 10,000	H3	0.1 M sodium phosphate pH 6.5, 20 % PEG 10,000
D4	0.1 M MES pH 6.5, 21 % PEG 10,000	H4	0.1 M sodium phosphate pH 6.5, 21 % PEG 10,000
D5	0.1 M MES pH 6.5, 22 % PEG 10,000	H5	0.1 M sodium phosphate pH 6.5, 22 % PEG 10,000
D6	0.1 M MES pH 6.5, 23 % PEG 10,000	H6	0.1 M sodium phosphate pH 6.5, 23 % PEG 10,000
D7	0.1 M MES pH 6.5, 13 % PEG 20,000	H7	0.1 M sodium phosphate pH 6.5, 13 % PEG 20,000
D8	0.1 M MES pH 6.5, 14 % PEG 20,000	H8	0.1 M sodium phosphate pH 6.5, 14 % PEG 20,000
D9	0.1 M MES pH 6.5, 15 % PEG 20,000	H9	0.1 M sodium phosphate pH 6.5, 15 % PEG 20,000
D10	0.1 M MES pH 6.5, 16 % PEG 20,000	H10	0.1 M sodium phosphate pH 6.5, 16 % PEG 20,000
D11	0.1 M MES pH 6.5, 17 % PEG 20,000	H11	0.1 M sodium phosphate pH 6.5, 17 % PEG 20,000
D12	0.1 M MES pH 6.5, 18 % PEG 20,000	H12	0.1 M sodium phosphate pH 6.5, 18 % PEG 20,000

Table 15 – Definition of the MITat fine-screen.

Well no.	Crystallisation parameters	Well no.	Crystallisation parameters
A1	0.1 M citric acid pH 4.0, 1.6 M ammonium sulfate	E1	0.1 M tris pH 7.0, 1.6 M ammonium sulfate
A2	0.1 M citric acid pH 4.0, 2.0 M ammonium sulfate	E2	0.1 M tris pH 7.0, 2.0 M ammonium sulfate
A3	0.1 M citric acid pH 4.0, 2.4 M ammonium sulfate	E3	0.1 M tris pH 7.0, 2.4 M ammonium sulfate
A4	0.1 M citric acid pH 4.0, 2.8 M ammonium sulfate	E4	0.1 M tris pH 7.0, 2.8 M ammonium sulfate
A5	0.1 M citric acid pH 4.0, 3.0 M ammonium sulfate	E5	0.1 M tris pH 7.0, 3.0 M ammonium sulfate
A6	0.1 M citric acid pH 4.0, 3.2 M ammonium sulfate	E6	0.1 M tris pH 7.0, 3.2 M ammonium sulfate
A7	0.1 M MES pH 5.5, 1.6 M ammonium sulfate	E7	0.1 M bicine pH 8.5, 1.6 M ammonium sulfate
A8	0.1 M MES pH 5.5, 2.0 M ammonium sulfate	E8	0.1 M bicine pH 8.5, 2.0 M ammonium sulfate
A9	0.1 M MES pH 5.5, 2.4 M ammonium sulfate	E9	0.1 M bicine pH 8.5, 2.4 M ammonium sulfate
A10	0.1 M MES pH 5.5, 2.6 M ammonium sulfate	E10	0.1 M bicine pH 8.5, 2.8 M ammonium sulfate
A11	0.1 M MES pH 5.5, 2.8 M ammonium sulfate	E11	0.1 M bicine pH 8.5, 3.0 M ammonium sulfate
A12	0.1 M MES pH 5.5, 3.0 M ammonium sulfate	E12	0.1 M bicine pH 8.5, 3.2 M ammonium sulfate
B1	0.1 M citric acid pH 4.5, 1.6 M ammonium sulfate	F1	0.1 M tris pH 7.5, 1.6 M ammonium sulfate
B2	0.1 M citric acid pH 4.5, 2.0 M ammonium sulfate	F2	0.1 M tris pH 7.5, 2.0 M ammonium sulfate
B3	0.1 M citric acid pH 4.5, 2.4 M ammonium sulfate	F3	0.1 M tris pH 7.5, 2.4 M ammonium sulfate
B4	0.1 M citric acid pH 4.5, 2.8 M ammonium sulfate	F4	0.1 M tris pH 7.5, 2.8 M ammonium sulfate
B5	0.1 M citric acid pH 4.5, 3.0 M ammonium sulfate	F5	0.1 M tris pH 7.5, 3.0 M ammonium sulfate
B6	0.1 M citric acid pH 4.5, 3.2 M ammonium sulfate	F6	0.1 M tris pH 7.5, 3.2 M ammonium sulfate
B7	0.1 M MES pH 6.0, 1.6 M ammonium sulfate	F7	0.1 M bicine pH 9.0, 1.6 M ammonium sulfate
B8	0.1 M MES pH 6.0, 2.0 M ammonium sulfate	F8	0.1 M bicine pH 9.0, 2.0 M ammonium sulfate
B9	0.1 M MES pH 6.0, 2.4 M ammonium sulfate	F9	0.1 M bicine pH 9.0, 2.4 M ammonium sulfate
B10	0.1 M MES pH 6.0, 2.6 M ammonium sulfate	F10	0.1 M bicine pH 9.0, 2.8 M ammonium sulfate
B11	0.1 M MES pH 6.0, 2.8 M ammonium sulfate	F11	0.1 M bicine pH 9.0, 3.0 M ammonium sulfate
B12	0.1 M MES pH 6.0, 3.0 M ammonium sulfate	F12	0.1 M bicine pH 9.0, 3.2 M ammonium sulfate
C1	0.1 M citric acid pH 5.0, 1.6 M ammonium sulfate	G1	0.1 M tris pH 8.0, 1.6 M ammonium sulfate
C2	0.1 M citric acid pH 5.0, 2.0 M ammonium sulfate	G2	0.1 M tris pH 8.0, 2.0 M ammonium sulfate
C3	0.1 M citric acid pH 5.0, 2.4 M ammonium sulfate	G3	0.1 M tris pH 8.0, 2.4 M ammonium sulfate
C4	0.1 M citric acid pH 5.0, 2.8 M ammonium sulfate	G4	0.1 M tris pH 8.0, 2.8 M ammonium sulfate
C5	0.1 M citric acid pH 5.0, 3.0 M ammonium sulfate	G5	0.1 M tris pH 8.0, 3.0 M ammonium sulfate
C6	0.1 M citric acid pH 5.0, 3.2 M ammonium sulfate	G6	0.1 M tris pH 8.0, 3.2 M ammonium sulfate
C7	0.1 M MES pH 6.5, 1.6 M ammonium sulfate	G7	0.1 M hepes pH 7.0, 1.6 M ammonium sulfate
C8	0.1 M MES pH 6.5, 2.0 M ammonium sulfate	G8	0.1 M hepes pH 7.0, 2.0 M ammonium sulfate
C9	0.1 M MES pH 6.5, 2.4 M ammonium sulfate	G9	0.1 M hepes pH 7.0, 2.4 M ammonium sulfate
C10	0.1 M MES pH 6.5, 2.6 M ammonium sulfate	G10	0.1 M hepes pH 7.0, 2.8 M ammonium sulfate
C11	0.1 M MES pH 6.5, 2.8 M ammonium sulfate	G11	0.1 M hepes pH 7.0, 3.0 M ammonium sulfate
C12	0.1 M MES pH 6.5, 3.0 M ammonium sulfate	G12	0.1 M hepes pH 7.0, 3.2 M ammonium sulfate
D1	0.1 M citric acid pH 5.5, 1.6 M ammonium sulfate	H1	0.1 M tris pH 8.5, 1.6 M ammonium sulfate
D2	0.1 M citric acid pH 5.5, 2.0 M ammonium sulfate	H2	0.1 M tris pH 8.5, 2.0 M ammonium sulfate
D3	0.1 M citric acid pH 5.5, 2.4 M ammonium sulfate	H3	0.1 M tris pH 8.5, 2.4 M ammonium sulfate
D4	0.1 M citric acid pH 5.5, 2.8 M ammonium sulfate	H4	0.1 M tris pH 8.5, 2.8 M ammonium sulfate
D5	0.1 M citric acid pH 5.5, 3.0 M ammonium sulfate	H5	0.1 M tris pH 8.5, 3.0 M ammonium sulfate
D6	0.1 M citric acid pH 5.5, 3.2 M ammonium sulfate	H6	0.1 M tris pH 8.5, 3.2 M ammonium sulfate
D7	0.1 M bicine pH 8.0, 1.6 M ammonium sulfate	H7	0.1 M hepes pH 7.5, 1.6 M ammonium sulfate
D8	0.1 M bicine pH 8.0, 2.0 M ammonium sulfate	H8	0.1 M hepes pH 7.5, 2.0 M ammonium sulfate
D9	0.1 M bicine pH 8.0, 2.4 M ammonium sulfate	H9	0.1 M hepes pH 7.5, 2.4 M ammonium sulfate
D10	0.1 M bicine pH 8.0, 2.8 M ammonium sulfate	H10	0.1 M hepes pH 7.5, 2.8 M ammonium sulfate
D11	0.1 M bicine pH 8.0, 3.0 M ammonium sulfate	H11	0.1 M hepes pH 7.5, 3.0 M ammonium sulfate
D12	0.1 M bicine pH 8.0, 3.2 M ammonium sulfate	H12	0.1 M hepes pH 7.5, 3.2 M ammonium sulfate

8.2 Affidavit

In accordance to § 4, Abs. 3, Nr. 3, 5 and 8 of the PhD regulations of the faculty of biology of the Bavarian Julius-Maximilians-Universität Würzburg, I hereby declare that my thesis entitled: **"Structural and functional analysis of the trypanosomal variant surface glycoprotein using x-ray scattering techniques and fluorescence microscopy"** is the result of my own work.

I did not receive any help or support from commercial consultants. All sources and /or materials applied are listed and specified in the thesis.

Furthermore I verify that the thesis has not been submitted as part of another examination process neither in identical nor in similar form.

Eidesstattliche Erklärung

Die vorliegende Arbeit wurde am Lehrstuhl für Zell- und Entwicklungsbiologie der Universität Würzburg in der Arbeitsgruppe von Prof. Dr. Markus Engstler von Juli 2011 bis Februar 2017 angefertigt.

Gemäß § 4, Abs. 3, Nr. 3, 5 und 8 der Promotionsordnung der Fakultät für Biologie der Bayerischen Julius-Maximilians-Universität Würzburg erkläre ich hiermit ehrenwörtlich, dass ich die vorliegende Dissertation mit dem Titel: **"Structural and functional analysis of the trypanosomal variant surface glycoprotein using x-ray scattering techniques and fluorescence microscopy"** selbstständig angefertig und keine anderen als die angegebenen Quellen als Hilfsmittel verwendet habe.

Ich erkläre weiterhin, dass die vorliegende Dissertation weder in gleicher, noch in ähnlicher Form bereits in einem anderen Prüfungsverfahren vorgelegen hat.

Ort, Datum

Thomas Bartossek

8.3 Publications

Parts of this thesis are included in following publications:

Bartossek, T.*, Jones, N. G.*, Schäfer, C., Mott, H. R., Kuper J., Brennich, M., Carrington, M., Kisker, C. and Engstler M. Structural basis for the shielding function of the trypanosome VSG coat. (Manuscript submitted to Nature Microbiology).
*The authors contributed equally to this work.

8.4 Acknowledgements

Naturgemäß ist dies die erste und wichtigste Seite jeder Abschlussarbeit. Hier möchte ich allen Danken die mich während meiner Promotionszeit auf dem Weg begleitet und ihn mitgestaltet haben. **Danke!** Falls ich jemanden vergessen habe, mach ich das auf ein Bierchen wieder wett. Ihr müsst mich aber daran erinnern. Besonderer Dank gilt:

Markus, für die Freiheit und das Vertrauen deinem heimlichen Lieblingsthema meinen Stempel aufdrücken zu dürfen. Hätte schlimmer ausgehen können, oder? ;)

Prof. Dr. Thomas Dandekar, für die bereitwillige Übernahme des Zweitgutachtens.

Nicola, für Beistand in guten und in schlechten Zeiten und von Anfang an. Btw.: "1.6**5**" bleibt Referenz bis etwas besseres publiziert ist :P

Jamin, Christopher, Andi, Marius, Carina, Henriette, Sarah & Erick für das Teilen eines kleinen, schwankenden Boots. Ich hab alle von euch ein- oder aussteigen sehen ohne dass jemand dabei über Bord gegangen ist.

Ines & Henriette, dafür mit eiserner Hand die Zellkultur zu regieren. Ohne euch hätten wir längst einen Sündenpfuhl daraus gemacht!

Tine, Caroline, Wolfgang, Jochen und allen Helfershelfern aus der AG Kisker, ohne deren Zeit und Expertise viele meiner Ergebnisse nicht zustande gekommen wären.

Kathrin, Reinhild, Beate, Lidia, Elisabeth, Elina, Silke & Barbara, ohne die das Labor sehr viel leiser wäre aber niemals laufen könnte!

Tim & Susanne, für die Expertise sobald Dinge physikalisch wurden oder zu leuchten begannen.

Uli, für die Hilfe und Unterstützung während der ganzen Zeit.

Dem gesamten Lehrstuhl der Zoologie 1, für eine einzigartige Atmosphäre, ob bei der Arbeit, in der Weinstube, oder auf der Weihnachtsfeier. PS: Ab jetzt müsst ihr mich für die Weihnachtshows buchen. Ich lasse ggf. mit mir über Freundschaftspreise verhandeln.

Meinen Freunden in Würzburg, in der Heimat und "abroad". Schön dass ihr euch meldet wenn ich es vergesse und das auch nach längerer Zeit alles wie früher bleibt. Das verankert einen in der Realität.

Meiner WG, für ein entspanntes zusammen- & nebeneinander Wohnen!

Lisa, dafür dich nach etwas Einarbeitungszeit auf das Langzeitexperiment mit mir einzulassen! Ohne dich wären die vergangenen 4 Jahre nicht mal halb so erträglich gewesen. Für unendliche Geduld, Inspiration, Freude und dafür dass du nunmal bist wie du bist *Kopf schüttel*. Ich freu mich auf die Zukunft :)

Meinen Eltern und meiner Familie. Ich bin die Summe eurer (mehr oder weniger) guten Qualitäten. Seid ihr stolz auf mich, könnt ihr auch stolz auf euch selbst sein. ;)